ISSN 0973-3302

JOURNAL OF ACOUSTICAL SOCIETY OF INDIA

Volume 42 Number 1 January 2015

A Quarterly Publication of the JASI

http://www.acousticsindia.org

Journal of Acoustical Society of India

Volume 42 Number 1 January 2015 pp 1-60

JASI

Journal of Acoustical Society of India

The Refereed Journal of the Acoustical Society of India (JASI)

The Journal of Acoustical Society of India is a refereed journal of the Acoustical Society of India **(ASI)**. The **ASI** is a non-profit national society founded in 31st July, 1971. The primary objective of the society is to advance the science of acoustics by creating an organization that is responsive to the needs of scientists and engineers concerned with acoustics problems all around the world.

Manuscripts of articles, technical notes and letter to the editor should be submitted to the Chief Editor. Copies of articles on specific topics listed above should also be submitted to the respective Associate Scientific Editor. Manuscripts are refereed by at least two referees and are reviewed by Publication Committee (all editors) before acceptance. On acceptance, revised articles with the text and figures scanned as separate files on a diskette should be submitted to the Editor by express mail. Manuscripts of articles must be prepared in strict accordance with the author instructions.

All information concerning subscription, new books, journals, conferences, etc. should be submitted to Chief Editor:

B. Chakraborty, CSIR - National Institute of Oceanography, Dona Paula, Goa-403 004,
Tel: +91.832.2450.318, Fax: +91.832.2450.602, e-mail: bishwajit@nio.org

Annual subscription price including mail postage is Rs. 2500/= for institutions, companies and libraries and Rs. 2500/= for individuals who are not **ASI** members. The Journal of Acoustical Society of India will be sent to **ASI** members free of any extra charge. Requests for specimen copies and claims for missing issues as well as address changes should be sent to the Editorial Office:

ASI Secretariat, C/o Acoustics, Ultrasonics & Vibration Section, CSIR-National Physical Laboratory, Dr. KS Krishnan Road, New Delhi 110 012, Tel: +91.11.4560.8317, Fax: +91.11.4560.9310, e-mail: asisecretariat.india@gmail.com

ISSN 0973-3302

Printed at Alpha Printers, WZ-35/C, Naraina, Near Ring Road, New Delhi-110028 Tel.: 9810804196. JASI is sent to ASI members free of charge.

JASI

Journal of Acoustical Society of India (JASI)

A quarterly publication of the Acoustical Society of India

Volume 42, Number 1, January 2015

ARTICLES

INFORMATION

Journal of Acoustical Society of India : Vol. 42, No. 1, 2015 (pp. 1-7)

Effective Thickness and Eigenmodes of a Plate with Blind Holes

Dubois Jérôme and IngRosKiri
Instrumentation&Signal Processing(ISP) Section, ESPCI ParisTech,
CNRS UMR 7587, 1 Rue Jus-sieu, 75005 Paris, France.
e-mail: jerome.dubois@espci.fr

[Received:12.12.2013; Revised: 28.03.2014; Accepted: 10.07.2014]

ABSTRACT

In order to focus ultrasound in air, generally, a focused transducer or a transducers array with beamforming are used. We have recently shown that it is possible to focus acoustic waves in air with a thin square plate using time reversal process. This device allows focusing the acoustic waves with a small number of transducers. The contrast of focusing is enhanced proportionally to the square root of the number of modes of the plates. This can be made, for example, by drilling an array of resonant blind holes in the plate. Near the first frequency resonance of the blind holes, the dispersion relation of a phononic crystal composed of a plate with blind holes has flat bands along all the principal directions of the Bloch wavenumber. This means that there are localized modes inside the blind holes, so we can expect a local augmentation of the eigenmodes of this plate near these flat bands. The question is: can we determine the increase of modes of a plate with blind holes? In order to do that, we have studied the cumulative eigenmodes as a function of the frequency of simple plates and plates with blinds holes using ComsolMultiphysics. The cumulative eigenmodes of a simple plate increase linearly with the frequency and analytical formula of this increase can be found in the literature. For the plate with blind holes, there is local augmentation of the cumulative eigenmodes around the resonances of the blind holes. However, they increase linearly between these resonances with the same slope which is greater than the case of the simple plate with same thickness. This means that this plate behaves like an effective plate with a lower flexural rigidity. Considering that the plates are made with a unique material (because the blind holes are drilled into the plate), the Young's modulus, the Poisson's ratio and the mass density of the effective plate are identical to the ones of the initial plate. So the only property remaining is the effective thickness.This effective thickness has been deduced numerically by minimizing the error between the analytical curve of the cumulative eigenmodes and the one obtained with ComsolMultiphysics. It appears that the effective thickness is defined by the average of the mean thickness of the plate and the thickness defined by the mean flexural rigidity. On all our simulations this effective thickness differs from the one obtained numerically by less than 3%. Moreover, the local augmentation of the eigenmodes around the resonances of the blind holes has been calculated and is roughly equal to the number of blind holes. With these results we are able to predict the augmentation of the cumulative eigenmodes as a function of the frequency for a plate of any shape with a regular or random array of blind holes.

1. INTRODUCTION

Acoustic focusing is widely used in medical imaging or non-destructive evaluation. In order to fo-cus ultrasound in air, generally, a focused transducer or a transducers array with beamforming are used. We

have recently shown that it is possible to focus acoustic waves in air with a thin square plate using time reversal process [1].With this device,it is possible to focus acoustic waves with a small number of transducers but with a non optimal contrast level.

The contrast of focusing is enhanced proportionally to the square root of the number of modes of the plates [2]. So the contrast of focusing can be improved by drilling an array of resonant blind holes in a plate for example. Indeed, the dispersion relation of a phononic crystal composed of a plate with resonant blind holes has flat bands nearthe first frequency resonance of the blind holes,along all the principal directions of the Bloch wavenumber.This means that there are localized modes inside the blind holes, so we can expect a local augmentation of the eigenmodes of this plate near these flat bands. Moreover the flexural rigidity of the phononic crystal seems to be lower than the one of a simple plate [1].

The goal of this paper is to predict the augmentation of eigenmodes of a plate with blind holes compared to a regular thin plate. In order to do that, we first study the cumulative eigenmodes of different regular and drilled plates. It appears that the cumulative eigenmodes of plates with blind holes increase linearly with the frequency such as for the regular plates, expect in the vicinity of the resonances of the blind holes. Then we extract an empirical expression of the effective thickness of an equivalent plate which has the same cumulative eigenmodes behaviour. Moreover we determine the local augmentation of the eigenmodes due to the resonances of the blind holes.

2. NUMBER OF EIGEN MODES IN A PLATE

In this section, we present the evolution of the cumulative eigenmodes in a plate for different geometries, areas and types of plates. The two geometries consider here are square plates and chaotic cavities which consist in a disk with one segment cut off (Fig. 1). These plates can be regular (plate with the same thickness everywhere) or with blind holes drilled into them. In a first part, we present an analytical expression of the cumulative eigenmodes in a regular rectangular plate. Then w compare this formula with the cumulative eigenmodes obtained by numerical simulations made with COMSOL. After, we look at the evolution of the cumulative eigenmodes for plate with a periodic or random array of blind holes.

2.1 Regular plates

2.1.1 Theory

We consider here the flexural vibrations of a plate using the Kirchhoff theory. The flexural wave equation of motion of a plate of thickness h_0 is given by:

$$D\Delta^2 w(\mathbf{r},t) + \rho h_0 \frac{\partial^2 w(\mathbf{r},t)}{\partial t^2} = 0, \tag{1}$$

where $w(\mathbf{r}, t)$ is the vertical displacement of a point at the position $\mathbf{r}$ and time t and Δ is the Laplacian operator. $D = Eh_0^3 \Big/ 12\left(1-\nu^2\right)$ is the flexural rigidity of the plate, E, ν and ρ are the Young's modulus, the Poisson's ratio and the mass density of the plate respectively. The equation (1) leads to the dispersion relation:

$$k^4 = \frac{\rho h_0 \omega^2}{D}, \tag{2}$$

where ω is the angular frequency. In this case, Xie *et al.* [3] have shown that the cumulative eigen-modes $N(k)$ of a rectangular plate of length L and width l, with free boundary conditions, is given by:

$$N(k) = \frac{k^2 Ll}{4\pi} + \frac{k}{\pi}(L+l) - \delta, \tag{3}$$

where δ is a corrective constant.

2.1.2 Numerical results

Numerically, the cumulative eigenmodes are obtained using the Mindlinplate's model of the soft-ware COMSOL. The two geometries studied here are presented in the figure 1. We consider a Duralumin plate of

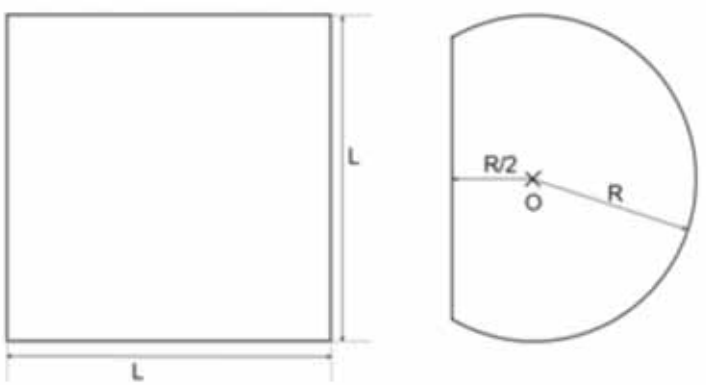

Fig. 1. Geometry of the plates: the square plate (left) and the chaotic cavity (right).

thickness h_0=1 mm with a Young's modulus, a Poisson's ratio and a mass density equal to 74 GPa, 0.33 and 2790 kg.m^{-3} respectively. We have determined the cumulative eigen-modes of these plates for three different areas: A_1=0.01 m^2, A_2=2.25 A_1 and A_3=4 A_1. These areas correspond to L_1=100 mm, L_2=150 mm and L_3=200 mm respectively for the square plate and R_1=62.9 mm, R_2=94.35 mm and R_1=125.8 mm respectively for the chaotic cavity.

The cumulative eigenmodes obtained with COMSOL and with Eq. (3) are reported on Fig. 2.a, they increase linearly with the frequency. The value of δ is found to be roughly equal to four by minimizing the square relative error between Eq. (3) and the numerical results, without taking into account the static eigenmodes of the plates. The analytical formula fits very well with the numerical curves, the relative error is less than 5% (except at very low frequency). We can notice that both the analytical formula and the numerical results count two eigenmodes when there are degenerative modes.

The cumulative eigenmodes of the square plates and the chaotic cavities are represented on Fig. 2.b. It seems that the evolution of the cumulative eigenmodes of regular plate does not depend on the shape of the plate but only on the surface and boundary conditions when the degenerative modes are count. So we can predict the cumulative eigenmodes of a chaotic cavity with the Eq. (3) considering $L = l = \sqrt{A}$.

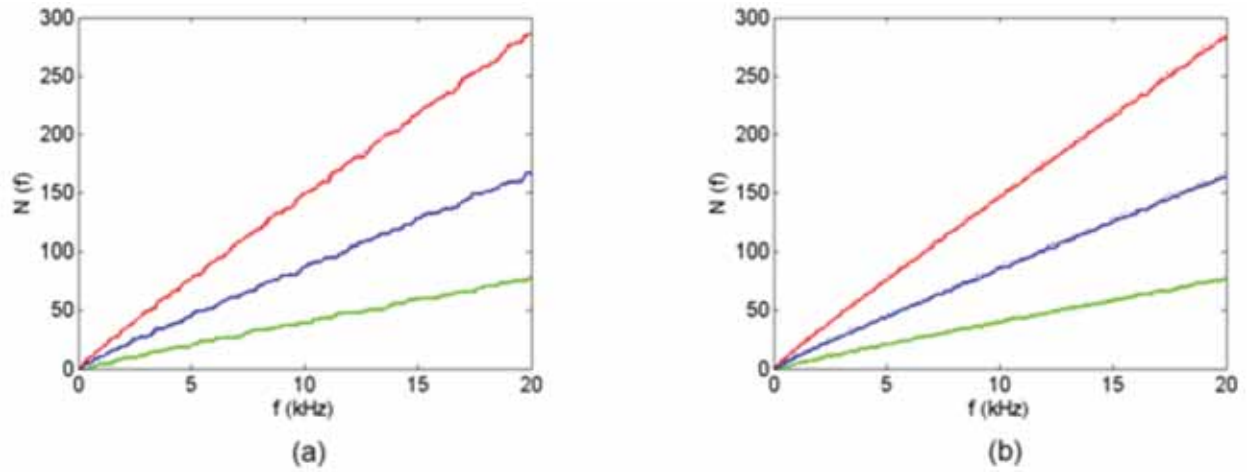

Fig. 2.Cumulative eigenmodes of the plates of area A1 (green), A2 (blue) and A3 (red), a: obtained numerically (solid lines) and analytically (dotted lines);b: obtained numerically for the square plates (solid lines) and for chaotic cavities (dotted lines).

2.2 Plates with blind holes

We now study the evolution of the cumulative eigenmodes of plates in which there are n blind holes of radius a=5.5 mm and thickness h_1=0.1 mm arranged periodically or randomly (Fig. 3). There are n_1=25, n_2=49 and n_3=100 holes in the plate of area A_1, A_2 and A_3 respectively. This kind of blind holeshas a monopolar resonance at f=8.2 kHz and a dipolar resonance at f =16.4 kHz [1].

It has been shown that the dispersion curve of a phononic crystal composed of a square array of blind holes presents flat bands at the first frequency resonance of the blind holes, which means that there are localized modes in the holes at this frequency [2]. This is confirmed with the cumulative eigenmodes of our plates because the curves have a jump in the vicinity of the monopolar and dipolar resonances (Fig. 3). One can notice that the jump is more important at the dipolar than at the monopolar resonance.

Except in the vicinity of the resonances, the cumulative eigenmodes increase linearly with the frequency and with the same slop everywhere. Moreover this slop is more important than the one of a regular plate with the same area (figure 3.a), this means that the flexural rigidity of the plate with holes is lower than the one of the simple plate. So, at low frequency, it should be possible to determine an equivalent plate which has the same cumulative eigenmodes than a plate with scatterers (except for the jumps at the frequency resonances).

The cumulative eigenmodes do not depend on the arrangement of the holes (Fig. 3.b), but the mode density of the random arrangement is smoother than the one of the periodic array. Moreover the degeneration of the eigenmodes is broken by the random arrangement of the blind holes. We do not show it here, but we have the same results for chaotic cavities.

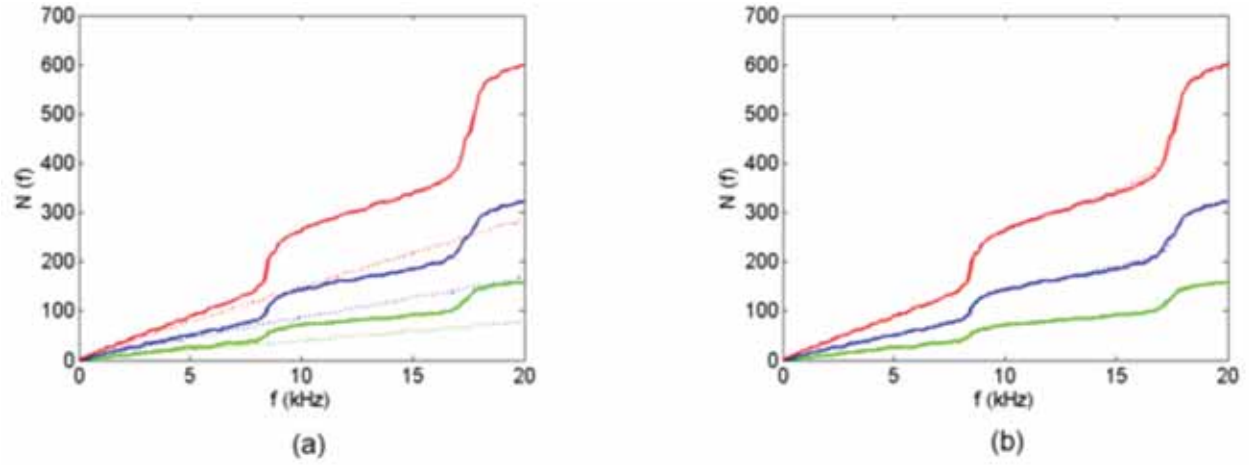

Fig. 3.Numerical cumulative eigenmodes of the platesof area A_1 (green), A_2 (blue) and A_3 (red), a: regular plates (dotted lines) and plates with a periodic array of blind holes (solid lines); b: plates with a periodic (solid lines) or random (dotted lines) array of blind holes.

3. PREDICTION OF THE CUMULATIVE EIGENMODES

3.1 Effective thickness

As we have seen in the previous section, the flexural rigidity of the plate with blind holes seems to be lower than the one of the simple plate. The question is: is it possible to determine the effective properties of the plate with scatterers? Considering that the plates are made with a unique material (because the scatterers are drilled into the plate), the Young's modulus, the Poisson's ratio and the mass density of the equivalent plate are identical to the ones of the initial plate. So the only property remaining is the effective thickness. In order to determine this thickness, we have counted the eigenmodes of different plates with different numbers and geometries of blind holes. A *priori*, the effective thickness can be the mean thickness of the plate:

$$h_{\text{eff}}^{\text{mt}} = h_0\left(1-\phi\right)+h_1\phi, \tag{4}$$

orit can be the thickness which defines the mean flexural rigidity of the plate:

$$h_{\text{eff}}^{\text{mfr}} = \sqrt[3]{h_0^3\left(1-\phi\right)+h_1^3\phi}, \tag{5}$$

or even the one which defines the mean wavenumber in the plate:

$$h_{\text{eff}}^{\text{mw}} = \sqrt{\frac{h_0^2 h_1^2}{h_1^2\left(1-\phi\right)+h_0^2\phi}}. \tag{6}$$

Empirically we have found that the effective thickness is the mean of mean thickness and the thickness which defines the mean flexural thickness: $h_{\text{eff}} = \left(h_{\text{eff}}^{\text{mt}} + h_{\text{eff}}^{\text{mfr}}\right)/2$. The comparison between this expression and the effective thickness obtained numerically by minimizing the square relative error between Eq. (3) (we minimize the quadratic error by tuning the value of h in Eq. (3)) and the numerical cumulative eigenmodes is presented in Fig. 4 for various concentrations while kipping h_0=1 mm and h_1= 0.1 mm. This process is made on the first linear part of the cumulative eigen-modes, before the first jump of the curves. Our expression of the effective thickness is accurate (the relative error is less than 3%) except at very high concentration.

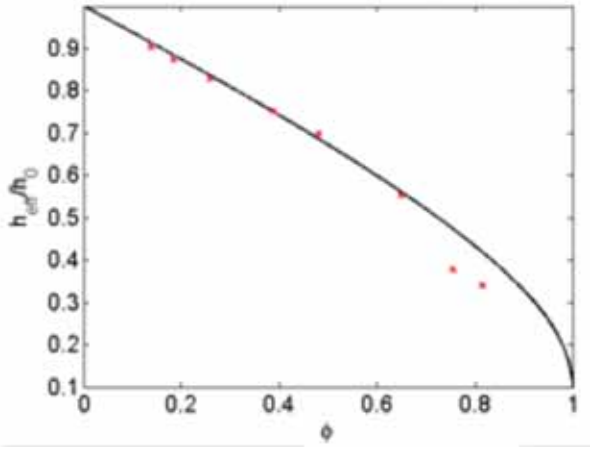

Fig. 4.Effective thickness versus concentration, comparison between $h_{\text{eff}} = \left(h_{\text{eff}}^{\text{mt}} + h_{\text{eff}}^{\text{mfr}}\right)/2$ (black line) and numerical results (red crosses).

3.2 Increase of the eigenmodes in the vicinity of the holes resonances

We have seen in Section 2 that the slop of the cumulative eigenmodes of a plate with blind holes is the same everywhere except in the vicinity of the resonancesof the holes. Moreover, numerically or analytically we can determine the effective thickness of the plate. So before the monopolar resonance, the cumulative eigenmodes can be expressed by Eq. (3) and between the monopolar and the dipolar resonance they can be expressed by Eq. (3) plus a constant (considering h=h_{eff} in Eq. (3)). This constant is equal to the increase of the eigenmodes due to the holes monopolar resonance. The same process can be applied after the dipolar resonance in order to determine the increase of the eigenmodes due to the dipolar resonance. By doing this for different number of blind holes in a plate with constant area, we access to the increase of the eigenmodes as a function of the number of holes as we can see in Fig. 5.a for a plate of area A3 with different number of blind holes of radius a =2.5 mm and thickness h_1=0.1 mm. The increase of eigenmodes can be expressed as a linear function of the number of holes n : $N\left(n\right) = Y_1 n + Y_2$ where the increase factor Y_1 is close to 1 (for the monopolar resonance) or 2 (for the over resonances) and Y_2 is a small corrective constant.

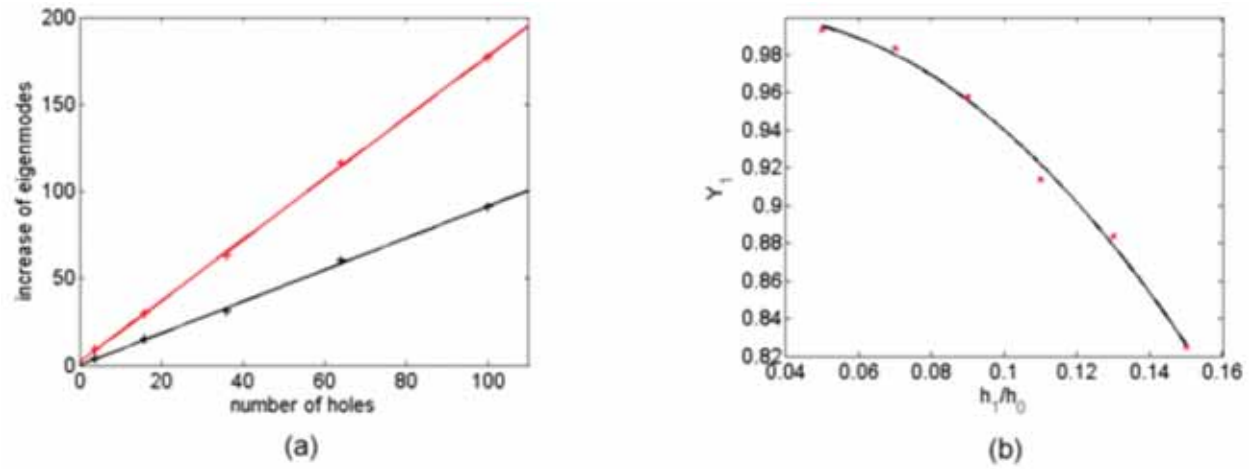

Fig. 5.a: increase of eigenmodes due to the monopolar (black) and dipolar (red) resonances, numerical simulation (cross) and linear interpolation (solid line); b: increase factor Y_1 versus h_1/h_0, numerical simulation (red cross) and quadratic interpolation (black line).

By determining the increase factor for different types of blind holes, it appears that this factor decreases with the ratio h_1/h_0 (Fig. 5.b):

$$Y_1 \approx -11,73\left(\frac{h_1}{h_0}\right)^2 + 0.65\frac{h_1}{h_0} + 0.99, \tag{7}$$

for the first resonance. This is probably due to the fact than the more the ratio h_1/h_0 increases, the more the resonance is flat. So there is maybe a coupling of the resonances of different holes.

4. CONCLUSION

The increase of cumulative eigenmodes of different types of thin plates has been investigated: regular plates and plates with a periodic or random array of blind holes. It appears that the cumulative eigenmodes do not depend on the shape of the plate and on the arrangement of the blind holes. Moreover, for regular plate, the cumulative eigenmodes are well defined by the formula given by Xie *et al.* [1] and they increase linearly with the frequency.

When there is an array of blind holes, there is local augmentation of the cumulative eigenmodes in the vicinity of the resonances of the holes. Except in these frequency bandwidths the cumulative eigenmodes still increase linearly with the frequency with a greater slop than in the case of regular plate. This means that this kind of plate can be described by an equivalent plate which has the same mechanical properties but with a weaker effective thickness.

This effective thickness is determined numerically by minimizing the square error between the formula of Xie *et al.* [1] and the numerical cumulative eigenmodes. It appears, empirically, that this effective thickness is given by the average between the mean thickness of the plate and the thickness defined by the mean flexural rigidity of the plate.

The local augmentation of the cumulative eigenmodes is also determined. It appears to be roughly equal to the number of blind holes in the plate for the monopolar resonance and twice this number for the other resonances.

5. REFERENCES

[1] N. ETAIX, J. DUBOIS, M. FINK and R.-K.ING, 2013. Increasing the modal density in plates for mono-element focusing in air,*Journal of the Acoustical Society of America*,**134** (2),1049–1054.

[2] A. DERODE, A. TOURIN and M. FINK, 2001. Random multiple scattering of ultrasound. II. Is time reversal a self-averaging process?,*Physical Review E,* **64** (3), 036606.

[3] G. XIE, D. J. THOMPSON and C. J. C. JONES, 2004.Mode count and modal density of structural systems: relationships with boundary conditions,*Journal of sound and vibration*, **274**, 621–651.

Journal of Acoustical Society of India : Vol. 42, No. 1, 2015 (pp. 8-16)

Characterisation and Evaluation of Viscoelastic Material Properties

V.V.S. Bhaskara Raju[1*] and T. Subrahmanyam[2]
[1]Naval Science & Technological Laboratory,
Visakhapatnam, 530027, India
[2]Department of Mechanical Engineering, Andhra University,
Visakhapatnam, 530003, India
**e-mail: bhaskararajuvvs@gmail.com*

[Received:16.12.2013; Revised: 21.05.2014; Accepted: 07.08.2014]

ABSTRACT

Viscoelastic material has a wide range of applications in the field of engineering. For machine tool structure, the builtin damping generally proves insufficient for a good dynamic performance of the machine. Additional damping is necessary and can be achieved through Viscoelastic material. For Electrical machinery requires insulation resistance in different environmental conditions due to the mixture of pollutants like salt and urea, plus the humidity form a layer on the material that can become conductor and allow passing currents that will facilitate the conditions of short circuit. Thermal equipment application requires thermal conductivity of Viscoelastic materials. For this the material was tested for mechanical, electrical and thermal properties in addition to damping attenuation.

This paper covers the test methods for evaluation of the properties like physical, mechanical, viscoelastic, electrical and thermal properties to select its utility for any specific application for viscoelastic material. Mechanical properties evaluated and methods & values can be compared with standards. Physical properties and method of testing as per the standard carried out and compared with British standards & BIS. Electrical properties are compared with IEC standards. Thermal properties are compared with DIN 52612 standards. Viscoelastic properties are evaluated with standard experimental tests and are validated with FEA software analysis. For FEA software validation, three dimensional modelling was done using CATIA. The geometric model was imported into the GUI through a parasolid file to Patran Software for discretization (meshing), the basic idea of mesh generation is to generate element connectivity data and nodal coordinate data. For non-linear structures, hexahedron element is taken for meshing, 3d elements take the form of cubes called hexahedrons (hexes). The actual forces and boundary conditions were given to the model and the harmonic response analysis was performed. The model response at the frequency range 10Hz to 6 KHz are obtained. This was analyzed using Msc. Marc software. Msc.Marc module developed by Micro software Corporation, USA, is specifically used for the Non-Linear materials. The material properties for the hyperelastic material was obtained by curve fit of experimental uniaxial (Stress vs. Strain) test data with standard material model using Msc. Marc Software to analyse and compared the frequency response with the experimental damping attenuation.

1. INTRODUCTION

Viscoelastic material testing is categorized into two categories. One is the testing of unvulcanized material and other is of vulcanized material. The most important tests of unvulcanized material compound is the Mooney viscometry. Curing characteristics and processibility study are also the major studies of the unvulcanized compounds. For vulcanized samples physical, mechanical, viscoelastic and tribological tests are very important to evaluate the strength and failure characteristics. Beside these, thermal, electrical and specific environmental resistance tests are important to qualify material for specific applications.

For successful employments of any viscoelastic material testing in engineering applications are lies on their ability to meet design and service requirements.The capability of materials to meet the requirements is determined by the mechanical and physical properties. Physical properties are measured by the methods not requiring the applications of mechanical force. These physical properties are density, thermal conductivity, electrical conductivity, coefficient & thermal expensive, specific heat etc, where as mechanical properties are measured by the application of force. These properties are primarily related to forces and deformation. These properties are stress, strain, and elongation, reduction in area, hardness, fatigue resistance and facture toughness.

The present paper mainly focuses on evaluating some of the specific properties of viscoelastic material like physical properties viz thermal conductivity, electrical conductivity and mechanical properties viz stress, strain and hardness. For the present study, the author considered EPDM material sample for evaluating these properties. All the tests were compared with the ASTM and IEC standards, where ever standards are not available for those tests are compared with Finite Element Analysis.

2. EXPERIMENTAL TESTING METHODS FOR VISCOELASTIC MATERIAL

Different types of tests for evaluating the properties of a Viscoelastic material are discussed in this section. Basically some of the tests are illustrated *i.e.*, tensile test, hardness, DMA test, electrical and thermal properties.

2.1 Tensile Strength & Elongation at Break

For tensile strength and elongation at break tests were carried out in a universal tensile testing machine as per ASTM D-412 with the standard requirements as per BS 2751.

EQUIPMENT SPECIFICATIONS

1.	Capacity	-	500kg
2.	Make	-	HUNG TA

APPLICATIONS

1.	Tensile strength	-
2.	Tear strength	-
3.	Elongation at break	-
4.	Adhesive strength	-

Fig. 1. Universal Testing Machine

The Experiment was carried out by using Universal Tensile Test Machine, having 500 N capacity, with computer aided operating machine provided by software. From the test results to calculate the Tensile Strength, Shear strength and Adhesive Strength. The stress was calculated as the ratio of observed force to the cross-sectional area of the unstretched specimen. Elongation for dumbbell specimen was given by:

$$\text{Elongation Percent} = \frac{(L - Lo)}{Lo} x$$

Consider the Viscoelastic material specimen of dumble shape of size 75 mm Gauge Length 75 mm as shown in the Fig. 2.

Fig. 2. Dumble Specimen for tensile test

2.2 Hardness

This test was carried out in a dead load hardness testing machine and specimen shown in the figure 3 and 4 respectively as per ASTM D-2240.

Fig. 3. Hardness test equipment

Fig. 4. Hardness test specimens

2.3 Compression set

This test was carried in a special jig under constant strain method as per ASTM D-395. Samples were compressed up to 25% and kept in a hot air oven at 70°C for 24 hrs.

2.4 Hot air Ageing property using Hot air oven

Test samples like tensile test piece (dumble) and hardness buttons were kept in a hot air oven at 70°C & after regular intervals samples were removed from hot air oven. Tests were carried out and results were compared before & after ageing.

2.5 Environmental properties using Hot air oven

Samples were prepared as per ASTM D-371 and were exposed to liquid-B for 22 hrs at 30°C and the change in weight was measured by noting the weight of samples before and after immersion in test liquid. Sea water absorption: Samples were exposed to sea water for 22 hrs at 30°C and the change in volume was measured by water displacement method.

2.6 Testing of Viscoelastic properties using DMA (Dynamic Mechanical Analyzer)

This test was carried out in a Dynamic Mechanical Analyzer model No: GABO Eplexor 500 N at Rubber Technology Division, NSTL, DRDO Laboratory.

Fig. 5. Dynamic Analyzer

Samples were tested for elastic modulus, loss modulus, complex modulus & tanδ in tension mode as a function of time, temperature and frequency. Temp-Freq. sweep had been carried out between temp. –50°C to +50°C and frequency from 2 Hz to 10 Hz. Then extrapolation of all the properties with respect to frequency had been carried out.

2.7 Electrical Testing

For electrical testing the EPDM rubber sample shown in figure 4 (sample size of 300 × 100 × 10 & 300 × 100 x 30 mm was made using 150 ton compression machine) were made to carryout test HV testing using High voltage testing equipment shown in figure 5) is conducted to determine its performance characteristics.

Fig. 6. Electrical testing sample

Performance characteristics can be determined by applying voltage the details of the corresponding leakage current are tabulated and the voltage is varied in steps until the material gets flashover.

Fig. 7. Electrical testing equipment

The material begins to fail when the pollutants that exist in the air settle in the surface of the material and combine with the humidity of the fog, rain, or dew, so in order to determine the efficiency of the material it is needed to be tested in different environmental conditions, so that the rubber material is first tested in dry condition by applying voltage and the details of corresponding leakage current are tabulated, from the obtained voltage and leakage current readings V-I characteristics are plotted. In the same way the rubber material will be tested in wet condition and in polluted conditions.For all consumer and mechanical devices, the safe values of leakage currents are specified by IEC950 safety standard, values for double insulated and grounded devices are listed in table.1.

Table-1. Leakage current values from IEC950 standards

S.No.	Device insulation type	Maximum Safe leakage current
1	Double insulated	0.25 mA
2	Grounded hand held	0.75 mA
3	Movable	3.50 mA
4	Stationary (Not Mounted)	4.00 mA
5	Stationary (Permanently Mounted)	5.00 mA

2.8 Thermal Testing

It was conducted using hot plate method for EPDM with the two same samples of Viscoelastic material. The amount of heat and thermal conductivity of the samples were calculated as per ASTM - E 1530.

2.9 Damping Testing

An F.F.T. analyzer was used for generating the input signal (the excitation) and the output signal (the response) to produce the Fourier Response Frequency spectra in-order to account for damping criteria.

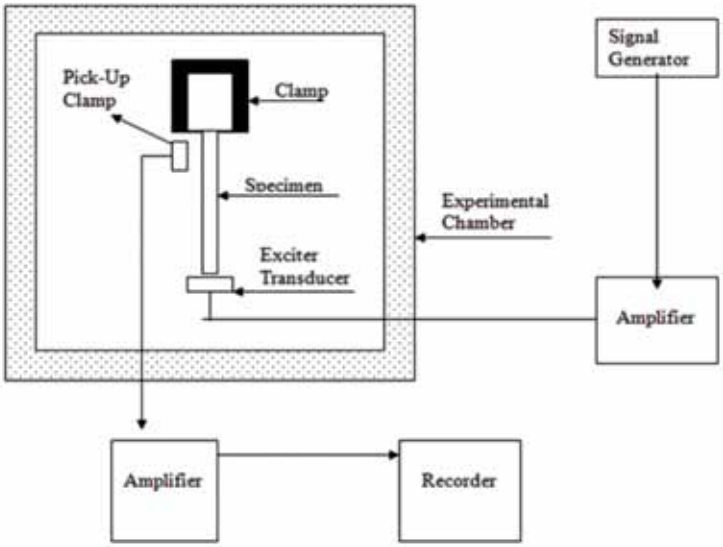

Fig. 8. Block Diagram of FFT Analyzer

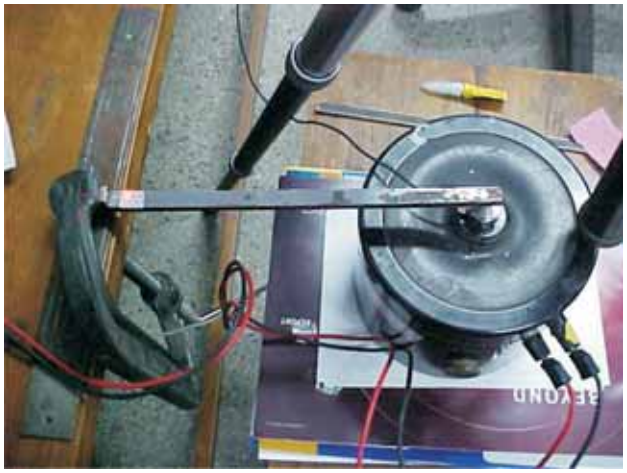

Fig. 9. FFT Analyzer experimental setup

2.10 Validation of Damping Testing

The CLD model was analyzed with the actual boundary conditions to study the frequency response of the model. The model was developed using CATIA v5 R17.The model was meshed using Msc.Patran with Hexa element. Meshed model was analyzed using Msc.Marc Software. The model and Harmonic analysis was done to validate with the experimentation results.

3. RESULTS AND DISCUSSION

The tests were conducted for evaluation of tensile strength, elongation at break, hardness, compression set, hot air aging, The mechanical and physical properties of the materials are evaluated and are tabulated in the table.2. Table.3 and Table.4 shows the Electrical properties and thermal properties of Viscoelastic material with compound A & B.

Table-2. Mechanical and Physical properties

Mechanical and Physical Properties	Composition - A	Composition - B
Tensile Strength (MPa)	13.00	2.0
Elongation at Break (%)	390	565
Hardness (IRHD)	65	35
Compression Set (%) (70°C for 24 hrs)	8.50	21
Resistance to Liquid-B (Change in Weight %)	+18.63	+33.76
Sea water Absorption (Change in Volume %)	+0.70	+0.95
Hot Air Ageing at 70°C for 72 hrs		
Change in Tensile Strength (%)	- 2.5	- 11.5
Change in Elongation at Break (%)	- 6.0	- 21
Change in Hardness (Shore - A)	+ 1	+ 2

Table-3. Electrical properties of Viscoelastic material with compound A & B

S.No.	TEST TYPE	withstandability Composition-A kV	withstandability Composition-B kV
1	Dry test	10.5	5
2	Wet test	7	5
3	Pollutant Urea	7.5	4.5
4	Non Pollutant Urea	7	4
5	Pollutant Salt	6.5	5
6	Non Pollutant Salt	6	4.5

Table-4. Thermal Conductivity properties

S.No.	Viscoelastic Material	Property	Standard	Results Obtained w/mk	Specified Requirements
1	Compound-A	Thermal Conductivity	ASTM E-1530	0.264	-
2	Compound-B	Thermal Conductivity	ASTM E-1530	0.207	-

Damping test results (Frequency response test results) are shown in the following graphs Figure.10 (a) and Figure.10 (b) plotted between frequency vs. decibels.

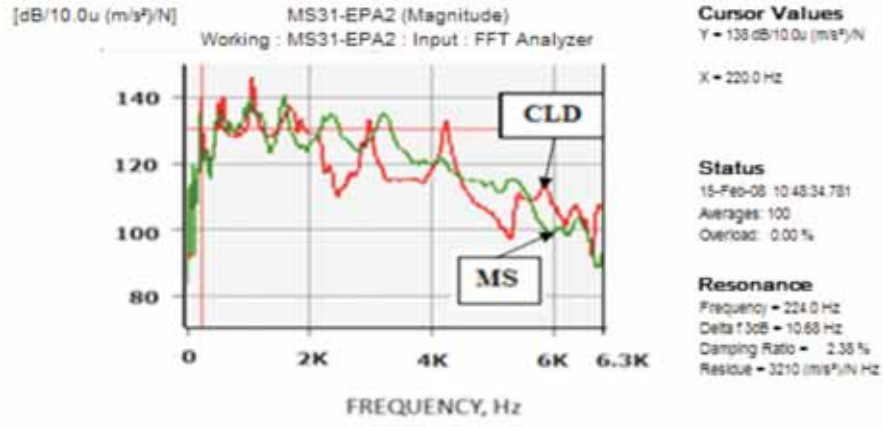

Fig. 10 (a) Experimental damping results on EPDM - Composition A

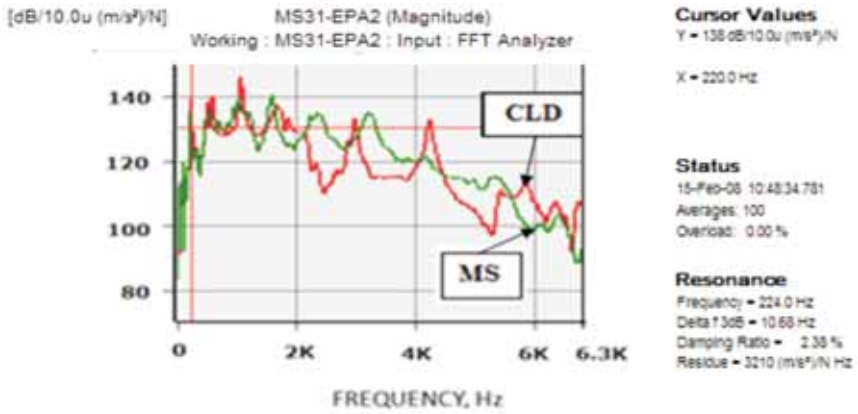

Fig. 10 (b) Experimental damping results on EPDM - Composition B

Validation of damping test results with Msc.Marc FEA Software are shown in the following graph Figure 11 shows the graph plotted between frequency vs. decibels

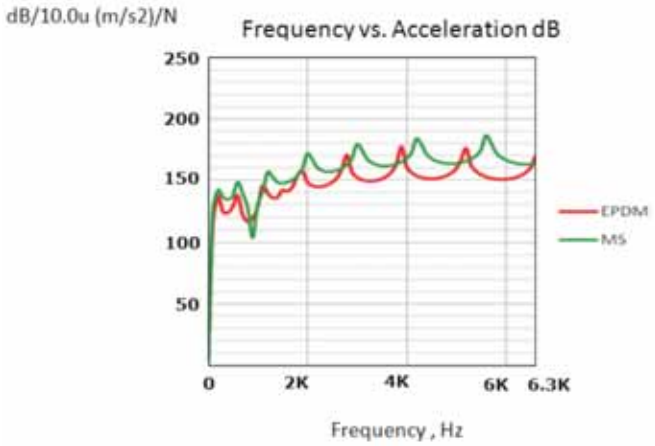

Fig. 11. Frequency Response of CLD & Base layer Software Result for EPDM - Composition A

4. CONCLUSIONS

a. It is evident developed EPDM rubber compound reduces surface vibration in mode of CLD treatment.

b. EPDM compound A is suitable in the frequency range up to 7 kHz reducing vibration levels 1-9 dB. In the frequency extrapolation this composition shows linear values for all modulus and loss factor up to 10+12 Hz.

c. EPDM compound B is suitable in the frequency range up to 3.5 kHz reducing vibration levels 1-5 dB. In the frequency extrapolation this composition shows linear values for all modulus and loss factor up to 10+7.5 Hz.

d. Developed EPDM compound is suitable electrical structural applications with environmental conditions as per standards IEC 950. EPDM rubber compound A is able to with-stand 5 to 10 KV with minimum leakage current when compound with EPDM compound B. EPDM compound A is having better damping properties than EPDM compound B in the frequency range upto 6.3 kHz. EPDM compound A is best suited for damping along with electrical properties.

e. If we consider the cost effectiveness for the application of CLD, composition B is cheaper than composition A.

f. If we consider thermal conductivity along with structural damping composition B is best suited.

5. ACKNOWLEDGEMENT

The authors would like to express sincere thanks to Shri S.V.RangaRajan, Out-Standing Scientist, Director, NSTL, Sri AVS Chari, Scientist-G, Head WT, Sri P.V.S.Ganesh Kumar Scientist-G, Head Rubber Technology & Vibration of NSTL, Smt.N.Sumathi, Assistant professor, JNTU, Kakinada and Dr. N. Ramaniah, Associate Professor, Andhra University College of Engineering-(A), for their encouragement during the course of work. The authors are also grateful to Shri Ch.S.R.K. Sharma, Scientist-D, Shri Pradeep Kumar Garu, Scientist-C, NSTL for their cooperation & assistance during the course of work.

6. REFERENCES

[1] NAVIN KUMAR and S.P. SINGH, 2009. "Vibration and damping characteristics of beams with active constrained layer treatments under parametric variations" published in *Science direct, Materials & Design*, **30**(10), 4162-4174.

[2] K.P. SAU, T.K. CHAKI, and D. KHASTGIR, 1999. "Electrical and mechanical properties of conducting carbon black filled composites based on rubber and rubber blends**"**. *J. Appl. Polym. Sci.,* 71(6) 887–895.

[3] CRISTINE CANAUD, LEILA LEA YUAN VISCONTE, MARCIO ANTÔNIO SENS and REGINA CELIA REIS NUNES, 2000. "*Dielectric properties of flame resistant EPDM composites*" 70(2), 259–262.

[4] M.A.M. EIDA* and D.E. EL-NASHARB, 2006. "Filling Effect of Silica on Electrical and Mechanical Properties of EPDM / NBR Blends" *Polymer-Plastics Technology and Engineering*" **45**(6), 675-684.

[5] WEIZHI WANG, LONGXIANG TANG and BAOJUN QU, 2003. "Mechanical properties and morphological structures of short glass fiber reinforced PP / EPDM composite" *European Polymer Journal*, **39**(11), 2129–2134.

[6] JOSEF VACIK, RADEK KOTTNER and VACLAVA LASOVA, 2011. "Structure Optimization of Passive Damped Composite Beam" published on *Bulletin of Applied Mechanics*, **7**(27).

Journal of Acoustical Society of India : Vol. 42, No. 1, 2015 (pp. 17-23)

Use of Hand held Array for NVH Measurement in the Automotive Industry

Svend Gade, Jesper Gomes and Jørgen Hald
IBrüel & Kjær Sound & Vibration Measurements, Skodsborgvej 307,2850 Nærum,Denmark
e-mail: sgade@bksv.com

[Received:13.01.2014; Revised: 28.05.2014; Accepted: 08.06.2014]

ABSTRACT

The use of microphone arrays has been greatly extended within the last decade. This paper summarizes how a small double layer array with typically 128 microphones can be used in automotive NVH cabin measurements for mapping various acoustical properties. There are four major applications. The first one is General Patch Holography of basic acoustical quantities like sound pressure, particle velocity and sound intensity. Other applications are In-situ absorption measurement, intensity component analysis (e.g. incident, reflected, scattered, net intensity etc.) and panel contribution. Some measurements are done in operational condition and some are reference laboratory measurement of typical Frequency Response Functions.Traditional Nearfield Acoustic Holography, NAH was introduced in the mid 1980'ies. NAH allows you to obtain a complete model of the sound field in the vicinity of a sound source, i.e. all sound field quantities (sound pressure, particle velocity, active and reactive intensity) can be calculated in at any location based of pressure measurements on a planar surface in front of the sound source. In particular, the sound field can be mapped closer to the surface than the measurement plane, which can provide very high spatial resolution of the source distribution. NAH was typically implemented in the spatial frequency domain using a two dimensional (2D) Spatial Fourier Transform. One of the drawbacks of the original formulation was that the measurement area should adequately cover the full source plus some "additional" more, so the basic hypothesis that practically all energy of the sound field radiated into the half-space passes through the measurement window was fulfilled. The upper frequency limit is given by that microphone spacing must be less than half wavelength in order to avoid spatial aliasing. Practical measurement were performed using a sub-array and scan techniques. Reference transducers are needed in order to link the scan measurement together. Statistically Optimized Nearfield Acoustic Holography, SONAH became a new formulation of NAH performing the plane-to-plane transformation directly in the spatial domain avoiding the use of spatial DFT thus avoiding / eliminating windowing and leakage errors associated with FFT / DFT calculations. SONAH opens up for the use of holography measurements with an array that is much smaller than the source, e.g. small hand-held arrays and still keeping errors at an acceptable level. SONAH also opens up for introduction of irregular array geometries that can be used for both holography measurements (low to medium frequencies) and beamforming (medium to high frequencies) thus covering the full frequency range.

1. INTRODUCTION

The first application of a small array was patch holography, where you just take measurement where it is relevant (for example around a door seal for sound leakage detection) rather than measuring around the

whole vehicle. Today the use of a small array has been extended to several applications such as In-situ absorption measurement, intensity component analysis (e.g. incident, reflected, scattered, net intensity etc.) and panel contribution. Also a more precise core holography algorithm - similar to SONAH - Equivalent Source Method, ESM for measuring on curved surfaces has been developed recently. This paper will give an overview of the four applications, as well as the new ESM algorithm.

2. EQUIVALENT SOURCE METHOD, ESM

Using ESM the acoustic field is predicted directly by a mesh set of equivalent monopole sources located inside the vibrating body so the method is suitable for arbitrary source shapes, see Fig. 1. Here the requirement of having a model that can represent all contributions to the sound field in the test region is not fulfilled, but because of the short distance between the measurement area and reconstruction area a good approximation for the local patch can be expected.

Furthermore if the mesh is arranged, so that it surrounds a two-layer microphone array, and with a part of the mesh surface coinciding with the patch of interest then the requirement of having a model that can represent all contributions to the sound field in the test region is fulfilled. Global sound field modeling is then obtained by a series of patch measurement. Furthermore, using an array with two layers, sources are allowed behind the array, see Fig. 1.

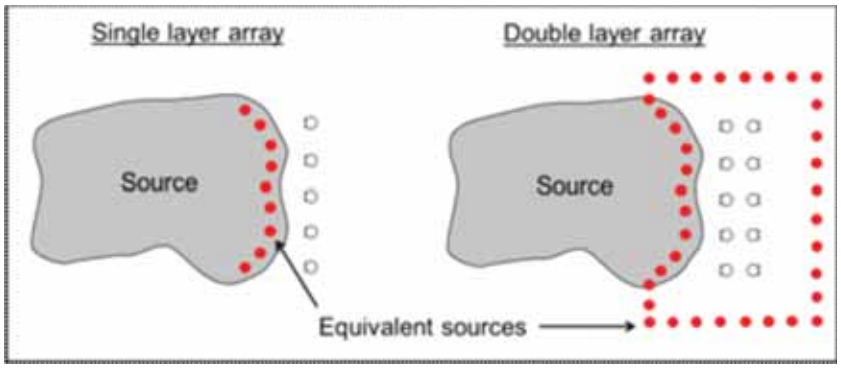

Fig. 1.ESM modeling using Single Layer Array and Double Layer Array

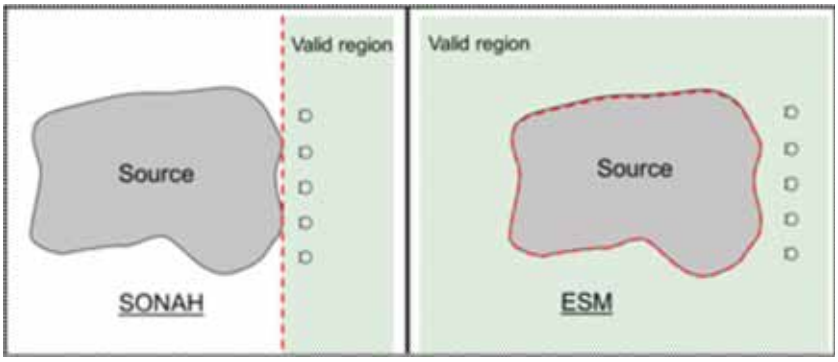

Fig. 2.Valid region of SONAH algorithm and EMS algorithm

The major difference between SONAH and ESM from an application point of view is that ESM handles arbitrary shaped sources and curved surfaces better than SONAH, see Fig. 2. SONAH uses a sound field model in terms of plane propagating and evanescent waves, whereas EMS uses a source model. So where ESM relies on the definition of a sufficient set of monopole sources this is not the case for SONAH.

3. INSTRUMENTATION

The measurement system is described in details in Ref. [11]. The sound field measuring part consist of a 128 ch. hand held microphone array (Fig. 3a), a 132 ch. LAN-XI front end (Fig. 3b), a positioning system integrated into the array frame and a pc with dedicated software.

The array has 8x8 microphones mounted in 2 layers, resulting in a total of 128 microphones. The microphones are spaced 25 mm (various distances 25-50 mm are available) apart in both directions and with a spacing of 31 mm between the two layers. This results in an upper frequency limit for the array of 5 kHz (spatial sampling limit). Due to corrections for phase response (stored in Transducer Electronic Data Sheet, TEDS information) the array performs to frequencies very well below 200 Hz. In general TEDS corrections will improve the available dynamic range over a broad frequency range [13-14]. The array is connected to the front end via a single cable as shown in Fig. 3b.

A 3D Creator system consisting of an optical sensor unit, a digitizer control unit, a wireless hand-held probe, and a wired Dynamic Reference Frame enables precise three-dimensional measurement of array position in real-time as well as capturing of the surface geometry of the device under test.

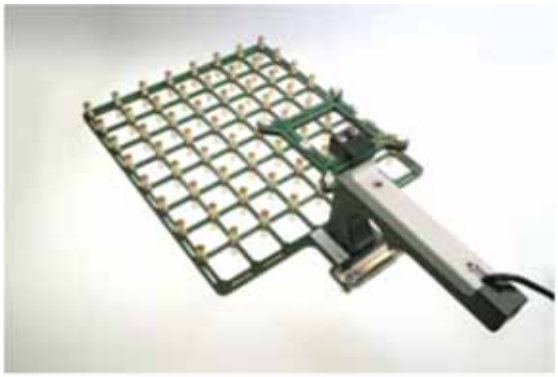

Fig. 3a. Double layer array

Fig. 3b. 132 ch. Front end with single cable

4. APPLICATIONS OF HAND HELD ARRAY

Today four major applications of a small hand held array exist: Patch holography, absorption measurements, intensity component analysis and panel contribution.

4.1 Patch Holography / Conformal Mapping

This is the fundamental application of a hand held microphone array. First a geometry surface model can be created by the positioning system or imported from a CAD model. The actual measurements are done with the small, double layer array, DLA (or single layer array, SLA) mounted on a handle with a builtin 3D position measurement system, see Fig. 3a. The system continuously determines the positions of the array microphones relative to some user-defined coordinate system. To map the sound field on a surface larger than the array, patch measurements are made with the array in neighboring (preferably overlapping) positions over the surface. In each array patch position, acoustic and position data belonging together is recorded. Patch positions already visited / measured are displayed in a 3D view along with the real-time updated current position of the array. Also shown in the 3D view is a surface model of the test object. In this way, the user is guided in covering the surface area with sufficient array patch positions in order to obtain a reliable surface mapping result. To minimize the errors in the patch holography calculations, a very small measurement distance is recommended, typically equal to half of the microphone grid spacing. If this is not possible, then patches with significant overlap should be used, avoiding the need to perform

calculations near the boundaries of the array areas. Typical sound field quantities like sound pressure, particle velocity and sound intensity can be mapped. Optionally Sound Quality (SQ) metrics like loudness, sharpness, fluctuation strength and roughness etc. for describing human annoyance can also be mapped.

4.2 In situ absorption measurement

All The double layer array in combination with holography calculations yields the three intensity components, the net / total intensity, the radiated (from vibration) and absorbed intensity.

$$I_{tot}\,(I_{net}) = I_{front} + I_{rear} = I_{rad} + I_{abs} \tag{1}$$

When measuring for the estimation of surface absorption, a number of loudspeakers must beplaced in the cabin interior and driven by uncorrelated noise sources, to create a distributed and (close-to) diffuse excitation field. In this simple case the absorption coefficient, α can be calculated from

$$I_{tot} = I_{abs} = \alpha I_{rear} \tag{2}$$

i.e. α can be calculated when I_{tot} and I_{rear} are known. See Refs. [11,15] for a more detailed discussion.

To illustrate the use of the proposed techniques in an automotive application, measurements were made with the DLA system in the cabin of a Volvo S60 passenger car to determine the in-situ absorption coefficient of selected surfaces in the cabin. Firstly, the cabin surfaces to be investigated were digitized using the 3D position measurement system and dedicated digitizing software. Next, array measurements were made with the DLA covering the surfaces patch by patch. Four loudspeakers were distributed in the cabin and driven by white noise to provide the acoustic excitation needed for the estimation of the absorption coefficient, Ref. [11].

Fig. 4 shows a 3D contour plot of the estimated absorption coefficient on the cabin surfaces for the 200 Hz 1/3 octave band. The absorption coefficient was estimated by first doing 1/3 octave band synthesis of the estimated total and incident intensities, and then doing area averaging of these quantities over e.g. the seat or window surface before estimating the final absorption coefficient as the ratio between the two. Fig.

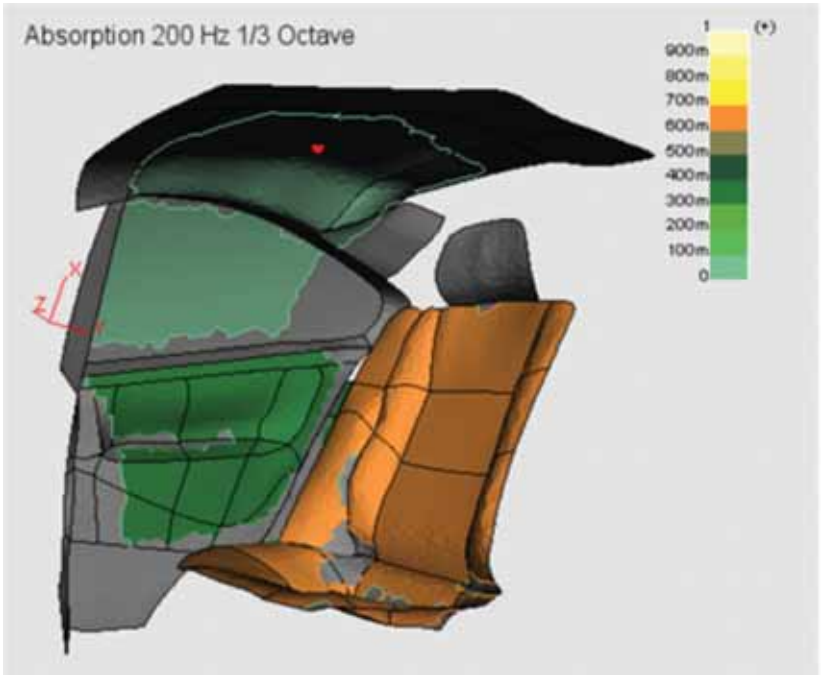

Fig. 4. Contour plot of the estimated absorption coefficient of seat, door, window and roof in a car cabin

4 shows that in the 200 Hz frequency band the seat has quite a high absorption coefficient compared to the door, window and roof.

4.3 Intensity component analysis

Consider the radiation of sound from a small surface segment in a cabin environment. Such a surface segment may radiate sound energy because of external forcing, causing the surface to vibrate, and it may absorb energy from an incident sound field because of finite surface acoustic impedance. When measuring the sound intensity over the surface segment with an intensity probe, the total (or net) intensity Itot will be estimated, while using holography the front and rear sources can be separated. For each principal component the front and rear source field is separated, See Fig. 5a and Eq. (3).

$$(p_{total},u_{total}) = (p_{front},u_{front}) + (p_{rear},u_{rear}) \quad (3)$$

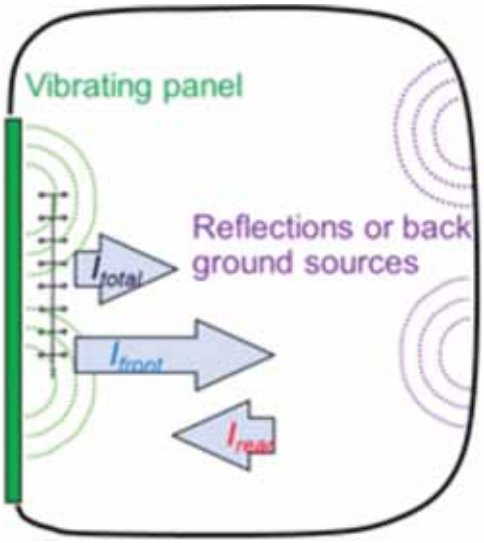

Fig. 5a. Net intensity is a summation of positive and negative going intensities

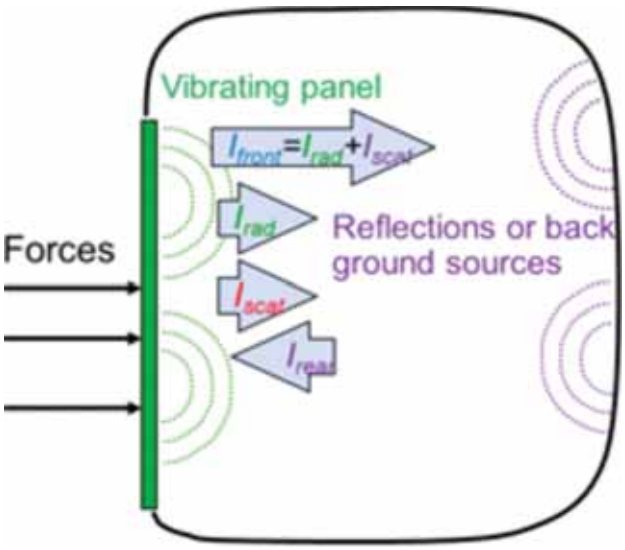

Fig. 5b. Positive intensity is a summation of radiated and scattered intensities

By visualizing Figs. 5a & 5b we can further more set up a couple of additional equations relating the different intensity components, radiated or entering intensity and (back) scattered intensity. As shown in Eqs. 4 & 5, it requires knowledge about the absorption coefficient, α measured as described in the previous chapter.

$$I_{scat} = -(1-\alpha)\cdot I_{rear} \quad (4)$$

$$I_{rad} = I_{front} - I_{scat} \quad (5)$$

The method which is presented here is based on separation of different sound field components via the spatial sound field information provided by an array. The radiated intensity is estimated as the intensity that would exist, if the incident (rear) and scattered field components could be taken away. So a free-field radiation condition is simulated. The idea is to first separate the incident field component into what is absorbed and what is scattered Eq. (4), *i.e.* use separately measured information about the scattering/absorbing properties of the panel to calculate the scattered field, and finally subtract the incident and scattered fields from the total sound field. In this way the intensity is decomposed into separate components. Of special interest is the radiated (entering) intensity, which is the amount of sound energy that is entering into a cabin due to the external forces.

4.4 Panel contribution analysis, PCA

As a final consequence of being able to map the interior panels in a cabin with a long list of different sound field quantities, it is also desirable to calculate the contribution from the various panels to the perceived pressure at the operators / drivers position. The idea was first presented in Ref. [12].

The sound pressure contribution at a position in a cabin from a section ΔS_{panel} can be expressed as:

$$\Delta p_{ear} = \iint_{\Delta S} \left[H_{p,Q} u_n - H_{u,Q} p \right] dS \tag{6}$$

where p is the sound pressure on the panel section, u_n is the particle velocity in the normal direction of the surface, and $H_{p,Q}$, and $H_{u,Q}$ are the two frequency response functions (FRFs) from volume velocity to pressure and velocity on the panels.

The FRFs are measured by placing a volume velocity source (VVS) at the target position, *e.g.*, the driver's ear position and calculating the resulting sound pressure and particle velocity on the panels. This is done by measuring the sound pressure with a microphone array (DLA) at different positions covering the panels of interest, and then applying the ESM or SONAH algorithm to get pressure and velocity at the surface. Using the output from holography together with the measured radiated volume velocity from the VVS, the FRFs can be directly calculated.

Next, array measurements are performed under operational conditions, and the resulting surface quantities, p and u_n, are found by applying the ESM / SONAH algorithm again.

5. SUMMARY/CONCLUSIONS

Patch holography and Absorption coefficient requires only one type of measurements, while Panel Contribution and Intensity Component analysis is a combination of two sets of measurement (one operational measurement and one "laboratory" measurement). Patch Holography is performed by measuring close to the vibrating panels in order to map the noise radiation. Absorption measurements are done the same way except that the panels are absorbing sound, which has to be generated by loudspeakers.

Intensity Component Analysis requires measurement of the absorption coefficient in combination with a Patch Holography measurement in operational condition. In this way the measured intensity can be decomposed into its various components.

Panel contribution (f.ex. to the drivers ear position) requires measurements of Frequency Response Functions (FRF) by use of a Volume Velocity Source, VVS from listening position (drivers ear) to the panels of interest in combination with measuring the Patch Holography patches in operational condition.

6. REFERENCES

[1] J.D. MAYNARD, E.G. WILLIAMS and Y. LEE, 1985. “Nearfield acoustic holography: I. Theory of generalized holography and the development of NAH”, *Journal Acoustical Society America*, **78**(4), 1395–1413

[2] Earl G. Williams, 1999. “Fourier Acoustics, Sound Radiation and Nearfield Acoustical Holography”, (Acedemic Press, London, Book 306).

[3] W.A. VERONESI and J.D. MAYNARD, 1987. “Nearfield acoustic holography (NAH) II. Holographic reconstruction algorithms and computer implementation”, *Journal Acoustical Society America*, **81**(5), 1307–1322.

[4] J. HALD, 1989. “STSF – a unique technique for scan based Near-field Acoustic Holography without Restrictions on Coherence”, *Brüel&Kjær Technical Review no.* 1.

[5] K.B. GINN and J. HALD, 1989. “STSF – Practical instrumentation and applications”, *Brüel&Kjær Technical Review no.* 2.

[6] R. STEINER and J. HALD, 2001. “Nearfield Acoustical Holography Without the Errors and Limitations Caused by the Use of Spatial DFT”, *International Journal of Acoustics and Vibration*, **6**(2).

[7] J. HALD, 2001. “Planar Near-field Acoustical Holography with Arrays Smaller Than the Sound Source”, Proceedings o ICA.

[8] J. HALD, 2005. “Combining NAH and Beamforming Using the Same Array”, *Brüel&Kjær Technical Review no.* 1

[9] M. PINHO and J. ARRUDA, 2004. “On The Use of the Equivalent Source Method for Nearfield Acoustic Holography”, *ABCM Symposium Series in Mechatronics* – **1**, 590-599.

[10] J. GOMES, 2007. “Patch holography using a double layer microphone array”, *Proceedings of Inter-noise*.

[11] J. MØRKHOLT, J. HALD and S. GADE, 2010. “Measurement of Absorption Coefficient, Radiated and Absorbed Intensity on the panels of a Vehicle Cabin using a Dual Layer Array with Integrated Position Measuremen”, JSAE Paper 20105022.

[12] J. HALD, 2006. “ Panel Contribution analysis using a Volume Velocity Source and a Double Layer Array with SONAH Algorithm”, *Proceedings of Inter-noise.*

[13] J. GOMES, M. WADA, Y. FUKUJU, Y. ISHII, J. HALD and T. SATOH, 2011. “In-cabin Array-based Panel Contribution Analysis with a Vehicle Running on a Dyno”, *JSAE Paper* 20115359

[14] J. HALD, 2011. “Performance Investigation of the Dual-Layer Array (DLA) at Low Frequencies”, (Brüel&Kjær Technical Review No. 1, 2011)

[15] J. HALD, J. MØRKHOLT, P. HARDY, D. TRENTIN, M. BACH-ANDERSEN and G. KEITH, 2008. “Array Based measurement of radiated and absorbed sound intensity components”, *Proceedings of EuroNoise.*

Journal of Acoustical Society of India : Vol. 42, No. 1, 2015 (pp. 24-34)

Practical Prediction Models for Building Acoustics

Eddy Gerretsen[1] and Mahavir Singh[2]
[1]Level Acoustics BV, De Rondom 10, NL-5612 AP Eindhoven, The Netherlands
[2]AUV Standards, CSIR-National Physical Laboratory, New Delhi, India
e-mail : eddy.gerretsen@planet.nl; mahavir.acoustics@gmail.com

[Received:18.01.2014; Revised: 20.06.2014; Accepted: 11.08.2014]

ABSTRACT

The acoustic performance of buildings is an important aspect of the quality of the environ-ment in which we live and work. It concerns the airborne and impact sound insulation be-tween rooms, the sound reduction by facades for outdoor sounds, mainly traffic noise, the sound levels due to service equipment in buildings and the reverberant sound in common areas like staircases or corridors. In various countries requirements are specified for some or all of these aspects. How to achieve the required building performance has long been based on experience in construction and a trial-and-error approach by builders. In times that the building methods and materials only change gradually there is indeed time enough to gain the necessary experience in that way. But construction methods are changing more and more, new materials are introduced to the market and the call for an improved building performance becomes louder nowadays. And that is the case for new buildings as well as for renovating and improving the existing building stock, a task that will become increasingly important. This means there is no time anymore to gain experience by making mistakes, it becomes ne-cessary to design the required quality. In order to do so prediction models, simulation models, for the sound transmission in buildings are needed and the appropriate product data on buildings elements as input to those models. This need became obvious at the time the EU started to create the common market for building products around 1990, so this momentum was used within CEN, the European Standardization Organization, to start working on such models that specify the link between the acoustic performance of building elements and the performance of buildings. This resulted in the standard series EN 12354 of which the first parts were published in 2000 and the last of the six parts has become final in 2009. The first four parts have also been accepted as ISO standard, ISO 14712, being identical to the CEN standards. This paper will give a short overview of the standards, their influence on newly developed product standards and the ongoing activities in extending and improving the standards.

1. INTRODUCTION

The acoustic performance of buildings is an important aspect of the quality of the environment in which we live and work. There is currently a clear need to be able to predict the acoustic performance in the design stage. To this end prediction models, simulation models, have been developed and standardized standard series EN 12354 of which the first parts were published in 2000 and the last of the six parts has become final in 2009 [1]. The first four parts have also been accepted as ISO standard, ISO 14712, being identical to the CEN standards.

2. PREDICTION MODELS

2.1 Airborne and impact so und insulation

EN 12354 1 & 2 deal with the prediction of airborne and impact sound insulation between rooms. This could be based largely on earlier research, at least for more or less homogeneous structures [2]. The sound transmission between rooms is divided in the transmission by different transmission paths; see figure 1. For each path the transmission of sound power is considered. Though originally derived in a different way, this approach is essentially equal to a SEA-modelling of the sound transmission [3]. But instead of typical SEA quantities, the model uses well-known quantities as the sound reduction index R of all involved building elements and the normalized impact sound pressure level L_n of floors as measured in accordance with ISO 10140 [4].

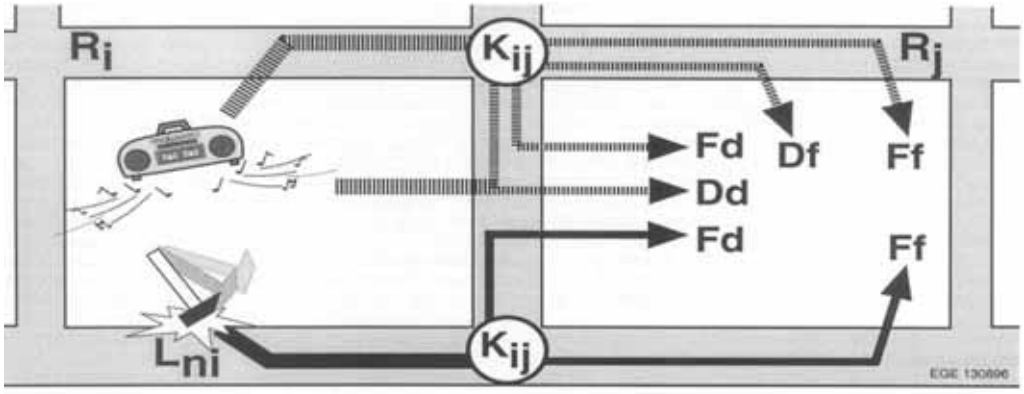

Fig. 1. - Illustration of airborne and impact sound transmission path with relevant quantities.

In order to get a practical quantity that describes the sound transmission through junctions, K_{ij}, use has been made of the principle of reciprocity in deriving the relations. And at least for relatively heavy building elements the field performance is influenced by the in-situ damping of the elements as mainly determined by the surrounding building structures. This can be taken into account through estimation of the structural reverberation time. However, taking average field values for the damping the most simple form for the flanking sound reduction index R_{ij} and the normalized impact level $L_{n,ij}$ for transmission path ij can be written as in eq. 1 and 2.

While for floor coverings and floating floors a method to measure the improvements is available (ΔL, ISO 140-8), this was clearly missing for linings and suspended ceilings (ΔR). Hence this work item was added and included in the current laboratory standard [4]. However, the main missing aspect was the performance of junctions between building elements as characterised by the vibration reduction index K_{ij}. Historical data have been used to give estimates for common junctions in the standard, while a laboratory measurement standard was established: ISO 10848 [5]. This standard then also covered the measurement of the total flanking transmission by element combinations, including suspended ceilings and raised floors, formally treated in some of the ISO 140 parts. The remaining parameters follow from the dimensions of the considered situation (junction length l_{ij}, area of the separating element S_s and the area of the excited element S_i).

$$R_{ij} = \frac{R_i + R_j}{2} + \Delta R_i + \Delta R_j + K_{ij} + 10\lg\frac{S_s}{l_{ij}} \tag{1}$$

$$L_{n,ij} = L_{n,ii} - \Delta L_i - \Delta R_j + \frac{R_i - R_j}{2} - K_{ij} - 10\lg\frac{S_i}{l_{ij}} \tag{2}$$

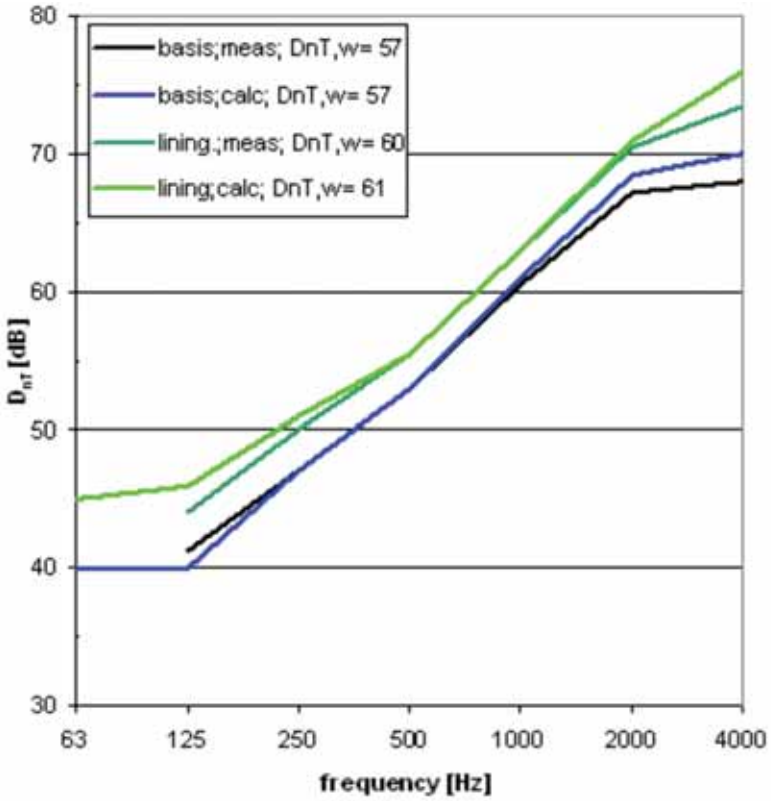

Fig. 2. – Measured and calculated sound level differences between living rooms; illustration of effect of an acoustic lining (ΔR_w =16 dB).

Figure 2 illustrates some prediction results in comparison with measurements for the sound reduction between rooms with a separating brick wall of 465 kg / m^2. Both measurements and prediction result in $D_{nT,w}$ = 57 dB. To improve the situation an acoustic lining is applied at one side of the wall; this lining showed an improvement of ΔR_w = 16 dB in the laboratory. Both measurement and prediction show only an improvement of about 3 dB in the actual field situation, clearly showing the effect of flanking transmission.

2.2 Façade insulation and radiation

In EN 12354 3 & 4: the sound transmission through facades is treated, either to protect against outdoor noise (mainly traffic noise) or to protect the outside against radiated noise (workplaces, disco's *etc.*). These parts are based mainly on well-known theories, the main discussions were on what to consider as element: for instance the window as a whole or the composing parts like the glass, the frame and the sealing. Finally both approaches were covered by the standard. Since in various countries the requirements are specified quite different, the prediction result has to reflect this too. Often the requirements consider the sound reduction index of the façade, R_{facade}, or the overall normalized level difference, $D_{2m,nT}$, or even the indoor level. These are of course all related and two of these are presented in eq. 3a and 3b for a façade composed from N elements with area S_j in a façade with a total area of S in front of a room with volume V.

$$R_{facade} = -10\lg \sum_{j=1}^{N} 10^{-R_{part,j}/10} \qquad (3^a)$$

$$R_{part} = R_j + 10\lg\frac{S}{S_j} \quad \text{or} \quad R_{part} = D_{ne,j} + 10\lg\frac{S}{A_o}$$

$$D_{2m,nT} = R_{\text{facade}} + 10\lg\frac{0,16V}{T_o S} + \Delta L_{fs} \qquad (3^b)$$

For many building elements as applied in facades measurement methods are available for the element performance R and D_{ne} [4]. Problems might arise with large elements for which no representative version can be tested in the laboratory test opening; there dedicated field measurements in selected situations can be helpful. Missing are standards to characterize sealing of slits, though such measurements can be based on the existing methods. Proposals to add this to the laboratory measurement standards (ISO 10140) are currently discussed.

Another important element for façade sound reduction can be the influence of the façade shape, the presence of balconies and such (ΔL_{fs}); see figure 3. However, it is not likely that a general measurement method can be established for this aspect. The data in the standard can best be extended by results of research or be replaced by a future engineering prediction method for these effects. One of the input data then needed will be the absorption of elements and surface treatments for which a standard is available [6].

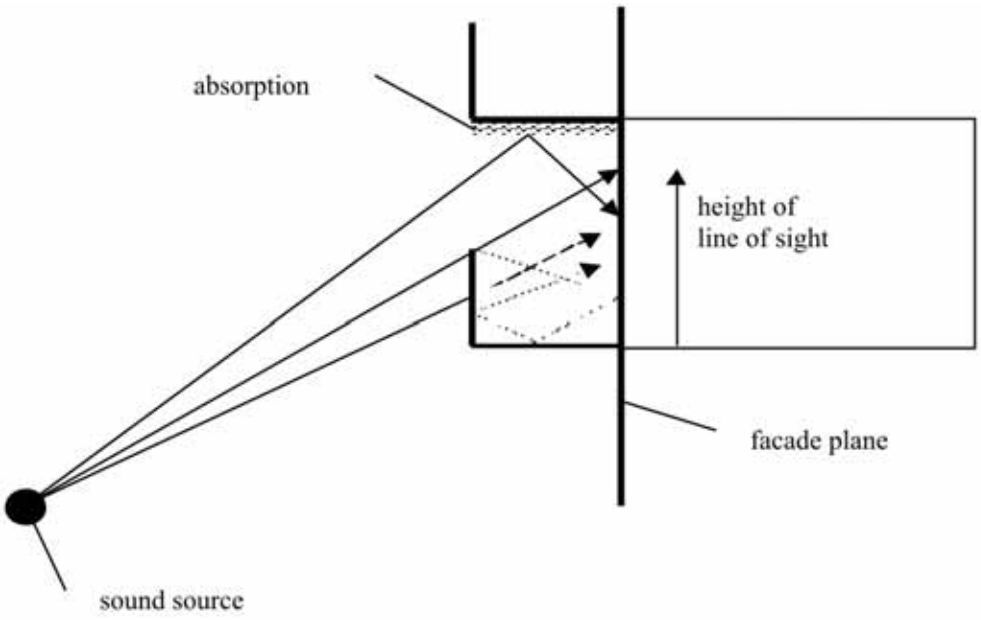

Fig. 3. Illustration of the effects (screening, reflections) of balconies on the sound transmission through a facade.

Part 4 actually deals only with the façade itself and thus gives no direct answers to outdoor sound levels. Both the estimation of the inside sound levels as caused by the sound sources as the sound propagation outdoors are outside the scope of the standard and should be dealt with by other prediction models. Just to be helpful an informative annex gives a complete prediction model for the sound level outside for very simple situations.

2.3 Service equipment

The most complicated part of the series is EN 12354 5 for sound levels due to service equipment in buildings. This is partly caused by the large variety of equipment concerned and the various mechanisms of sound generation and propagation. The standard has to deal with sound propagation through ducts and pipes, airborne sound as radiated from sources and structure-borne sound form sources, where it must be realized that each equipment or installation can be composed of many sources. A lot is already known and studied

concerning the first item (see f.i. [7]) and the second item can largely be based on available knowledge, but there is a huge lack of practical research results concerning the last parts [8].

Though some measurement methods for elements existed [9, 10], an overall scheme was missing in which the various elements and quantities used could find a logical place. This was therefore the first objective for part 5 of EN 12345: to create a general framework. For structure-borne sound the transmission through the building starts with the injected sound power by the source, applying the transmission as described in parts 1 and 2. The injected power by the installed equipment, $L_{Ws,installed}$, follows from the characteristic sound power $L_{Ws,c}$ for the source and a coupling term D_C including the appropriate source and building properties; see figure 4. For the time being various methods can be used to deduce those source properties, as indicated in the standard. Hopefully in due time the measurement methods for sources will show a more direct link to these quantities. Indeed, the development of EN 12354 has triggered already a lot of research activities, also leading to new measurement standards for equipment noise, as relevant for heavy building structures [11]. But a lot of questions are still to be solved.

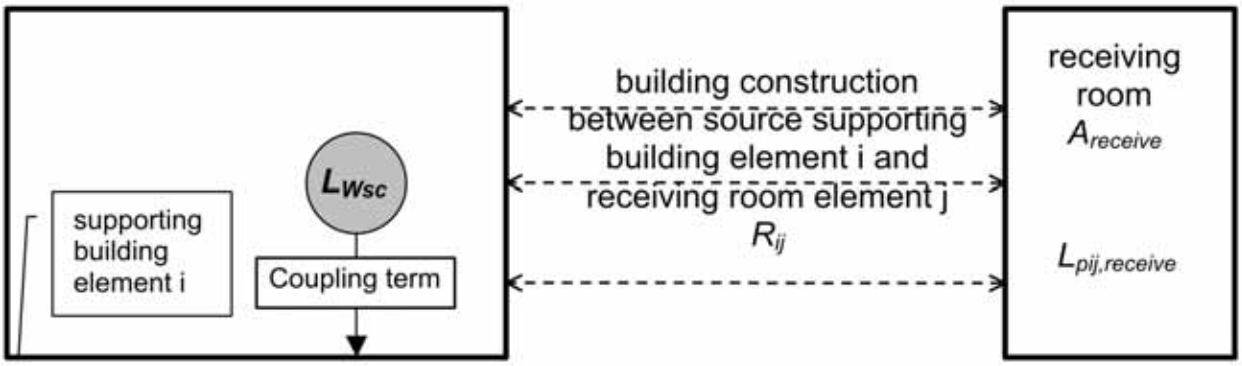

Fig. 4 - Illustration of parameters for the structure-borne sound transmission from a source to a receiver room.

The normalized sound level due to transmission of structure-borne sound via path ij, $L_{n,s,ij,}$ normalized to an absorption area of A_{ref} = 10 m^2, follows from eq. 4

$$L_{n,s,ij} = L_{Ws,installed,i} - D_{sa,i} - R_{ij,ref} - 10\lg\frac{S_i}{S_{ref}} - 10\lg\frac{A_{ref}}{4} \tag{4}$$

As stated the transmission is characterised by the flanking sound reduction index R_{ij}, but since the separating element is not well defined in this case, the area of the separating element is replaced by a reference area S_{ref} = 10 m^2. Though we are considering structure-borne sound excitation on element i here, the transmission is actually the same for airborne and structure-borne sound, hence the use of the sound reduction index also here and adding a transfer function D_{sa}, relating the injected structure-borne sound power to an equivalent airborne sound power. This quantity is only depending on the properties of the excited element.

The source strength for structure-borne sound is expressed in the characteristic sound power $L_{Ws,c}$, which is about the maximum power that the source could inject in a building element. The actual injected power is specified by the coupling term which in its simplest form contains the mobilities of the considered element, Y_i, and the considered source Y_s; see eq. 5^a and 5$^{b.}$

$$L_{Ws,installed} = L_{W,sc} - D_C \tag{5^a}$$

$$D_C = 10\lg \frac{\left|Y_s + Y_r\right|^2}{\left|Y_s\right|\mathrm{Re}(Y_r)} \qquad (5^b)$$

$$L_{Ws,installed} = L_F + 10\lg \mathrm{Re}(Y_r) \qquad (5^c)$$

In case the source could be considered as a force source, with force level L_F, this reduces to the well-known eq. 5^c. Figure 5 gives some examples for this situation of the force level of various sources. These equations are valid for a single point connection; in the normal case of several contact points the mobilities are to be considered as equivalent mobilities.

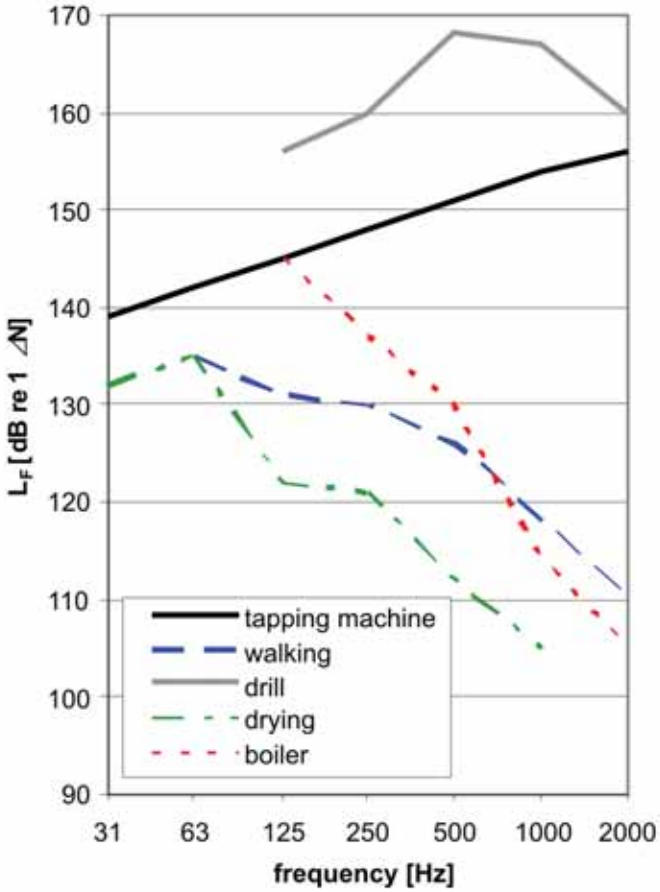

Fig. 5 : Force level for various structure-borne sound sources including the ISO tapping machine.

2.4 Reverberant sound

As is normal practice, EN 12354 6 used Sabine's relation to link reverberation time T to absorption data for building elements, α_s, and objects, A_{obj}, as determined by ISO 354 [6], see eq. 6^a and 6^b. V is the volume of the space and S_i the wall area with given absorption coefficient. Especially for the use in larger or occupied spaces, attention is given to the actual empty volume to be used and the effect of air absorption. However, the main problem is that for various enclosed spaces the Sabine-relation is not really adequate since the sound field is far from diffuse or the absorption is rather localized, for instance only the ceiling. To indicate at least possible deviations from the Sabine results an informative annex is included with a more detailed prediction model [13]. The effects are illustrated in figure 6, giving for a large room with absorbing ceiling

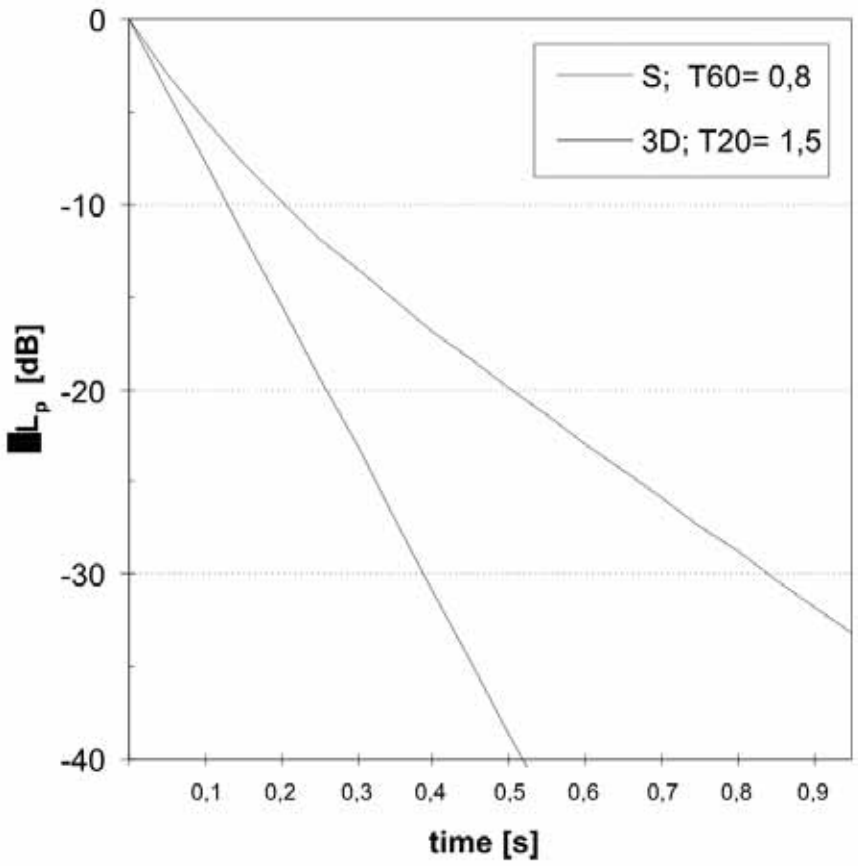

Fig. 6 : Calculated reverberation curves and times according to Sabine (S) and the estimation (3D) according to annex D of EN 12354-6.

and some scattering objects, the reverberation curve and time according to Sabine (S) and the estimation (3D) according to the annex of the standard. This certainly will not be the last answer, but at least as important for reliable predictions is the fact that the uncertainty in the input data as deduced from ISO 354 is still rather large.

$$A = \sum_{i=1}^{n} \alpha_{s,i} S_i + \sum_{j=1}^{o} A_{obj,j} \qquad (6^a)$$

$$T = 0,16 \frac{V}{A} \qquad (6^b)$$

3. CURRENT ACTIVITIES FOR EN 12354

The prediction models of part 1 and 2 of EN 12354 have been used quite extensively over the last years and have shown to be very useful, at least for buildings with mainly homogeneous structures. A point of concern has been to best way to apply the methods for light weight building structures. How to interpret the equations? How to adjust or extent them? How to collect the relevant input data?

With light weight elements the damping is less depending on the surrounding of the elements and more an inherent property of the elements concerned, hence the vibration reduction index could get a different meaning, being composed of a junction effect and an element effect [13]. But also the role of the radiation efficiency, being different for forced and resonant transmission, has to be reconsidered [14].

In the years around 2010 a lot of research has been going on in this area with concrete proposals to extend and adjust EN 12354-1&2 as well as ISO 10848 in the near future in order to cover also light weight structures [15], [16], [17]. The main results have been collected and presented in the eBook of the European COST Action FP 0702 on the acoustics of lightweight, wooden, constructions [18]. The conclusion being that for lightweight building elements the measurement results in a mock-up or a field situation with reasonable dimension will give results that can easier by transferred to other situations and dimensions. In other words, the results for the overall flanking transmission, D_{nf} or L_{nf}, in one - laboratory - situation can be transferred to other situations as already indicated in EN 12354 [4].

$$R_{ij} = D_{nf} + 10\lg\frac{S_s l_{ij,lab}}{A_0 l_{ij}}; \quad L_{n,ij} = L_{nf} - 10\lg\frac{S_i l_{ij,lab}}{S_{i,lab} l_{ij}} \tag{7}$$

where l_{ij} and S_i refer to coupling length and excited area in the field situation and the same quantities with the additional subscript 'lab' to the laboratory situation. This can be combined with estimations for other paths, either using the same equation or combining it with predictions following EN 12354 if appropriate. D_{nf} or L_{nf} for the path Ff can be measured in accordance with ISO 10848; though it seems that in many lightweight buildings that indeed is the dominating flanking path, sometimes other paths, like Fd or Df, can have a considerable contribution. For such paths the principles of ISO 10848 could be applied likewise.

Besides direct measurements the overall flanking transmission could also be estimated from a combination of measured and calculated data. If the element damping is indeed not varying much between situations, as is the presumption for the application of D_{nf}, than it could be expressed as:

$$\begin{aligned} D_{nf} &= \frac{R_i}{2} + \frac{R_j}{2} + \Delta R_i + \Delta R_j + \overline{D_{v,ij,n}} + 10\lg\frac{A_o}{l_{ij,lab}} \\ L_{nf} &= L_{n,ii} + \frac{(R_i - R_j)}{2} - \Delta L_i - \Delta R_j - \overline{D_{v,ij,n}} - 10\lg\frac{S_{i,lab}}{l_{ij,lab}} \end{aligned} \tag{8}$$

where $l_{ij,lab}$ = 4,5 m (horizontal junction) or 2, 6 m (vertical junction) and $S_{i,lab}$ H ≈ 19 m², R is the sound reduction index of the indicated element, L_n the normalized impact sound pressure level and ΔR the improvement of the sound reduction index by a lining for the indicated element. Indications are also given for methods to estimate for light weight elements R for resonant transmission only from measured values including the forced transmission. The new quantity for the junction is actually the K_{ij} from ISO 10848 and EN 12354 with standardization to (measurement) area. To make a more clear distinction this is further denoted as $\overline{D_{v,ij,n}}$. The advantage of this approach is that it can also be estimated more easily what would be the effect of changes in the elements.

Since these lightweight building elements normally consists of various layers (f.i. basic floor, suspended ceiling and floating floor) it is important to know which part of the construction is considered for R and what elements are considered as additional (ΔR). Various choices are possible and can lead to the same end result, but the choice for R prescribes what type of $\overline{D_{v,ij,n}}$ is to be used.

Research is still going on to find out how well such hybrid estimations of D_{nf} can be [18]. An example of that is given in figure 7 for a junction of lightweight walls and floors for which the vibration reduction index has been studied experimentally as well as with a Finite Element (FEM) and a SEA approach. The results compare quite well.

4. CONCLUSION

Developing prediction models for the acoustic performance of buildings was triggered by the creation of the free market within Europe, but the need for such models was also felt in Europe and elsewhere to be

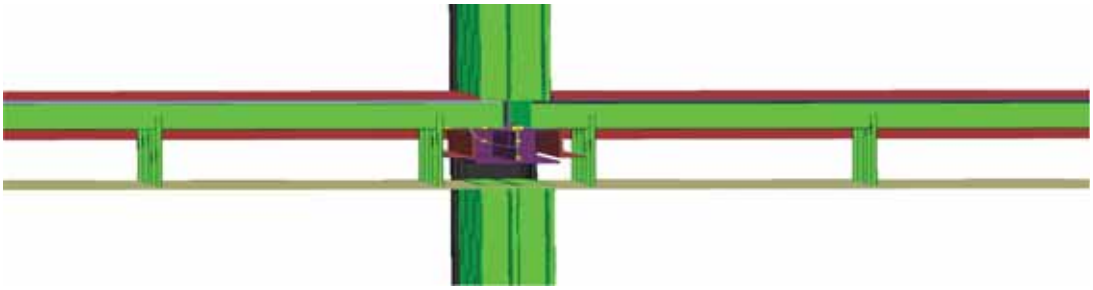

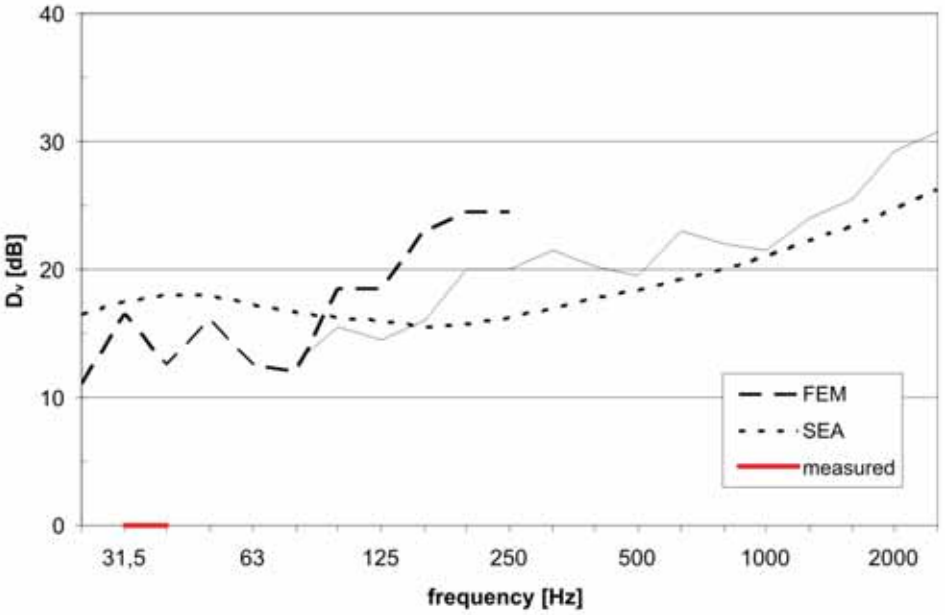

Fig. 7 : Illustration of a laboratory setup of a lightweight junction to determine $\overline{D_{v,ij,n}}$ together with the FEM-modelling and the comparison of measurement results with FEM and SEA calculations.

able to erect buildings with new methods and materials and improved performance which can no longer be achieved with the 'trial-and-error' approach, so common for the construction industry.

However, to be able to predict the building performance it is necessary to have data on the performance of all building elements involved. Drafting the prediction models made clear that indeed measurement standards were available for some elements, but needed adjustment for others or were just simply missing. Hence activities were started to develop or improve all standards that could produce the necessary input data for predictions.

The various parts of EN 12354 are to be considered as framework documents, giving the basic models and providing a common Building Acoustic language, thus facilitating exchange of information. However, to apply these models successfully guidelines and input data on elements are needed as they are relevant to the national or even local construction methods.

5. ACKNOWLEDGEMENT

The author acknowledges the valuable and often anonym contribution of all those active members in the various standardization working groups in establishing and improving standards.

6. REFERENCES

[1] EN 12354, 2000-2009. *Estimation of acoustic building performance from the performance of buildings elements, parts …6*; part 1..4 also available as ISO 15712

[2] E. GERRETSEN, 1994. *European developments in prediction models for building acoustics*, Acta Acustica 2205-14.

[3] T.T.R. NIGHTINGALE and I. BOSMANS, *Expressions for first-order flanking paths in homogeneous isotropic nd lightly damped buildings*, Acta Acustica united with Acustica 89 (2003), 110-122

[4] ISO 10140, 2010. Acoustics – *Laboratory measurements of sound insulation of building elements, 5 parts.*

[5] ISO 10848, *Acoustics – Laboratory measurement of the flanking transmission of airborne and impact sound between adjoining rooms*

[6] ISO 354, *Acoustics - Measurement of sound absorption in a reverberation room*

[7] VDI 2081, 2000. *Sound production and reduction in ventilation systems*, 2000.

[8] E. GERRETSEN, 2000. *Prediction model for sound transmission from machinery in buildings: feasible approaches and problems to be solved*, Internoise Nice.

[9] ISO 3822, *Acoustics – Laboratory tests on noise emission from appliances and equipment used in water supply installations*

[10] EN 14366, *Building Acoustics - Laboratory measurement of noise from waste water installations*

[11] EN 15657-1, *Building Acoustics - Laboratory measurement of airborne and structure-borne sound from service equipment. Part 1: Equipment mounted on low mobility receiver, taking whirlpool baths as an example*

[12] E. GERRETSEN, 2006. *Estimation methods for sound levels and reverberation time in a room with irregular shape or absorption distribution*, Acta Acustica nr.

[13] E. GERRETSEN, 2007. *Some aspects to improve sound insulation prediction models for lightweight elements*, Internoise Istanbul.

[14] M. VILLOT and C. GUIGOU-CARTER, 2005. *Prediction method adapted to lightweight constructions and related laboratory characterizations*, Forum Acusticum Budapest.

[15] S. SCHOENWALD and T.R.T. NIGHTINGALE e.a., 2006. *Application of the direct method of ISO 10848 to flanking transmission through double leaf gypsum board walls*, Internoise Honolulu.

[16] J. BRUNSKOG, A. LHOMOND and M. OHLRICH, 2007. *Attenuation and flanking transmission in light weight structures*, ICA Madrid.

[17] J.D. QUIRT and T.R.T. NIGHTINGALE, 2007. *On a semi-empirical approach to predicting sound insulation in lightweight framed construction*, Internoise Istanbul.

[18] eBook of European COST-Action FP0702 about lightweight (wooden) building elements (http://extranet.cstb.fr/sites/cost/ebook)

Journal of Acoustical Society of India : Vol. 42, No. 1, 2015 (pp. 35-45)

Artificial Neural Network Modeling for Estimating the Grain Size in Austenitic Stainless Steel Using Ultrasonic A-scan Signals

P. Madhumitha[1], S. Ramkishore[2], N. Chandrasekhar[3], M. Vasudevan[3] and P. Palanichamy[4*]

[1]Paypal India Pvt. Ltd, Sholinganallur, Chennai - 600119

[2]Akamai Technologies India Pvt. Ltd, Bellandur Village, ORR, Bangalore - 560037

[3]Materials Technology Division

[4]Nondestructive Evaluation Division

Indira Gandhi Centre for Atomic Research, Kalpakkam - 603102

**e-mail: ppc@igcar.gov.in*

[Received:15.02.2014; Revised: 24.08.2014; Accepted: 11.10.2014]

ABSTRACT

Among nondestructive testing (NDT) techniques, ultrasonic NDT play a key role in industries for the reliable defect detection and material evaluation. In recent times, application of artificial neural network (ANN) has been seriously considered for the evaluation of defect in industrial materials. In this work, we extend the application of ANN for the characterization of material microstructures viz. classification and estimation of average grain size in austenitic stainless steel AISI type 316. Three samples of AISI type 316 SS with varied grain sizes (fine, medium and coarse) were obtained by giving suitable heat treatments. They were subjected to ultrasonic measurements and A-scan data were acquired in each sample by using 2 MHz normal beam longitudinal wave probe. Optical metallography of the samples was carried out to quantify their grain sizes. From the acquired A-scan data of each sample, ANN models were developed to classify and estimate the average grain sizes. It is found that reliable and quick classification of grain size and quantitative estimation is also possible by the developed ANN models.

1. INTRODUCTION

Ultrasonic nondestructive testing (NDT) technique play major role in testing of industrial materials and components. The concept of ultrasonic testing only for defects / flaws has long been extended to their flaw sizing and evaluation and that is called nondestructive evaluation (NDE). Later, NDE had been extended to the evaluation of microstructures such as grain size, precipitates, *etc*. and residual stress measurements of industrial materials and components. At the same time, manual ultrasonic NDT and NDE have been replaced by automation and computerization to the maximum extent. Increasing automation in industries demands newer NDT procedures and data acquisition and interpretation techniques. In this way a large amount of acquired ultrasonic A-scan data must be quickly stored and efficiently handled in a shortest time period. The cost effectiveness and reliability of the developed testing technique and the defect free and qualified product output are the most important factors. In recent times, application of artificial neural network (ANN)

seriously considered for the evaluation of defect in industrial materials. In this work, we extend the application of ANN for the characterization of material microstructures viz. classification and estimation of average grain size in austenitic stainless steel AISI type 316.his document contains all the information necessary to prepare a manuscript for the 1st International Conference on Acoustics (Acoustics 2013 New Delhi), to be held in New Delhi, India, November 10-15, 2013. All papers should strictly follow the instructions given below.

Microstructures, especially average grain size of engineering metals / alloys is an important physical parameter and it governs the mechanical properties such as yield strength, fatigue, creep properties, *etc*. [1-2]. Austenitic stainless steels are preferred and used as structural and core material in Fast Breeder Reactors (FBRs). The knowledge of microstructures of this steel is important to ensure optimum mechanical properties of the manufactured components / structures. Among austenitic steels, AISI type 316 stainless steel and its modified forms are being used as structural materials in FBRs. Various studies have been reported in steels for grain size and other structural characterization by metallography and ultrasonic nondestructive techniques since 1980's [2-7]. The grain size of a material is an important engineering parameter which influences the mechanical properties such as fatigue, creep, yield strength, impact transition temperature etc. The importance of the estimation of grain size in a polycrystalline metal / alloy can also be understood from the Hall-Petch relation $ó_y = ó_i + k_y / \sqrt{D}$ where where $ó_y$ is the yield stress, $ó_o$ is a materials constant for the starting stress for dislocation movement (or the resistance of the lattice to dislocation motion), k_y is the strengthening coefficient (a constant unique to each material), and D is the average grain diameter. k_y is also known as Petch parameter and as unpinning constant [8]. Usually grain size is measured either from optical photomicrographs or while viewing the microstructure under a microscope. It is advantageous to use a non-destructive method for the measurement of grain size of a material since optical microscopic method is time consuming and some times requires cutting of samples from the material / component. Additionally, the optical method gives the grain size only at the selected locations and spatial variations, if any, cannot be obtained. In recent years, various techniques based on ultrasonic attenuation and velocity measurements have been developed for grain size measurements. Ultrasonic attenuation and velocity measurement have been mainly used for the determination of grain size [5-7]. Other ultrasonic parameters less used for grain size determination are: first back wall echo amplitude [9], back scattered bulk wave amplitude [3-4], back scattered leaky Rayleigh wave amplitude [10] and spectral amplitude of the first back wall echo [11]. However, average grain size measured as per the procedure given in the ASTM standard E112 using the linear intercept method has only been taken as the standard for comparison purpose [12]. Generally accepted steps involved in the grain size estimation using any ultrasonic method are as follows: (i) specimen preparation, (ii) measurement of ultrasonic parameter, (iii) metallographic examination of specimens, (iv) generation of calibration or master graph between the ultrasonic parameter and the metallographically estimated grain size, and (v) estimation of grain size in new specimens to validate the calibration graph and also to establish the accuracy.

Comparison of ultrasonic attenuation (UA) measurements made at different frequencies showed that measurements made at 4MHz longitudinal wave transducer gave better results for the grain size estimation [5]. Problems connected with the attenuation method such as couplant and diffraction corrections are eliminated in the method based on ultrasonic relative attenuation (URA) [9]. Measurements with a 10MHz immersion transducer gave the best result. This is a first of its kind approach. Ultrasonic velocity (UV) measurements were tried for the first time for the grain size estimation [6]. Accurate velocity measurements at 2MHz were made for longitudinal and shear waves using pulse echo overlap technique. A linear relationship was found to exist between the velocity and the metallographically estimated grain size. Unlike the attenuation and first back wall echo amplitude methods, velocity measurements were also found to be less affected by changes in the grain size distribution. For the estimation of only surface / subsurface grain size, a method based on the measurement of the amplitudes of the back scattered leaky Rayleigh wave (LRW) was employed [10]. Results indicated that confidence level of 75% only could be achieved using conventional attenuation method and the repeatability of the measurement data was also found to be poor. Measurements using first back wall echoes and LRW amplitudes gave better than 80% confidence level. It was found that best confidence level of 85% in the grain size estimation was achieved using velocity measurements.

As compared to the longitudinal waves, shear waves were found to be more sensitive in grain size estimation using the velocity measurements. Selection of proper frequency also plays an important role in grain size estimation by different methods. These studies show that: (i) Ultrasonic methods can replace time consuming metallographic methods for grain size estimation. (ii) URA method is most useful for coarse grained and thick stainless steels. The method is also amenable for continuous measurements in production line. (iii) Method based on velocity measurements is best for achieving higher accuracy level in grain size measurements. Recently, method based on ultrasonic spectral approach (USA-shift in the peak frequency due to grain size variation) has also been proposed and advantage of this method in average grain size determination is that variation in couplant thickness does not affect the results. Qualitative performance of all conventional ultrasonic attenuation and velocity measurements based methods in comparison with metallographic method is summarized in Table I.

Table 1: Performance of ultrasonic based methods in comparison with metallography on the the determination of average grain size in AISI type 316 Stainless Steel.

PROPERTY	UA	UB	URA	LRW	UV	USA	Metallography
Volume Analysis	Yes	No	Yes	No	Yes	Yes	Possible
Standard	Offing	No	No	No	No	No	Yes
Instrumentation	Less costly	Costly	Moderate	Moderate	Moderate	Costly	Costly
Coarse Grain	Yes	Possible	Best	Best	Good	Better	Better
Thicker Specimen	Poor	Best	Best	Better	Better	Poor	Better
Online Measurement	No	Possible	Best	Possible	No	Possible	No
Correction Factors	Yes	Yes	No	No	No	No	Not applicable
Confidence Level	70%	75%	80%	80%	85%	75%	Standard

Note: UA - Ultrasonic attenuation method; UB - Ultrasonic backscattering; URA - Ultrasonic rela-tive attenuation; LRW - Leaky Rayleigh wave; UV - Ultrasonic velocity; USA - Ultrasonic spectral approach

In recent years a totally new concepts are being adopted for flaw evaluation and microstructural characterization using signal analysis approach. Barat *et al.* have stuied microstructural characterization of materials by neural network (NN) technique [13]. They have used backscattered ultrasonic signal between two back wall echoes instead of using conventional technique for their studies. The signal dimension representation is reduced by Modified Karhunen Loeve Transform method and the result shows good reliability for differentiating the sample with changing microstructure [13]. The crack, slag and porosity of weld defects in weld joints on 20 mm thick are investigated by classification methodology by ANN. This methodology was developed for automatic recognition of weld defects by P-scan ultrasonic system [14]. The ANN technique is used for accurate flaw detection in steel plates on various samples such as non-defective plates, side drilled hole, inclusions and porosity together with smooth and rough cracks. The obtained result shows that significant benefits were achieved using this method [15].

2. SAMPLE PREPARATION, INSTRUMENTATION AND DATA ACQUISITION

Several specimens having dimensions 50 mm diameter and 20mm thickness were heat treated at different temperatures (1353K to 1473K) for different time durations (15 min to 2 hr). These specimens were next given heat treatment at 1323K for 30 minutes followed by water quenching treatment to homogenize the grain structure [6]. The grain size in these specimens, measured as per the procedure given in the ASTM standard E112 in the range 30-168 m. Out of which only three specimens with fine (30 μm), medium (78 μm) and coarse grain (138 μm) sizes were selected for this study. Figure 1 shows the metallographic microstructures of these specimens. Figure 2 shows the schematic experimental arrangement for the ultrasonic A-scan data

acquisition from the samples using 20 mm diameter broad band 2 MHz normal beam longitudinal wave transducer. A minimum of 40 A-scan signals for each sample was acquired for the purpose of training ANN.

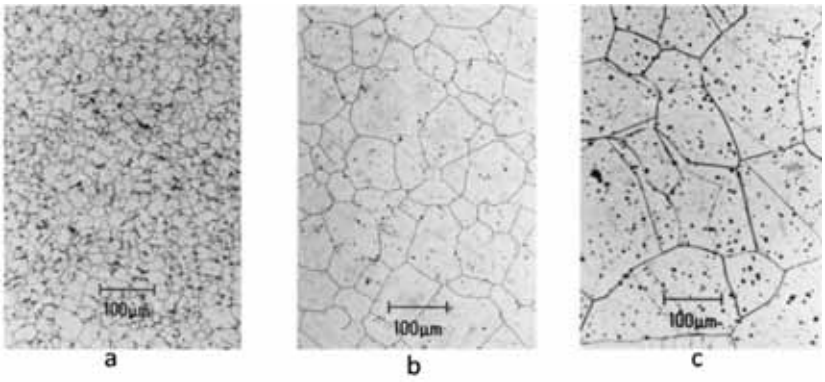

Fig. 1. Photomicrographs of the stainless steel specimens (a) 30 µm, (b) 78 µm and (c) 138 µm.

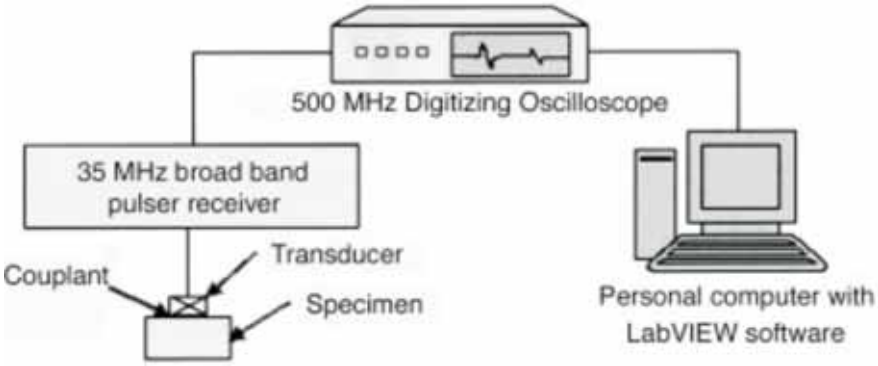

Fig. 2. Experimental setup used for ultrasonic A-scan data acquisition.

3. ARTIFICIAL NEURAL NETWORK APPROACH

Increasing automation needs newer NDT procedures and data acquisition and interpretation techniques. Besides this, large amount of acquired A-scan data must be handled quickly and quantitatively. The cost effectiveness and reliability of the developed NDT&E technique and also the product output are most important. In recent times, application of ANN seriously considered for the evaluation of defect. In one of the earlier study Roy et al. used ultrasonic back wall echoes for the classification of materials through neural network (NN) [16]. A multi-layered feed-forward ANN was trained by the frequency domain signals of the two classes, obtained from aluminum and copper samples. It was found that the performance of the learned network was quite reliable on the test samples even where the thickness of the test sample is different from the learned samples. Polikar et al studied the intergranular stress corrosion cracking in weld joints by using frequency invariant classification of ultrasonic A-scan signals [17]. Pattern Classification NN involves configuring the input signal feature space to an output space of several classes. The multilayer feed forward network is the one of the popular network for pattern recognition. The perspective of pattern recognition, NN can be regarded as an expansion of the many conventional techniques which have been developed over several decades. In the regression model predicting the values for continuous variable is for the given input variables. In the classification network involves input pattern of discrete classes. This can formulate as a classification problem in terms of a set of functions which configure inputs to outputs where the outputs maps the which of the classes the input pattern belongs to. The reliability of ultrasonic characterization of welds by the ANN was recently studied by Bettayab [18]. In this work, we extend the application of this

ANN approach for the characterization of material microstructures viz. the estimation of average grain size in austenitic stainless steel AISI type 316. The Figure 3 shows that the flow diagram of various steps involved in the model development and Figure 4 shows that neural network structure of developed model.

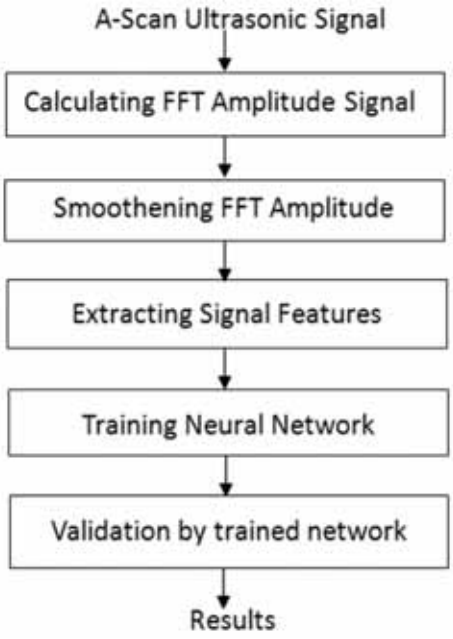

Fig. 3. Flow diagram of Model Development.

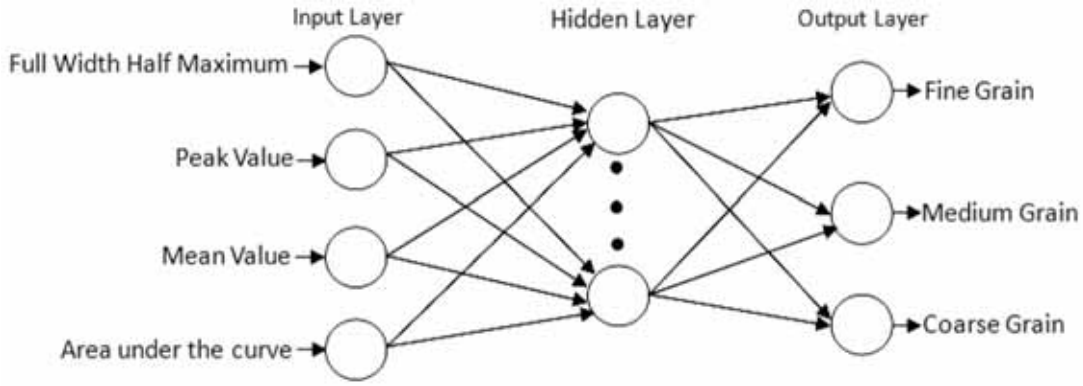

Fig. 4. Developed ANN model structure.

3.1 Feature Extraction

In this investigation, four features have been extracted for characterization of material microstructures *viz.* classification and estimation of average grain size in austenitic stainless steel AISI type 316. Three samples of AISI type 316 SS with varied grain sizes of fine (30 m), medium (78 m) and coarse (138 m) is subjected to ultrasonic measurements and acquiring A-scan data. The samples were acquired using 2MHz normal beam longitudinal wave probes. The 114 number of signal is simulated for each grain sizes trained to classify and estimate the average grain sizes. The Fast Fourier Transforms (FFTs) were carried on the time domain of recorded signal. The typical signal of ultrasonic measurement is shown in Figure 5. The amplitude of FFT frequency spectrum is smoothed by five points of FFT technique using Origin software for further processing. The FFT amplitude and smoothed signal is shown in Figure 6. From the smoothed signal the fallowing four

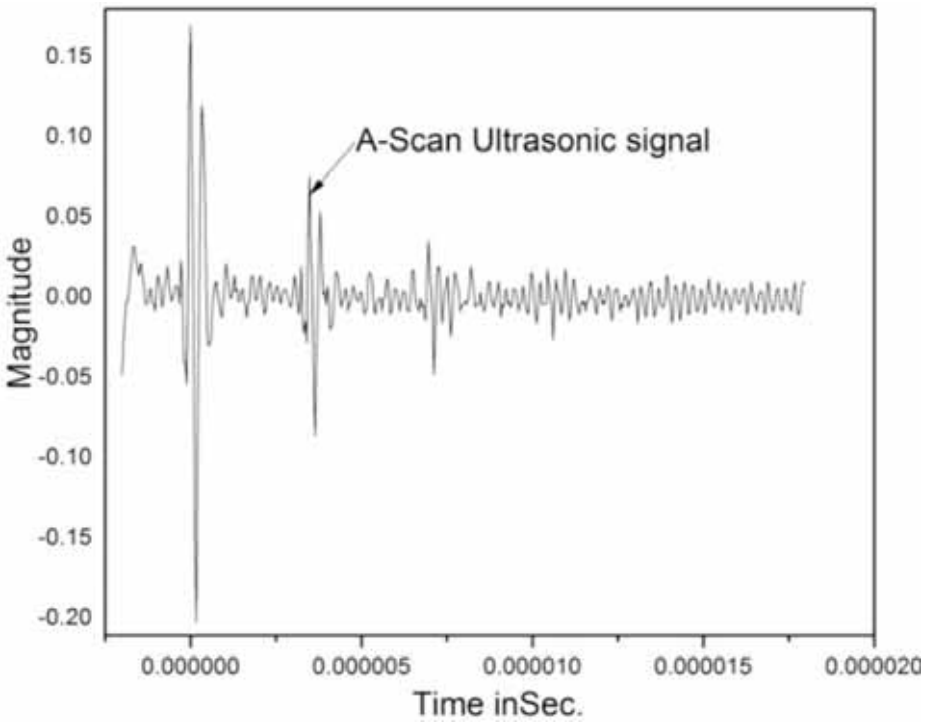

Fig. 5. Typical ultrasonic A-scan (time domain) signal

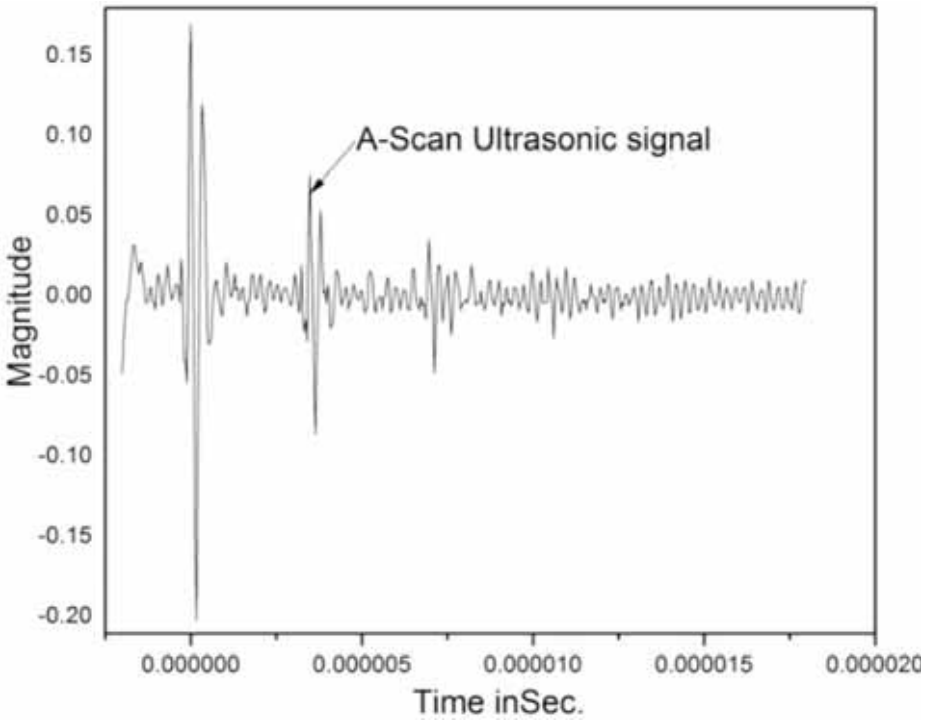

Fig. 6. FFT amplitude (frequency domain) and smoothed signal.

signal features were extracted to develop the NN model. The extracted features are Full Width Half Maximum, Area under curve, Mean and Peak value of the ultrasonic measurement signal. They have a number of features and tools for quantitative analysis of the ultrasonic measurements signals. The selected features alone more accurate to classify the input signals. The extracted features are created a dataset to train the NN model.

3.2 Dataset Preparation

From the extracted four features, a total of 114 data points were created. The total dataset was uniformly scaled to (0-1) by following normalization formula before generation of the model. After applying normalization, the total dataset was randomized for training NN. Among the 114 data points, 97 were used for training, 10 for testing and 6 for validation. The properly organized data-sets were commonly used for both regression and patter classification NN.

$$X_N = (X - X_{min}) \; / \; (X_{max} - X_{min})\text{; Data normalization}$$

3.3 Neural network model development

The objective of this model development is to classify the micro structural grain sizes corresponding to the given input ultrasonic measurement signals. Two individual models (regression and pattern classification) were developed for comparing the performance. The feed-forward NN architecture consists of three layers namely input, hidden and output layer. Among the prepared dataset 85% were used for training, 10% were used for testing and 5% were used for validation. The feed-forward back propagation regression NN was created with one hidden and one output layer using Matlab toolbox. The four input variables consist of FWHM, Area under the curve, Peak and Mean value of ultrasonic measurement. The output consists of Fine, Medium and Coarse of microstructure of grain sizes. The network was trained with various hidden neurons. The number of hidden neurons was calibrated till it reached the minimum RMS error in the learning curve. It was observed that six hidden neurons exhibit minimum RMS error value. The Tansigmoidal and pure linear function were used for activation. The network was trained with Levenberg-Marquardt algorithm and it converged in 57 epochs with an RMS error of 0.00000017. The learning performance curve is as shown in Figure 7.

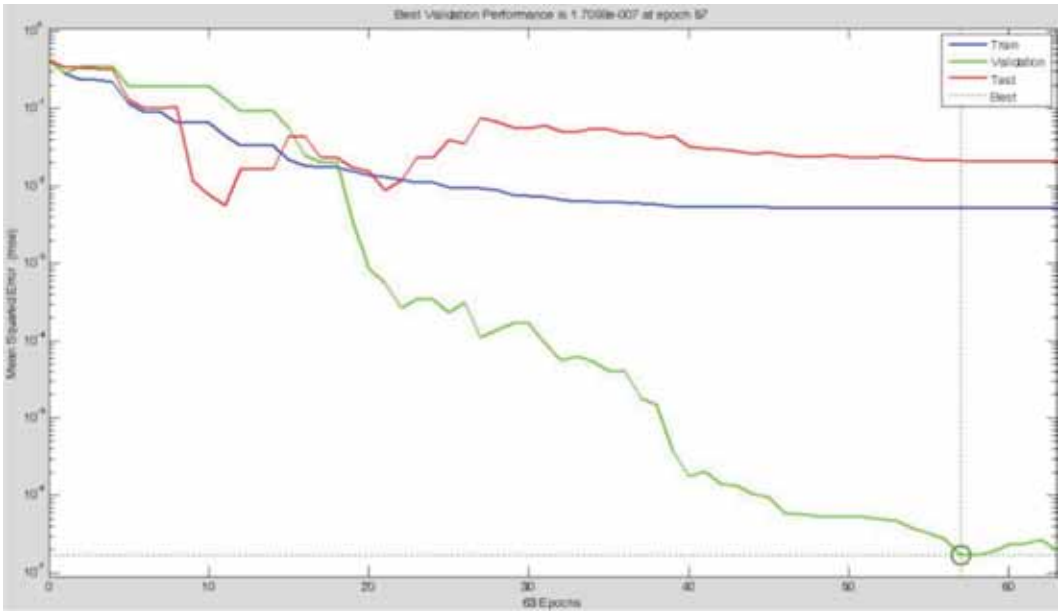

Fig. 7. Learning Performance curveof regression method

The pattern classification model consists of feature selection stage fallowed by classifier. In the feature selection, large dimensional input signal is transformed to minimized dimensional feature vectors. The classifier produce decision surface to discriminate the feature vector of different classes. The model developed for extracted feature signals are associated with three different classes. The 'patternet' Matlab toolbox command is used to create feed-forward pattern classification network. The toolbox automatically selects 10 hidden neurons.

The input data vectors are automatically divides into training, validation and test sets and training continues till there is improvement on the validation set. The rapidly decreased performance of learning curve shows that the minimum RMS error of 0.0051724 is reached at 25 epochs. The learning curve is as shown in Figure 8. The mean squared error of the trained network is measured with respect to the testing samples. The network output range is in 0 to 1 is fitted into the confusion plot. The first measure in classification is by confusion matrix. The confusion matrix is plotted across all samples for training, testing, validation and overall. The confusion matrix shows the various types of error occurred in final network as a percentage of correct and incorrect classifications. Correct classifications are mentioned in green squares of 'all confusion matrices' plot and the diagonal is 35.1% and 64%. Incorrect classifications mentioned in red squares is 0.9%. The blue cell in the bottom right shows the total percentage of correct classification which is 99.1%. The second measure in classification is by Receiver Operating Characteristic (ROC) plot. This shows that false positive and true positive rate relates as the thresholding of outputs is varied from 0 to 1. The green line in the ROC plot going from bottom left corner to the top corner shows the best accurate classification of our model.

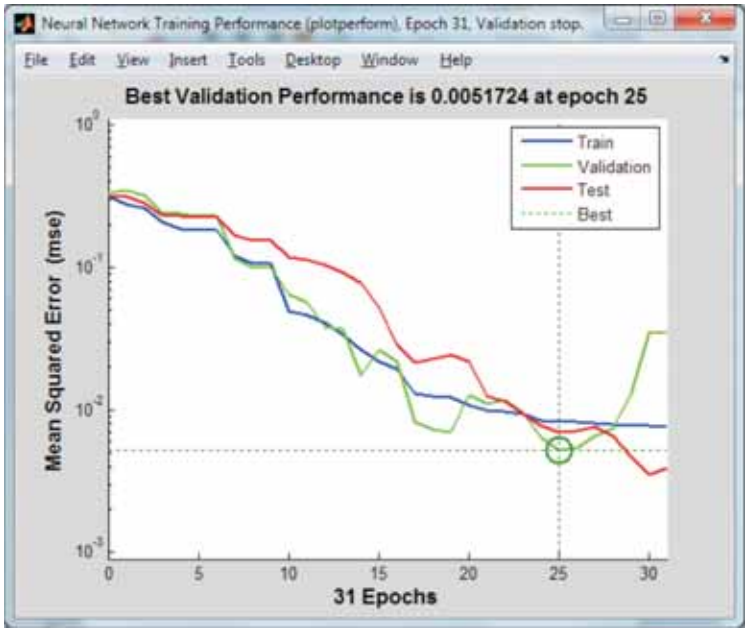

Fig. 8. Learning Performance curve of Pattern classification method

4. DISCUSSION

From the introduction part of this paper it is understood that ultrasonic attenuation, velocity, back scattered wave amplitude measurements based methods are acceptable for average grain size estimation in AISI type 316 stainless steels. As compared to metallographic methods, ultrasonic methods have several advantageous including their main advantage of nondestructively evaluating the mean grain sizes. However, for industrial based automation and quick and quantization analysis of grain sizes and other microstructural features,

ANN based A-Scan signal analysis methods are most preferable. They have become popular for defect characterization and evaluation in recent times. In this work ANN approach has been judiously considered for one of the important aspect of micro-structural characterization viz. grain size classification and estimation. Acquired A-Scan signals from each sample are the prime important for application of ANN in addition to the appropriate selection of suitable ANN approach for adaptation. Training of ANN algorithm assumes importance next. Once the above procedures have been followed then the classification and quantitative estimation of grain size become simple. The feed forward regression model of neural network exhibits minimum RMS error of 0.00000017 and it is converged at 57 epochs. The classification neural network model gives an accuracy of 99.1% for the classification of grain sizes. The confusion and ROC plots are shown in Figure 9 and Figure 10.

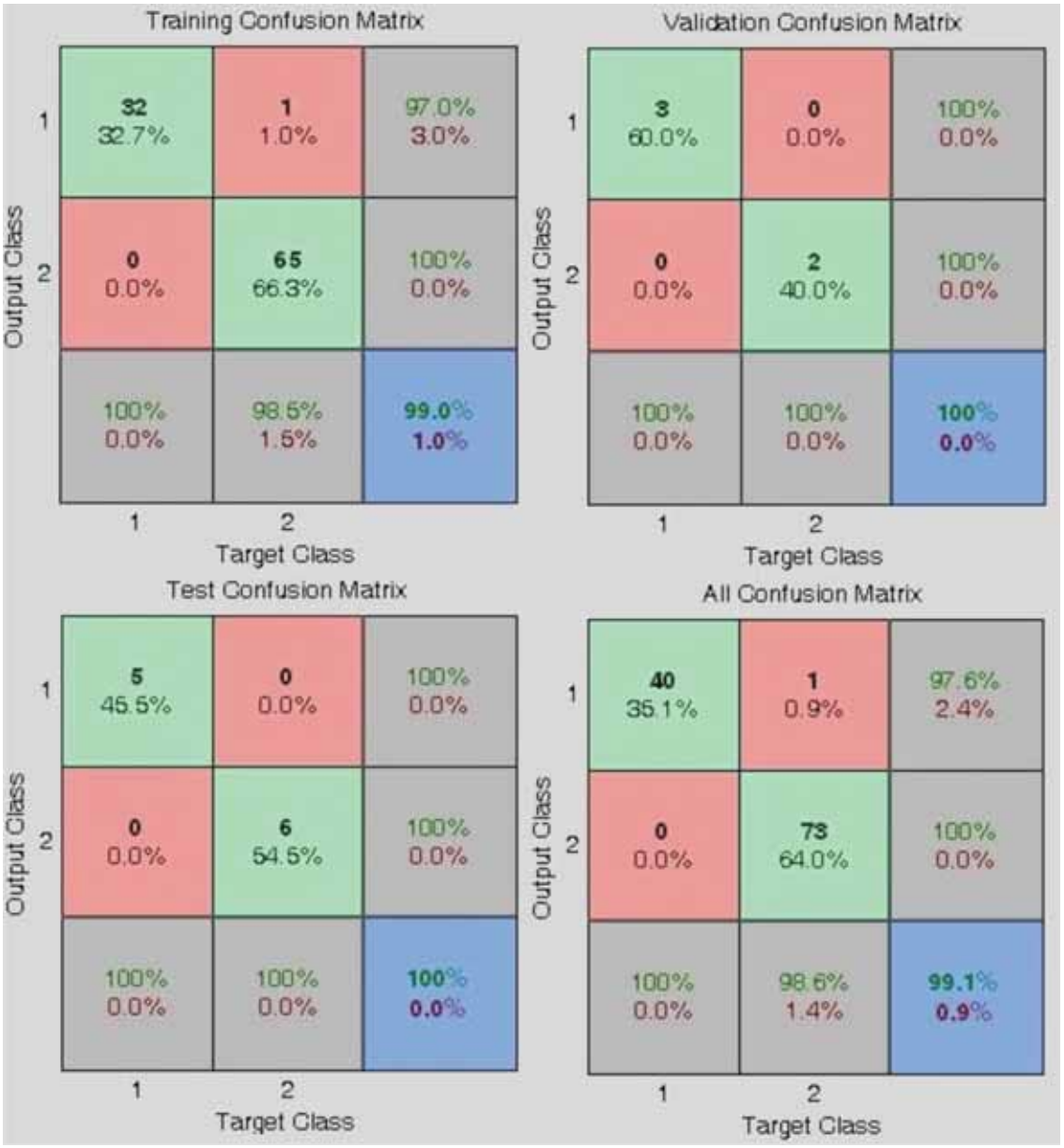

Fig. 9. Confusion matrix plot

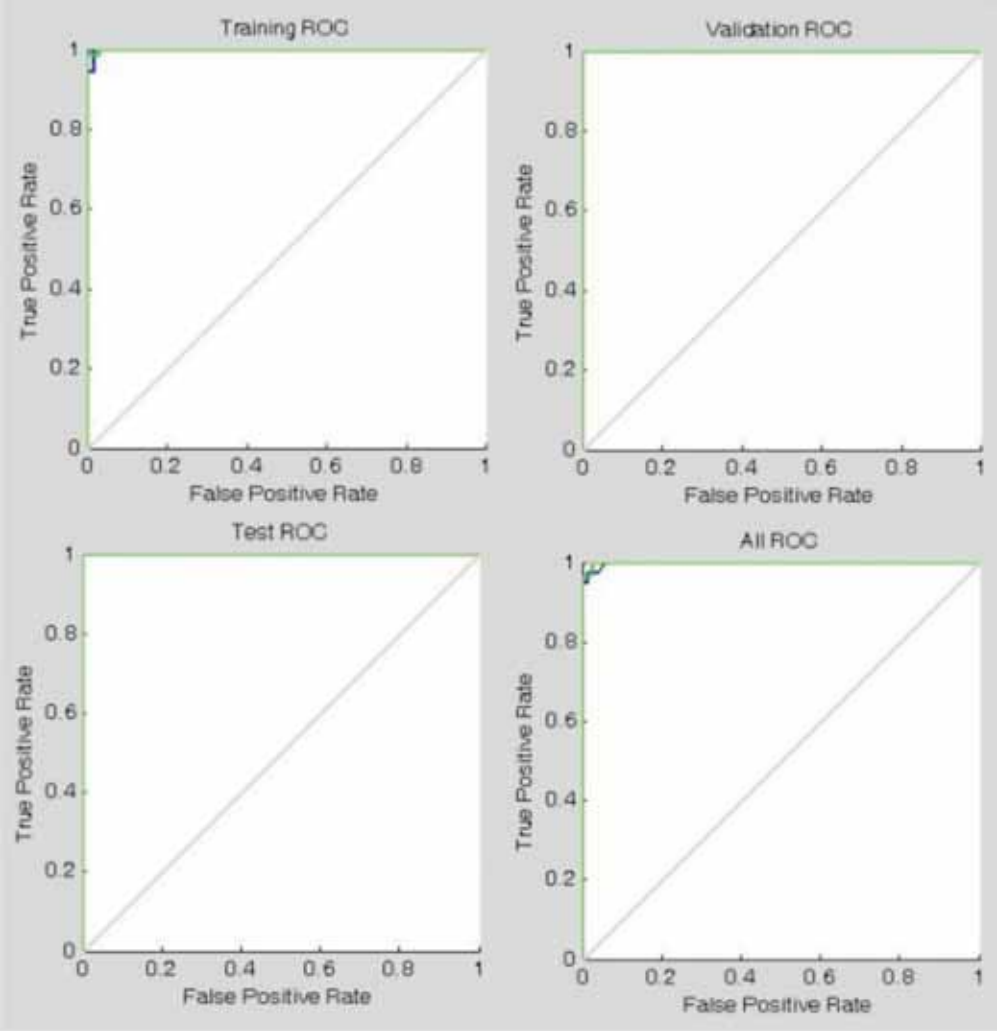

Fig. 10. Receiver operating characteristic plots

5. CONCLUSIONS

1. Artificial neural network based approach has been successfully used for estimating grain size in austenitic stainless steel using ultrasonic A-Scan data.
2. Compared to regression neural network, classification neural network is found to be more accurate in estimating grain size in 316 stainless steel.
3. The model is found to be very quick and quantitative and can be adopted easily in the industries for estimating grain size.

6. ACKNOWLEDGEMENTS

First and second authors of this work are former graduate students from Department of Computer Science and Engineering, Anna University, Guindy Campus, Chennai - 600028 and they would like to profoundly thank their Professors and Faculties who helped them during the course of this study at the Indira Gandhi Centre for Atomic Research, Kalpakkam - 603102.

7. REFERENCES

[1] E.P. PAPADAKIS, 1984. Physical Acoustics and microstructures of iron alloys, *International Metals Reviews*, **1**, 1-24.

[2] A. VARY, 1990. Ultrasonic Measurements of Material Properties, In *"Research Techniques in NDT"*, Ed. R.S. Sharpe, Academic Press, London, **4**, 189-204.

[3] A. HECTH, *et al.*, 1981. Nondestructive Determination of grain size in austenitic stainless steel by ultrasonic back scattering, *Materials Evaluation*, **39**, 934-938.

[4] H. WILLIAMS and K. GOEBBLES, 1981. Characterisation of microstructures by back scattered ultrasonic waves, *Metal Science*, **15**, 549-554.

[5] P. PALANICHAMY, C.V. SUBRAMANIAN, P. BARAT, D.K. BHATTACHARYA and BALDEV RAJ, 1988. A NDT method for grain size determination in austenitic stainless steel, *Trans. IIM*, **41**(5), 485 488.

[6] P. PALANICHAMY, A. JOSEPH, T. JAYAKUMAR and BALDEV RAJ, 1995. Determination of average grain size in austenitic stainless steel by ultrasonic velocity measurements", NDT & E International, **28**(3), 179 185.

[7] http://www4.ncsu.edu/~murty/NE509/NOTES/Ch5d-Strengthening.pdf

[8] R. KLINMAN and E.T. STEPHENSON, 1981. Ultrasonic prediction of average grain size and mechanical properties in plain carbon steel, *Mater. Eval.*, **39**, 1116-1120.

[9] P. PALANICHAMY, A. JOSEPH and T. JAYAKUMAR, 1994. Grain size measurements in austenitic stainless steel using ultrasonics, *Insight*, **36**(11), 874-877.

[10] P. PALANICHAMY and T. JAYAKUMAR, 1996. Grain size measurements by ultrasonic rayleigh surface waves, 14th WCNDT, Dec. 8-13, New Delhi, India.

[11] ANISH KUMAR, T. JAYAKUMAR, P. PALANICHAMY and BALDEV RAJ, 1999. Influence of grain size on ultrasonic spectral parameters in AISI Type 316 stainless steel, *Scripta Materiala*, **40**(3), 333-340.

[12] ASTM Standard E112-10, Standard Test Methods for Determining Average Grain Size, Annual Book of ASTM Standard, 03.03, (2010).

[13] P. BARAT, A. CHATTERJEEE, P. MUKHERJEE, N. GAYATHRI, T. JAYAKUMAR and BALDEV RAJ, 2010. Microstructural characterization of materials by neural network technique, Physics Letters A, **375**, 6-10.

[14] A. MASANATA and M. SUNSERI, 1996. Neural network classification of flaws detected by ultrasonic means, NDT&E International, **29**(2), 87-93.

[15] F.W. MARGRAVE, K. RIGAS, D.A. BRADLEY and P. BARROWCLIFFE, The use of neural networks in ultrasonic flaw detection, *Measurement*, **25**, 143-154

[16] A. ROY, P. BARAT and S.K. DE, 1994. ULTRASONICS, **33**(3), 175-180.

[17] R. POLIKAR, L. UDPA, S. UDPA and T. TAYLOR, 1998. *IEEE Trans. Ult. Ferr. & Freq. Cont.*, 45(3), 614-625.

[18] F. BETTAYAB, H. BENBARATOUI and B. RAOURAOU, 2008. The reliability of the ultrasonic characterisation of welds by the artificial neural network, 17th WCNDT, 25-28, Shanghai, China.

Journal of Acoustical Society of India : Vol. 42, No. 1, 2015 (pp. 54-60)

A Numerical Study to Optimize A Partially Covered Damping Structure

Selmen Naimia[1,2*], Samir Assaf[1] and Mohamed Ali Hamdi[2]

[1]PôleMécanique,Ecole Supérieur des Technologie Aéronautique et de Construction Automobile (ESTACA-ISAE),34,Rue Victor Hugo,92300 Levallois-Perret, France

[2]Laboratoire Roberval, Université de Technologie de Compiègne, Rue Personne de Roberval, Centre de Recherche CRD338, B.P. 20529, Compiègne 60205, France

**e-mail: selmen.naimi@estaca.fr*

[Received: 10.02.2014; Revised: 30.06.2014; Accepted: 05.08.2014]

ABSTRACT

One of the most effective ways of reducing vibration in structures is to apply a viscoelastic damping treatment. Nowadays, the constrained layer damping treatment is widely used in mechanical engineering applications particularly in automotive and aerospace industries. However, the efficiency of the damping patches is very sensitive to the localization of the treatment on a structure and to the relative properties of the elastic and viscoelastic layers. Thus, an optimized damping design is required to achieve good performance with constraints like limited weight and restricted space for the treatment. In this work, a numerical study based on a finite element approachis done. The undamped plate structure is modeled using a discrete Kirchhoff theory (DKT) element while the damped plate is modeled with a specific sandwich plate element.An indicator to select the best damping patch locations is used, which is based on the energy dissipated through the viscoelastic layer of the damped plate. Then, a parametric study, regarding the variation in the damping characteristics,is conducted by fixing the total weight of the added treatment and varying pair of design parameters as the thickness of the viscoelastic layer and the constraining layer. It is shown that an appropriate selection of added patch parameter can significantly improve the damping characteristics while reducing the added mass. These results are now used to suggestan optimization schemein order to find the optimal configuration of the damping patches with a limited added weight.

1. INTRODUCTION

Sandwich structure with viscoelastic core has been used as a way to reduce efficiently vibration and noise such as in automotive, aeronautical and aerospace industry[1]. In order to reduce cost and weight, partial damping treatment is often used. In this design only a portion of the base structure is covered with damping patches. The earliest study of a partially covered sandwich structure was done by Nokes and Nelson [2]. Later, an analytical study was carried out by Lallet al. for a beam [3] and for a plate [4] with a single damping patch. A multiple patches study was presented by Kung and Singh [5]. Recently, Sher and Moreira [6]presented a dimensionless analysis on the effect of design parameters, as the thickness length ratio, constraining layer thickness, material modulus, natural mode and boundary conditions, on the treatment efficiency. Such works show the usefulness of implementing an optimization methodology.

Thereafter, targeting to optimize structure damping, various works have been done to optimally design vibrating structures. For the case of fully covered sandwich beams, Lifshitz and Leibowitz [7] determined an optimal configuration by taking as design variables the layer thickness. Marcelinet al.[8-9] performed an optimization study of constrained layer damping (CLD) treatments covering one or several portions of a beam. They considered treatment dimensions and locations as design variables and the damping factor as objective function. Nakra [10]carried out optimum design studies for partially covered plates, where the objective function was to maximize the system loss factor, and the design parameters were the dimensions of the patch, and the thicknesses of the constraining layer and the viscoelastic layer. The patch coverage area was restricted.Chen and Huang [11] applied a topographical method in junction with the complex method to search the optimum of constrained layer treatment for vibration suppression. Zheng et al.[12] presented the optimization of the vibrational energy of beams with CLD treatments considering patch location and length and viscoealstic material shear modulus as design variables. They used a genetic algorithm based optimization methodology. Hao and Rao [13], based on analytical model to predict the damping, they presented a procedure for the optimization of simply supported beams covered with a CLD treatment, the objective was to maximize the damping within given temperature and frequency range.

This work aims to present an investigation study of sandwich plate optimality conditions in the case of patch constant weight and variable layers thicknesses of patch, in order to prepare the optimization scheme. It uses a numerical approach, well adapted to parametric and optimization studies, based on a finite element model with reduced degrees of freedom.The first section presents the theoretical formulation, followed by a finite element formulation description. Next, a parametric study is conducted to investigatethe effects of patch layers thickness and material properties on the damping capacity of the system. Finally, an optimization study performed to scan the best patch parameter option for a given patch weight, that ends by a proposition of an optimization scheme.

2. ANALYTICAL FORMULATION

The sandwich plate under study is in the (x, y) reference plane and takes the origin of the z-axis as a carrying surface of the core as shown in Fig. 1. The displacement field of each layer is written according to assumptions as follows : (1) all displacements are small as in linear elastic theory; (2)all the layers are assumed to be isotropic and homogeneous; (3)planes transverse to the middle plane before deformation remain plane and continuous after deformation; (4) the transverse displacement remains constant throughout the thickness of the plate; (5) the shear deformations in the base plate and the constraining layer are neglected; (6) the viscoelastic layer is subjected to extension, bending, in-plane shear deformations and transverse shear deformations; (7) there is no slip considered at the layer interfaces.

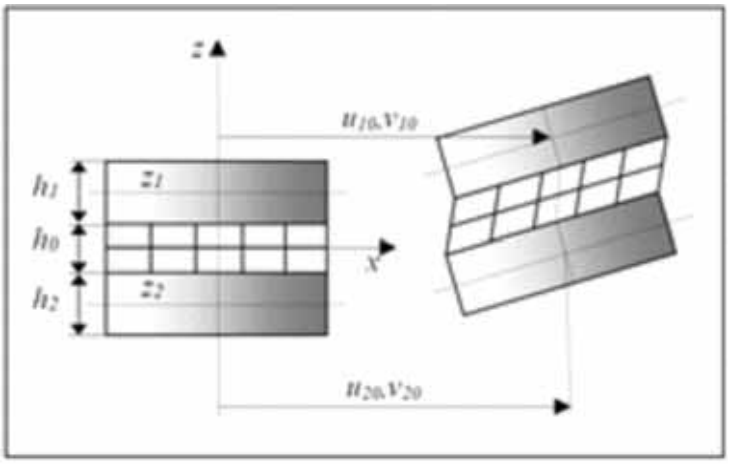

Fig. 1. Kinetic model of the sandwich plate.

Subsequently, taking into account the continuity inter layer, the displacement field of the elastic layers and of the viscoelastic core can be expressed in the following form:

$$u_i = u_{i0} - (z - z_i)\frac{\partial w}{\partial x};\ v_i = v_{i0} - (z - z_i)\frac{\partial w}{\partial y};\ i = 1,2 \tag{1}$$

$$u_0 = \frac{u_{10} + u_{20}}{2} + z_m \frac{\partial w}{\partial x} + z\varphi_x;\ v_0 = \frac{v_{10} + v_{20}}{2} + z_m \frac{\partial w}{\partial y} + z\varphi_y \tag{2}$$

$$w(x, y, z) = w(x, y) \tag{3}$$

where u_{i0} et v_{i0} (i=1,2) are the mid-surface displacements of the elastic layers in the *x* and *y* directions, *w*(*x*,*y*) is the transverse displacement of the plate, *zi* are the z-coordinates of the mid-planes of the elasticlayers, h_0 is the thickness of the core and $z_m=((z_1+z_2))/2$ *et* $d=z_1-z_2$. φ_x and φ_y are the rotations of the normal to the core middle plane around *x* and *y* axes :

$$\varphi_x = \frac{u_{10} + u_{20}}{h_0} + \left(\frac{d}{h_0} - 1\right)\frac{\partial w}{\partial x};\ \varphi_y = \frac{v_{10} + v_{20}}{h_0} + \left(\frac{d}{h_0} - 1\right)\frac{\partial w}{\partial y} \tag{4}$$

Strain and stress field are determined from the above displacement field, hence, strain and kinetic energies of the sandwich are deducted.

3. FINITE ELEMENT FORMULATION

In order to model a partially damped sandwich plate, two models are assembled: one describing the undamped part of the plate and a second one for the dampedpart. The first one is built according to the DKT which is a three-node triangular element with only 5 degrees-of-freedom per node: the transversedisplacementw, the rotations $\theta_x = \frac{\partial w}{\partial y}$ and $\theta_y = -\frac{\partial w}{\partial x}$ and the in-plane displacements u_{20}, v_{20} [14]. The formulation of the sandwich plate element stiffness and mass matrices is done through the discretization of strain and kinetic energy integrals, adding two extra degree of freedom, which represent the constraining layer displacements u_{10} and v_{10}.

The modal damping of the sandwich plate containing the viscoelastic material is analyzed referring to the Modal Strain Energy (MSE) approach[15]. The overall stiffness matrix can be decomposed as following:

$$K = K^R + jK^I = \sum_{i=0}^{2} K_i + j\eta_0 K_0 \tag{5}$$

Where $\boldsymbol{K_0}$ and $\boldsymbol{K^R}$ are the real parts of the stiffness matrices for the viscoelastic core and for the total structure, respectively. $\boldsymbol{K_i}$ is the stiffness matrix for the ith layer. η_0 is the loss factor of the viscoelastic material. Therefore, for a vibration mode Ψ_m the modal loss factor based on the MSE is computed as:

$$\eta = \frac{\Psi_m^T K^I \Psi_m}{\Psi_m^T K^R \Psi_m} \tag{6}$$

It represents the ratio of the dissipated energy through the viscoelastic layer to the elastic strain energy of the sandwich plate for a given vibrating mode. More detailscan be found in [16].

4. PARAMETRIC STUDY

The interaction among the various structure parameters had a dominant importance on its damping ratio. In connection with the content and purposes of this work, the parameter investigation will concern thepatch layers thicknesses and viscoelastic material (VEM) shear modulus.A numerical study is carried out to assess their effect on the structure loss factor and a brief presentation of the obtained results is done.

In this study, a simply supported square plate is considered, for the base plate, its dimensionsare 0.4m×0.4m and 5mm of thickness.The storage modulus is E_2=2.07·10^{11} N / m^2, Poisson's ratio was ν2= 0.3, loss factor η2= 0 and mass density is ρ2=7800 kg / m^3. It ispartially damped with aviscoelastic core constrained by an elastic layer with the same material properties as for the base structure. Similar case has been broadly treated in [4],[10] and [17], so that the numerical model has gotten validation by comparison with results of mentioned work. In all this work, 50% of the plate surface is covered by a damping treatment. The patch location is chosen according to the modal dissipated energy distribution indicator (MDEDI),which is based on the dissipated energy distribution in the fully damped structure as presented in fig.2.a.The damping patches are applied on zones with high dissipation index as shown in fig.2.b. This indicatorhad shown a better result compared to other previously used location indicator [16].

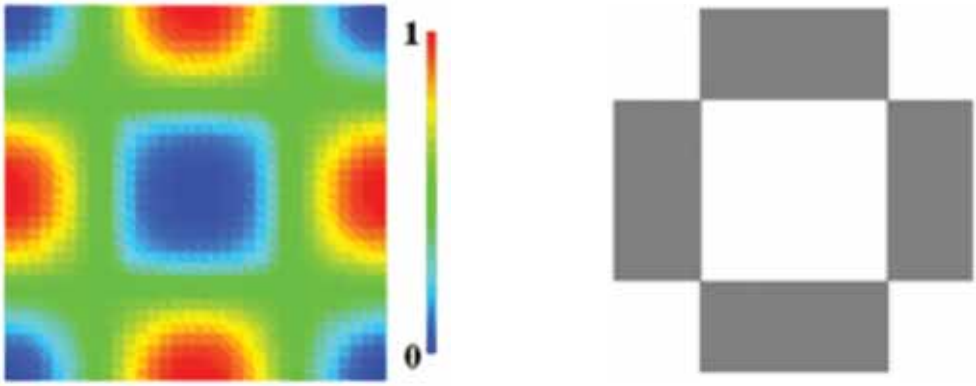

(a) **(b)**

Fig. 2. (a) Normalized modal dissipated energy distribution in the sandwich plate for the first mode. (b) Damping patches location according to the modal dissipated energy distribution indicator.

4.1 Layer thickness effect

In the following, the material properties of the viscoelastic layer are fixed to h_0=2·10-^{3}m,G_0=8·10^{7}N / m² and η_0=0.38 and the thickness of the constraining layer is varied from 10-^{5}m till 10^{-1} m. Itcanbeseen in Fig. 3, that the damping effect increases with the rise of the constraining layer thickness, until reaching an optimum value of damping.Beyond this one, the increasing of the constraining thickness value leads to a loss factor drop. A skinny constraining layer involves less shear strain energy in the viscoelastic material which affects

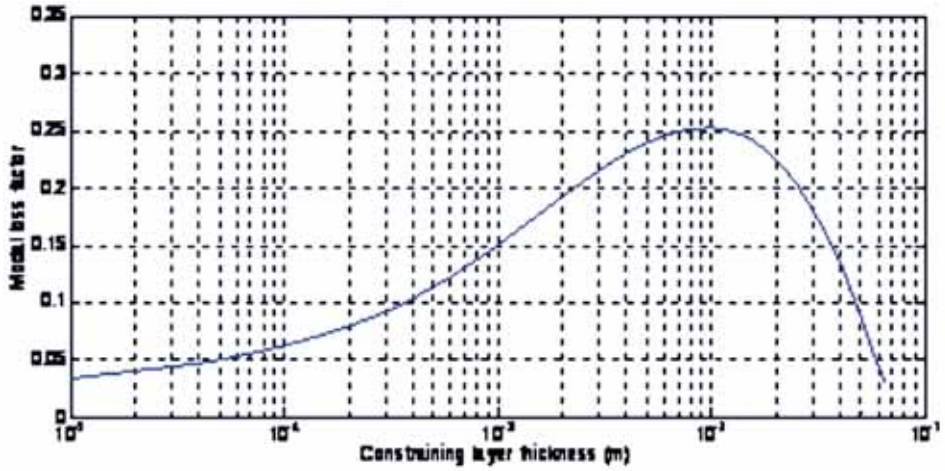

Fig. 3. Effect of constraining layerthickness on partialdamped plate modal loss factor - 1st mode.

the damping in the structure because the system loss factoris directly proportional to the strainenergy in theVEM. An increase of its thickness produces a higher loss-factor.

An optimal thickness value of the VEM can be also observed. However, for thickness greater than the optimal value, the increase in the stiffness of the constraining layer contributes more to the elastic strain energy stored in the plate than the dissipated energy through the shear deformation of the viscoelastic layer resulting in a decrease in the modal loss factor. Actually, in most instances, this maximum is reached for high and unreal value of VEM layer thickness, that's why for a scan of an optimal value, a wise choice of parameters should be taken. A sample of such choice is done usingthe following set of parameters: $h_1=5\cdot10^{-3}$m, $G_0=8\cdot10^6$N / m² and $\eta_0=0.38$ and results are illustrated in the Fig.4.

The previous results highlight the main effect of either the constraining or the VEM layer thickness, then a requirement should be done to the optimum choice of their thicknesses in order to further optimization of plate damping.

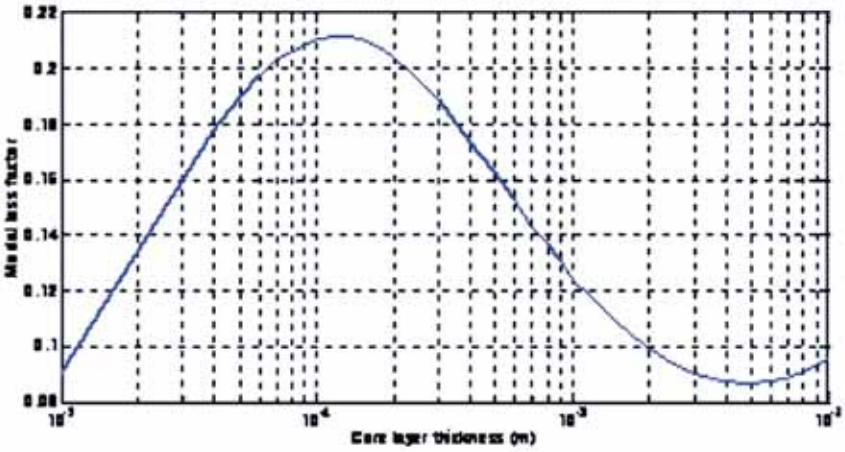

Fig. 4. Effect of VEM layer thickness on partial damped plate modal loss factor - 1st mode.

4.2 Materials properties effect

Hereinafter, patch parameters are fixed as follows: $h_0=2.5\cdot10^{-3}$m, $h_1=0.5\cdot10^{-3}$m. A numerical study shows that by varying shear modulus value, the plate loss factor increase until achieving a peak. Over a giving value of shear modulus, the damping structure decreases.In the sandwich patch, the base and the

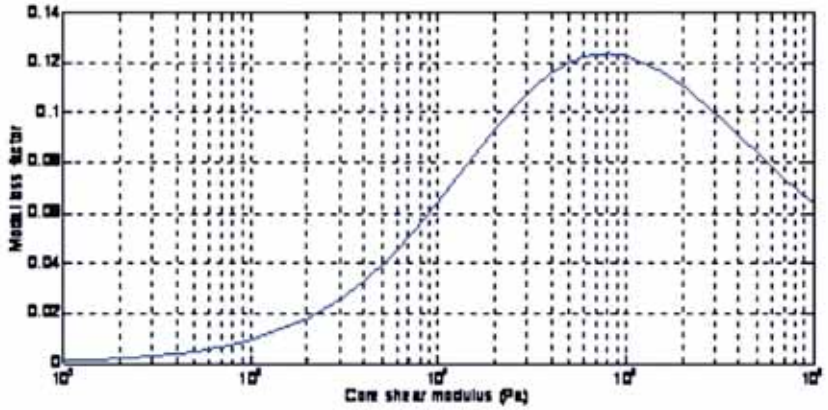

Fig. 5. Effect of core shear modulus on partial damped plate modal loss factor – 1st mode.

constraining layersforcethe viscoelastic material to deform in shear. This deformation is the mechanism by which the energy is dissipated. Then, the structure damping is mostly dependant on the relative Young's modulus of the outer layers and the storages hear modulus and loss factor of the viscoelastic core. As illustrated in Fig. 5, there is an optimum value of shear modulus to be determined for getting an optimized result of damping in a given case.

5. OPTIMALITY CONDITION

5.1 Patch layers thicknesses effect based on constant weight

In the previous parametric study, the obtained results show the plate sensibility to the variation of the treatment parameters and the tendency to get an optimum by varying one parameter and fixing all the others. In this part, patch layers thicknesses are varied together and coordinately in order to retain the patch weight constant on a prefixed value. Fig. 6 presents the obtained modal loss factor for $G_0 = 8{\cdot}10^7$ N / m^2 and $\eta_0 = 0.38$. It is shown that for the same weight of patchand diverse set of patch layers thicknesses, the modal loss factor varied substantially. Moreover, Fig. 6.a. and b. give an idea about the improvement that could be done to the damping result by an optimal choice of patch layers thicknesses and weight. A suitable choice of those factorsissignificantin industrial application. Therefore,an enhanced damping result could be reached with reduced weight and cost.

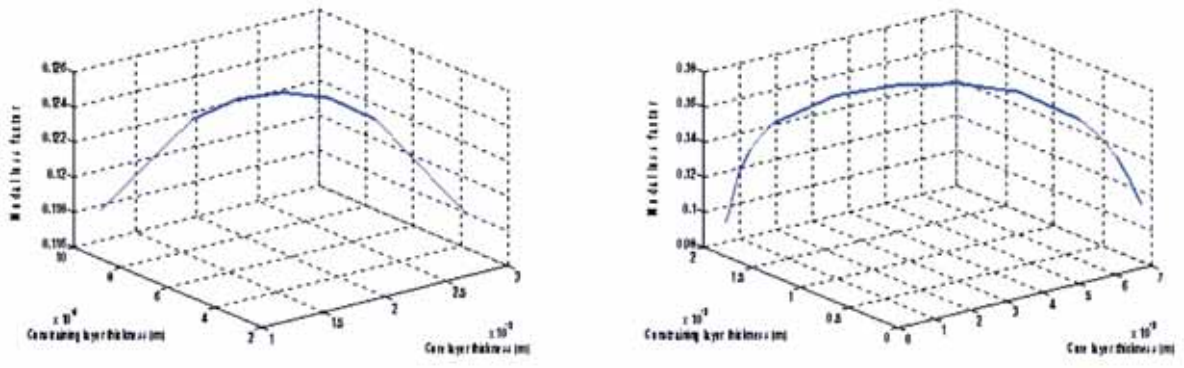

(a) **(b)**

Figure 6.Patch layers thicknesses effect on partial damped plate modal loss factor with a constant patch weight- 1st mode.(a) mass of patch = 0.712 kg (b)mass of patch = 1.185 kg.

5.2 Proposition of an optimization scheme

Sandwich structures with viscoelastic core are widely used, as mentioned [1], in car, aircraft and aerospace applications. Nowadays, the challenge in those applications is to get an efficient damping with a reduced weight, which is directly attached to energy reducing consumption as well as improving performance. The target is to get an optimal design of the sandwich structurewith a constraint on its mass. Then, the objective function is the maximum modal damping factor of the partial damped plate η:

$$\max(\eta = \frac{\Psi^T K^I \Psi}{\Psi^T K^R \Psi}) \tag{7}$$

The design variables are the patch layers thicknesses h_0 and h_1, the constraints are the total thickness and the mass of the patches.

$$h_0 + h_1 < H_{max}; \; mp < M_{max} \tag{8}$$

The maximization of η will besearched using a genetic algorithm (GA).The main advantage of GA is that, unlike conventional optimization techniques, it does not require continuity or differentiability of the objective function with respect to design variables and probability of finding a local optimum is smaller [18].

6. CONCLUSIONS

In this work, a numerical study ispresented using a finite element model of partially covered damping plate. A parametric investigation of the effect of patch layer thickness and core shear modulus on plate modal loss factorisdone. Fromthe obtained results, an investigation of optimality condition islaunched, where a mutual coordination of patch layers thicknesses value is done preserving a constant added mass.This shows that the performance of damping of the added patch can be enhanced by a proper choice of patch layers thicknesseswith a limitation on added patch weight. The obtained bell curves predict optimality conditions.Thereafter, an optimization scheme is proposed. It is expected that improved result will be achieved by using this optimization methodology.

7. REFERENCES

[1] M.D. RAO, 2003. Recent applications of viscoelastic damping for noise control in automobiles and commercial airplanes, *J. Sound Vib.*, **262**(3), 457–474.

[2] D.S. NOKES and F.C. NELSON, 1968. Constrained Layer Damping With Partial Coverage, *Shock Vib. Bull*., **38**, 5–12.

[3] A.K. LALL, N.T. ASNANI and B.C. NAKRA, 1988. Damping analysis of partially covered sandwich beams, *J. Sound Vib.*, **123**(2), 247–259.

[4] A.K. LALL, N.T. ASNANI and B.C. NAKRA, 1987. Vibration and Damping Analysis of Rectangular Plate With Partially Covered Constrained Viscoelastic Layer, *J. Vib. Acoust. Stress Reliab. Des.*, **109**(3), 241–247.

[5] S.W. KUNG and R. SINGH, 1998. Vibration Analysis of Beams With Multiple Constrained Layer Damping Patches, *J. Sound Vib.*, **212**(5), 781–805.

[6] B.R. SHER and R.A.S. MOREIRA, 2013. Dimensionless analysis of constrained damping treatments, *Compos. Struct.*, **99**, 241–254.

[7] J.M. LIFSHITZ and M. LEIBOWITZ, 1987. Optimal sandwich beam design for maximum viscoelastic damping, *Int. J. Solids Struct.*, **23**(7), 1027–1034.

[8] J.L. MARCELIN, P. TROMPETTE and A. SMATI, 1992. Optimal constrained layer damping with partial coverage, *Finite Elem. Anal. Des.*, **12**(3–4), 273–280.

[9] J.L. MARCELIN, S. SHAKHESI and F. POURROY, 1995. Optimal Constrained Layer Damping of Beams: Experimental and Numerical Studies, *Shock Vib.*, **2**(6), 445–450.

[10] B.C. NAKRA, 1998, Vibration Control In Machines And Structures Using Viscoelastic Damping, *J. Sound Vib.*, **211**(3), 449–466.

[11] Y.C. CHEN and S.C. HUANG, 2002. An optimal placement of CLD treatment for vibration suppression of plates, *Int. J. Mech. Sci.*, **44**(8), 1801–1821.

[12] H. ZHENG, C. CAI and X.M. TAN, 2004. Optimization of partial constrained layer damping treatment for vibrational energy minimization of vibrating beams, *Comput. Struct.*, **82**(29–30), 2493–2507.

[13] M. HAO and M.D. RAO, 2005. Vibration and Damping Analysis of a Sandwich Beam Containing a Viscoelastic Constraining Layer, *J. Compos. Mater.*, **39**(18), 1621–1643.

[14] J.L. BATOZ, BATHE K.-JÜR. and L. W. HO, 1980. A study of three-node triangular plate bending elements, *Int. J. Numer. Methods Eng.*, **15**(12), 1771–1812.

[15] C.D. JOHNSON and D.A. KIENHOLZ, 1982. Finite Element Prediction of Damping in Structures with Constrained Viscoelastic Layers, *AIAA J.*, **20**(09), 1284–1290.

[16] S. ASSAF, M. GUERICH and P. CUVELIER, 2011. Vibration and Damping Analysis of Plates with Partially Covered Damping Layers, *Acta Acust. United Acust.*, **97**(4), 553–568.

[17] B.C. NAKRA, 2000. Structural dynamic modification using additive damping, *Sadhana*, **25**(3), 277–289.

[18] D.E. GOLDBERG, 1989. *Genetic Algorithms in Search, Optimization, and Machine Learning*, Addison Wesley.

Journal of Acoustical Society of India : Vol. 42, No. 1, 2015 (pp. 46-53)

Multi-user and Multi-resolution Localization Algorithm

Nadia Aloui, Kosai Raoof and Ammar Bouallegue
GIPSA-lab, CNRS UMR5216,
Université Joseph Fourier, Grenoble, France
e-mail: nadia.aloui@gipsa-lab.grenoble-inp.fr, kosai.raoof@univ-lemans.fr

[Received:13.01.2014; Revised: 29.07.2014; Accepted: 17.09.2014]

ABSTRACT

In this paper, we propose a new acoustic indoor location system that aims to localize simultaneously N sources with different precision based on time reversal. This method allows the acoustic signal to focus efficiently on the initial source regardless of its position and regardless of the heterogeneity of the propagation medium. The main idea of our method is to assign to each source a unique Gold code that is used to scramble two carrier frequencies. The resulted signals are emitted by sources, recorded by four transducers, time-reversed and then reemitted simultaneously into the medium. A receiver that searches to locate one of the existing sources demodulates the received signals in function of the desired precision and then descrambles the resulted signal with the corresponding source code. First, it uses the low frequency descrambled signal in order to localize the source within a coarse precision. Then, it switches to high frequency signal in order to estimate the source position within a fine precision based on the previously estimated position. Simulations have shown that the proposed method provides location estimates of better than 2 cm accuracy with 87.5 % precision in the case of four sources.

1. INTRODUCTION

Location systems can be categorized into outdoor and indoor systems. The most popular outdoor location system is the Global Positioning System (GPS). It affords good performance in outdoors but fails indoors. For indoor areas, several location systems have been developed such that proposed in [1] and DOLPHIN system [2-3]. They make use of Infrared technology, Radiofrequency and acoustic technologies. They have useful applications in our everyday life. To name a few, indoor location systems allow doctors to reach their patients rapidly. They also afford protection of equipments against stealing by monitoring and tracking them.

Indoor location systems are mainly based on triangulation and fingerprinting technique. Triangulation requires line of sight between transmitter and receiver. Fingerprinting, on the other hand, estimates the target location by comparing its signature with a previously built database of known information location data via pattern matching algorithms.

Time reversal has many applications comprising underwater acoustics, telecommunications, room acoustics and ultrasound medical imaging and therapy [4]. It is based on the invariance of wave propagation equation if time is reversed. In a non-dissipative medium, whatever its complexity, the wave equation guarantees that for every wave diverging from a source corresponds a wave converging to it. If the source is pointlike, this allows a focusing on target regardless of the complexity of the propagation medium [4].

In this paper, we present an acoustic indoor location system that aims to localize simultaneously 4 sources with different precision based on time reversal.

The following section gives a brief overview of time reversal. Section (3) explains the time reversal from signal processing point of view. The proposed system is described in section (4). Section (5) presents the simulated annealing algorithm. System performance is given in section (6). In Section (7), we conclude our work and point out future directions.

2. TIME REVERSAL

In a non-dissipative medium, the acoustic wave equation is invariant under a time-reversal operation. Indeed, it comprises a second-order-time-derivative operator. Therefore, to any wave $p(r, t)$ diverging from the source corresponds a wave $p(r, -t)$ converging to the source.

Based on this property and on the principle of Helmoltz-Kirchoff, D.Cassereau and M. Fink [5] have developed the concept of the cavity of Time reversal. Indeed, they have demonstrated that by exploiting the Helmoltz-Kirchoff principle, the operation of time reversal does no longer consist in reversing the acoustic wave in every point of the considered volume, but only the wave and its normal derivative in the surface bounding the volume.

The time reversal operation can then be described in two phases: the reception phase and the emission phase. In the first phase, the source transmits a pulse. Transducers of the cavity record the wave and its normal derivative. In the second phase, every transducer behaves as a source and transmits the recorded waves in inverse chronology.

Didier Cassereau and Mathias Fink have demonstrated that these waves converge to the initial source and the created field is equal to the initially emitted wave but time reversed [5]. They have also demonstrated that the size of the focal spot, defined as the width at half-height of the zone where the energy is concentrated, is approximately the half of the wavelength of the wave.

Nevertheless, the concept of Time reversal cavity is theoric. Indeed, in order to create the cavity a large number of transducers is required. For example, if we would like to create a spherical cavity of radius 1 meter operating with a limited signal to 5 kHz band, we would require transducers every 3.45 cm, which corresponds to more than 2600 transducers on the surface of the cavity [6]. In practice, the cavity is replaced by a non-closed surface, called the time reversal mirror.

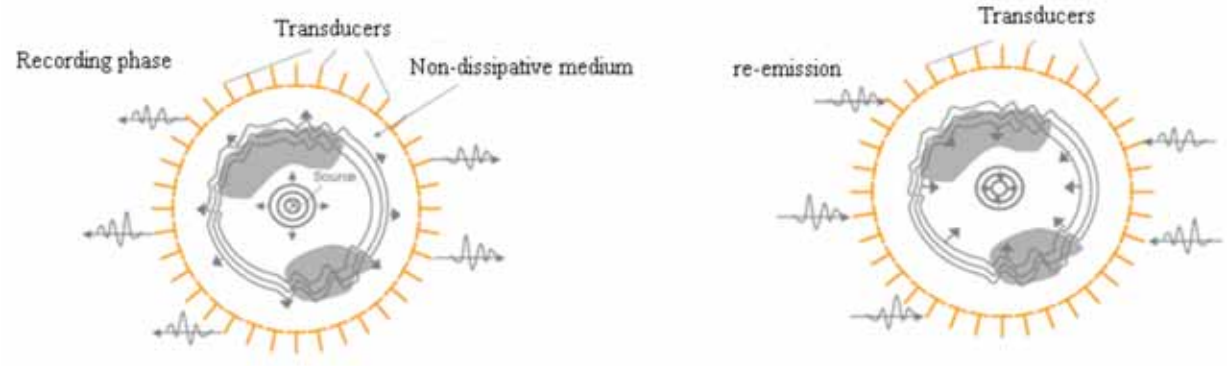

(a) Reception phase **(b)** Emission phase

Fig. 1. Time reversal experience

3. FORMALISM OF TIME REVERSAL FROM SIGNAL PROCESSING POINT OF VIEW

Assuming a linear time-invariant system with channel impulse response $h(S, S_i, t)$ between a point situated at s and a point situated at S_i, for any signal $G(t)$ emitted at the point S, the received signal r (t) can be always written as:

$$r(t) = G(t) \otimes h(s, s_i, t) \tag{1}$$

We consider that every elementary source S_i of the cavity emits the signal that it has received but in inverse chronology:

$$r^*(-t) = G^*(-t) \otimes h^*(s, s_i, -t) \tag{2}$$

Where * denotes complex conjugation.

The signal received at any point SS can therefore be written as:

$$Y(t) = \sum_i G^*(-t) \otimes h^*(s, s_i, -t) \otimes h(s_i, ss, t) \tag{3}$$

At $SS = S$, which corresponds to the position of the initial source, we obtain:

$$Y(t) = \sum_i G^*(-t) \otimes h^*(s, s_i, -t) \otimes h(s_i, ss, t) \tag{4}$$

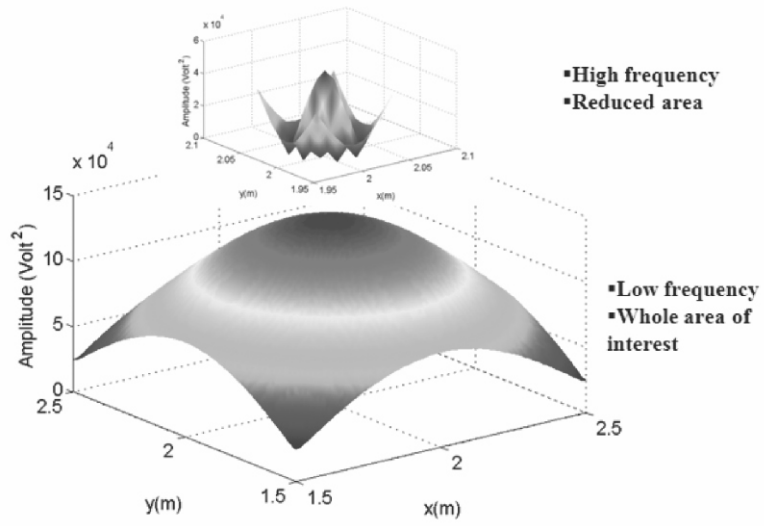

Fig. 2. Multi -resolution Location Method

The time reversal is then a matched filter in the sense of signal processing. It adapts the various frequency components of each impulse response to the environment and offsets their phases so that they summon all consistently at a point and at a given time.

In the following, we describe our proposed method.

4. MULTI-RESOLUTION LOCATION METHOD

The main idea of the proposed method is to localize simultaneously N sources with different precisions in order to attain high location precision. For that purpose, every source, identified by a unique Gold sequence, emits two signals simultaneously with different frequencies. The receiver searches for the sources in the whole zone of interest using the low frequency range. Then, it switches to high frequency range to localize the source in a reduced area based on the previously estimated position (see figure (2)).

The method can be described in the following steps:

- A source j , at position p_j , emits two carrier frequencies scrambled with Gold sequence $_j$ (t)

$$G_j(t) = g_j(t) \times \sin(2 \times \pi \times f_1 \times t) + g_j(t) \times \sin(2 \times \pi \times f_2 \times t) \tag{5}$$

  f_1 and f_2 are respectively the low and high carrier frequencies.

- A transducer i, at position S_i, receives the signal

$$y_{j,i}(t) = G_j(t) \otimes h_{j,i}(p_j, s_i, t) + n_i(t) \tag{6}$$

Where $n_i(t)$ denotes the channel noise at the transducer i and $h_{j\,i}$, (p_j, S_i, t)) denotes the channel impulse response between the source $_j$ and the transducer $_i$ and is given by:

$$h_{j,i}(p_j, s_i, t) = \sum_l \alpha_l^{j,i} \times \delta(t - \tau_l^{j,i}) \tag{7}$$

Where α_l^{ji} and $\tau_l^{j,i}$ are respectively the attenuation and the delay of the path *l* between the source *j* and the transducer i .

- The received signals are time reversed and reemitted simultaneously and continuously by four transducers

$$y_{j,i}^*(-t) = G_j^*(-t) \otimes h_{j,i}^*(p_j, s_i, -t) + n_i(-t) \qquad i = 1, \ldots 4. \tag{8}$$

- A microphone, at position **ss**, that wants to locate the sources, receives the aggregate signal:

$$Y(t) = \sum_{j=1}^{N} \sum_{i=1}^{4} y_{j,i}^*(-t) \otimes h'_i(s_i, ss, t) + b(t) \tag{9}$$

Where b (t) denotes the channel noise at the microphone and $h'_i(s_i, ss, t)$ denotes the channel impulse response between the transducer *i* and the microphone and is given by :

$$h'_i(s_i, ss, t) = \sum_k \beta_k^i \times \delta(t - \theta_k^i) \tag{10}$$

Where β_k^i and θ_k^i are respectively the attenuation and the delay of the path k .

- The receiver demodulates and descrambles the two signals in function of the desired precision (figure (3)).
- First, it uses the low frequency descrambled signal $C_{LF}(j_0, ss, t)$ to estimate the position of the source j_0 in the whole area within a coarse precision.
- It computes **the low frequency spatial correlation diagram** given by :

$$d_{LF}(j_0, ss) = \max_t(\left|c_{LF}(j_0, ss, t)\right|) \tag{11}$$

- It moves in the interested area, according to an optimization algorithm, in order to search for the position that maximizes $d_{LF}(j_0, ss)$.
- Second, it switches to high frequency signal in order to localize the source j_0 in a reduced area within a fine precision. So, it computes the high frequency descrambled signal $c_{HF}(j_0, ss, t)$ and **the high frequency spatial correlation diagram**

$$d_{HF}(j_0, ss) = \max_t(|C_{HF}(j_0, ss, t)|) \tag{12}$$

The reduced area is a square centered on the position obtained with the low frequency signal.

An example of low and high frequency spatial correlation diagrams are given in figure (4). For a low value of frequency **f**, the diagram is flat, while, for high frequency, it contains sharp peaks. It is then difficult to detect the source position based on one single frequency. However, using the low and high frequencies allows high localization accuracy.

In this paper, we have adopted the simulated algorithm as an optimization algorithm. A description of this algorithm is given in the next section.

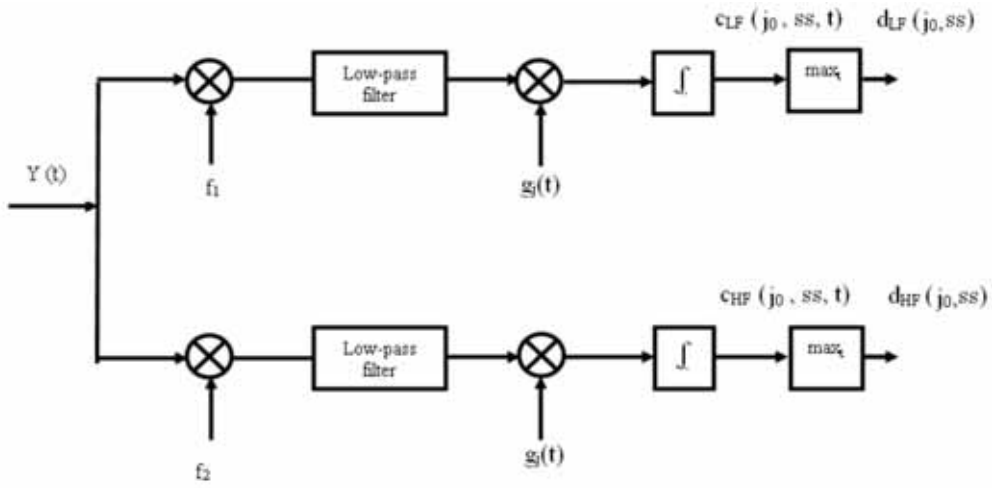

Fig. 3. Signal processing at the receiver

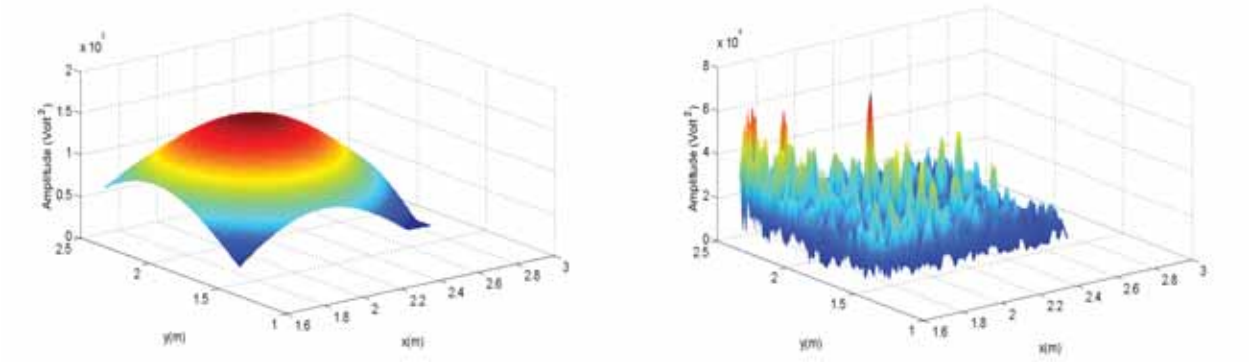

(a) Low frequency **(b)** high frequency

Fig. 4. Spatial correlation diagrams

5. SIMULATED ANNEALING ALGORITHM

Simulated annealing is a metaheuristic random technique for finding global extremums. It exploits the analogy between the annealing process of a metal and the search for a minimum in a general system [7]. The objective function is the system energy and the system temperature is a control parameter.

The algorithm begins at high temperature. It accepts solutions that are not necessarily optimizing the objective function. Then, the temperature declines. The solutions optimizing the function are accepted, but, others may be accepted. The probability of acceptance is given as follows:

$$\exp(-\frac{\Delta f}{T(t)}) \tag{13}$$

Where Δf denotes the variation of the objective function f and T is the control parameter corresponding to the system temperature in the physical process.

Therefore, at high temperatures, the probability of acceptance is close to 1. At low temperatures, the probability is small. The acceptance of bad solutions prevents the algorithm from falling into local optimums.

Assuming a minimization problem, the steps of simulated annealing algorithm are the following :

1. Choose an initial solution x_0 and compute $f(x_0)$
2. Put $i = 1$
3. Choose a neighbor x_{new} of x_{i-1} at random
4. Compute $\Delta f = f(x_{new}) - f(x_{i-1})$
   (a) If $\Delta f \leq 0$,
   (b) If $\Delta f \leq 0$, then
   - $x_i = x_{new}$ with probability $\exp(-\frac{\Delta f}{T(t)})$
   - $x_i = x_{i-1}$ otherwise.
5. Increment i by one and repeat the process from point 3

Generally, the temperature is reduced each time a certain number of iterations is performed. For temperature decrease, we have adopted the following rule:

$$T_j = T_0 \times \alpha^j \tag{14}$$

Where $j \in \{0, 1, \ldots\}$, T_0 the initial temperature and $0.9 < \alpha < 1$.

The simulated annealing is adopted in order to prevent the pseudo peaks that may appear in the low frequency correlation diagram. Simulations have proven that, for high frequency signal, the simulated annealing needs too much time to escape pseudo peaks. For this case, the receiver will compute $d_{HF}(j_0, ss)$ at every position of the reduced area and saves the maximum value of $d_{HF}(j_0, ss)$ and the corresponding position. The estimate position of the source j_0 corresponds to the last saved position.

6. EVALUATION

The system performance is evaluated through simulations. Performance is given in terms of precision versus accuracy plots and in terms of precision distributions in the work area. The accuracy is referred to the highest tolerated error for a measure to be regarded as successful. And the precision is the ratio of the measurements with errors equal to or less than the accuracy.

6.1 Simulations Environment

In order to emulate the acoustic reflections in an empty room, we have chosen the channel model given by Allen and Berkley [8], which is based on image technique. The impulse response for a source situated at $r_s = (x_s, y_s, z_s)$ and microphone placed at $r = (x, y, z)$ is then given by :

$$h(r_s, r, t) = \sum_{p \in P} \sum_{m \in M} \beta_{x_1}^{|m_x - q|} \times \beta_{x_2}^{|m_x|} \times \beta_{y_1}^{|m_y - j|} \times \beta_{y_2}^{|m_x|} \times \beta_{z_1}^{|m_z - k|} \times \beta_{z_2}^{|m_z|} \times \frac{\delta(t - \tau)}{4\pi d} \tag{15}$$

d is the distance between the microphone and any source image, τ is the time delay of arrival of the reflected sound ray corresponding to any source and β_{x1} β_{x2}, β_{y1}, β_{y2}, β_{z1} and β_{z2} are the reflection coefficients of the six walls.

We have placed four transducers at positions *(0.2 m, 2 m, 2 m), (2 m, 0.2 m, 2 m), (2 m, 3.8 m, 2 m)* and *(3.8 m, 2 m, 2 m)* in a room of dimensions *4m x 4m x 2.2*.

The length of Gold sequences $(g_j(t))_{j=1,\ldots,N}$ emitted by the N sources is 127 chips and the carrier frequencies are set to 200 Hz and 4 kHz.

The reflection coefficients of the six walls are fixed to 0.7 and reflections till order 12 are considered.

6.2 System Performance

We place fifteen groups of four sources separated by a distance of 0.2 m (see figure (5)).

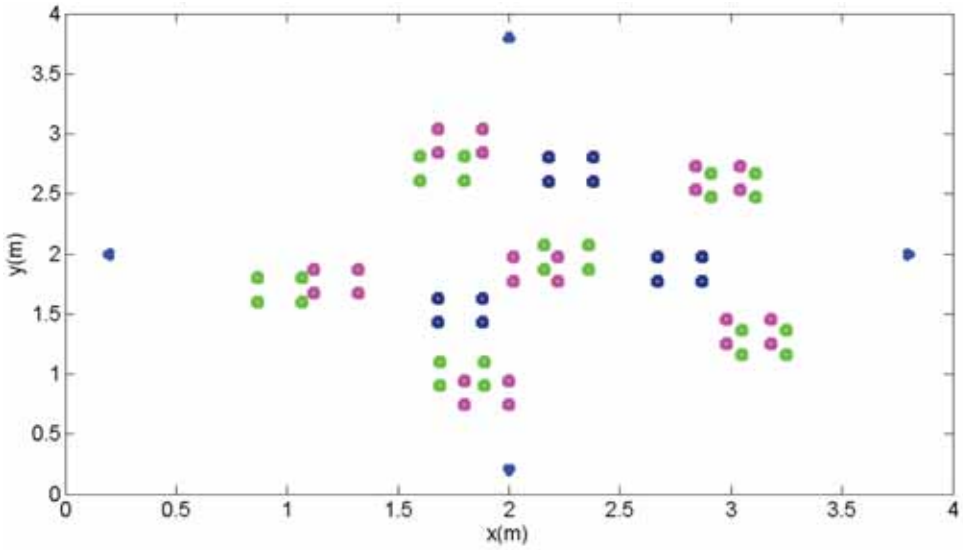

Fig. 5. The layout of the experiment setup

We assume that the receiver that wants to estimate the positions of the sources is situated in a square of dimensions 1*m* x 1*m* centered on the center of the square formed by each group of 4 sources. First, it uses the low frequency descrambled signal in order to estimate its position in the whole area within a coarse precision, then, it moves in the interested area according to the simulated annealing algorithm with a step of maximum 1 cm in x direction and 1 cm in y direction. Second, it switches to high frequency descrambled signal in order to estimate the sources positions in the reduced area within a fine precision.

The parameters of the simulated annealing algorithm are adjusted empirically: the parameter α and the initial temperature T_0 are set to 0.98 and 100 respectively. At fine resolution, the side of the reduced square is set to 18 cm.

500 positions of the receiver are generated randomly in the whole search area.

Results are plotted in figure (6). They have shown that the system provides an accuracy of ~0 cm within 62% precision, 1 cm within 84% precision and 2 cm within 87.5% precision.

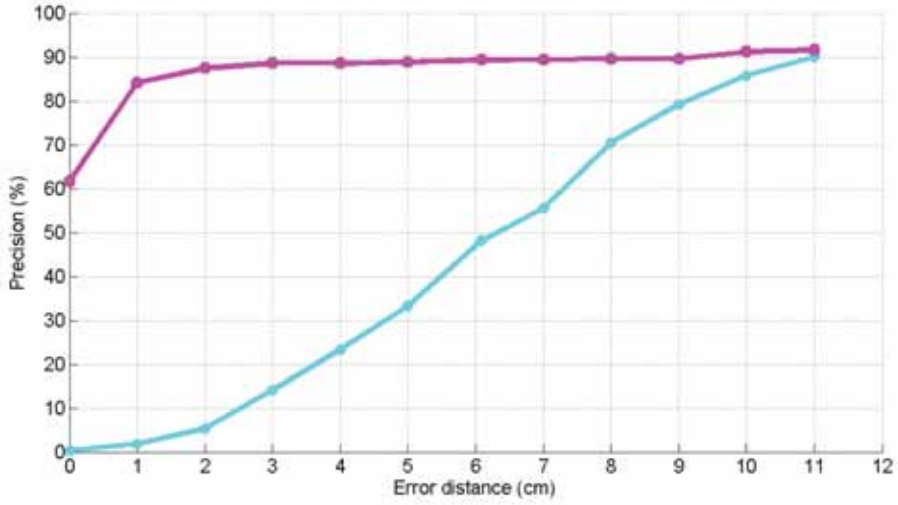

Fig. 6. Precision versus accuracy

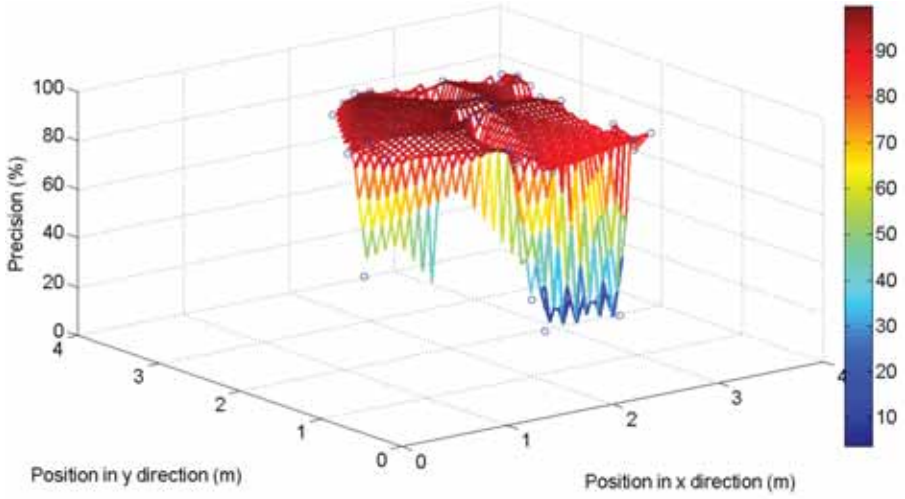

Fig. 7. Precision distribution for 2 cm accuracy

Precision per position for accuracy of 2 cm is depicted in figure (7). A high location precision is obtained for fifty-eight sources and a very low location precision is observed for only two sources. This low precision is due to the presence of pseudo-peaks in the reduced area.

7. CONCLUSION

This paper has presented a new acoustic indoor location system that aims to localize simultaneously 4 sources with different precision based on time reversal. Results have shown that the system has subcentimeter accuracy.

In our future work, we aim to increase the number of the deployed sources. Then, we would like to vary the values of the carrier frequencies in order to cover larger search area.

8. REFERENCES

[1] NADIA ALOUI, KOSAI RAOOF, AMMAR BOUALLEGUE, STEPHANE LETOURNEUR and SONIA ZAIBI, 2012. A Novel Indoor Localization Scheme Based On Fingerprinting Technique And CDMA Signals, 2012 International Conference on Indoor Positioning and Indoor Navigation.

[2] MIKE HAZAS and ANDY WARD, 2003. A High Performance Privacy-Oriented Location System, *Proceedings of the first IEEE International Conference on Pervasive Computing and Communications* (PerCom), 216-223.

[3] MIKE HAZAS and ANDY HOPPER, 2006. Broadband Ultrasonic Location Systems for Improved Indoor Positioning. *IEEE Transactions on Mobile Computing*, **5**(5), 536-547.

[4] M.FINK, G.MONTALDO and M. TANTER, 1992. *Time Reversal Acoustics*. 2004 *IEEE International Ultrasound, Ferroelectrics, and frequency Control Joint 50th Anniversary Conference.*

[5] D. CASSEREAU and M. FINK. *Time-reversal of ultrasonic fields*. iii. theory of the closed time-reversal cavity. *IEEE Trans. Ultra. Ferr. Freq. Cont.*, 39(5), 579–592.

[6] S. YON, 2001. *Contrôle du champ acoustique en milieu réverbérant et applications à la Communication*. Thèse de doctorat, Laboratoire Ondes et Acoustique, ESPCI, Université Paris VII, U.M.R. 7587 C.N.R.S., 10, rue Vauquelin, 75005, Paris, France.

[7] LIACS / Natural Computing Group. *Simulated Annealing.* Leiden University.-2009.

[8] J.B. ALLEN and D.A BERKLEY. 1979. *Image method for efficiently simulating small-room acoustics. J. Acoust. Soc. Am.* **65**(4).

INFORMATION FOR AUTHORS

ARTICLES

The Journal of Acoustical Society of India (JASI) is a refereed publication published quarterly by the Acoustical Society of India (ASI). JASI includes refereed articles, technical notes, letters-to-the-editor, book review and announcements of general interest to readers.

Articles may be theoretical or experimental in nature. But those which combine theoretical and experimental approaches to solve acoustics problems are particularly welcome. Technical notes, letters-to-the-editor and announcements may also be submitted. Articles must not have been published previously in other engineering or scientific journals. Articles in the following are particularly encouraged: applied acoustics, acoustical materials, active noise & vibration control, bioacoustics, communication acoustics including speech, computational acoustics, electro-acoustics and audio engineering, environmental acoustics, musical acoustics, non-linear acoustics, noise, physical acoustics, physiological and psychological acoustics, quieter technologies, room and building acoustics, structural acoustics and vibration, ultrasonics, underwater acoustics.

Authors whose articles are accepted for publication must transfer copyright of their articles to the ASI. This transfer involves publication only and does not in any way alter the author's traditional right regarding his/her articles.

PREPARATION OF MANUSCRIPTS

All manuscripts are refereed by at least two referees and are reviewed by the Publication Committee (all editors) before acceptance. Manuscripts of articles and technical notes should be submitted for review electronically to the Chief Editor by e-mail or by express mail on a disc. JASI maintains a high standard in the reviewing process and only accept papers of high quality. On acceptance, revised articles of all authors should be submitted to the Chief Editor by e-mail or by express mail.

Text of the manuscript should be double-spaced on A4 size paper, subdivided by main headings-typed in upper and lower case flush centre, with one line of space above and below and sub-headings within a section-typed in upper and lower case understood, flush left, followed by a period. Sub-sub headings should be italic. Articles should be written so that readers in different fields of acoustics can understand them easily. Manuscripts are only published if not normally exceeding twenty double-spaced text pages. If figures and illustrations are included then normally they should be restricted to no more than twelve-fifteen.

The first page of manuscripts should include on separate lines, the title of article, the names, of authors, affiliations and mailing addresses of authors in upper and lowers case. Do not include the author's title, position or degrees. Give an adequate post office address including pin or other postal code and the name of the city. An abstract of not more than 200 words should be included with each article. References should be numbered consecutively throughout the article with the number appearing as a superscript at the end of the sentence unless such placement causes ambiguity. The references should be grouped together, double spaced at the end of the article on a separate page. Footnotes are discouraged. Abbreviations and special terms must be defined if used.

EQUATIONS

Mathematical expressions should be typewritten as completely as possible. Equation should be numbered consecutively throughout the body of the article at the right hand margin in parentheses. Use letters and numbers for any equations in an appendix: Appendix A: (A1, (A2), etc. Equation numbers in the running text should be enclosed in parentheses, i.e., Eq. (1), Eqs. (1a) and (2a). Figures should be referred to as Fig. 1, Fig. 2, etc. Reference to table is in full: Table 1, Table 2, etc. Metric units should be used: the preferred from of metric unit is the System International (SI).

REFERENCES

The order and style of information differs slightly between periodical and book references and between published and unpublished references, depending on the available publication entries. A few examples are shown below.

Periodicals:

[1] S.R. Pride and M.W. Haartsen, 1996. Electroseismic wave properties, *J. Acoust. Soc. Am.*, **100** (3), 1301-1315.

[2] S.-H. Kim and I. Lee, 1996. Aeroelastic analysis of a flexible airfoil with free play non-linearity, *J. Sound Vib.*, **193** (4), 823-846.

Books:

[1] E.S. Skudzryk, 1968. *Simple and Comlex Vibratory Systems*, the Pennsylvania State University Press, London.

[2] E.H. Dowell, 1975. *Aeroelasticity of plates and shells*, Nordhoff, Leyden.

Others:

[1] J.N. Yang and A. Akbarpour, 1987. Technical Report NCEER-87-0007, Instantaneous Optimal Control Law For Tall Buildings Under Seismic Excitations.

SUMISSIONS

All materials from authors should be submitted in electronic form to the JASI Chief Editor: B. Chakraborty, CSIR - National Institute of Oceanography, Dona Paula, Goa-403 004, Tel: +91.832.2450.318, Fax: +91.832.2450.602,(e-mail: bishwajit@nio.org) For the item to be published in a given issue of a journal, the manuscript must reach the Chief Editor at least twelve week before the publication date.

SUMISSION OF ACCEPTED MANUSCRIPT

On acceptance, revised articles should be submitted in electronic form to the JASI Chief Editor (bishwajit@nio.org)

ISSN 0973-3302

JOURNAL OF ACOUSTICAL SOCIETY OF INDIA

Volume 42 Number 2 April 2015

A Quarterly Publication of the JASI

http://www.acousticsindia.org

Journal of Acoustical Society of India

Volume 42 Number 2 April 2015 pp 61-118

JASI

Journal of Acoustical Society of India

The Refereed Journal of the Acoustical Society of India (JASI)

The Journal of Acoustical Society of India is a refereed journal of the Acoustical Society of India **(ASI)**. The **ASI** is a non-profit national society founded in 31st July, 1971. The primary objective of the society is to advance the science of acoustics by creating an organization that is responsive to the needs of scientists and engineers concerned with acoustics problems all around the world.

Manuscripts of articles, technical notes and letter to the editor should be submitted to the Chief Editor. Copies of articles on specific topics listed above should also be submitted to the respective Associate Scientific Editor. Manuscripts are refereed by at least two referees and are reviewed by Publication Committee (all editors) before acceptance. On acceptance, revised articles with the text and figures scanned as separate files on a diskette should be submitted to the Editor by express mail. Manuscripts of articles must be prepared in strict accordance with the author instructions.

All information concerning subscription, new books, journals, conferences, etc. should be submitted to Chief Editor:

B. Chakraborty, CSIR - National Institute of Oceanography, Dona Paula, Goa-403 004,
Tel: +91.832.2450.318, Fax: +91.832.2450.602, e-mail: bishwajit@nio.org

Annual subscription price including mail postage is Rs. 2500/= for institutions, companies and libraries and Rs. 2500/= for individuals who are not **ASI** members. The Journal of Acoustical Society of India will be sent to **ASI** members free of any extra charge. Requests for specimen copies and claims for missing issues as well as address changes should be sent to the Editorial Office:

ASI Secretariat, C/o Acoustics, Ultrasonics & Vibration Section, CSIR-National Physical Laboratory, Dr. KS Krishnan Road, New Delhi 110 012, Tel: +91.11.4560.8317, Fax: +91.11.4560.9310, e-mail: asisecretariat.india@gmail.com

ISSN 0973-3302

Printed at Alpha Printers, WZ-35/C, Naraina, Near Ring Road, New Delhi-110028 Tel.: 9810804196. JASI is sent to ASI members free of charge.

JASI

Journal of Acoustical Society of India (JASI)

A quarterly publication of the Acoustical Society of India

Volume 42, Number 2, April 2015

ARTICLES

INFORMATION

Journal of Acoustical Society of India : Vol. 42, No. 2, 2015 (pp. 61-68)

Optimization of an Acoustic Leaky-Wave Antenna based on Acoustic Metamaterial

S. H. S. Esfahlani, S. Karkar and H. Lissek
Ecole Polytechnique Fédérale de Lausanne, EPFL-STI-IEL-LEMA,
Station 11, CH-1015 Lausanne, Switzerland
**e-mail: hussein.esfahlani@epfl.ch*

[Received: 21.12.2013; Revised: 02.04.2014; Accepted: 10.07.2014]

ABSTRACT

In recent years, an increasing number of pioneering studies have been carried out in the field of acoustic metamaterials, following the path of electromagnetic metamaterials. These artificial engineered materials are designed in such a way so as to achieve new macroscopic properties, like negative refraction, that are not readily present in nature. While the design and the fabrication of these artificial materials is a hot topic among scientists in different fields of physics such as photonic, electromagnetic, acoustic and recently mechanic, an important part of the scientific research is now oriented towards the identification of actual applications for these structures. As the novel idea of metamaterial was first developed in the electromagnetic realm and for the microwave frequency range, it is somehow more mature in these fields than in acoustics. Metamaterial applications are now widely developed in electromagnetics espe-cially for the design of new antenna. Among other examples, metamaterial concepts are aim-ing at reducing the coupling between two adjacent radiating elements of the array and in-creasing the operating bandwidth of radiating elements. It is also used for phase compensa-tion in microwave transistors, and many more applications are rising in the recent literature. In year 2009, in analogy with electromagnetic transmission line metamaterial, our group pro-posed a concept of acoustic transmission line metamaterial, consisting of a waveguide pe-riodically loaded with membranes along the duct, and transverse open channels (denoted "stubs"). Based on our proposed structure and in analogy with applications of transmission line electromagnetic metamaterials, researchers proposed the idea of an acoustic counterpart to the "backward wave antenna". These antennas or radiating devices have a very special property such that the radiation angle or the directivity changes with the frequency. In this ar-ticle, a comprehensive, step by step, design methodology for acoustic backward wave anten-na is presented. For this purpose we use the model proposed in our 2009 publication for acoustic transmission line metamaterial, but we focus the discussion on the optimization of the antenna performance. We also propose some closed form formulas for the practical design of such devices, and a formal validation of the structure is proposed using Comsol Mul-tiphysics®.

1. INTRODUCTION

Metamaterials are artificial engineered materials designed to achieve some macroscopic properties that are not available in nature. In 1968 Russian physicist Victor Veselago studied the electromagnetic properties of a hypothetical medium in which both the permittivity and permeability were simultaneously negative [1]

and three decades later Pendry and Smith created the first proto-type of such material and called it Electromagnetic Left-Handed Metamaterial (LHM). Later, Electromagnetic Transmission Line (TL) metamaterials were proposed to overcome the problem of narrow bandwidth of the resonant type LHM [2] and very soon they found many applications such as Leaky Wave Antenna (LWA).

Leaky Wave (LW) is a term that refers to a mechanism to leak power all along a waveguide. It was first developed in 1940 [3] as an Electromagnetic LWA. Owing to its high directivity and frequency scanning capability, these antennas are very attractive in electromagnetics, but conventional TL-LW antennas use positive wavenumbers and as a consequence, they have the drawback of scanning only the half-space from broadside to endfire. After the advent of composite right/left handed (CRLH) TL-metamaterials, which were supporting both positive and negative wavenumbers, the backfire to endfire electromagnetic antenna was designed and fabricated [4].

In 2004 the analogue of electromagnetic LHM was proposed for acoustics [5]. In 2009 our group reported a transmission line acoustic metamaterial with a considerable bandwidth compared to resonant type acoustic metamaterials, and in the same article the leaky wave nature of this structure was discussed in [6] and [7]. Later, the same prototype was fabricated and measured [8].

In this paper, we present aspects of acoustic leaky wave structures that have not been covered up to date and try to develop a methodology for the design of acoustic leaky wave structures. First, we introduce a method for the design of these structures. Then, we use that method to design a structure that satisfies the needs of a LW antenna. Last, we show the simulated results of our proposed structure and give some guidelines to improve the structure.

2. THEORY OF CRLH METAMATERIALS

An incremental section of a conventional fluid (with positive refractive index) can be modelled as in Figure 1 (a), where $m_a = (\rho/S)dz$ is an acoustic mass and $C_a = (S/K)dz$ is an acoustic compliance and ρ and K are the density and bulk modulus of the medium, respectively. Figure 1 (b) shows the dual topology of the conventional TL, which is often referred to as the dual TL. Such a structure is known to exhibit a negative refractive index. Combining these two structures, as in Figure 1 (c), results in the transmission line model of a CRLH metamaterial, the response of which is dominated by m_{ap} and C_{as} in the low frequencies, resulting in a left-handed (LH) behaviour (or negative refrac-tive index). At higher frequencies, m_{as} and C_{ap} are predominant, resulting in a right-handed (RH) behaviour (or positive refractive index).

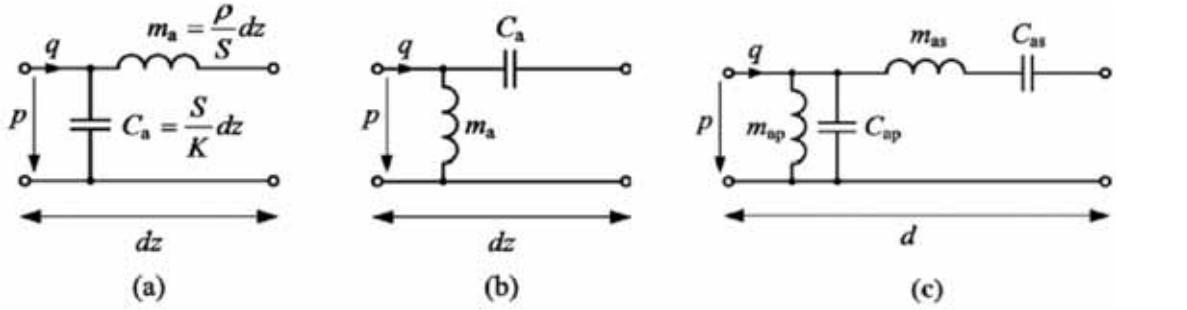

Fig. 1. Lumped element model for (a) a conventional medium (right-hand) (b) a dual medium (left-hand) (c) a CRLH metamaterial.

On the basis of circuit modelling of CRLH metamaterials *Bongard et al.* [4] implemented the CRLH acoustic metamaterial using acoustic waveguides, membranes and stubs (see Figure 2). Here the host "medium" is an acoustic waveguide with circular cross section and perfectly rigid walls operating as series acoustic mass and shunt acoustic compliance. By using membranes, a series mass and compliance are introduced, and a shunt acoustic masse is simply achieved with transversally connected open channels. Detailed explanation about the design of this structure is available in [6] and [7].

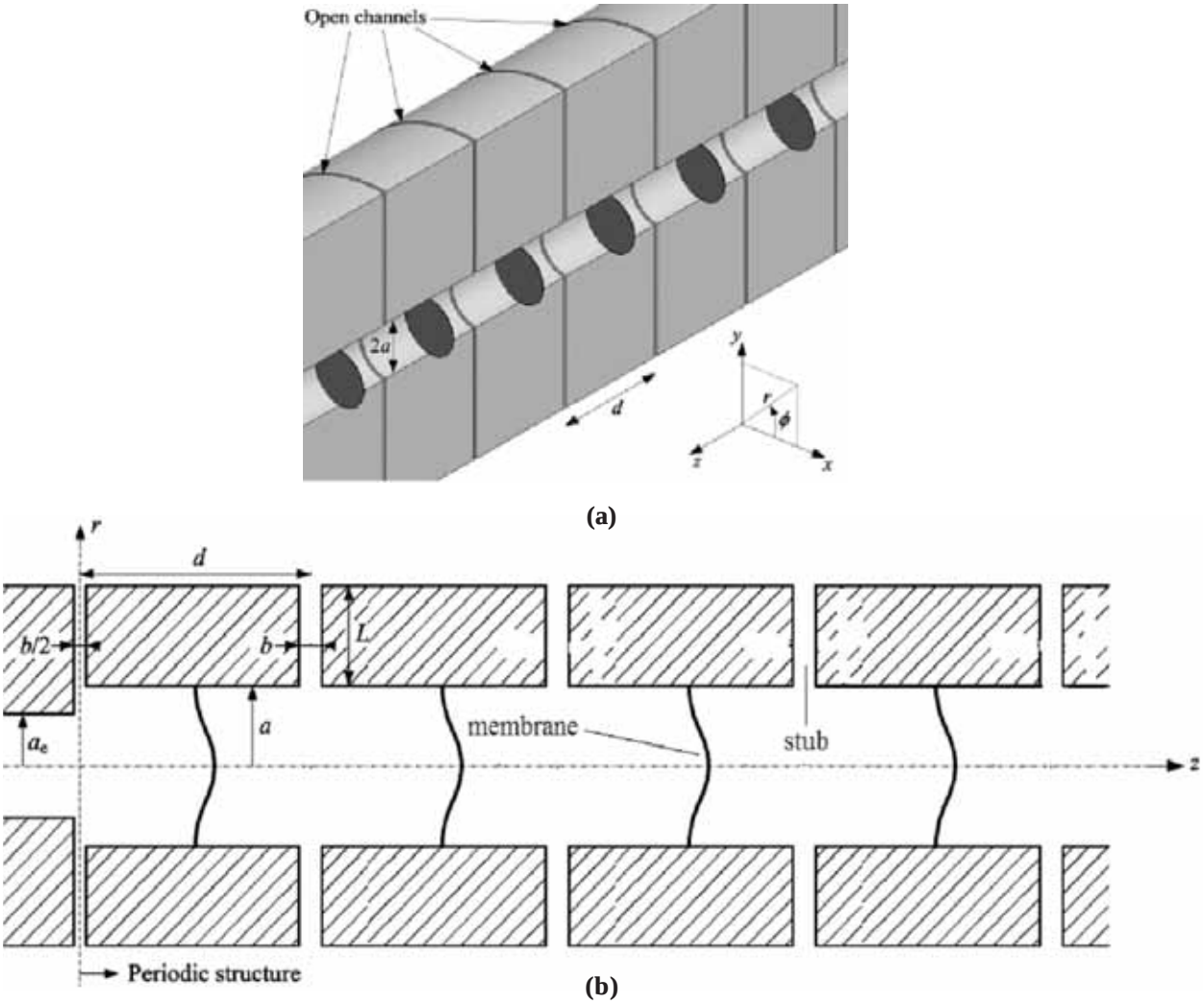

Fig. 2. CRLH TL combining membrane and radial open stub. (a) 3D view (yz-plane cut) (b) 2D axisymmetric view.

3. DESIGNING ACOUSTIC LEAKY WAVE ANTENNA (LWA)

The radiating formulas of acoustic LWA, such as radiation angle and radiation pattern were discussed in [8] so here we will discuss about the leaky wave trait and the efficiency of the antenna that are the most important factors in LWA. The leaky-mode (LM) time-space harmonic dependence takes the form $e^{-j(\omega t - k_z z)}$, where k_z is the complex longitudinal propagation constant. It is well known that k_z is related to the pointing angle θ_{RAD} and the radiation efficiency η_{RAD} through the following expressions [9]:

$$k_z = \beta_z - j\alpha_z, \tag{1}$$

$$\sin(\theta_{RAD}) = \frac{\beta_z}{k_0} \tag{2}$$

$$\eta_{RAD} = 1 - e^{-2\alpha_z, L_A} \tag{3}$$

where z is the longitudinal direction of the LWA (see Figure 2), β_z is the LM phase constant, α_z is

the LM leakage rate, k_0 is the free-space wavenumber, L_A is the LWA length. The independent control of the LM phase β_z and leakage constants α_z is of key importance for the synthesis and the flexible adjustment of the radiation pattern of a practical LWA [9]. In order to make our analysis and synthesis easier we do not consider losses in our model so the total input power is divided between transmitted, reflected and radiated power :

$$P_{in} = P_{reflection} + P_{transmission} + P_{radiation} \tag{4}$$

It is important to note that designing a structure to have a specific leakage constant α_z is difficult. Thus, L_A is taken as the free parameter in view of optimizing η_{RAD} by means of equation (3). The value of α_z is fixed by the internal structure of the cells and can be determined by using the following equation :

$$P_2 = P_1 e^{-2\alpha_z l_{12}} \tag{5}$$

where P_2 and P_1 are the average power measured in two different cross sections of the transmission line that are separated by length l_{12}.

As numerical simulations of these structures are time consuming, the following steps can be followed to decrease the difficulty of design :

- First, the internal structure of the CRLH cell should be designed (here, using COMSOL Multiphysics).
- Then, using equation (5), the leakage constant α_z is calculated. The value of α_z is frequency dependent, so a mean value will be used in the next steps.
- Last, using equation (3), the appropriate length of L_A is calculated for any value of radiation efficiency (usually 90%).

4. RESULT

We now present a practical example, using the same cell structure as in [6]. The dimensions and ma-terial properties of this structure are listed in Table 1. Its Bloch diagram is depicted in Figure 3, highlighting the radiation region.

Table 1: Geometric sizes and material properties of the structure

Physical quantity	Value/unit	Physical quantity	Value/unit
ρ (mass density of air)	1.188 kg/m^3	a_e (radius matching waveguide)	5.54 mm
K (bulk modulus of air)	137.4 kPa	d (length of each cell)	34 mm
C (celerity of air)	340 m/s	b (width of stub)	1 mm
E (membrane Young's modulus)	2.758 GPa	L (length of stub)	43.5 mm
ν (Poisson ratio)	0.34	h (thickness of the membrane)	125 µm
ρ_m (mass density of membrane)	1420 kg/m^3	a (waveguide/membrane radius)	9.06 mm

A short length structure is simulated to derive the value of α_z. Here four different structures with 10, 19, 29 and 80-cell are shown to validate the consistency of the results but usually a short length structure like 10-cell is enough for defining the value of α_z. According to Figure 4, an average value of 0.5 is assigned for α_z.

Using equation (3) and assigning an efficiency of 0.9 as our goal, L_A should be approximately 230 cm or 67 cells. Because α_z has values lower than 0.5 at certain frequencies, equation (3) implies that L_A should be higher than 67, in order to ensure the efficiency of 90% in most of the bandwidth. In the present case, an 80-cell prototype has been chosen and simulated using Comsol.

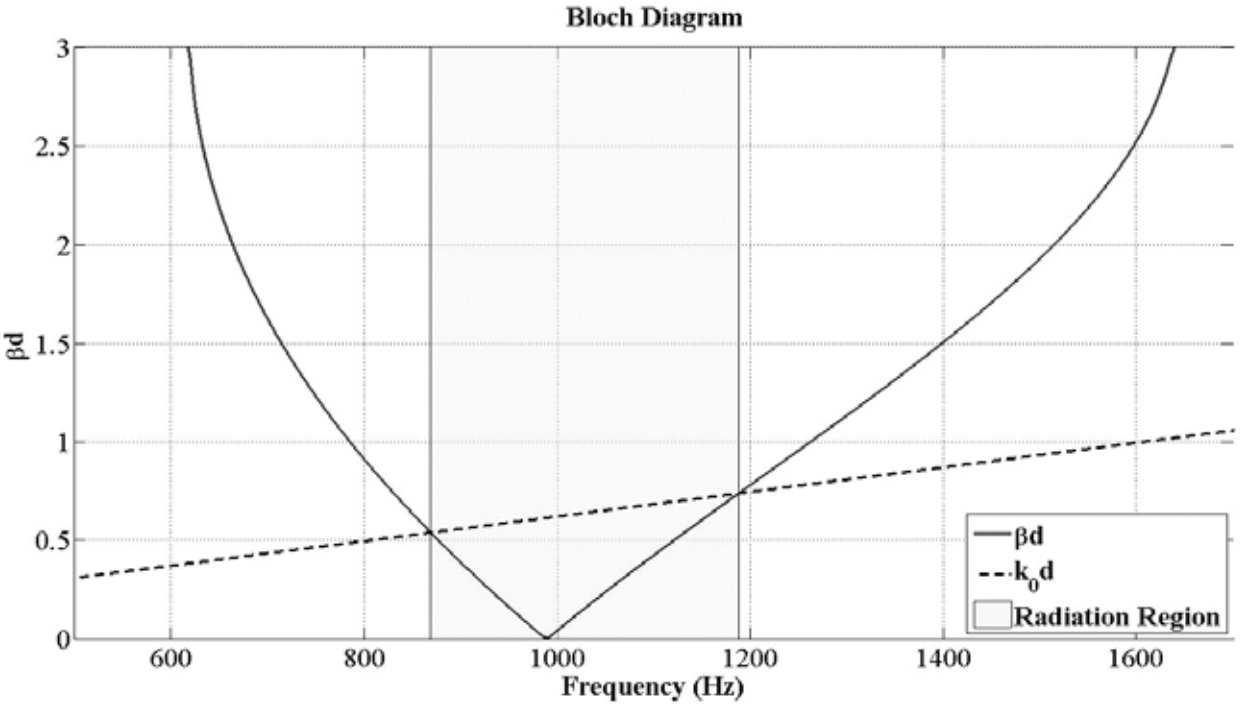

Fig. 3. Dispersion diagram

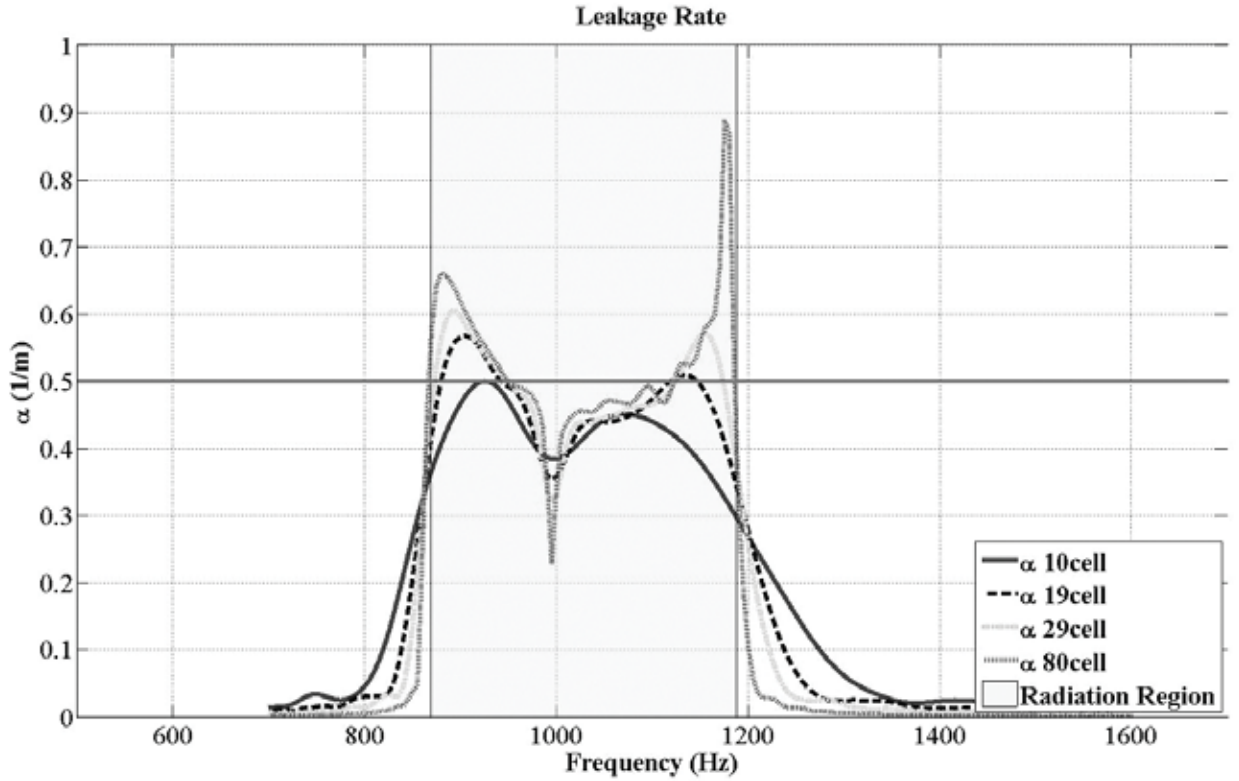

Fig. 4. Leakage constant α as a function of frequency

Figure 5 shows the reflection and transmission coefficient diagram. The impedance match in the radiating region seems satisfying as S_{11} is on average below $-20dB$ over the whole radiation region, except for a very sharp peak at the transition frequency.

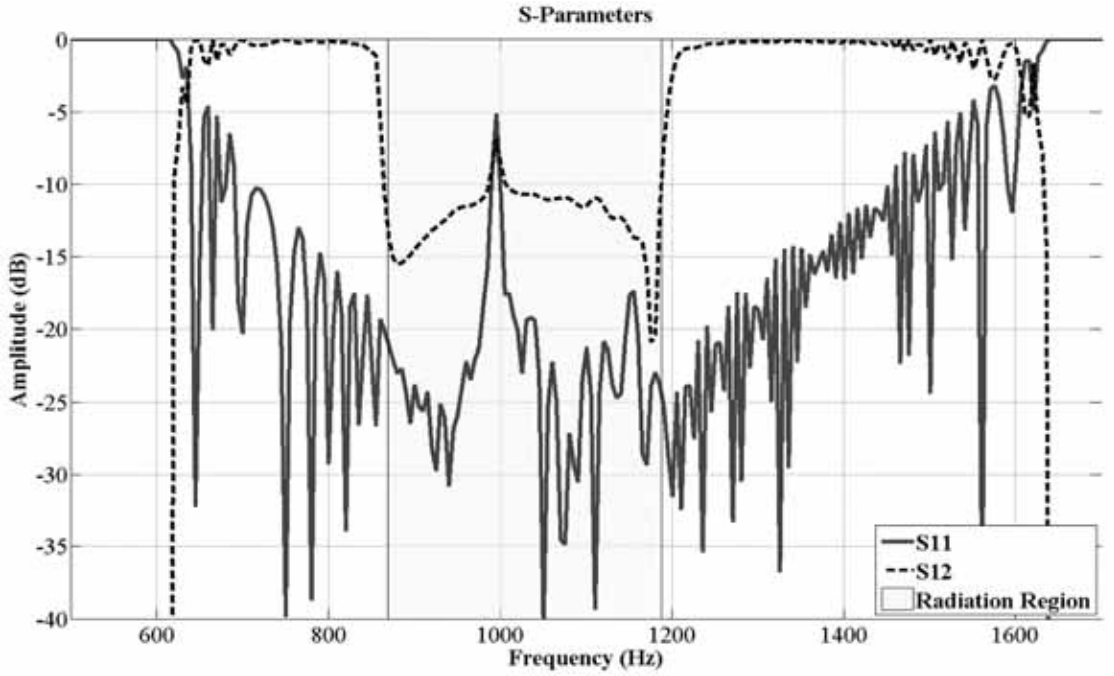

Fig. 5. Transmission and Reflection coefficients for 80-cell leaky wave structure

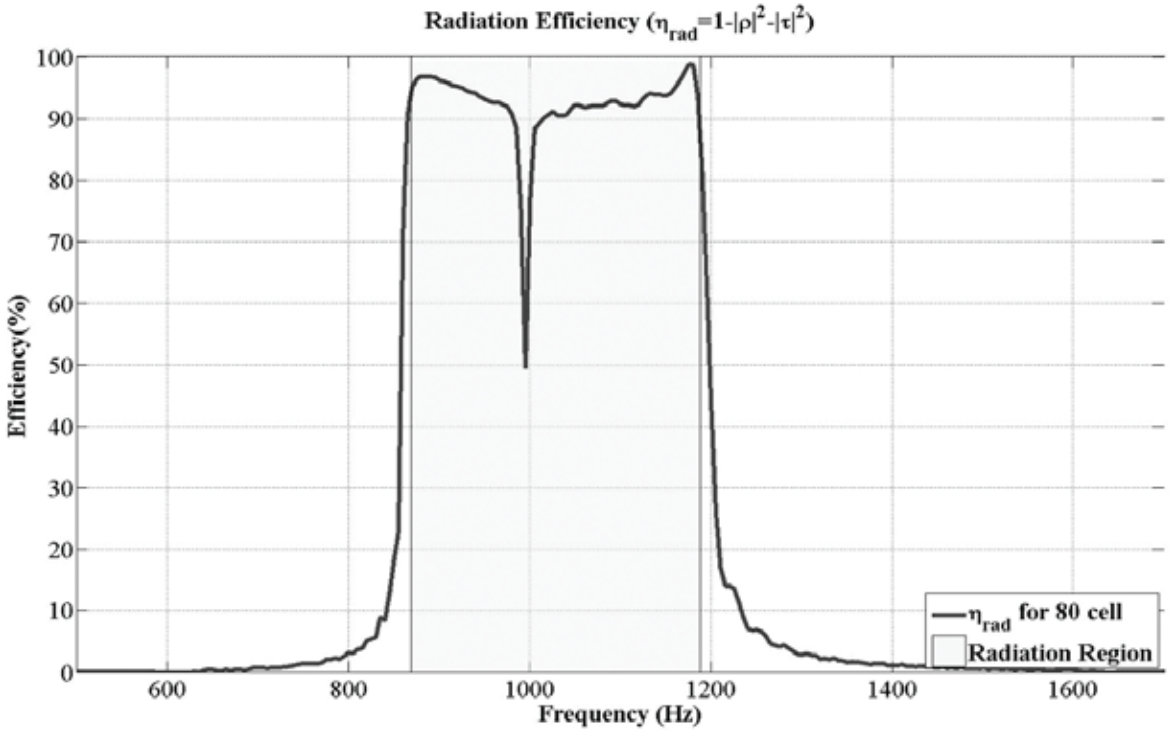

Fig. 6. Radiation efficiency for 80-cell leaky wave structure

Figure 6 shows the radiation efficiency of the antenna that is calculated using equation (4). Clearly an efficiency of above 90% is guaranteed for the entire radiation bandwidth, except for a very sharp deep at the transition frequency.

Last, Figure 7 shows the radiating pattern of this antenna. Sweeping the frequency, the antenna pattern is scanning from back-fire to end-fire.

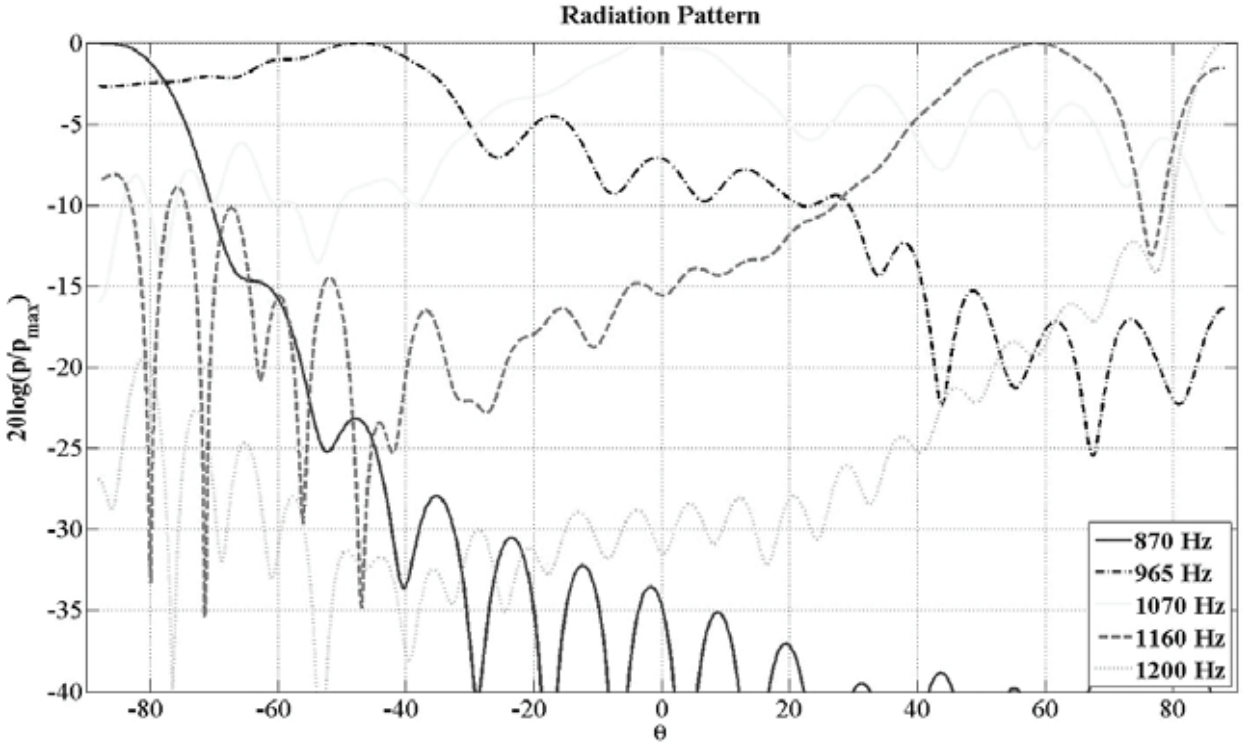

Fig. 7. Radiation pattern of leaky wave structure normalized to maximum

5. CONCLUSIONS

As acoustic leaky wave structures are new in acoustics and have not yet been fully covered, a certain amount of research is still to be done in the field. Among the different topics to be addressed, we can cite a few such as increasing the directivity, optimizing side lobe level, controlling leakage constant or modelling the lossy structures. Also, using it in real life will motivate more research in this field. It is worth noting that our structure is axisymmetrical and radiates into whole 3D. But antenna structures or sensors are more likely to radiate or detect in only one hemisphere thus, another interesting topic would be to design a leaky wave structure that would radiate in only one hemisphere.

6. REFERENCES

[1] V.G. VESELAGO, 1968. "*The electrodynamics of substances with simultaneously negative values of epsilon and mu*" Soviet Physics Uspekhi, **10**(4), 509-514.

[2] C. CALOZ and T. ITOH, 2006. "*Electromagnetic Metamaterials: Transmission Line Theory and Microwave Applications*" Wiely-Interscience and IEEE press.

[3] W. W. HANSEN, 1940. "*Radiating Electromagnetic Waveguide*" U.S. Pat., **2**, 402,622.

[4] L. LIU, C. CALOZ and T. ITOH, 2002. "*Dominant mode (DM) leaky-wave antenna with backfire-to-endfire scanning capability*", Electron. Lett., **38**(23), 1414-1416.

[5] J. Li and C.T. Chan, 2004. "*Double negative acoustic metamaterial*" Phy. Rev. E **70**, 055602.

[6] F. BONGARD, H. LISSEK and J.R. MOSIG, 2010. "*Acoustic transmission line metamaterial with negative/zero/positive refractive index*" Phy. Rev. B **82**, 094306.

[7] A. MOREAU, H. LISSEK and F. BONGARD, 2010. "*Design of Acoustic Metamaterials based on the Concept of Dual Transmission Line*" in preceedings of the Comsol Conference, Paris, France, 17-19.

[8] C. J. NAIFY, C.N. LAYMAN, T. P. MARTIN, M. NICHOLAS, D. C. CALVO and G. J. ORISS, 2013. "*Experimental realization of variable index transmission line metamaterial as an acoustic leaky-wave antenna*" Appl. Phys. Lett **102**, 203508.

[9] M. GARCÍA-VIGUERAS, J. L. GÓMEZ-TORNERO, G. GOUSSETIS, A. R. WEILY and Y. J. GUO, 2011. "*1D Leaky wave antenna employing parallel-plate waveguide loaded with PRS and HIS*", IEEE Trans. Antennas Propag., **59**(10), 3687-3694.

Journal of Acoustical Society of India : Vol. 42, No. 2, 2015 (pp. 69-76)

Use of the Acoustic Remote Sensing for the Mixing Layer Height Determination

Lokoshchenko M.A.
Department of Meteorology and Climatology, Faculty of Geography, Lomonosov Moscow State University. 119991, Lengory, Moscow, Russia
Phone: +7-495-9394284; Fax: +7-495-9392479;
E-mail: loko@geogr.msu.su`

[Received: 16.12.2013; Revised: 24.05.2014; Accepted: 27.07.2014]

ABSTRACT

The problem of the mixing layer height (MLH) determination with the use of the sodar data is discussed. Unlike the most of other methods a new suggestion is to determine separately two different mixing layer heights: "upper" or "stable" MLH which indicates a top of an inversion inside wind shear layer (in which dynamical turbulence exists and creates echo-signal) and "lower" or "unstable" MLH which indicates as a rule unstable or weak-stable stratification below the elevated inversion bottom. Some experimental data confirm that two different MLH sometimes, usually in the morning, exist simultaneously one above another. According to this idea the diurnal courses of mixing layer heights - both "upper", and "lower" - have been calculated on a base of long-term sodar sounding at Moscow State University (MSU) during 15 years. Dynamics of both heights at various seasons is discussed.

1. INTRODUCTION

The mixing layer height (MLH) is an important parameter of the lower troposphere which allows determining of the maximal possible range of the air pollution dispersion. The MLH was suggested for the first time by Holzworth in 1962 and initially it was measured on a base only of direct measurements (using radiosonde and the ground meteorological data). Accordingly to classical method, this parameter is equal to the first intersection of the diurnal thermal profile and dry-adiabatic line (which means the value of $\gamma = -\partial T / \partial z = 0.98$ °C / 100 m) from the ground point of the maximal daily temperature. It should be noted that, instead of its clear physical meaning, in itself the MLH demonstrates often poor statistical relations with real levels of the air pollution (Aron, 1983). Indeed, it is only one of important atmospheric parameters which must be accounted together with MLH. Later, in addition to MLH, one more parameter - the 'mixing volume' - was used as well. It is product of MLH and average wind velocity V below this height so that the 'mixing volume' may be presented geometrically as a cube which vertical size is equal to MLH and which horizontal size along one axis is equal to the mean V. However, it should be noted as well that both MLH and 'mixing volume' represent not real range of the air pollution dispersion but the potential, i.e. the highest possible one. It may be real in case if air pollutants have sufficient time to reach it. In other words, both parameters indicate potential limit of dispersion in stationary conditions.

The acoustic remote sensing since the pioneer work (McAllister, 1969) discovered new possibilities for more accurate determination of MLH. Now sodars are well-known everywhere all over the world mostly as a tool for wind profiling. However, it is not the only application of the sodar data. Besides Doppler wind

measurements, classic so-called 'sodar record' of old non-Doppler sodars (i.e. an echo-signal intensity in time-height coordinates) allows indicating of the thermal stratification type, including inversion layers which prevents to upward dispersion of the air pollutants (Krasnenko, 1986; Lokoshchenko, 1996 and others). Fine spatial resolution of sodars (as a rule, 10-20 m) represents the main advantage of the acoustic remote sensing of the atmosphere due to comparatively low sound velocity (331 m / s in normal conditions). As a result sodars is an almost ideal tool for studying of the atmospheric boundary layer fine-structure. Among others, sodars allows indicating of low level jets in wind profiles as well as thin elevated inversions on sodar records.

The long-term rows of sodar data about thermal stratification were received only in New Delhi in India (Singal et al., 1984), in Krakow in Poland and in Moscow in USSR and Russia (Lokosh-chenko, 2006 and 2007). It should be noted that works of famous Indian school of the acoustic remote sensing are well-known everywhere. The sodar sounding is carried out at Moscow University since 1988, i.e. during last quarter a century. The observation site is situated at the South-Western periphery of Moscow city on 7 km from the city centre. It represents quite flat and open locality. Two sodars have been used there: vertical sodar "ECHO-1" by GDR production since 1988 and Doppler sodar "MODOS" by production of METEK firm (Germany) since 2004. However, only classic data about the thermal stratification which were received at MSU by the use of the "ECHO-1" sodar will be discussed below. Its vertical range is from 25 to 800 m, the operation frequency is 1666.6 Hz, the spatial resolution of the data is equal to 12.5 m.

2. MIXING LAYER HEIGHT BY THE SODAR DATA

As it is said above a sodar record, besides determination of a thermal stratification type, is a useful tool for the MLH estimation as well. The initial determination of the MLH following the Holz-worth's idea was limited only by the unstable stratification, although he wrote by himself later that nocturnal mixing in conditions of the stable stratification due to wind shear "in some cases… may be important". When sodar records began to be used a lot of works were devoted to determination of the MLH by the sodar data including the stable stratification (Kallistratova et al., 1991; Krasnenko and Fursov, 1992; Maughan et al., 1982; Singal et al., 1984, etc.). It should be noted that comparatively small range of the sodar data - as a rule, from 500 to 1000 m - doesn't allow measuring diurnal mixing height in the afternoon directly - unlike, e.g., some lidar systems (Emeis et al., Münkel, 2009). A top of vertical turbulent structures on sodar records ("plumes", "roots", "grass", "stalagmite", "prongs of a comb", etc.) which are connected with separate convective cells is usually significantly less than their real upper height. Sometimes, however, the MLH in the afternoon is considered to be equal to the average top of convective "plumes" on sodar records (e.g., Krasnenko and Fursov, 1992). Another way is to suppose formally that the diurnal MLH is equal to the height range of a sodar if any elevated inversions are absent above convective structures on a record (Maughan et al., 1982). But the best possible way with the use of a sodar is to receive indirect estimations of this parameter by comparisons between a top of vertical turbulent structures on sodar records and real diurnal mixing height. As it is shown in (Lokoshchenko, 2002) with the use of radiosonde data the ratio between these parameters is close to 1:4 for conditions of Moscow. It is important to note that this estimation was received by the data of the same sodar "ECHO-1" and that its gain factor didn't be changed during a long time. It should be noted as well that in conditions of India this ratio was nearly the same (Singal et al., 1984). One of well-known summary methodic of the MLH determination with the use of sodar records was suggested by (Kallistratova et al., 1991). It should be noted that, in spite of great variety of different turbulent structures on sodar records, it is quite simple for everybody to discern four general types: layers of strong echo-signal intensity connected with inversions, intermitted patchy structures of weak echo-signal intensity connected as a rule with weak-stable stratification (close to isothermal when $\partial T / \partial z = 0$), vertical "plumes" connected with the unstable stratification and totally blank record in time of indifferent stratification. At the latter case a record can't give any information about real MLH but, fortunately, absolutely blank records which mean exactly adiabatic vertical profile of T (when $\partial \Theta / \partial z = 0$) can be seen extremely rarely. So, following (Kallistratova et al., 1991), the MLH is supposed to be equal either to a top of the surface inversion, or to a top of an air layer with weak-stable stratification, or to a bottom of the elevated inversion (if the

surface one is absent below), or to a quadruple height of the average top of convective structures, so-called 'plumes' (if this value is less than a bottom of elevated inversion above).

Author used this scheme during a long time. Additionally, author suggested using the instability energy for calculations of the MLH when the data of radiosonde profiling of T are available (Lokoshchenko, 2002). As for the sodar data of the MLH, the results of measurements on a base of hourly coding of sodar records at Moscow University were published by (Kallistratova and Lokoshchenko, 1998) for period 1988-1991 and later by (Lokoshchenko, 2002) for longer period 1988-1998. In fact, an average MLH calculation accordingly to (Kallistratova et al., 1991) represents generally quite logical results in common features - both at the

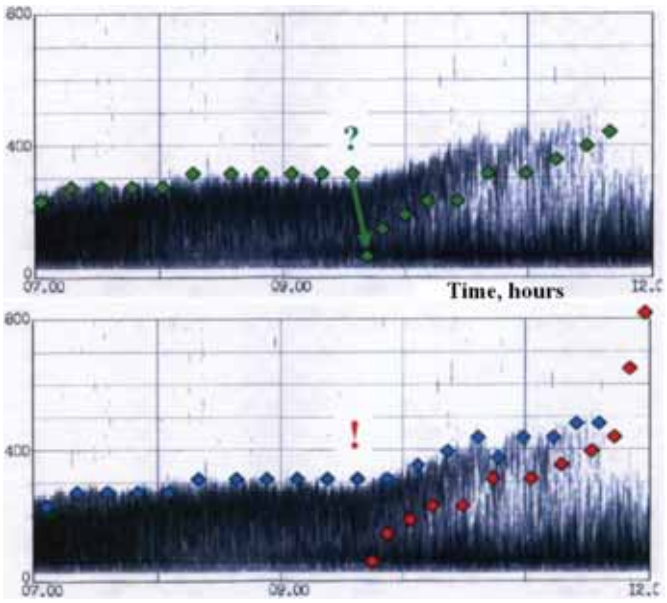

Fig. 1. Dynamics of MLH in morning time in conditions of elevated inversion: traditional methodic (paradoxical fall) - upper part; new suggestion at the same sodar record - lower part. Green rhombuses - traditional MLH; blue rhombuses - upper MLH (new suggestion); red rhombuses - lower MLH (new suggestion).

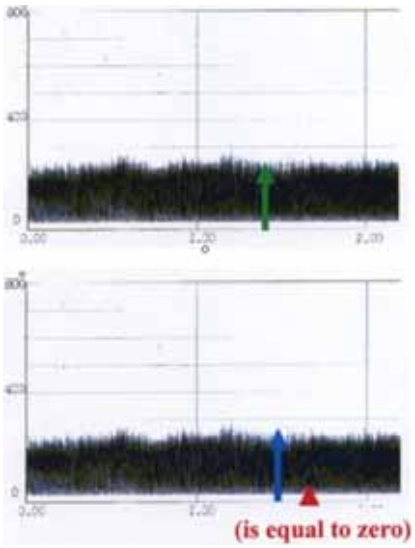

(a) Surface inversion;

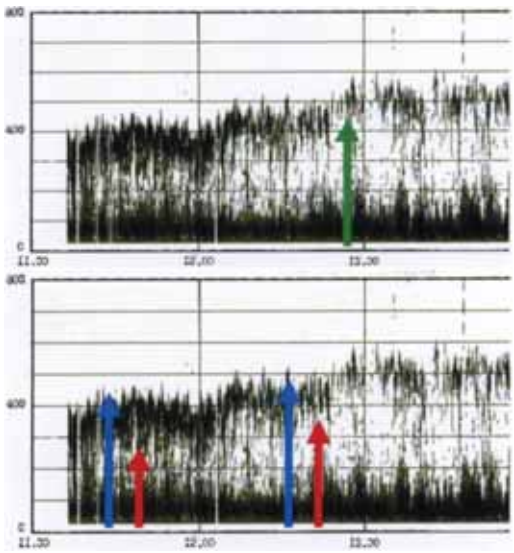

(b) Elevated inversion;

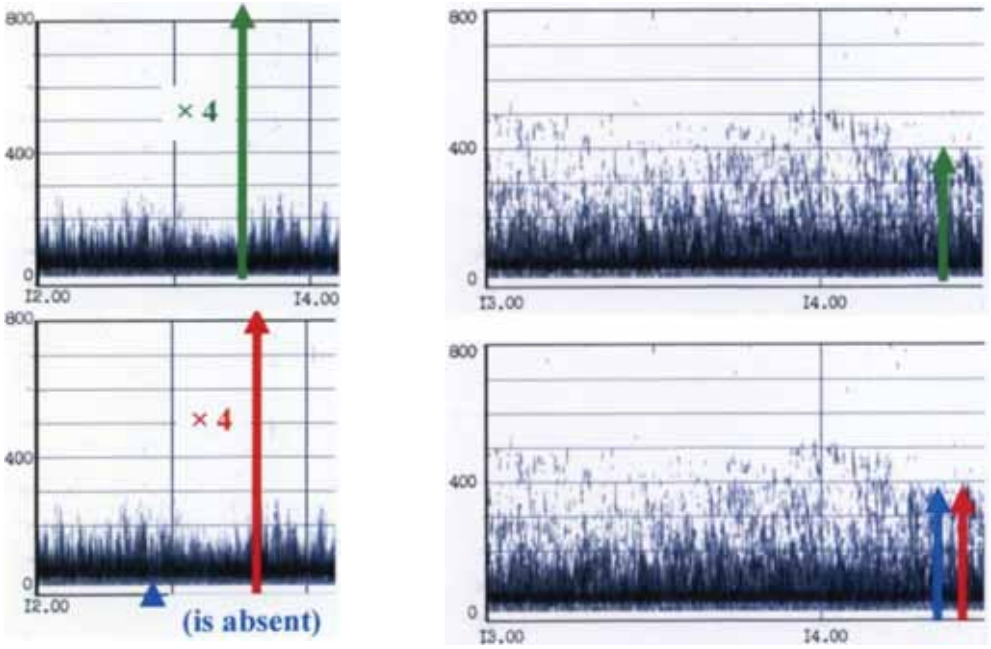

(c) Unstable stratification; **(d) Weak-stable stratification**

Fig. 2. Mixing layer heights by the sodar data. Green lines indicate the traditional MLH; blue lines - "stable" MLH (new suggestion); red lines - "unstable" MLH (new suggestion).

annual course (with maximum in the warm period) and at the diurnal one (with a strong maximum in the afternoon, especially in summer). However, a joining of different stratification types at the same parameter sometimes leads to illogical and paradoxical dynamics of the MLH. For example, after sunrise when the surface inversion begins to lift above the ground the MLH value accordingly to (Kallistratova et al., 1991) is sharply changed from a top of the surface inversion to its bottom (when it lifts already) - see Fig.1. At the diurnal course this change may be seen as a sudden fall of the MLH in the early morning like a jump although it is evident mixture of two principally different physical processes. Evidently it is a disadvantage of methodic which was suggested by (Kallistratova et al., 1991).

For more correct studying of the MLH at its dynamic a new approach is to analyze separately two mixing heights: "stable" or "upper" and "unstable" or "lower" (see Fig.1 and 2). This idea was published briefly for the first time in (Lokoshchenko, 2010). Accordingly to it, the "stable" MLH is equal either to a top of any inversion (i.e. a height of an upper margin of turbulent structure connected with an inversion layer on a sodar record), or to a top of an air layer with weak-stable stratification. The "unstable" MLH means either a top of a layer with weak-stable stratification as well or a quadruple average height of convective structures ("plumes") when elevated inversion is absent above. If the unstable stratification exists in a layer below the elevated inversion the "unstable" MLH is equal either to a bottom of the inversion if it is less than a quadruple height of plumes or to a quadruple height of plumes otherwise. Thus, when weak-stable stratification takes place at any layer a top of this layer represents both "upper" and "lower" heights because this type is intermediate and frontier between stable and unstable stratification.

In conditions of unstable stratification the "upper (stable)" MLH is absent. From the other hand, in time of the surface inversion the "lower (unstable)" MLH is considered to be equal to zero.

As one can see in Fig.1 sudden fall of MLH is absent accordingly to new suggestion. In fact the stable MLH which indicated a top of former surface inversion during night really exists even later - in morning when the same inversion became elevated already. At the same time new unstable MLH appears simultaneously below the stable one. Thus, new method of two different MLH represents successful solution of this paradoxical dynamics.

3. EXPERIMENTAL CONFIRMATION

Indeed, experimental data often demonstrate two different MLH simultaneously - especially, in morning time. One of confirmations is given by lidar data (e.g., Emeis S., K.Schäfer, C.Münkel, 2009). In Fig.3 the diurnal course of the lidar backscatter density is presented for Hamburg city. As one can see in color scale of this parameter, three air layers with different background levels existed simultaneously in time from 05 to 11 a.m.: the highest values - in the ground air layer, the middle ones - in the upper part of the ABL above and, finally, the lowest values (blue color) - in free troposphere since 1.8-2.3 km. Correspondingly, two MLH existed simultaneously between these three layers.

One more experimental confirmation was received by author in time of special experiment when sodar and tethered balloon operated simultaneously (Lokoshchenko and Shifrin, 2009; Lokoshchenko, 2010). The tethered balloon was supplied, among others, by electrochemical ozonosonde. The experimental ozone profiling with fine resolution in the lower atmosphere demonstrated as well that two different MLH sometimes exist in the morning simultaneously one above another - both below the elevated inversion and above it.

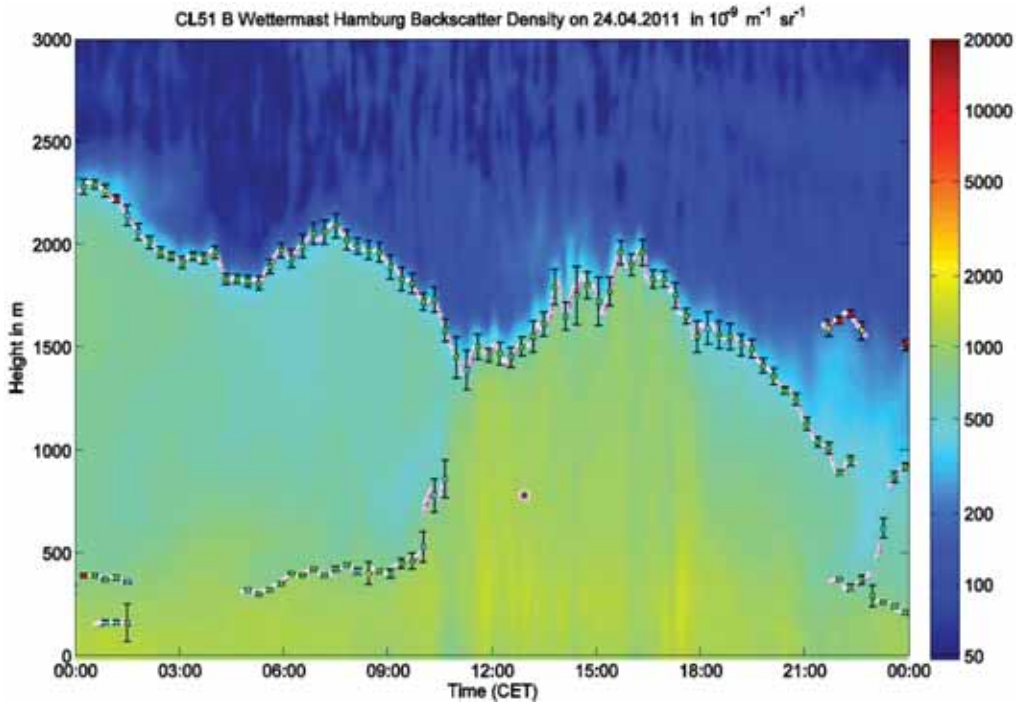

Fig. 3. The diurnal course of the lidar backscatter density in Hamburg accordingly to (Emeis et al., 2009)

4. CLIMATOLOGY OF MIXING LAYER HEIGHTS

The daily courses of both mixing layer heights at different seasons are presented on Figure 4. They were calculated on a base of hourly coding of sodar records which were received at Moscow University in period from 1988 to 2003 (totally - almost of 35.000 hours of records were analyzed by author). As it is seen the "upper" MLH (blue rhombs) in winter doesn't demonstrate any significant changes during a day. However, it is slightly higher at night and a bit lower in the afternoon. In spring and in summer the "upper" MLH which is connected with stable conditions increases in the morning that is a result of lifting of the morning elevated inversion (which is as a rule former surface inversion) top. Except morning time, the "upper" stable MLH is nearly the same from one hour to another during all the rest of a day. The average value of the "upper" MLH is close to 300 m and varies in limits from 250 to 350 m. It is highest in winter due to more

thickness of surface inversions and lowest in summer. In the middle of a day in spring, in summer and in autumn the stable stratification exists extremely rarely so that calculation of the average "upper" MLH in these conditions is not supported by sufficient statistical sampling. Vice versa, the "lower" MLH that is either unstable or weak-stable stratification (red circles) may be observed very rarely after midnight. Only in winter the diurnal course of the "lower" MLH is full due to comparatively often cases of weak-stable stratification at night - both in presence and in absence of elevated inversions above it [12].

Unlike the "upper" MLH the "lower" one connected mostly with unstable conditions has a clear diurnal course with maximum in the afternoon which is especially strong in spring and in summer. The maximal average values of the "lower" MLH in the middle of a day consist up to 700 m in spring and up to 800 m in summer. In fact, the diurnal convective mixing layer in mid-latitudes may be really equal to 800 m in summer as it was demonstrated by lidar in [1]. However, usually it seems to be more and convective turbulent structures on sodar records in summer are often higher than 200 m as well. The average values of the "lower" MLH on Fig.4 indicate total calculation including cases of elevated inversions which sometimes exist at low levels. Due to them the average "lower" MLH is not so large. It should be noted that the diurnal course of this parameter is quite similar in spring and in summer whereas in autumn the daily maximum of the "lower" MLH is very weak already. Thus, there is an evident asymmetry of mixing conditions at transitional seasons.

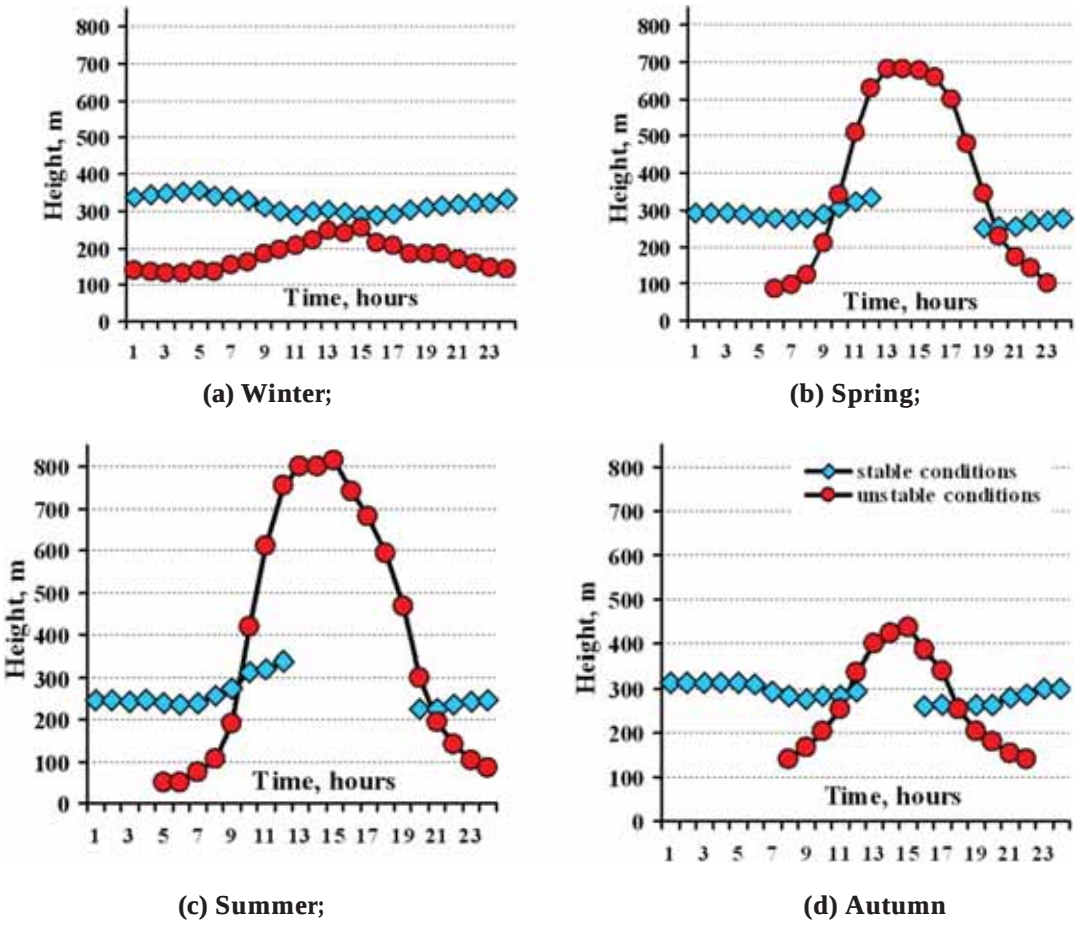

Fig. 4. The diurnal course of both mixing layer heights at various seasons by the sodar data for the period 1988-2003. Moscow.

5. CONCLUSIONS

1. The acoustic remote sensing is a useful tool for determination of the mixing layer height, especially at nocturnal and morning time. If inversion layers exist in the lower atmosphere real mixing height as a rule is close to their margins which may be detected on a sodar record. As regard as diurnal convective mixing layer, only indirect estimations of the MLH are possible by the use of a sodar.
2. Different physical processes of mixing can operate at the same time at various levels of the atmosphere. Among others, sometimes in the morning two mixing heights exist simultaneously below and above elevated inversion.
3. It seems to be useful to analyze separately two different mixing heights one of which is connected as a rule with a top of an inversion and another one - mainly with a bottom of an inversion or with a top of convective cells. The weak-stable stratification has an intermediate position between these processes. This approach of two kinds allows understanding and studying the dynamics of the MLH more correctly.
4. Accordingly to long-term sodar observations at Moscow University the "upper" MLH connected with stable conditions consists in average nearly of 300 m (from 200 to 400 m). It is the largest in winter and the smallest in summer.
5. The "lower" MLH connected mostly with unstable conditions is the largest in summer and in spring (up to 700-800 m in average in the afternoon) and the smallest in winter. There is clear asymmetry between conditions of mixing in spring and in autumn.

6. REFERENCES

1. R. ARON, 1983. Mixing height – an inconsistent indicator of potential air pollution concentrations. Atmospheric Environment, **17**(11), 2193-2197.
2. S. AUTUMN EMEIS, K. SCHÄFER, C. MÜNKEL, 2009. Observation of the structure of the urban boundary layer with different ceilometers and validation by RASS data. *Meteorologische Zeitschrift*, **18**(2), 149-154.
3. G.C. HOLZWORTH, 1962. A study of air pollution potential for the western United States. *J. of Applied Meteorology*, 1, 366-382.
4. M.A. KALLISTRATOVA *et al.*, 1991. Method of remote measurement of mixing layer parameters by Doppler sodar. *Preprint of IAP,* Moscow, **1**, 77-94 (in Russian).
5. M.A. KALLISTRATOVA and M.A. LOKOSHCHENKO, 1998. Studying of mixing layer height by radiosonde and sodar observations. In: *Proceedings of the 9-th ISARS*, Vienna, Austria, 285-288.
6. N.P. KRASNENKO, 1986. The Acoustic Remote Sensing of Atmosphere – a monograph (in Russian). Novosibirsk: Nauka, Siberian division, 168 p.
7. N.P. KRASNENKO and M.G. FURSOV, 1992. The remote acoustic monitoring of meteorological parameters in atmospheric boundary layer. *Atmospheric and Oceanic Optics*, Tomsk, **5**(6), 652-654.
8. M.A. LOKOSHCHENKO, 1996. Use of vertical sodars in meteorology (review), *Atmospheric and Oceanic Optics*, Tomsk, **9**(7), 616-628.
9. M.A. LOKOSHCHENKO, 2002. Long-term sodar observations in Moscow and a new approach of the potential mixing determination by radiosonde data, *Journal of Atmospheric & Oceanic Technology*, **19**, 1151-1162.
10. M.A. LOKOSHCHENKO, 2006. Thermal Stratification and Weather Phenomena on Sodar Records. In: *Proceedings of the 13th ISARS,* Garmisch-Partenkirchen, Germany, 131-136.
11. M.A. LOKOSHCHENKO, 2007. Temperature stratification of the lower atmosphere over Moscow, *Russian Meteorology and Hydrology*, **32**(1), 35-42.

12. M.A. LOKOSHCHENKO, 2010. Climatology of the mixing layer height by long-term sodar data. In: *Proceedings of the 15th ISARS*, Paris, France.

13. M.A. LOKOSHCHENKO and D.M. SHIFRIN, 2009. Temperature stratification and altitude ozone variability in the low troposphere from acoustic and balloon sounding, *Russian Meteorology and Hydrology*, **34**(2), 72-82.

14. R.A. MAUGHAN, A.M. SPANTON and M.L. WILLIAMS, 1982. An analysis of the frequency distribution of sodar derived mixing heights classified by atmospheric stability. *Atmospheric Environment*, **16**(5), 1209-1218.

15. L.G. McALLISTER *et al.,* 1969. A new approach to the study of atmospheric structure. In: *Proc. of the IEEE*, **57**(4), 579-587.

16. S.P. SINGAL, B.S. GERA and S.K. AGGARWAL, 1984. Nowcasting by aoustic remote sensing: experiences with the systems established at the National Physical Laboratory, New Delhi. *J. of Scientific & Industrial Research*, **43**, 469-488.

Journal of Acoustical Society of India : Vol. 42, No. 2, 2015 (pp. 77-83)

A Signal Processing Framework for the Infrasound Signature Generated by Snow Avalanches

Rajani Akula*, Arun Kumar and Monika Agrawal
Centre for Applied Research in Electronics,
Indian Institute of Technology Delhi, HauzKhas, New Delhi, 110016, India.
e-mail: ak.ece.cs@gmail.com

[Received: 15.01.2014; Revised: 21.04.2014; Accepted: 12.08.2014]

ABSTRACT

Snow avalanches are a source of hazard in mountaneous terrain. There has been some effort in recent years to autonomously detect and localize snow avalanches at some locations based on the infrasound generated by such events over a duration of few tens of seconds. This information can be transmitted in real-time to a base-station for disaster management and other purposes. The statistics of occurrence of snow avalanches generated from such monitoring activity over a period of time, along with the on-site environmental parameters is used for making predictive models of occurrence of avalanches.

In this work, we are concerned with the development of a parametrized signal processing model from the equations of motion of snow avalanche, for the purpose of synthesizing the infrasound signature that is generated by the event that can be detected and localized at a distant infrasonic receiver array. Subsequently, we shall fine-tune the model based on field data that is not available abundantly. The purpose of this work is two-fold: (i) to synthesize realistic infrasound signatures from an accurate model for varying values of the dependent variables such as speed profile of the avalanche, the size of the avalanche *etc.*, and (ii) to use inverse processing techniques to estimate the parameters of the snow avalanche from field measurements of infrasonic signatures and a signal processing model.

The time evolution of infrasound emitted by snow avalanches depends on the time evolution of different types of snow avalanche and their interaction with air. Snow avalanches can be classified as wet and dry avalanches based on the water content in the snow. They consist of different parts once it starts from a fracture on slopes greater than 30°. Dry avalanches start as the dense part and depending on the slope profile and snow mass involved, powder part is also generated. The sound sources of a snow avalanche can be of monopole, dipole, or quadrupole type. While a monopole may not be exactly applicable in this case, a dipole and quadrupole model is quite relevant. A dipole consists of two monopoles separated by a distance that is small compared to the wavelength it generates and can be used for modeling a translating sphere in fluid medium. The dense part of the snow body moving down a slope with a velocity is modelled as a dipole. When slow avalanches move on steep slopes with large velocities, the surface layer snow particles are lifted up and the interaction with the surrounding air particles forms a powder cloud. This powder part generated sound is modelled by a quadrupole.

In this work, we have recast the differential equation model of the generation of sound from a dipole into a signal processing framework comprising of an input, a time-varying linear system and an output that is the observable infrasound signature of the snow avalanche at a distant receiver. The input is taken as the velocity of the avalanche as a function of time, and the parameterized time-varying system models the dynamics of the snow avalanche that leads to the pressure signal

as the observable output at a distance 'r'. Initially, we consider the snow avalanche mass as a simple sphere, with a fixed radius *R* that is moving with velocity *u(t)*, thus, keeping the system as time-invariant. The output pressure signal is simulated for different sizes of the avalanche for various velocity profiles during the motion of the snow avalanche. The characteristic frequency is proportional to C / R where C is velocity of sound and R is radius of the body. Using Fourier analysis, the relation between the body size and velocity of avalanche is analyzed. In practice, the body size of snow avalanches is changing while it is moving down the slope. This case is considered as a parameterized time-varying system model in a signal processing framework to synthesize the pressure output. Examples of the synthesized pressure waveform and its Fourier representation shall also be presented.

1. INTRODUCTION

Snow Avalanches generates infrasonic acoustic waves and propagates in the atmosphere with the speed of sound [1-3]. The detection and localization of snow avalanches can be done based on this infrasound measured through an acoustic array [4-5]. The localization of snow avalanches is very much needed as mountains are becoming more sought place by visitors. For their safety, understanding snow avalanches, detecting and localizing them automatically and subsequently predicting them is essential. Snow avalanches are classified as wet and dry type based on the water content.

Snow avalanches generate relatively low noise band of the sub-audible infrasonic frequency spectrum and this infrasound signature is used for developing automated avalanche monitoring systems. This infrasound is accompanied with problematic ambient wind noise and interfering signals. The detection of infrasound signals is facilitated via spatial geographic filtering of unwanted noise and applying a threshold criterion to a correlation measure that estimates the coherency of data recorded between sensors. To start with detection, we need to know the received pressure level at the sensor location. To formulate mathematically the received signal at the sensors we need the pressure at the source level generated by the avalanche and its source model. The received signal also depends on the channel. The channel consists of a direct line of sight path and reflections from snow. The reflective strength will depend on the acoustic properties of snow at infrasound. The effects of wind and temperature cannot be neglected as sound velocity depends on both of them.

In the literature, sound models for infrasonic emissions from snow avalanches are scarcely presented. The general theory of acoustics is applied to infrasonic emissions. Bedard [2,6] gave an infrasonic model for dry avalanches with the dense part modelled as a dipole and the powder part as a quadrupole. For the powder cloud using quadrupole model, the sound intensity emitted is proportional to the eighth power of the ûow velocity as proposed by Lighthill [7-8].

Snow avalanches are broadly classified into two types, namely flow avalanches and powder snow avalanches. There are different avalanche ûow regimes that interact differently with the environment and hence yield infrasonic emissions. Dry avalanches have dense part and powder part. Using all this information we can simulate the received signal at the sensors using signal processing model. The velocity of the body is taken as the input to the system. As the snow avalanches move, its size will change, in particular, grow. This has been take care as the parameters of the system by modelling as a time varying system. Thus, a moving source has been put in a signal processing framework.

2. REVIEW OF PHYSICAL EQUATIONS FOR SOUND SOURCES

Sound sources can be of monopole or dipole or quadrupole type. A monopole is a source which radiates sound equally well in all directions. The simplest example of a monopole source would be a sphere whose radius alternately expands and contracts sinusoidally. The monopole source creates a sound wave by

alternately introducing and removing fluid into the surrounding area. A dipole source consists of two monopole sources of equal strength but opposite phase and separated by a small distance compared with the wavelength of sound. The result is that the fluid (air) near the two sources sloshes back and forth to produce the sound. A sphere which oscillates back and forth acts like a dipole source. Pressure disturbances caused by the motion of the body is felt as sound when this disturbance passes an observer. In the inhomogeneous wave equation, the source terms depend on the net local force of the body on the fluid (dipole) and normal velocity of the surface of the body (monopole).Sound generation by the dry avalanches movement is modeled as a body moving in the ambient air / fluid [9-13].

An avalanche starts at a point on slopes of more than 30° typically. In this case, the body is taken as a sphere of radius R moving on the slope due to gravity. Here, viscous forces are neglected. As the avalanche moves forward on a slope, it exerts force on the fluid based on its size. The strength of the dipole is equal to the force applied to unit volume of this linearly disturbed homogeneous field. This unsteady external force on the fluid is taken as a dipole source for sound. So, snow avalanche at an instant of time can be taken as a dipole where the filter parameters are defined by the radius of the sphere and sound velocity and the input to the filter is the velocity of the sphere. The velocity input is assumed to change in steps. Using linearity and time invariance for a short duration, the output is given as the convolution and is called step response output in view of the assumed nature of the input. The impulse response of the system is obtained by differentiation of this output. The wave equation with sources included becomes an inhomogeneous wave equation. Duhamel's principle is a general method for obtaining solutions to these inhomogeneous wave equations [10].Without spatial dependency, Duhamel's principle becomes a variation of parameters. Avalanche flow is treated as superposition of the dipoles at different instants of time. As it moves, the flow reaches different positions in space based on its velocity. All the signals generated by these dipoles should be coherently added to give the source signal.

We derive the relation for the pressure generated from differential equations of a dipole and use them for simulations [11-14]. When a sphere with radius R executes in an ideal compressible fluid, an arbitrary translatory motion with velocity small compared with that of sound, then the velocity potential is of the form

$$\phi = div\left[\frac{f(t)}{r}\right] \tag{1}$$

where $\boldsymbol{r}$ is the distance between the centre of the sphere and distance from the origin. The velocity of the sphere u is small compared with the velocity of sound therefore the movement of the origin is neglected [13]. The fluid velocity is given by :

$$v = grad\phi \tag{2}$$

Using the boundary condition that at $r = R$, $v_r = u.\boldsymbol{n}$, where $\boldsymbol{n}$ is a unit vector in the direction of $\boldsymbol{r}$ and substituted in Eq.(2) for v. We get

$$v_r = grad\left[div\frac{f(t)}{r}\right] = u.\boldsymbol{n} \tag{3}$$

By expanding the operations of gradient and divergence in Eq. (3), we get a second order differential equation.

$$f''(t)+\frac{2C}{R}f'(t)+\frac{2C^2}{R^2}f(t) = RC^2u(t) \tag{4}$$

Equation (4) is a non-homogeneous differential equation which is solved using Duhamel's principle. Without spatial dependency, this method becomes the variation of parameters methods.The superposition integral or Duhamel's integral is also known as convolution integral. This expresses the response of a system in terms of its unit step response, *i.e.*, the superposition integral tells the response of a system as a continuous sum of the responses to the step components of input.

$$f(t) = CR^2 e^{-\frac{c}{r}t} \int_o^t u(\tau) \sin \frac{c(t-\tau)}{R} e^{\frac{c_t}{R}} d\tau \tag{5}$$

The expression in eq. (5) can be represented as the convolution of the impulse response or characteristic function $h(t) = e^{-\frac{C}{R}t} \sin\left(\frac{C}{R}t\right)$ with the input *u(t) i.e.*,

$$f(t) = CR^2 h(t) * u(t) \tag{6}$$

The $h(t)$ depends on the radius of the body R and sound velocity C which defines the characteristic frequency. Once $f(t)$ is obtained, using the relation in Eq. (1) the velocity potential$f$ is obtained where $t' = t - \frac{(r-R)}{C}$. Finally, the pressure is related to velocity potential by $p(t) = \rho_0 \frac{\partial \phi}{\partial t}$.

3. SIGNAL PROCESSING MODEL

The infrasound generation process from the snow avalanches and the received signal at each sensor are modelled as given below. The dense part is taken as a sphere of radius R moving on the avalanche path. This is modelled as a dipole. This dense part which is in contact with the ground changes its size based on the slope of the path. Wet snow avalanches having high-density snow and the relatively slow speed of propagation are modelled as dipole. Dry avalanches will start as dense part and based on the slope profile, the powder part is generated. This powder part, also called as powder avalanches, consists of low-density snow, and has relatively high speed of propagation. In an avalanche, the dense part is modelled as a dipole and, and the powder part is modelled as a quadrupole. The signal generated by snow avalanches is propagated through the channel and received at the sensor. This entire process suggests that it can be considered as an appropriate excitation signal applied to a(linear, time-varying) filter and the output is the received pressure signal by a distant receiver.

The first channel is considered to be a linear time invariant (LTI) filter based on the distance between the source of the snow avalanche and the receiver. But a snow avalanche, as it moves, it grows in size and the distance between the source and the sensor reduces. So, the channel should be modelled as a time-variant filter where the parameters are changing with growing size of avalanches. The velocity input is represented as interms of steps i.e., constant during the stationarity period of the filter. The filter coefficients can be changed based on sample-by-sample adaptation or block based adaption algorithms.

4. SIMULATION RESULTS AND ANALYSIS

Using state variable analysis, Eq. (4) is solved for the input velocity as 10 m/s. First, linear time invariant (LTI) system output is generated. In the next step, we have taken time varying filter, for simulation purposes, in which the parameters are updated every 0.01s.

Step 1 : For LTI system, the input velocity is taken as 10 m/s step input and R is varied from 3 m to 300m insteps of 10 m.We calculate the impulse response and the results are shown below in the same figure 1.

Step 2 : To get the frequency response shown in fig. 2, we have used the value of R=12m.

Step 3 : For time varying filter,R is increased in steps of 0.01sec. The input velocity is taken from [4]. This was given for 71s with 1Hz sampling frequency.For simulation purposes, we resampleit at 100Hz. With this input applied for time varying filter, the pressure generated at 3km is given in fig 3.

Step 4 : The frequency response of this pressure is shown in Fig 4 which clearly shows dominant magnitude in the infrasound band

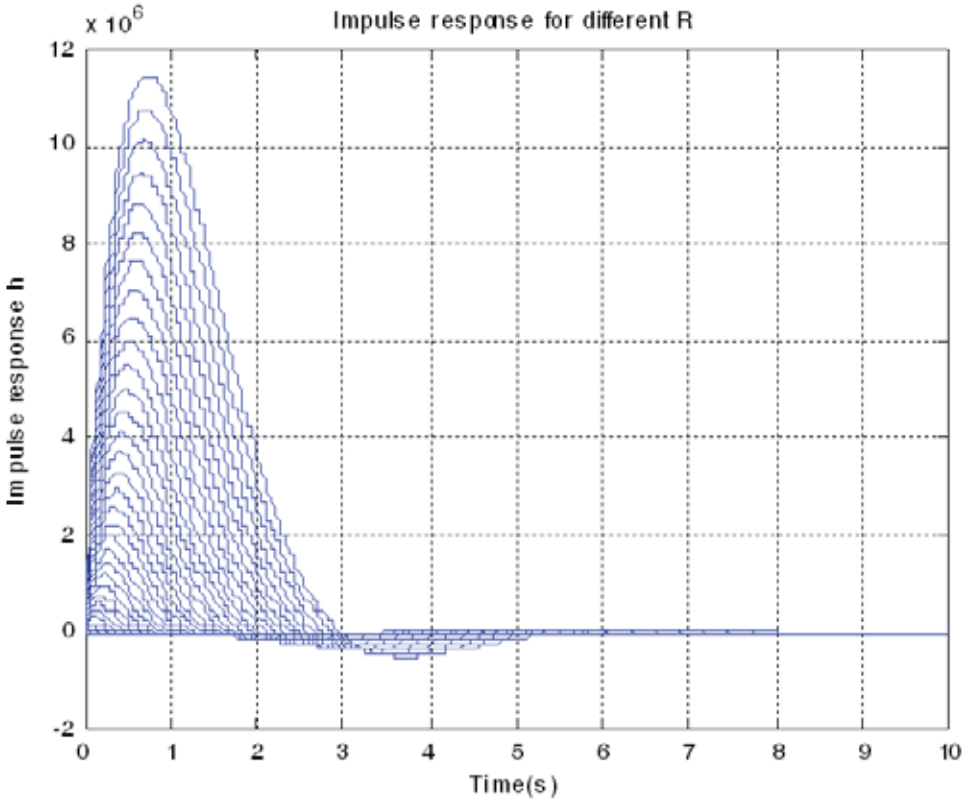

Fig. 1. Impulse response for different values of *R*.

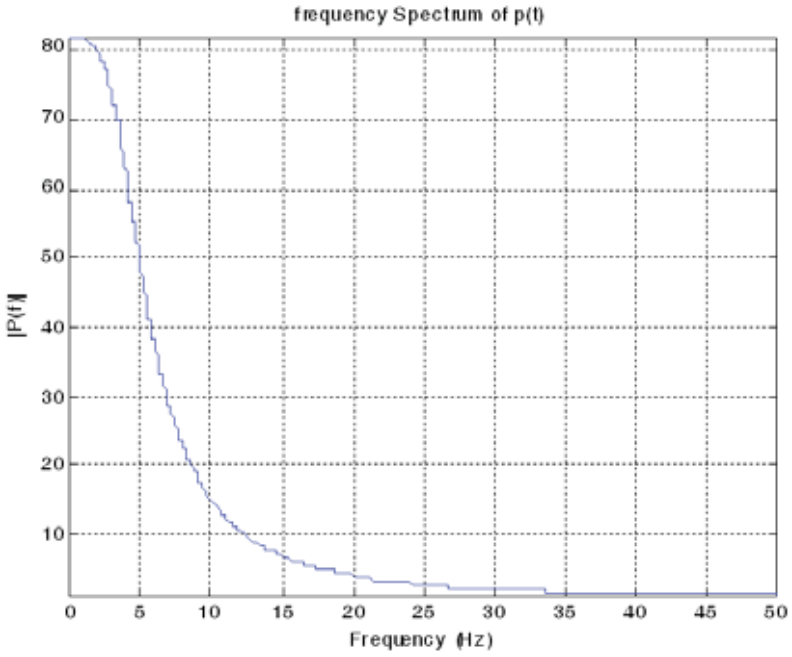

Fig. 2. Frequency response for R=12m

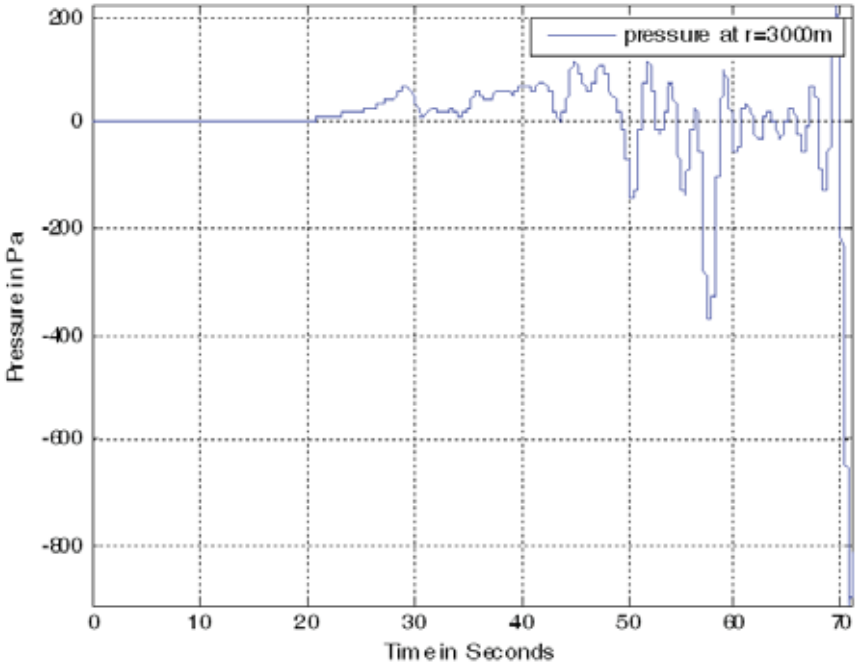

Fig. 3. Pressure generated using TV filter approach.

5. CONCLUSIONS

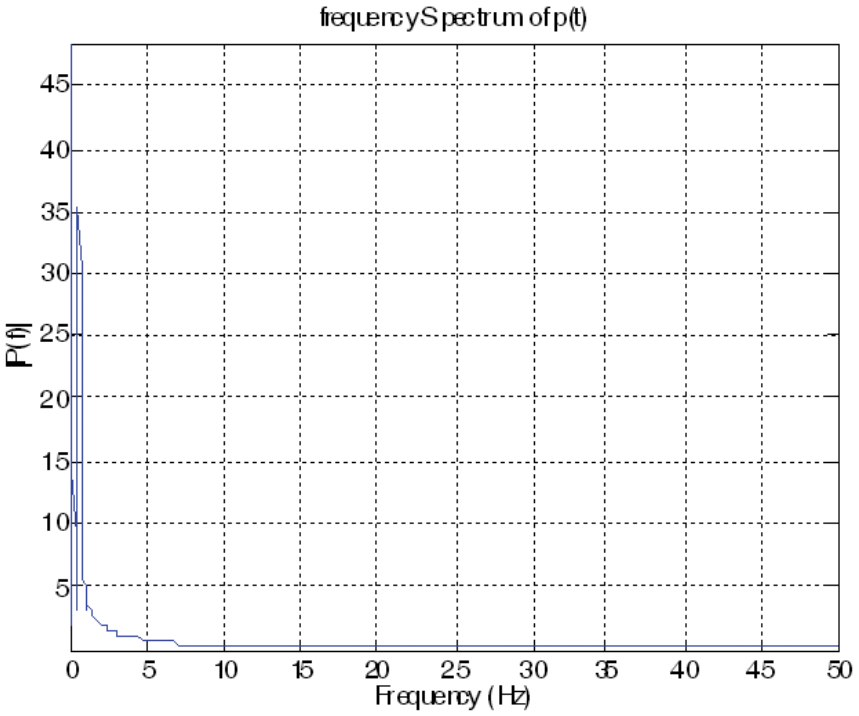

Fig. 4. Frequency responseof $p(t)$.

In this paper, we have theoretically modelled the signal generated at a receiver sensor due to a moving source that is a snow avalanche. We take dry avalanches which contain both dense part and powder part. The dense part is modelled as a dipole and for the moving source it has been represented as a time varying linear filter where the filter parameters are changing with time in block adaptive manner. For the dipole, the output is obtained as the convolution of the impulse response with velocity of the body. The impulse response of the filter depends on the size of the body. As the avalanche flows, the size will grow. The avalanche flow is modelled as the superposition of a moving sphere. The pressure calculation using dipole or quadrupole takes the avalanche front velocity into consideration. So it is required to know the timings of the generated dense and powder parts. By having this information, we can accurately simulate the pressure waveform generated at a distant receiver. An accurate signal processing model of the pressure waveform is useful in creating a simulation database for various parameters of snow avalanches. Such a database is necessary, for example, in developing snow avalanche detection and localization algorithms in the presence of noise and other interference sources.

6. REFERENCES

[1]. G. ULIVIERI , E. MARCHETTI, M. RIPEPE , I. CHIAMBRETTI , G. DE ROSA and V. SEGOR, 2011. Monitoring snow avalanches in North western Italian Alps using an infrasound array, *Cold Regions Science and Technology* **69**, 177-183.

[2]. A. BEDARD, 1989. Detection of avalanches using atmospheric infrasound, *Proceedings of the Western Snow Conference*, 52–58.

[3]. ALEXIS LE PICHON, ELISABETH BLANC and ALAIN HAUCHERNE. *Infrasound monitoring for atmospheric studies.*

[4]. A. KOGELNIG, E. SURINACH, I. VILAJOSANA, J. HUBL, B. SOVILLA, M. HILLER, and F. DUFOUR, 2011. On the complementariness of infrasound and seismic sensors for monitoring snow avalanches, *Nat. Hazards Earth Syst. Sci.*, **11**, 2355–2370.

[5]. B. TURNBULL and J. N. MCELWAINE, 2010. Potential flow models of suspension current air pressure, *Ann. Glaciol.*, **51**, 113-122.

[6]. A. BEDARD, K. NAUGOLNYKH, 2002. Amodel of the infrasonic radiation, *IEEE international Geoscience and remote sensing symposium*.

[7]. M. J. LIGHTHILL, 1952. On sound generated aerodynamically. I. General theory. *Proceedings of the Royal Society of London. A. Mathematical and Physical Sciences* **211**(1107), 564–587.

[8]. M. J. LIGHTHILL, 1954. On sound generated aerodynamically. II. Turbulence as a source of sound. *Proceedings of the Royal Society of London. A. Mathematical and Physical Sciences* **222**(1148).

[9]. A. HIRSCHBERG and S. RIENSTRA, 2004. *An introduction to aero acoustics*, Tech. rep., Eindhoven University of Technology, Dept. of App. Physics and Dept. of Mathematics and Comp. Science.

[10]. B.P. LATHI, 1965. *Signals, Systems, and Communication*, John Wiley & Sons, New York.

[11]. D. KARCZUB and M. P. NORTON, 2003. *Fundamentals of Noise and Vibration Analysis for Engineers*, Cambridge Univ. Press..

[12]. ANN P. DOWLING and JOHN E. FFOWCS WILLIAMS, 1983. *Sound and sources of sound,* Ellis Horwood series in engineering science. Publisher, E. Horwood.

[13]. L.D. LANDAU and E.M. LIFSHITZ, 1987. *Fluid mechanics*, Second edition, Oxford, Butterworth-Heinemann (Course in Theoretical Physics 6.).

[14]. J. FFOWCS WILLIAMS, 1963. The noise from Turbulence Convected at High Speed, *Philos. Transactions Royal Society Acoustics*, **255**, 469–503.

Journal of Acoustical Society of India : Vol. 42, No. 2, 2015 (pp. 84-94)

Feedback Control Strategies for Active Structural Acoustic Control of Interior Noise

Ashok K. Bagha and S.V. Modak*
Department of Mechanical Engineering, Indian Institute of Technology, Delhi
Hauz Khas, New Delhi -110016, India
**e-mail: svmodak@mech.iitd.ac.in*

[Received: 05.05.2014; Revised: 25.09.2014; Accepted: 29.10.2014]

ABSTRACT

An important problem in systems such as aerospace interiors, automobile passenger compartments and other cavities is the control of low frequency interior noise. Active control of this noise may offer a potentially better alternative to passive control due to constraints of weight and space. Previous studies in this direction have focused more on active noise control strategies using secondary acoustic sources. These, however, require large bulky loudspeakers and the relevant literature indicates that obtaining global control is also more difficult. Active structural-acoustic control studies in this direction have used acoustic sensors as the error sensors with many studies focusing on feedforward control. This strategy requires a large number of error sensors if control at a large number of local regions is required. This also may make control system more complex. Feedforward control also requires a reference signal corresponding to the disturbance and may not be as effective to control noise due to broadband sources and therefore in these situations feedback control is expected to be more useful. In view of above observations, this paper investigates global control of interior acoustic field through feedback control using structural sensing and structural actuation. Piezoelectric transducers are used for sensing vibrations of the structure and applying control inputs onto it. Two linear quadratic regulator (LQR) based control strategies are presented. In the first strategy, an LQR controller is designed by exploiting the knowledge of structural-acoustic coupling to obtain an indirect control of acoustic field through control of structural vibrations. A second strategy is developed that frames an LQR cost function to represent the acoustic potential energy in terms of structural modes of vibration. A numerical case study of a 3D rectangular cavity backed by a flexible plate is presented to validate the developed strategies.

1. INTRODUCTION

The active structural acoustic control (ASAC) strategy can be used for attenuating the radiated acoustic power or acoustic potential energy in the interior of a cavity. In ASAC, structural actuators such as shape memory alloys (SMA), piezoelectric materials (PZT), magnetostrictive materials, Magneto-rheological (MR) fluids and structural sensors such as PZT, PVDF, and fiber optics can be integrated into the walls in such a way as to modify or reconstruct the vibration of the flexible panels and reduce the sound radiation or transmission[1, 2]. The PZT patches can be glued on the structure to sense response and provide the necessary inputs for control of structural response as well as acoustic radiation[3].

Feedforward and feedback control are the two main control strategies that have been used for interior noise control. Feedforward control requires a reference signal corresponding to the disturbance and may

not be as effective to control noise due to broadband sources and therefore in these situations feedback control is expected to be more useful. Feedback control can be implemented to achieve global control of acoustic response with lesser level of control system complexity[2]. In view of this, the present paper considers feedback control of interior noise through an ASAC approach.

In the control of flexible structures, feedback control strategy is used either to add active damping or to achieve optimal feedback control[2]. Active damping can generally be achieved with direct velocity feedback. Optimal feedback control involves applying a control input that minimizes a certain cost function taken as a combination of quantity to be controlled and the control effort. Such an optimal control strategy is referred as Linear Quadratic Regulator (LQR) control. For noise control, the cost function provides a method of weighting heavily the modes of the structure that are known to be efficient acoustic radiators and similarly allows diminished weighting of the inefficiently radiating modes. Structural-acoustic coupling coefficients have been used in an active vibration control (AVC) strategy to judge the structural modes that may dominantly generate interior noise[4]. For suppressing periodic sound transmission into enclosed spaces, minimization of vibration and acoustic indices such as the acoustic potential energy in the enclosure, acoustic pressure amplitudes at discrete locations and kinetic energy of the structure has been studied[5].

In this paper two linear quadratic regulator (LQR) based control strategies are presented. In the first strategy, an LQR controller is designed by exploiting the knowledge of the structural-acoustic coupling to obtain an indirect control of acoustic field though control of structural vibrations. A second strategy is developed that frames an LQR cost function to represent the acoustic potential energy in terms of structural modes of vibration.

2. SIMULATION OF THE PIEZO-STRUCTURAL-ACOUSTIC SYSTEM

2.1 State space model of the plant and acoustic cavity

The finite element equation coupling the piezoelectric, structural and the acoustic domain in its final form can be written as,

$$\begin{bmatrix} \mathbf{M}_{\mathrm{T}} & \mathbf{0} & \mathbf{0} & \mathbf{0} \\ \mathbf{0} & \mathbf{0} & \mathbf{0} & \mathbf{0} \\ \mathbf{0} & \mathbf{0} & \mathbf{0} & \mathbf{0} \\ -\mathbf{S}^{\mathrm{T}} & \mathbf{0} & \mathbf{0} & \mathbf{M}_{\mathrm{A}} \end{bmatrix} \begin{Bmatrix} \ddot{\mathbf{w}} \\ \ddot{\phi}_{\mathrm{a}} \\ \ddot{\phi}_{\mathrm{s}} \\ \ddot{\mathbf{p}} \end{Bmatrix} + \begin{bmatrix} \mathbf{C}_{\mathrm{S}} & \mathbf{0} & \mathbf{0} & \mathbf{0} \\ \mathbf{0} & \mathbf{0} & \mathbf{0} & \mathbf{0} \\ \mathbf{0} & \mathbf{0} & \mathbf{0} & \mathbf{0} \\ \mathbf{0} & \mathbf{0} & \mathbf{0} & \mathbf{C}_{\mathrm{A}} \end{bmatrix} \begin{Bmatrix} \dot{\mathbf{w}} \\ \dot{\phi}_{\mathrm{a}} \\ \dot{\phi}_{\mathrm{s}} \\ \dot{\mathbf{p}} \end{Bmatrix} + \begin{bmatrix} \mathbf{K}_{\mathrm{T}} & \mathbf{K}^{\mathrm{a}}_{\mathrm{w}\phi} & \mathbf{K}^{\mathrm{s}}_{\mathrm{w}\phi} & \mathbf{0} \\ \mathbf{K}^{\mathrm{a}\ \mathrm{T}}_{\mathrm{w}\phi} & \mathbf{K}^{\mathrm{a}}_{\phi\phi} & \mathbf{0} & \mathbf{0} \\ \mathbf{K}^{\mathrm{s}\ \mathrm{T}}_{\mathrm{w}\phi} & \mathbf{0} & \mathbf{K}^{\mathrm{s}}_{\phi\phi} & \mathbf{0} \\ \mathbf{0} & \mathbf{0} & \mathbf{0} & \mathbf{K}_{\mathrm{A}} \end{bmatrix} \begin{Bmatrix} \mathbf{w} \\ \phi_{\mathrm{a}} \\ \phi_{\mathrm{s}} \\ \mathbf{p} \end{Bmatrix} = \begin{Bmatrix} \mathbf{f}_{\mathrm{d}} \\ -q_{\mathrm{a}} \\ -q_{\mathrm{s}} \\ \mathbf{0} \end{Bmatrix} \tag{1}$$

In the above equation **w** represents vector of structural degrees of freedom, ϕ_n represents a vector of voltage on piezoelectric patch used as actuator, ϕ_s represents a vector of voltage on piezoelectric patch used as sensor and **p** represents vector of nodal acoustic pressures. Similarly, f_d represents some disturbance acting on the cavity, which causes cavity structure to vibrate. q_a is a vector of electric charge at actuator electrodes, and q_s is a vector of electric charge at sensor electrodes. $\boldsymbol{M}_T$ is the combined structural and piezoelectric mass matrix, $\boldsymbol{M}_A$ is the acoustic mass matrix, **S** is the structure-acoustic coupling matrix, $\mathbf{C}_S$ is the structural damping matrix, $\mathbf{C}_A$ is the acoustic damping matrix, $\mathbf{K}_T$ is the combined structural and piezoelectric stiffness matrix, $\mathbf{K}^a_{w\phi}$ is the electro-mechanical coupling matrix of structure and piezoelectric actuator, $\mathbf{K}^s_{w\phi}$ is the electro-mechanical coupling matrix of structure and piezoelectric sensor, $\mathbf{K}^a_{\phi\phi}$ is the electric capacitance matrix for actuator, $\mathbf{K}^s_{\phi\phi}$ is the electric capacitance matrix for sensor, and $\mathbf{K}_A$ is the acoustic stiffness matrix. It is noted that in the FE equation presented above, the piezo and the structural domains are coupled through two-way coupling. On the other hand, the structural and the acoustic domains are assumed to have only one-way coupling from structure to acoustic. The coupling from acoustic domain to structure is neglected, as it is generally small in most of the cavities encountered in aerospace and automotive applications. The development of a finite element based state space model of the plant representing structure and piezoelectric sensor and actuator is presented in [8]. The state space equation of the plant can be written as,

$$\begin{Bmatrix}\dot{\eta}_1\\ \dot{\eta}_2\end{Bmatrix}=\begin{bmatrix}0 & I\\ -\lambda_S^2 & -\Lambda_S\end{bmatrix}\begin{Bmatrix}\eta_1\\ \eta_2\end{Bmatrix}+\begin{bmatrix}0 & 0\\ \psi_S^T & -\psi_S^T K^a_{w\phi}\end{bmatrix}\begin{Bmatrix}f_d\\ \phi_a\end{Bmatrix} \tag{2}$$

where ψ_s is the mass normalized mode shape matrix of piezo-structure system, λ_S^2 is the matrix of given values and Λ_s is a diagonal matrix such that $\Lambda_{sii} = 2\xi_{si}\lambda_{si}$. The output equation for the structural acceleration and modal velocities can be written as,

$$\ddot{w}=\begin{bmatrix}-\psi_S\lambda_S^2 & -\psi_S\Lambda_S\end{bmatrix}\begin{Bmatrix}\eta_1\\ \eta_2\end{Bmatrix}+\begin{bmatrix}\psi_S\psi_S^T & -\psi_S\psi_S^T K^a_{w\phi}\end{bmatrix}\begin{Bmatrix}f_d\\ \phi_a\end{Bmatrix} \tag{3}$$

$$\dot{\eta}_S=\begin{bmatrix}0 & 1\end{bmatrix}\begin{Bmatrix}\eta_1\\ \eta_2\end{Bmatrix}$$

From Eq. (1),

$$M_A\ddot{p}+C_A\dot{p}+K_A p=S^T\ddot{w} \tag{4}$$

The governing system dynamics Eq. (4) is expressed in modal space by introducing a new variable derived by taking modal transformation, $p = \psi_A\eta_A$, and using orthogonal properties for acoustic, Eq. (4) can be written in modal coordinates as,

$$I\ddot{\eta}_A+\Lambda_A\dot{\eta}_A+\lambda_A^2\eta_A=\psi_A^T S^T\ddot{w} \tag{5}$$

where λ_A^2 is the matrix of the rigid-wall eigenvalues of the acoustic cavity and Λ_A is a diagonal matrix such that $\lambda_{Aii} = 2\xi_{Ai}\lambda_{Ai}$. Choosing acoustic modal pressures (η_A) and their first derivative ($\dot{\eta}_A$) as state variables η_{A1} and η_{A2} respectively, we get state equation in the modal coordinates as,

$$\begin{Bmatrix}\dot{\eta}_{A1}\\ \dot{\eta}_{A2}\end{Bmatrix}=\begin{bmatrix}0 & I\\ -\lambda_A^2 & -\Lambda_A\end{bmatrix}\begin{Bmatrix}\eta_{A1}\\ \eta_{A2}\end{Bmatrix}+\begin{bmatrix}0\\ \psi_A^T S^T\end{bmatrix}\ddot{w} \tag{6}$$

Output equation for computing nodal acoustic pressure inside the cavity is given by,

$$p=\begin{bmatrix}\psi_A & 0\end{bmatrix}\begin{Bmatrix}\eta_{A1}\\ \eta_{A2}\end{Bmatrix} \tag{7}$$

2.2 State space model of the acoustic domain

In this section, an acoustic filter is developed that describes the process of generation of acoustic potential energy in the cavity. The global acoustic potential energy is written as[6,7],

$$E_p(\omega) = \eta_A{}^T\frac{V_m}{4\rho_0 c^2}\eta_A \tag{8}$$

where $V_m = \psi_A^T V\psi_A$ is the diagonal acoustic modal volume matrix. After substituting structural acceleration vector $\ddot{w} = \psi_S\ddot{\eta}_S$ into Eq. (5) and assuming harmonic excitation of the cavity structure, the relationship between the acoustic modal pressure vector (η_A) and structural modal velocity vector $(\dot{\eta}_S)$ is obtained as,

$$\eta_A = Z_a\dot{\eta}_S \tag{9}$$

where the $\mathbf{Z}_a$ is the structural to acoustics modal transfer function matrix at frequency ω. Substituting Eq. (9) into (8), the relationship between the structural modal velocity vector and global acoustic potential energy is obtained. The matrix $\mathbf{Z}_a$ can be factored as,

$$Z_a = F\bar{C}_{As} \tag{10}$$

where F is a *na* × *na* diagonal matrix and $\mathbf{F}(i,i) = \frac{s}{s^2 + 2\xi_{Ai}\lambda_{Ai}s + \lambda_{Ai}^2}$. where ξ_{Ai}, λ_{Ai}, λ_{Ai}^2, are the viscous damping loss factor, natural frequency, and given value of the i^{th} acoustic mode respectively. State space model for each **F**(i, i) is obtained and these models are combined to obtain state space model $\mathbf{A}_z$, $\mathbf{B}_z$, $\mathbf{C}_z$ and $\mathbf{D}_z$. The state space model of the acoustic filter corresponding to Eq. (8) and (10) is then obtained as,

$$\dot{\mathbf{d}} = \mathbf{A}_z\mathbf{d} + \mathbf{B}_z\bar{\mathbf{C}}_{As}\dot{\boldsymbol{\eta}}_S \tag{11}$$

$$\sqrt{E_p} = \sqrt{\mathbf{V}_m'}\mathbf{C}_z\mathbf{d} + \sqrt{\mathbf{V}_m'}\mathbf{D}_z\bar{\mathbf{C}}_{As}\dot{\boldsymbol{\eta}}_S \tag{12}$$

3. CONTROL FORMULATION

In the first control strategy, an LQR objective function is framed in order to minimize the structural vibrations along with the control effort.

Damping test results (Frequency response test results) are shown in the following graphs Figure.10 (a) and Figure.10 (b) plotted between frequency vs. decibels.

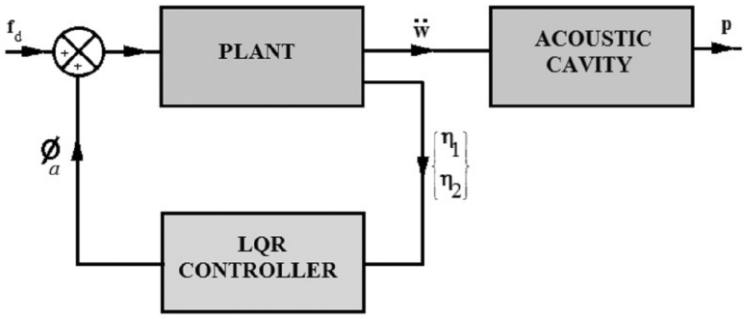

Fig. 1. First control strategy

$$J_{Vib} = \int_0^\infty \left(\boldsymbol{\eta}_P{}^T\mathbf{Q}_{Vib}\boldsymbol{\eta}_P + \phi_a^T\mathbf{R}\phi_a\right)dt \tag{13}$$

where $\eta_P = \{\eta_1 \ \eta_2\}^T$ is the state vector of the structural modal displacements and velocities. $\mathbf{Q}_{Vib}$ and **R** are the weighting matrices in the LQR controller. The matrix $\mathbf{Q}_{Vib}$ is chosen based on coupling coefficients between structural and acoustic modes as explained in the numerical study in the next section. The solution of the algebraic Riccati equation gives the full state feedback gain matrix $\mathbf{K}_{Vib}$. The input voltage to the actuator is then given by,

$$\phi_a = -K_{vib}\eta_P \tag{14}$$

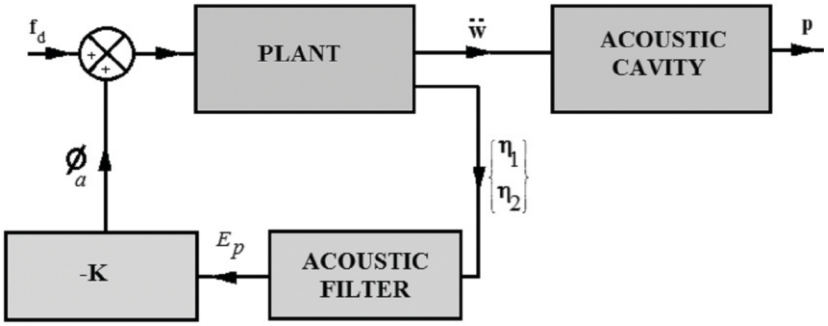

Fig. 2. Second control strategy

In the second control strategy, LQR cost function is designed to minimize the acoustic potential energy inside the cavity along with the control effort as shown in Fig. 2. The acoustic potential energy is estimated through an acoustic filter by sensing structural vibrations using piezoelectric patches.

$$J_{\mathrm{Ep}} = \int_0^{\infty} \left(\sqrt{E_p}^{\mathrm{T}} \sqrt{E_p} + \phi_a^{\mathrm{T}} \mathbf{R} \phi_a \right) dt \tag{15}$$

4. NUMERICAL EXAMPLE

A numerical study is presented here to demonstrate the effectiveness of two optimal control strategies briefly explained in the previous section. A proportional viscous damping is simulated in the structural and the acoustic domain of the cavity. A 3D rectangular box cavity of size 0.261 m × 0.300 m × 0.686 m backed by a flexible steel plate of size 0.261 m × 0.300 m of 0.001m thickness.

The cavity is filled with air of density $\rho_0 = 1.21$ Kg / m^3 and speed of sound $c = 340$ m / s. The cavity walls are rigid from five sides and the sixth side is made up of a flexible steel plate clamped at its four edges. The density of the plate is 7800 Kg / m^3; the Young's modulus is 200 GPa and Poisson's ratio 0.30. On the plate, a P-876 A12 Dura Act piezoelectric patch is bonded, whose in plane dimensions are 0.0522×0.050 m^2 along x and y and 5×10^{-4} m thick. The Young's modulus of the P-876 A12 Dura ACT piezoelectric patch is 23.3 GPa, density is 7800 Kg / m^3, Poisson's ratio is 0.34, piezoelectric strain coefficient e_{31} and e_{32} is –8.9678 C / m^2 and dielectric constant ε_{33} is 6.6075×10^{-9} F / m. The flexible-plate is discretized using 10 × 12 four-nodded Kirchhoff's thin plate bending elements that have three degrees of freedom, out of plane displacement and two rotations, at each of their nodes. The acoustic cavity is discretized using 10 × 12 × 14 eight-nodded solid acoustic elements with acoustic pressure as the degree of freedom at each of its nodes (Fig. 3). The piezoelectric patches that are supposed to be glued on the flexible plate are modeled with classical lamination theory using piezo-electric constitution relations and discretized into 2 × 2 four-nodded rectangular bending element with 12 mechanical DOFs and 2 electric DOFs (voltage). One of the electrodes for each patch is grounded. The sensor is short-circuited and the actuator applies control voltage. The first 10 acoustic modes and all the normal structural modes are extracted using the finite element model.

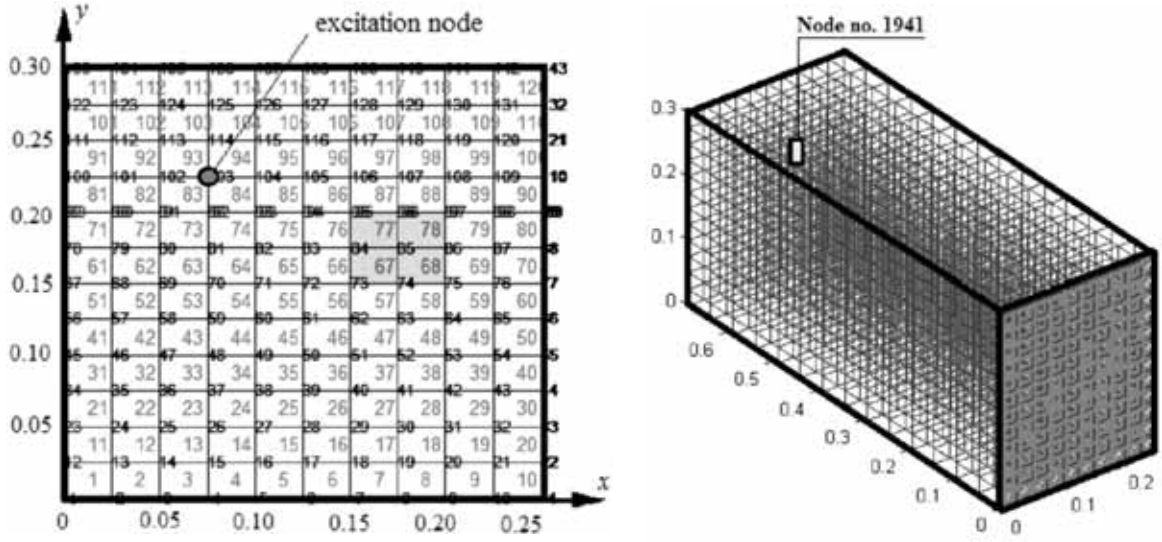

Fig. 3. Finite element mesh of the structural and acoustic domain of the cavity

4..1 Results using first control strategy

In this strategy, all the normal structural modes are simulated but the weighting matrix $\mathbf{Q}_{\mathrm{Vib}}$ is chosen to give selective weighting to the first eighth structural modes lying in the frequency range 0-500 Hz. The

weights for remaining modes are taken zero. Eq. (16) shows the weighting matrix taken with the objective of controlling structural vibrations without any consideration of their coupling to the acoustic modes. A constant weight of 10000 is given to modal displacement and modal velocities of the first eighth structural modes.

$$\mathbf{Q}_{Vib} = \begin{bmatrix} \mathbf{q}_d & \mathbf{0} & \mathbf{0} & \mathbf{0} \\ \mathbf{0} & \mathbf{0} & \mathbf{0} & \mathbf{0} \\ \mathbf{0} & \mathbf{0} & \mathbf{q}_v & \mathbf{0} \\ \mathbf{0} & \mathbf{0} & \mathbf{0} & \mathbf{0} \end{bmatrix}, \mathbf{R = 0.0001} \tag{16}$$

$$q_d = \text{diag}[10000 \quad 10000 \quad 10000 \quad 10000 \quad 10000 \quad 10000 \quad 10000 \quad 10000]_{8\times 8}$$

$$q_v = q_d$$

Table-1 shows the dominant structural-acoustic modal coupling coefficients $\bar{\mathbf{C}}_{ij}$ showing coupling betweenith acoustic andjth structural mode. The coefficients $\bar{\mathbf{C}}_{11}$, $\bar{\mathbf{C}}_{15}$, $\bar{\mathbf{C}}_{16}$, $\bar{\mathbf{C}}_{21}$, $\bar{\mathbf{C}}_{25}$, and $\bar{\mathbf{C}}_{26}$ are relatively large, which means that the structural modes **S1, S5** and **S6** can generatehigh levels of noise, when excited since they are strongly coupled with the first and second acoustic mode (**A1** and **A2**).

Table-1. Structural-acoustic modal coupling coefficients ($\bar{\mathbf{C}}_{As}$)

Structural Modes (Hz)	Frequency of piezo-structural Modes (Hz)	Structural- acoustic coupling coefficients	
		Acoustic modes	
		A1(250.5 Hz)	***A2(504.2 Hz)***
S1	111.19	**142.33**	**-144.13**
S2	213.23	7.09	-7.18
S3	251.25	10.43	-10.56
S4	334.64	2.14	-2.17
S5	369.45	**-64.31**	**65.12**
S6	461.69	**-63.15**	**63.95**
S7	477.34	-0.34	0.34
S8	545.07	-7.12	7.21

Eq. (17) shows the weighting matrix taken with the objective of controlling the structural vibrations but by taking into account the coupling of various structural and acoustic modes in the frequency range of interest (0-500 Hz). The weight for a particular structural mode is chosen by summing the coupling coefficients for it and then normalizing it. The total weightage in weighting schemes given by Eqs. (16) and (17) is same.

$$q_d = \text{diag}[38300 \quad 1900 \quad 2800 \quad 500 \quad 17300 \quad 10000 \quad 17000 \quad 92 \quad 1900]_{8\times 8} \tag{17}$$

A disturbance of 10 N of impulse force is applied at the node number 103 on the plate as shown in Fig. 3. Fig. 4 shows a comparison of modal velocity of the first and seventh structural mode with and without control for both the weighting schemes. It is observed that when weights are selected by using structural-acoustic coupling coefficients, the first normal mode, (which has high coupling coefficients) damps more quickly as compared to the case when structural vibrations are controlled without any regard to the structural-acoustic coupling. Similarly, the seventh structural mode (which has low coupling coefficients) is allowed to damp slowly when the weighting scheme based on structural-acoustic coupling coefficients is used. However, the weighting scheme that disregards the coupling-coefficients tends to give equal importance to this structural mode.

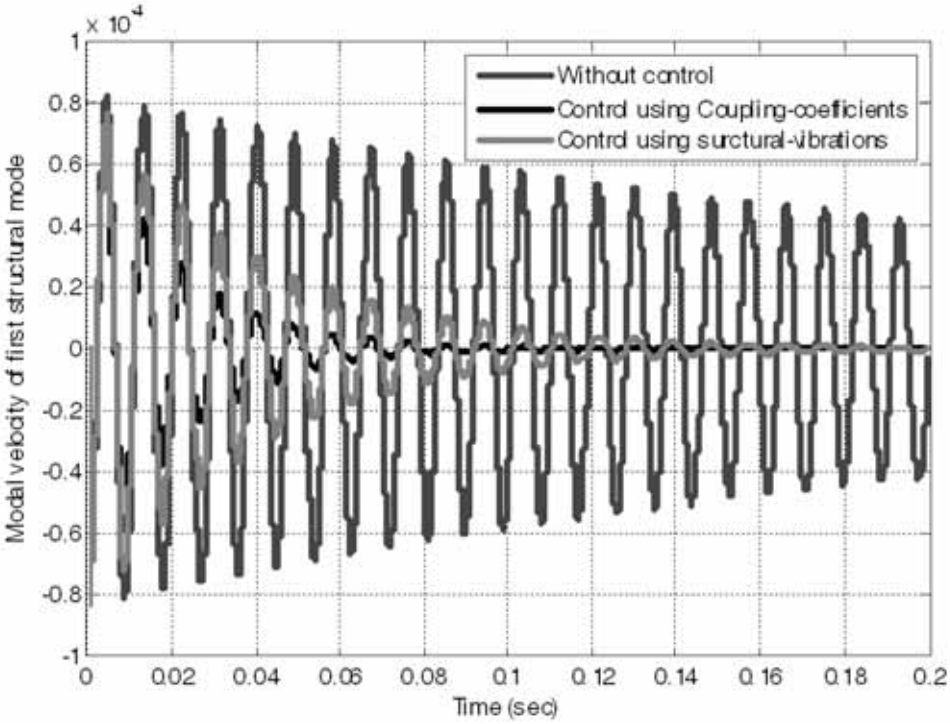

(a)

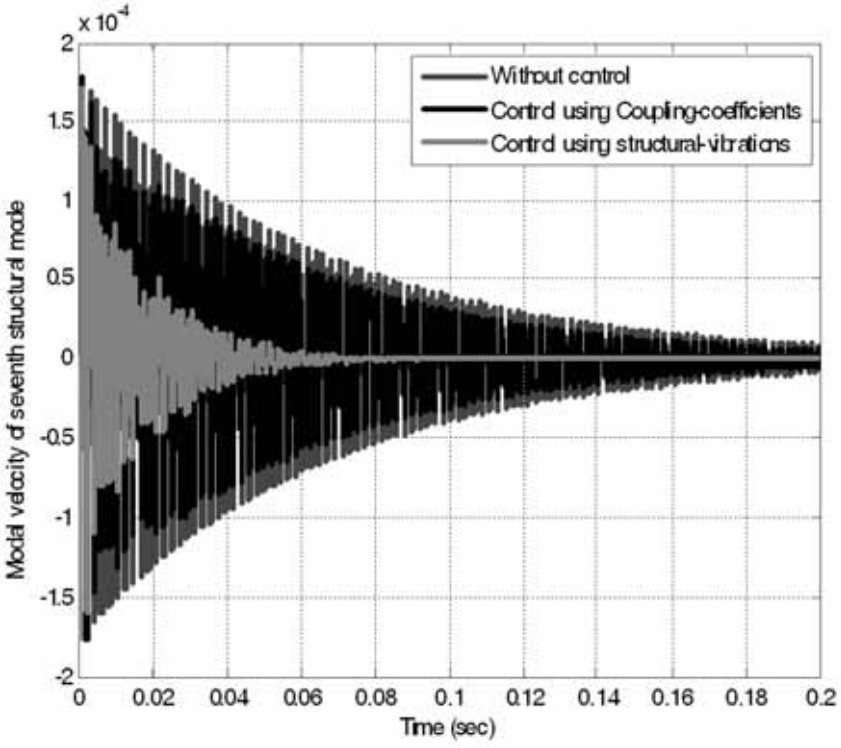

(b)

Fig. 4. Structural modal velocity (a) Modal velocity of first structural mode (b) Modal velocity of seventh structural mode

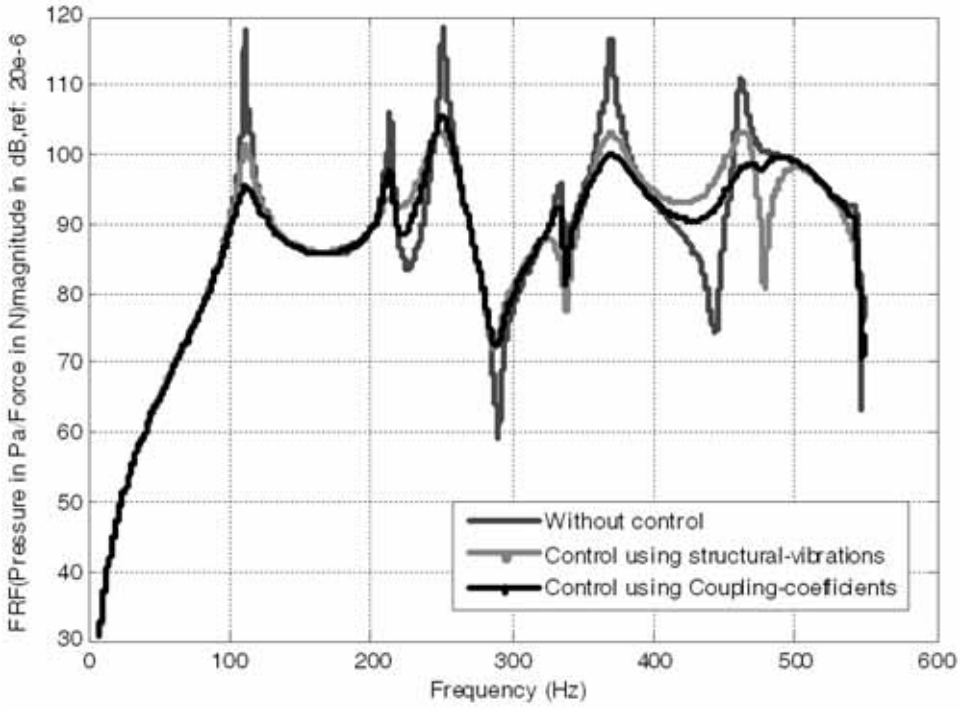

(a)

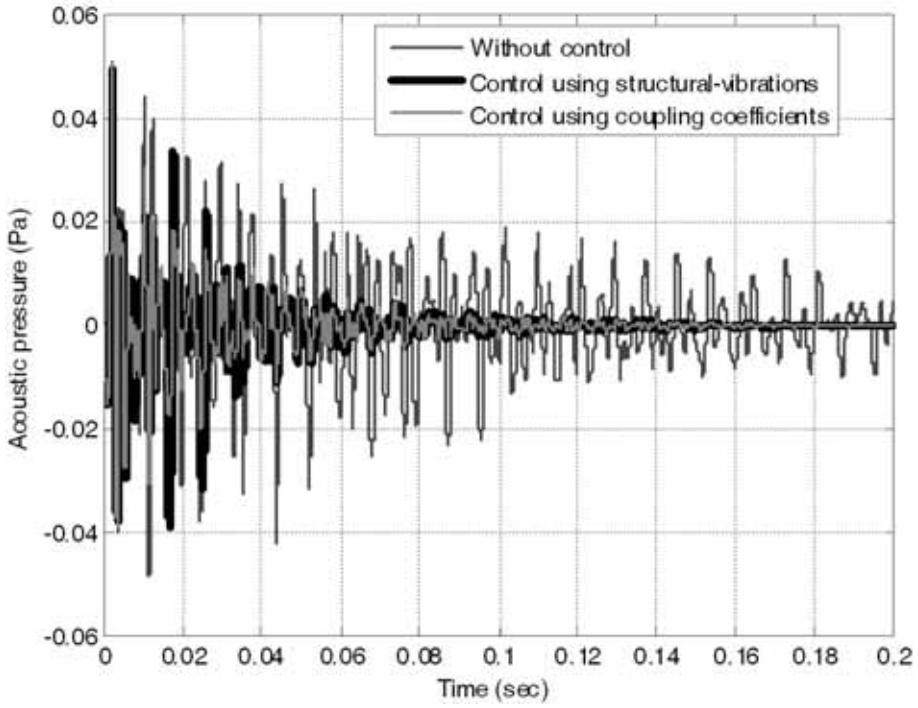

(b)

Fig. 5. Frequency response and acoustic nodal pressure with and without control
(a) FRF (acoustic pressure / force) (b) Acoustic nodal pressure at node number 1941

Fig. 5 shows frequency response function and acoustic nodal pressure with and without control when both the weighting schemes are used. It is again seen that the weighting scheme based on structural-acoustic coupling coefficients gives more importance to damp the structural modes that matter more for the interior noise. It is also observed that acoustic pressure is significantly reduced.

4..2 Results using second control strategy

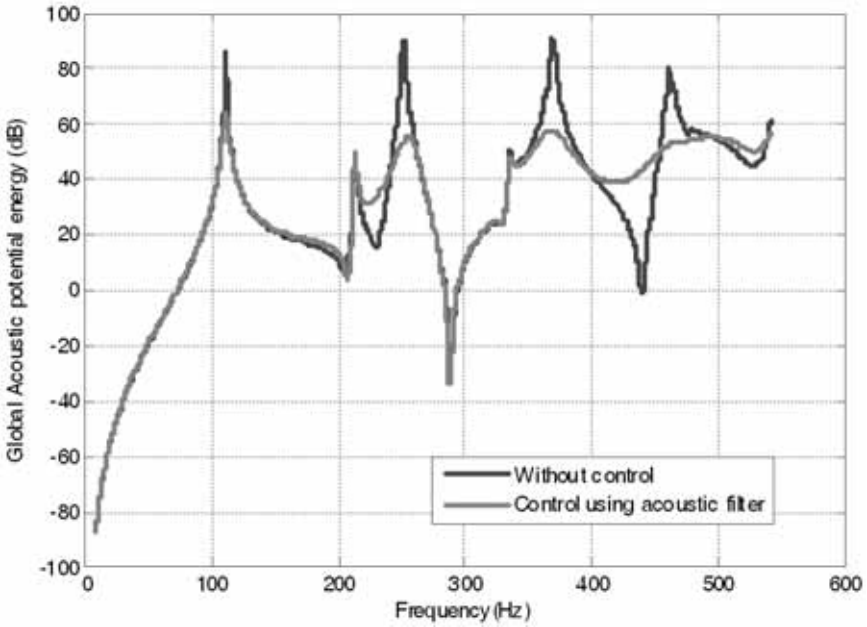

(a)

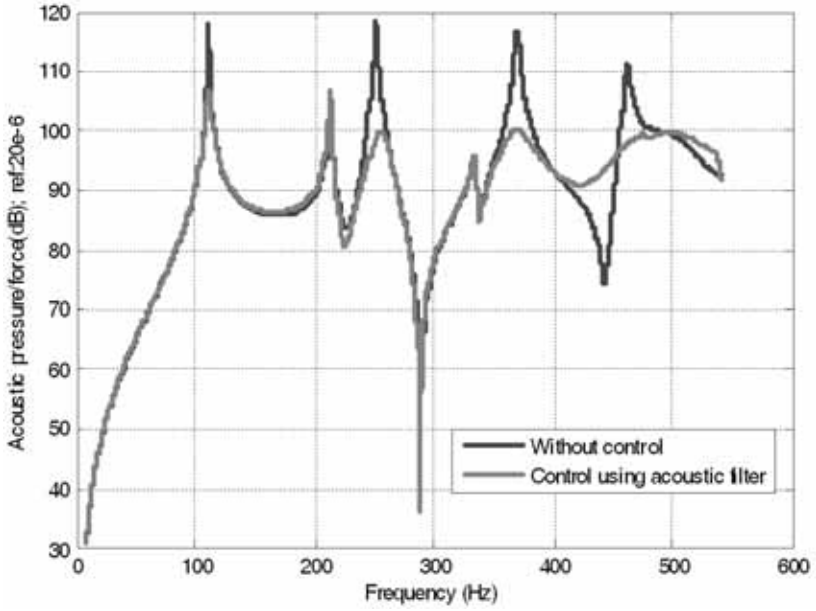

(b)

Fig. 6. Global acoustic potential energy and FRF with and without control
(a) Global acoustic potential energy (b) FRF (acoustic pressure / force)

Fig. 6 shows a comparison of open and closed loop acoustic potential energy and frequency response function (FRF) at node number 1941. It is seen that the feedback control is able to reduce the acoustic potential energy substantially at resonance frequencies. It is observed from the plot that second and fourth mode is not controlled. Fig. 7 and 8 shows a comparison of open and closed loop acoustic nodal pressure and also sound pressure level (dB) at node number 1941 inside the cavity. It is observed that acoustic nodal pressure and sound pressure level (SPL) is significantly reduced when feedback control is applied.

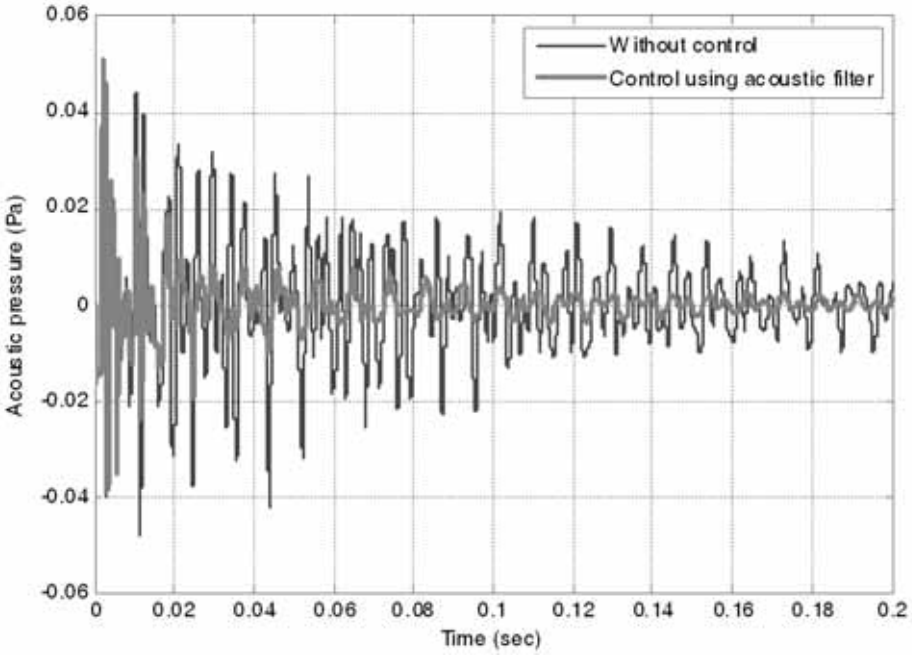

Fig. 7. Acoustic nodal pressure at node number 1941

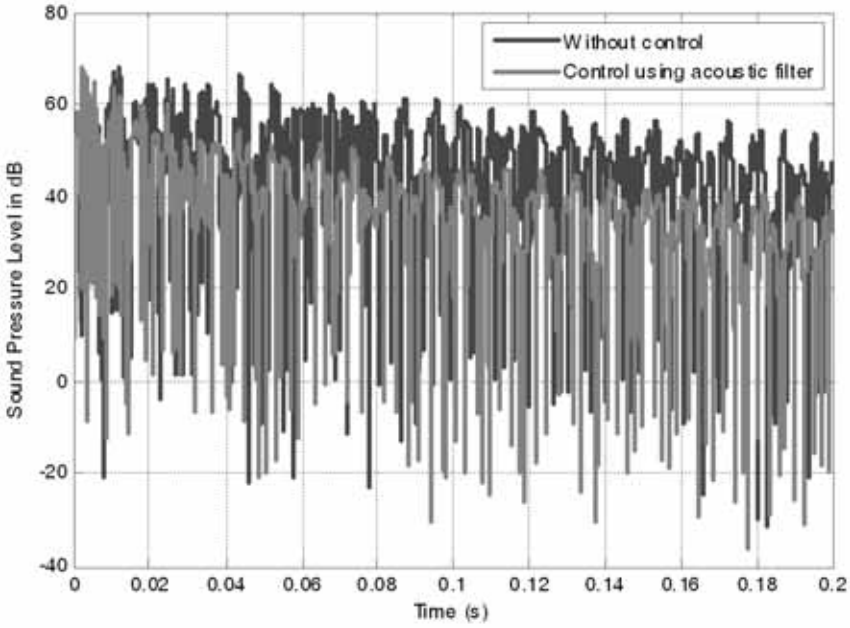

Fig. 8. Sound pressure level (dB) at node number 1941

5. CONCLUSIONS

In this paper two LQR based active structural acoustic control strategies are presented. In the first strategy, an LQR objective function is framed in order to minimize the structural vibrations along with the control effort. In this strategy two weighting schemes are used. The first weighting scheme weighs equally all the structural modes in the frequency range of interest, while the second weighting scheme weighs them in proportion to their coupling with the acoustic modes. It is seen that this weighting scheme is much more effective in achieving noise reduction as it utilizes the control effort in a more effective and an optimal manner. In the second control strategy, LQR cost function is designed to minimize the acoustic potential energy inside the cavity along with the control effort. An acoustic filter is used to indirectly sense the acoustic potential energy. It is seen that the second and fourth mode are not much affected after control. Further studies are required to optimally locate the piezoelectric transducers by taking into account structural-acoustic coupling.

6. ACKNOWLEDGEMENT

The financial support for this work under the project DARO/08/1051606/M/I provided by Aeronautics Research and Development board (Structures panel), Defense Research and Development Organization, Government of India, is gratefully acknowledged.

7. REFERENCES

[1] D.S. LI and L.CHENG, 2010. The design of synthesized structural acoustic sensors for active control of interior noise with experimental validation, *J. Sound Vib.*, **329**, 123-139.

[2] F. FAHY and P. GARDONIO, 1987. Sound and structural vibration: Radiation, Transmission and Response, Academic press, London.

[3] R. L. CLARK and C. R FULLER, 1992. Modal sensing of efficient acoustic radiators with polyvinylidene fluoride sensors in active structural acoustic control approaches, *J. Acoust. Soc. Am.*, **91**, 3321-3329.

[4] C. K. SONG, J. K. HWANG, J. M. LEE, and J. K. HEDRICK, 2003. Active vibration control for structural-acoustic coupling system of a 3-D vehicle cabin model, *J. Sound Vib.*, **267**, 851-865.

[5] S. D. SNYDER and C. H. HANSEN, 1994.The Design of systems to control actively periodic sound transmission into enclosed spaces, Part I: Analytical Models, *J. Sound Vib.*, **170**, 433-449.

[6] B. S. CAZZOLATO and C. H. HANSEN, 1998.Active control of sound transmission using structural error sensing, *J. Acoust. Soc. Am.*, **104**(5), 2878-2889.

[7] S.K. LAU and S.K.TANG 2001. Sound fields in a rectangular enclosure under active sound transmission control, *J. Acoust. Soc. Am.*, **110**(2), 925-938.

[8] A. KUMAR and S.V. MODAK, 2014. Virtual sensing of acoustic potential energy through a Kalman filter for active control of interior sound, *proceedings of the 32nd IMAC, A conference and exposition on structural dynamics,* 221-241.

Journal of Acoustical Society of India : Vol. 42, No. 2, 2015 (pp. 95-111)

Simulations, Measurements and Auralisations in Architectural Acoustics

Jens Holger Rindel[1], Claus Lynge Christensen[1], George Koutsouris[1] and Mahavir Singh[2]

[1]Odeon A/S, Scion-DTU, Diplomvej, Building 381, DK-2800 Kgs. Lyngby, Denmark
[2]AUV Section, CSIR-NPL, New Delhi, India
e-mail: jhr@odeon.dk; mahavir.acoustics@gmail.com

[Received: 15.03.2014; Revised: 19.08.2014; Accepted: 22.09.2014]

ABSTRACT

Room acoustic computer modelling has become an important tool in the acoustical design of rooms, and also the range of applications has increased in recent years. Also the room acoustic measurement technique has developed significantly in recent years, *e.g.* by new methods in ISO 18233. Considering computer modelling as a simulated measurement means that there is a close connection to the measurement methods, particularly as laid down in the ISO 3382 series that covers performance spaces, open plan offices and ordinary rooms. With these new standards the number of room acoustic parameters has grown, so in addition to the traditional reverberation time there is today a rather long list of more specialised parameters. The parameters are used for the design specifications, for the simulations during the design, and finally for the verification measurements. In some projects with special acoustical demands the use of auralisation in the design phase has become a useful supplement to the calculated parameters. In this paper the advantages and weaknesses of room acoustic measurements compared to simulations are discussed, and the state-of the-art methods as implemented in the ODEON room acoustics software are briefly presented with some examples. The measured impulse response is often used as a true reference of a real room impulse response and geometrical acoustic simulations are considered to be only a crude representation of it. However, both approaches have their own challenges and limitations. Geometrical acoustic models do not include wave phenomena, such as interferences and diffraction, as they simplify sound propagation by rays. The advantages of acoustic simulations with such models include a perfectly omnidirectional and impulsive sound source, no distortion problems, full control of the background noise, and a well-defined onset time of the impulse response. On the other hand, impulse response measurements include wave phenomena, but they do have their own weaknesses, which may cause significant errors in the derivation of the ISO-3382 room acoustic parameters. Due to the presence of background noise in the measured impulse response it is difficult to evaluate which part of the impulse response is valid. In addition, the directivity of the sound source used for measurements often has strong lobes at high frequencies and distortion artefacts may cause errors in the derived results. In this paper simulated and measured parameters are compared in a number of well documented cases and the various sources of errors are discussed. It is concluded that doing room acoustic measurements correctly may be more difficult than it appears at first glance, and both measurements and simulations require high level acoustical qualifications by the operator.

1. INTRODUCTION

The measured impulse response is often used as a true reference of a real room impulse response and

geometrical acoustic simulations are considered to be only a crude representation of it. However, both approaches have their own challenges and limitations. Geometrical acoustic models do not include wave phenomena, such as interferences and diffraction, as they simplify sound propagation by rays. The advantages of acoustic simulations with such models include a perfectly omni-directional and impulsive sound source, no distortion problems, full control of the background noise, and a well-defined onset time of the impulse response. On the other hand, impulse response measurements include wave phenomena, but they do have their own weaknesses, which may cause significant errors in the derivation of the room acoustic parameters. When there are differences between measured and simulated room acoustic parameters it is not obvious which one is the most reliable.

2. ROOM ACOUSTIC PARAMETERS

The room acoustic parameters described in the international standard ISO 3382-1 [1] are the reference for objective evaluation of acoustics in rooms from impulse responses. Evaluation of some of the ISO 3382-1 parameters for performance spaces is an important part of an acoustic report for a new or existing hall. The parameters can be derived either by measuring the acoustic impulse responses of existing rooms or by means of simulation, *e.g.* with some of the available geometrical acoustics algorithms. Both measurements and simulations have their own strengths and limitations. In any case it is not the question whether to simulate or measure the parameters, indeed we need both. If the room does not exist yet, simulations are useful in order to predict and optimize the acoustics, and when the same room has been built measurements are useful for documentation. When an existing room is to be refurbished, measurement of acoustic parameters in the room is an invaluable input in order to objectively evaluate the acoustics under existing conditions and as input to the simulation process, so that the initial simulation model can be calibrated to best mimic the existing conditions before starting to simulate changes. Precision of measurements and simulations are equally important - indeed making decisions based on imprecise measurement results or calibrating a simulation model to fit imprecise measurement data is just as bad as imperfect simulations. This has been one of our major motivations for implementing robust measurement facilities into the ODEON Room Acoustics Software, which is not too sensitive to user interaction or measurement conditions.

Impulse response measurements are important for the analysis of the acoustics in any kind of room, small or large, simple or complex. An impulse response is simply the response of a room to a Dirac function emitted as a sound signal from a source. In principle more than one source can be used for the impulse response excitation, but for ISO 3382-1 measurements only one omni-directional source should be used. The ISO 3382-1 standard gives the framework for measurement of room acoustic parameters, but lacks detail on the requirements needed for derivation of certain room acoustic parameters as discussed by Hak *et al.* [2]. One of the major problems is the truncation of the impulse response at the correct time. Any recording of a room impulse response is likely to have a degree of background noise, due to the ambient noise in the room and / or to the noise of the measuring equipment. This background noise is visible at the cease of the impulse response and needs to be left out of the analysis. Otherwise the real energy decay in the room might be misinterpreted, often leading to longer reverberation times. The truncation according to ISO 3382-1 can be done manually, without any guidelines given. This can be a source of serious errors, if not performed carefully for the different octave bands considered.

Another important aspect in the post-processing of an impulse response is correct detection of the onset time, i.e., the arrival of direct sound from the source to the receiver - this is tricky as the real life sound source will not produce a perfect Dirac function. Careless post-processing can result in large differences between measured and simulated results for parameters such as clarity C_{80} [1, eq. (A.10)], which is the ratio of energy in the impulse response before and after a time limit of 80 ms:

$$C_{80} = 10 \cdot \lg \frac{\int_0^{80\,\mathrm{ms}} p^2(t)\,\mathrm{d}t}{\int_{80\,\mathrm{ms}}^{\infty} p^2(t)\,\mathrm{d}t} \quad \text{(dB)} \tag{1}$$

where $p(t)$ is the sound pressure as a function of time t in the impulse response.

In this paper a selection of the most important ISO 3382-1 parameters is investigated in terms of *measurements* and *simulations*. The differences are discussed and their significance is concluded within the frame of the corresponding Just Noticeable Difference - JND. Table 1 shows the parameters used in the present study, together with the respective JND. Both *measurements* and *simulations* are carried out with the ODEON Room Acoustics Software, version 12.1.

Table 1. Room Acoustic Parameters investigated in this paper. All parameters are derived by formulas given in the ISO 3382-1 standard [1]

ISO 3382 Parameter	Symbol	Subjective Limen
Early Decay Time	*EDT* [s]	5%
Reverberation Time (20 dB range)	*T20* [s]	5%
Reverberation Time (30 dB range)	*T30* [s]	5%
Clarity (50 ms)	*C50* [dB]	1 dB
Clarity (80 ms)	*C80* [dB]	1 dB
Definition	*D50*	0.05
Centre Time	*Ts* [s]	10 ms
Sound Strength	*G* [dB]	1 dB

3. COMPARISON OF MEASUREMENT AND SIMULATION TECHNOLOGY

In contrast to impulse response simulations, measurements may be considered accurate in a broader frequency range due to the actual representation of wave phenomena (interaction due to phase shifts, diffraction etc.). Input data such as *absorption* and *scattering* coefficients are inherent and the room geometry is fully included by definition. On the other hand, a group of limitations, such as imperfect omni-directional sources, presence of background noise and distortion due to the loud-speaker and the filtering required impose errors in the final results. Table 2 summarizes the facts associated with existing measurement and simulation processes. The main issues for measurements are those related to the sound source and the background noise. For the simulations the most important issues are the uncertainly of material data and the approximation of the wave phenomena.

Table 2. Facts associated to measurements and simulations.

Facts	Measurements	Simulations
Room geometry	Fully included by definition	Approximated
Alteration of room geometry	Difficult	Easy
Wave phenomena (phase information, diffraction)	Fully included - inherent in the real sound field	Approximated with varying accuracy
Wall properties	Fully included - inherent in the real room	Absorption - scattering coefficients have to be measured or estimated, with limited accuracy
Air absorption (a function of temperature and humidity)	Fully included but may vary significantly in different measurements	Calculated, but very accurate
Source directivity	Not perfect: Lobes at high frequencies	Perfectly omni-directional

Table-2 Conted.....

Facts	Measurements	Simulations
Dynamic range of source	Insufficient at very low and very high frequencies. Distortion at high levels	Unlimited dynamic range at all frequencies. No distortion
Calibration of source	Special procedure needed for the strength parameter, *G*	Perfect per definition
Background Noise	Limits the dynamic range, compensation necessary	Not present
Microphone directivity	Omnidirectional microphone. Some parameters require figure-of eight pattern or a dummy head	All directivities available
Results in octave-bands	Filtering is required, which alters the original signal	Results are derived directly in different bands - no alteration due to filtering
Onset time of impulse response	Critical, especially at low frequencies	Perfect per definition
Reproducibility	Not perfect: Depends heavily on the source	Can be perfect, depending on the algorithm
Influence of operator	Knowledge and experience important	Knowledge and experience very important

4. SIMULATING THE ROOM IMPULSE RESPONSE

Simulations in room acoustics are well known to provide fast and effortless estimation for the ISO 3382 parameters. They are mainly based on geometrical acoustic algorithms which simplify the wave phenomena to fundamental geometrical tasks. Phase information is generally excluded, so that the results can be considered valid for frequencies above Schroeder's limiting frequency [3]: $f_S = 2000\sqrt{(T/V)}$ Hz, where T is the reverberation time in seconds and V is the volume in m^3. Below this limit the modes in a room are very distinct and prominent, but cannot be accurately predicted, due to the lack of phase information. On the other hand, above f_S a high modal overlap is present, so that wave effects due to phase can be neglected without significant loss of information for the acoustic field. Despite their simplified approach, geometrical acoustic simulations are invaluable for predicting the ISO 3382 parameters in a wide variety of rooms, from offices and music studios to auditoriums and concert halls. Even though simulations offer a simplified approach of a real-world sound field they still have a number of advantages over measurements: The source is perfectly omni-directional, there are no problems with distortion, there is no background noise so the dynamic range is infinite at all frequencies, no filtering is required and the results are reproducible if the stochastic nature of the algorithm used is eliminated (deterministic ray tracing [4]).

4.1 Modelling the room and acoustic properties of materials

The basis for simulating the impulse response is the digital model of the room. This implies that the geometry of the room is simplified, sometimes to make a very rough room model only representing the main shape of the room, and in other cases being a rather close approximation, if created directly from the architect's 3D model. However, because of the wavelength of audible sound, the degree of geometrical detail in the room model is generally not the main source of uncertainty in the simulations. The acoustical data representing the materials, i.e. the *absorption coefficients* (*á*) and the *scattering coefficients* (s) are often more important for the uncertainty. The available data for a well-defined highly absorbing material, which has been tested in the laboratory, come with a significant uncertainty (see Table 3 and Table 4).

Table 3. Uncertainty of measured absorption coefficients.

Frequency, Hz	125	250	500	1000	2000	4000
Type A mounting, α (mean)	0,26	0,85	1,11	1,07	1.02	1,03
Standard deviation	0,070	0,051	0,030	0,040	0,046	0,047
Type E-400 mounting, α (mean)	0,64	0,78	0,98	1,06	1,06	1,06
Standard deviation	0,107	0,053	0,038	0,032	0,035	0,047
Average std.dev.	0,088	0,052	0,034	0,036	0,040	0,047
95% confidence range	± 0,18	± 0,10	± 0,07	± 0,07	± 0,08	± 0,09

Table 4. Estimated uncertainty of measured scattering coefficients

Frequency, Hz	125	250	500	1000	2000	4000
Assumed α_s	0,25	0,25	0,25	0,25	0,25	0,25
Assumed α_{spec}	0,29	0,33	0,59	0,74	0,83	0,87
s (example)	0,05	0,10	0,45	0,65	0,77	0,83
Standard deviation, δ_s	0,04	0,04	0,04	0,04	0,04	0,07
95% confidence range	± 0,08	± 0,08	± 0,08	± 0,08	± 0,08	± 0,14

The standard deviation on absorption coefficients is the *Inter-laboratory reproducibility* from a Round Robin in 2002 organized by ASTM [5] with 16 participating laboratories. Two different test samples were applied, a 51 mm thick glass fibre panel, which was either laid directly on the floor (Type A mounting) or suspended 400 mm from a rigid surface (Type E-400 mounting). The mean value and the standard deviation between the 16 laboratory results are given in Table 3.

Looking at the 1 kHz octave band as an example, the absorption coefficient reported from a laboratory test has a 95% confidence range of ± 0.07, which means that with 95% probability the true value is within this range. In other words, there is a 5% risk that the true absorption coefficient deviates more than 0.07 from the measured value. At 125 Hz the 95% confidence range is even higher: ± 0.18. This clearly shows that the absorption data represents a significant source of uncertainty in any room acoustic calculation, including the traditional use of Sabine's equation.

The uncertainty on the scattering coefficient is also worth noting, although the influence on the uncertainty of the calculation results may be less dramatic as for the absorption. The standard deviation on scattering coefficients has been calculated here using equation (A5) found in ISO 17497-1 [6] and applying data on the *Intra-laboratory repeatability* on the measurement of absorption coefficients also reported in [5]. For the purpose of the calculations a typical set of scattering coefficients have been applied, having $s = 0.50$ at the mid-frequencies (between 500 and 1000 Hz).

Looking at the influence of scattering on the simulated room acoustic parameters, high scattering coefficients above 0.40 tend to give approximately the same results. However, low scattering coefficients in the range from 0.00 to 0.10 can have a very strong influence on the calculation results, and thus should always be regarded carefully. In fact, it is recommended to look at the scattering coefficients in a logarithmic scale; for example the following steps in scattering coefficient are approximately of equal importance: 0.40 – 0.20 – 0.10 – 0.05 – 0.025 – 0.0125. Finally, the quality of a simulation result is influenced by the knowledge and experience of the user. This is particularly important in relation to the input data for the materials.

4.2 Calculation of the impulse response

Although geometrical models for room acoustic simulation can be a fairly complicated matter, it is much easier to derive ISO 3382-1 parameters from such a simulation than it is from a real impulse response measurement: 1) the onset time of the impulse response is well defined from geometry, 2) there is no need for digital filtering which may blur octave band results in the time domain and 3) background noise is not a problem. Two types of parameters shall be described shortly. *Decay parameters* such as T_{30} and *time interval parameters* such as C_{80}.

ODEON makes use of hybrid calculation methods which is based on a combination of the *image source method* and a special *ray radiosity* method in order to predict arrival times of reflections at a receiver and the strength of reflections in octave bands [4]. The calculation methods are energy based, so adding the octave band energy to a time histogram forms directly the squared impulse response which is needed in order to derive parameters such as T_{30} and C_{80}, without the need for any digital filtering. The length of the impulse response predicted is usually limited by maximum path length for which the rays are traced. The early part of the response (early reflections) is determined by a list of image sources up to a certain transition order, typically 2nd order. For higher order reflections a Fibonacci-spiral shooting of rays is initiated, resulting in a large number of reflection points, distributed on the surfaces of the room. Each point is replaced by a *secondary source*, which radiates sound according to the relative strength and delay of the corresponding reflection. An algorithm called *reflection and vector based scattering* uses as input data the scattering coefficient of the surface, the distance between the present and the previous reflection points, as well as the angle of incidence, to produce a unique directivity pattern for the secondary source [4]. Once all image and secondary sources have been detected, the energy information they carry can be collected from all visible receivers in the room, effectively leading to a squared impulse response.

4.3 Deriving decay parameters

Decay parameters, such as T_{30}, can be derived from the *squared impulse response*. The ISO 3382-1 standard describes that T_{30} can be derived in the following way: The decay curve is the "graphical representation of the sound pressure level in a room as a function of time after the sound source has stopped" (interrupted noise assumed). The decay curve can also be derived from an impulse response measurement using Schroeder's backwards integration [7]. This backwards integrated decay curve, derived from an impulse response, corresponds to the decay curve obtained from the decay of interrupted noise – taking the average of curves from an infinite number of measurements:

$$E(t) = \int_{t}^{\infty} p^2(\tau)\,\mathrm{d}\,\tau = \int_{\infty}^{t} p^2(\tau)\,\mathrm{d}(-\tau) \tag{2}$$

where $p(\hat{o})$ is the sound pressure as a function of time in the impulse response.

One problem with the backwards integration is that some energy is not included in the real impulse response due to its finite length t_1. The problem can be corrected by estimating the energy that is lost due to the truncation. This amount of energy can be added as an optional constant C, so Eq. (2) changes to:

$$E(t) = \int_{t_1}^{t} p^2(\tau)\,\mathrm{d}(-\tau) + C \qquad \text{where} \quad t_1 > t \tag{3}$$

If the curve is not corrected for truncation, the estimated decay time may be too short.

In Figure 1 is shown a simulated decay curve at 1000 Hz. The two blue curves are the squared impulse response in dB and the backwards integrated curve, respectively. The black curve is the backwards integrated curve which has been corrected for truncation. In order to derive a decay parameter, the appropriate range of the backwards integrated and corrected decay curve is evaluated and a least-squares fitted line is computed for the range. For T_{20} the range is from 5 dB to 25 dB below the steady state level and for T_{30} the range is from 5 dB to 35 dB below the steady state level. The slope of the fitted line gives the decay rate, d in dB per second, from which the reverberation time is calculated e.g. as $T_{30} = 60/d$.

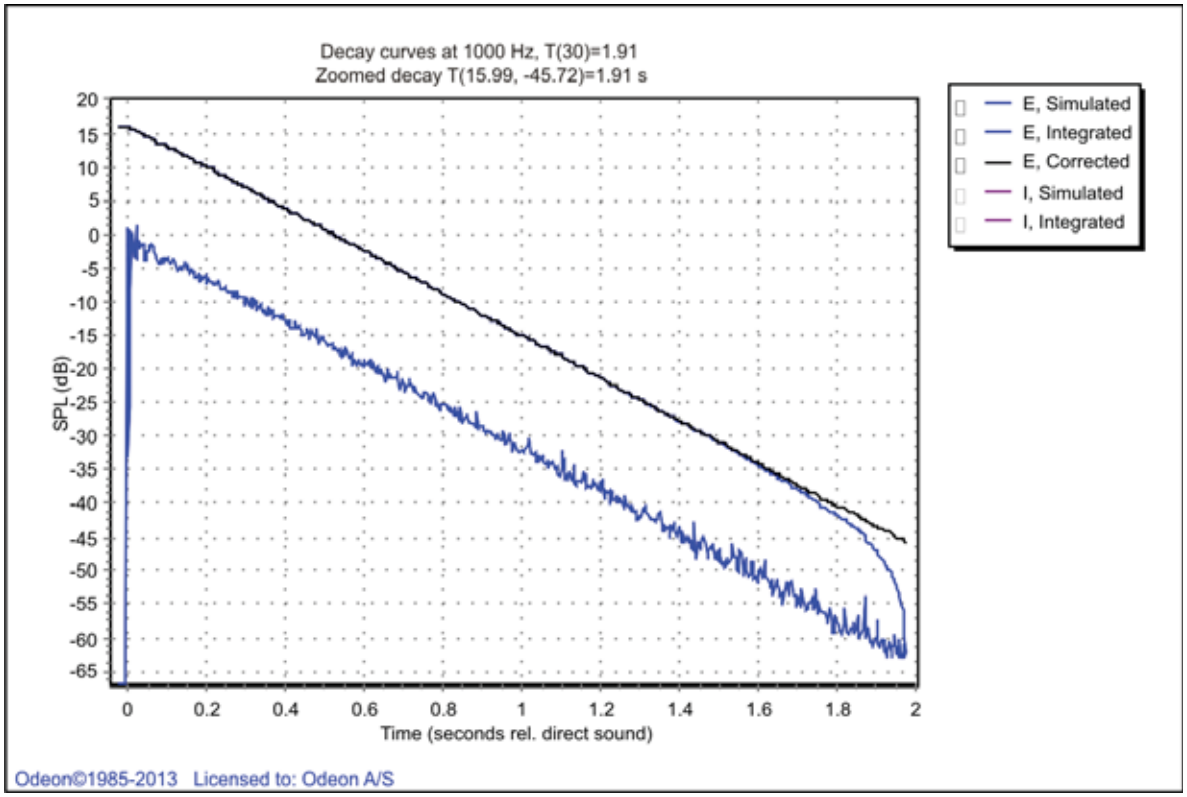

Fig. 1 : Example of simulated squared impulse response and integrated decay curve with and without correction for truncation.

4.4 Deriving time interval parameters

Parameters such as C_{80} make use of the energy arriving at the receiver in specific time intervals, relative to the direct sound. In the case of C_{80} the time intervals are from 0 to 80 ms and from 80 ms to infinity after the arrival of direct sound (see Eq. (1). In order to make a decent prediction of C_{80} it is important that the onset time is well defined. When the source is visible from the receiver this is not a problem as the onset time can be derived from source and receiver position and even in slightly coupled spaces this may be precise enough.

Measured time interval parameters may not be precisely derived if calculated directly from the filtered response, because filters create delay and smear the response in time. This can be particularly significant for the lower frequency octave bands where the filters are “long”. In order to bypass this filter problem, ISO 3382-1 suggests the “Window-before-filtering” approach which is the method implemented in ODEON. First the onset time is estimated from the broad band impulse response. In order to estimate the energy arriving for example during the first 80 ms, the response is gated from the onset time up to 80 ms and octave band filtered afterwards. This creates a filtered response which is longer than the original broad band response in order to include the filter tail. Then the energy of the gated filtered response is calculated including the tail of the filter, taking into account most of the smeared energy. Note that the C_{80} parameter may not make sense in a space where receiver and source positions are strongly decoupled as the build-up of the impulse response may take considerably longer than the 80 milliseconds.

4.5 Accuracy of a simulation due to number of rays and transition order

In order to derive a measure for the accuracy of the simulations, the global average deviation from measured results is considered. As the room acoustic parameters have different units (*e.g.* sec., dB, %) the deviation

between measured and simulated results is expressed in terms of JND. Then the global average of deviations from measurements is calculated like this:

$$Error = \frac{\sum_{n=1}^{N_{AP}} \sum_{i=1}^{N_{Freq}} \sum_{j=1}^{N_{Pos}} \frac{\left| AP_{measured}(n,i,j) - AP_{simulated}(n,i,j) \right|}{JND(n)}}{N_{AP} \cdot N_{Freq} \cdot N_{Pos}} \tag{4}$$

where

$AP_{measured}$ is the measured value of acoustic parameter n at frequency i and position j,
$AP_{simulated}$ is the simulated value of acoustic parameter n at frequency i and position j,
$JND(n)$ is the subjective limen (just noticeable difference) of acoustic parameter n,
N_{AP} is the number of acoustic parameters (5),
N_{Freq} is the number of frequency bands (3),
N_{Pos} is the number of source-receiver positions (10).

Figure 2 displays the results of the global average error for the auditorium, which is described in more detail later. Five acoustic parameters were considered: EDT, T_{30}, D_{50}, C_{80}, and T_S. The corresponding JND values are listed in Table 1. Three octave bands were used; 500, 1000 and 2000 Hz. Two source positions were combined with five microphone positions, i.e. in total 10, see Figure 7. The results show, that very good agreement is obtained with 5000 rays and transition orders 0, 1 or 2. The global average error is then

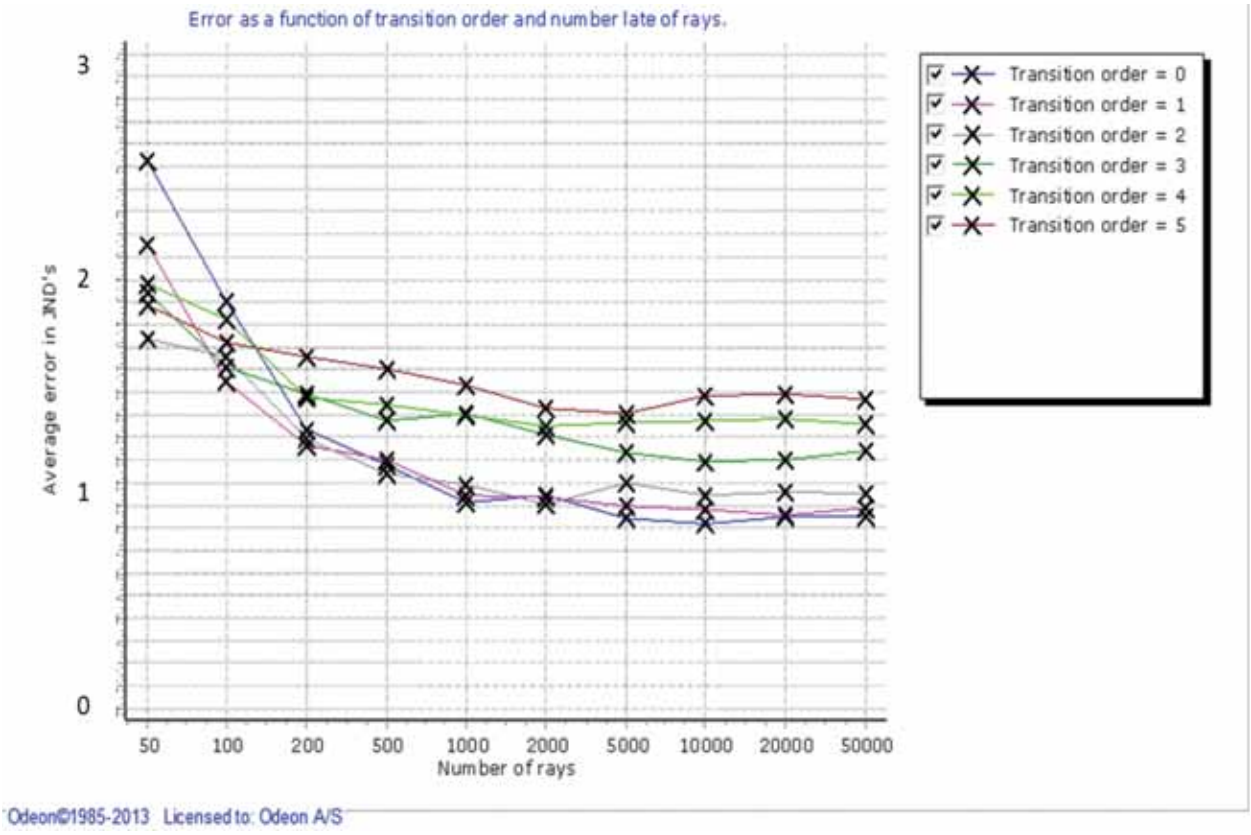

Fig. 2. Accuracy of calculations in the auditorium as a function of transition order TO and number of rays. The displayed parameter is the global average of deviations from measurements in units of JND for 5 parameters, 3 octave bands and 10 source-receiver positions.

around 1 JND. However, it is obvious that higher transition orders should be avoided. It is also seen that the results will not improve if more rays are used

4.6 Auralisation, how to explain room acoustics with sound

The room impulse response obtained from a simulation contains information about direction of incidence of each sound reflection in the 3D space. This means that the impulse response can be transferred to a so-called binaural room impulse response (BRIR) by means of a head related transfer function (HRTF). An example is shown in Figure 3. By convolving the BRIR with a sound recording (preferably from an anechoic environment), the resulting two-channel sound file, when presented through headphones, can give the impression of listening in the chosen receiver position the simulated (virtual) room. This is *auralisation*.

Auralisation can be used as a tool during the design process, and this can be particularly useful in order to avoid acoustical defects in the room design [8]. The technique has been further developed to the advanced *multi-channel*, *multi-source* auralisation, which may produce a highly realistic simulation of an orchestra in a concert hall [9].

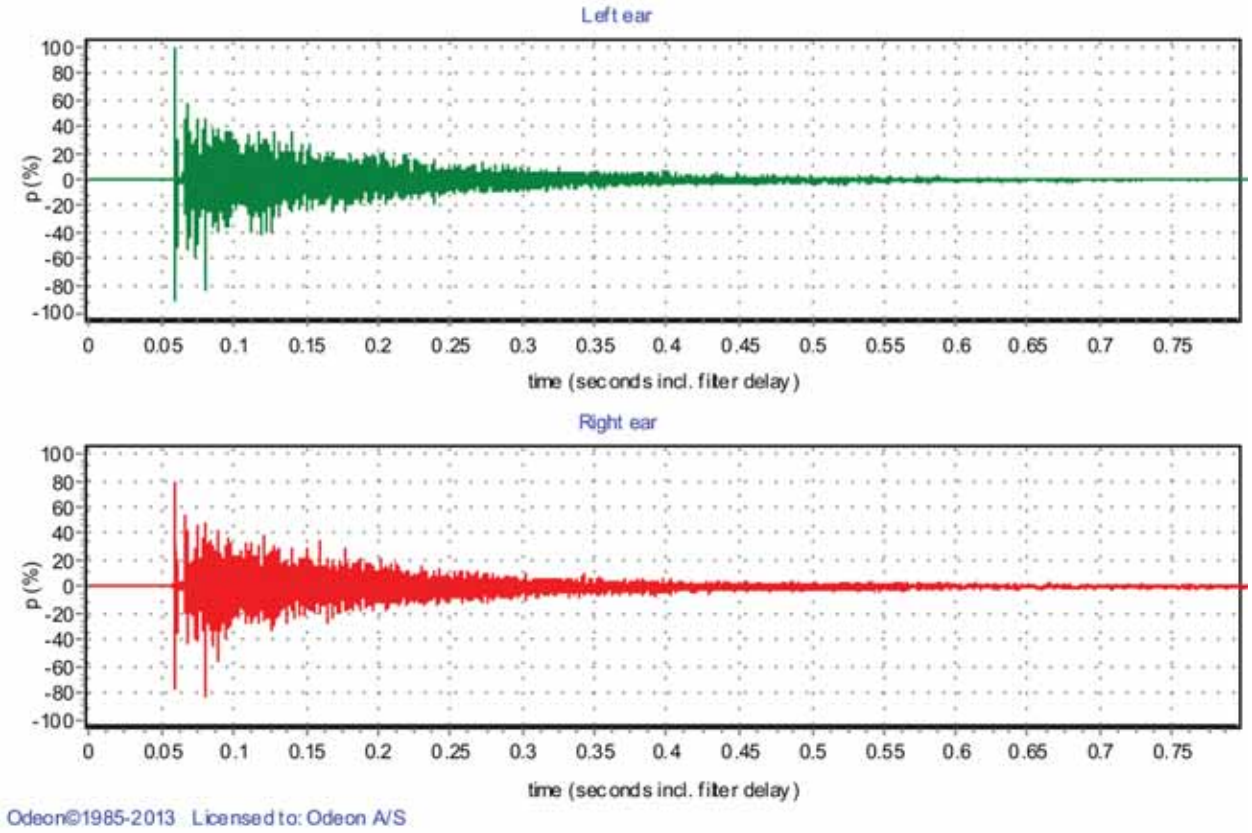

Fig. 3: Example of calculated binaural room impulse response (BRIR) that can be used for auralisation. Upper part is for the left ear and lower part for the right ear. In this example the BRIR is 1500 ms long, but zoomed to show the first 80 ms.

5. MEASURING THE ROOM IMPULSE RESPONSE

An impulse response can be obtained directly by recording the response to hand-clapping, popping of a balloon / paper-bag, a gunshot or even a hard footstep. As a modern alternative an impulse response can be obtained indirectly by producing a Maximum Length Sequence (MLS) or a sweep signal using an electro

acoustic source. The latter methods stretches the impulse (Dirac function) in time and the measured response is deconvolved in order to form the impulse response. Using time stretched excitation, a substantial amount of energy is emitted from an electro acoustic source with limited maximum acoustic output, allowing superior signal to noise ratio. Reproducibility is also easier to control with electro-acoustic stimuli, due to uniform radiation.

Among the many available measurement methods the preferred one today is the swept sine method using a rather long exponential sweep from very low to very high frequencies [10, 11]. This method can produce impulse responses with very good dynamic range and the harmonic distortion by the loudspeaker is separated from the true impulse response, since it will appear at negative arrival times, i.e. before the onset of the impulse response [11]. Still there can be some influence from non-harmonic distortion [12, 13], so a high quality loudspeaker and power amplifier is important.

5.1 Capturing the impulse response

The sound source is a critical part of the measuring chain. For the measurement of the ISO 3382 room acoustic parameters the source must be as omni-directional as possible. The most common choice is a *dodecahedron* source, *i.e*. a source with 12 loudspeaker units pointing in different directions. The directivity pattern for such a source is reasonably omni-directional at low and mid frequencies, but at 2000 and 4000 Hz the directivity is not perfect (typical variations between max. and min. are 5 – 7 dB).

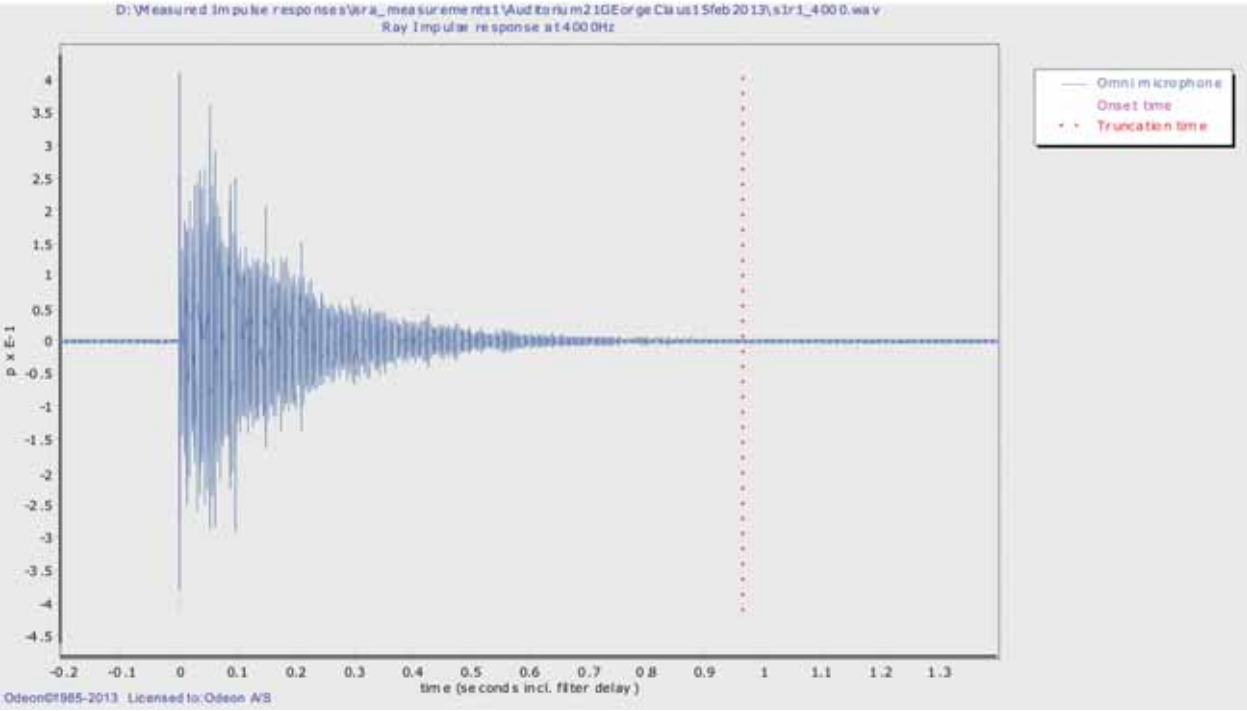

Fig. 4. Impulse response obtained with the sweep method in ODEON. Combination S1-R1 at 4000 Hz .in the auditorium described later.

5.2 Filtering the impulse response

The octave-band filters typically used in the processing of room impulse responses are 2nd order Butterworth filters in accordance with the IEC 61260 [14]. These analogue filters can be implemented using digital infinite impulse response (IIR) filters. ODEON uses such type of filters and defines a finite *effective length*, allowing 99.9% of the energy in the tail of the filtered impulse response to be included. The filtering process

introduces unwanted transient effects in the beginning of the response, which cease after about one effective length of the filter.

A *reverse* filtering algorithm is applied for decay analysis so that all the transients are re-positioned at the tail of the impulse response. ODEON automatically excludes this transient tail when processing the impulse response. The *reverse* method has also the advantage of eliminating the *stretching* of the filtered signal, which occurs due to the delay of the filter itself. This *stretching* effectively leads to energy smearing, altering the slope of the decay curve. After processing the signal with *reverse* filtering, an extra *forward* filtering is applied, allowing for suppression of phase distortion. This combination of *reverse-forward* filtering in the decay analysis is used for the calculation of *decay parameters*, such as T_{30}. For the *time interval parameters* only *forward* filtering is applied for each gated window. The smearing of the energy is precluded by taking into account the effective length of the filter at the end of each window, as extra impulse response time.

5.3 Noise floor and truncation of the impulse response

When measuring an impulse response the dynamic range is limited by background noise which may influence all parameters that can be derived from the impulse response significantly if its level isn't very low or compensated for. At some time after the onset time the impulse response will decay to the level of the noise floor and the rest of the recorded response is not valid – this time we denote *truncation time*. The Truncation time is unique to each band of interest. The energy of noise arriving after the Truncation time should be excluded from analysis; however energy before it is also influenced by noise. Most of the impulse response recordings, whether recorded directly or obtained using the sweep method, come with a noticeable noise tail, due to the ambient background noise and noise of the transmission line involved (PC sound card, cables and microphone). This noise tail should be removed before deriving the decay curve and the ISO 3382 room acoustic parameters. Lundeby *et al.* [15] have proposed an algorithm for detecting the noise floor and truncating the recording at the cross-point between the pure impulse response and the noise floor. The cross-point is estimated by an iteration process of impulse response smoothing and regression line fitting. The ODEON measurement system utilizes a modification of this method in order to estimate the appropriate truncation time for each octave-band.

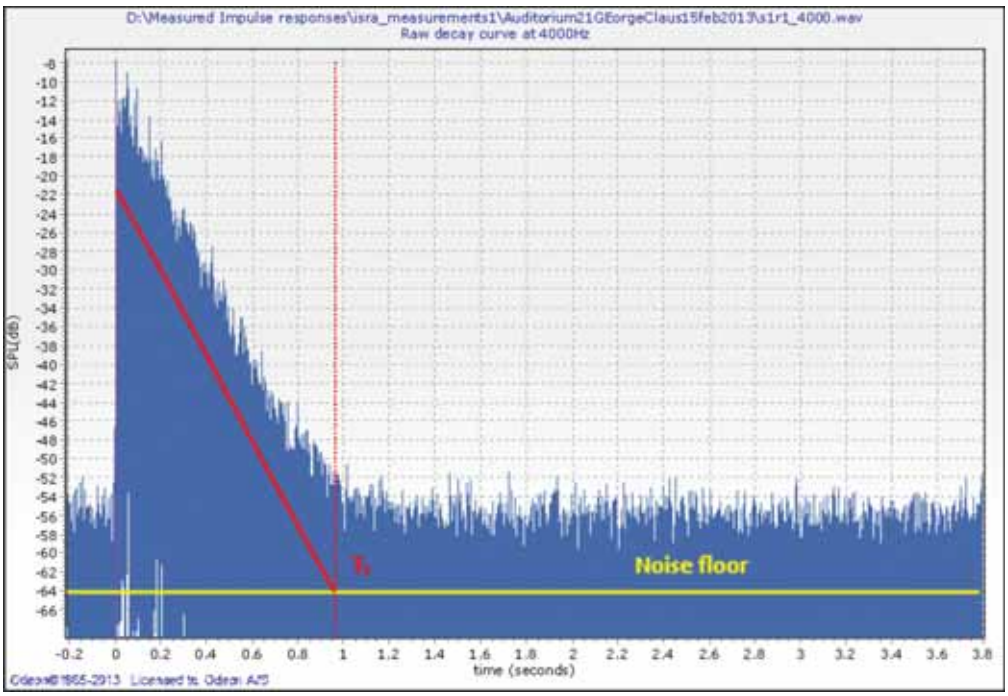

Fig. 5: Example of squared impulse response with indication of noise floor and truncation time *Tt*.

Still the background noise is present in the backwards integrated decay curve in the range be-tween the onset time and the truncation time and this will result in an over-estimation of the decay time when the energy contained in the noise floor is not negligible. However this may also be com-pensated for if the level of the noise floor is well estimated. In addition to the tail correction it is suggested that the background noise floor excluding the truncated tail can be subtracted from the valid part of the squared impulse response.

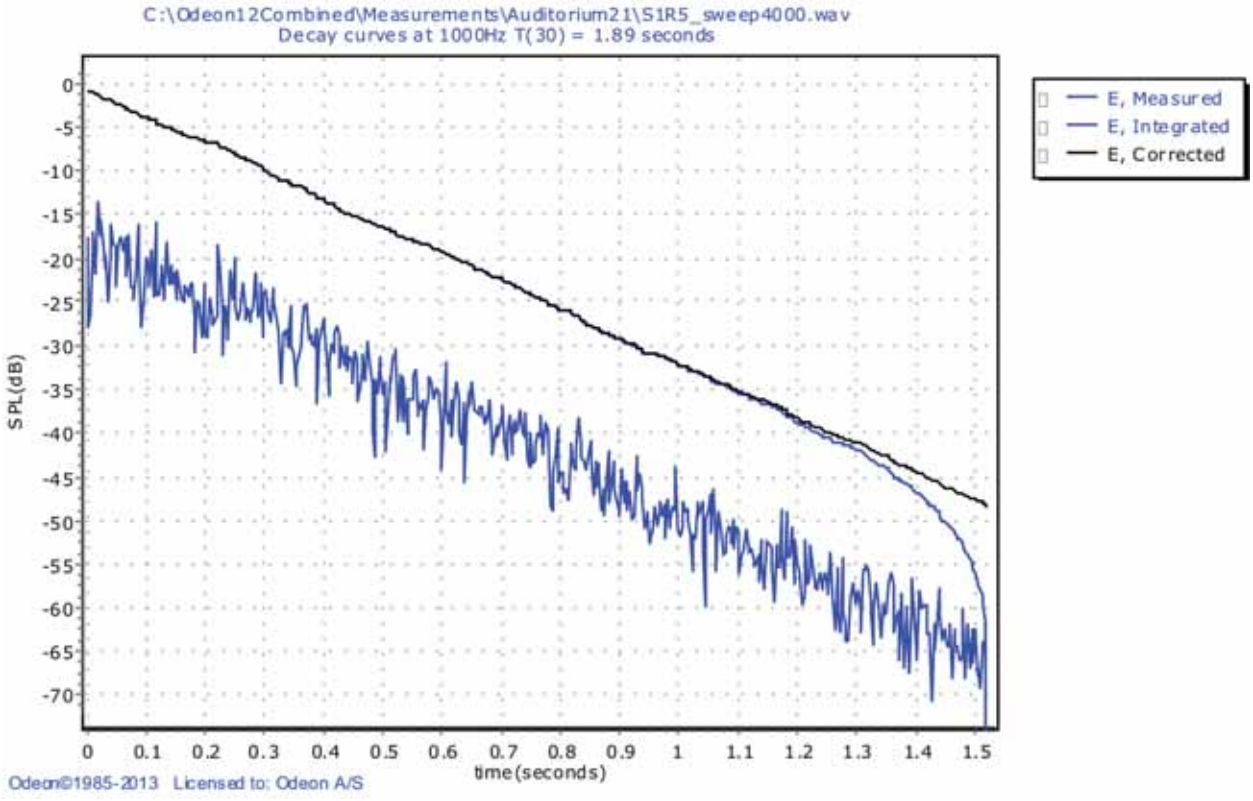

Fig. 6 : Example of measured squared impulse response curves and integrated decay curves.

6. EXAMPLE, MEASURING AND SIMULATING AN AUDITORIUM

6.1 Description of the room

The room which is used as an example for both simulations and measurements is Auditorium 21 located at the Technical University of Denmark. The volume is approximately 1160 m^3 and it has a capacity around 200 people.

The materials are mainly wood panels, glass, gypsum board and hard rows of chairs. The model shown in Figure 7 shows the absorption characteristics of the surfaces by the use of Acoustic Colours, a method introduced in ODEON in 2001 [16].

6.2 Measurements with varying the sweep length

For the combination P1-R5 the different impulse responses were obtained with sweep lengths of 0.5, 1, 2, 4, 8, 16 and 32 sec in order to evaluate whether the signal to noise ratio (S/N) increases by 3 dB per doubling of sweep length, as expected, and to evaluate the impact on derived values of T_{30}. These measurements were performed at very low level in order to obtain a wide span of S/N levels in the recorded impulse responses. The values of D_{50} and C_{80} only showed small differences with increasing sweep lengths. T_{30} did show some changes with increasing sweep lengths. Three approaches for deriving T_{30} were tested: 1) T_{30}

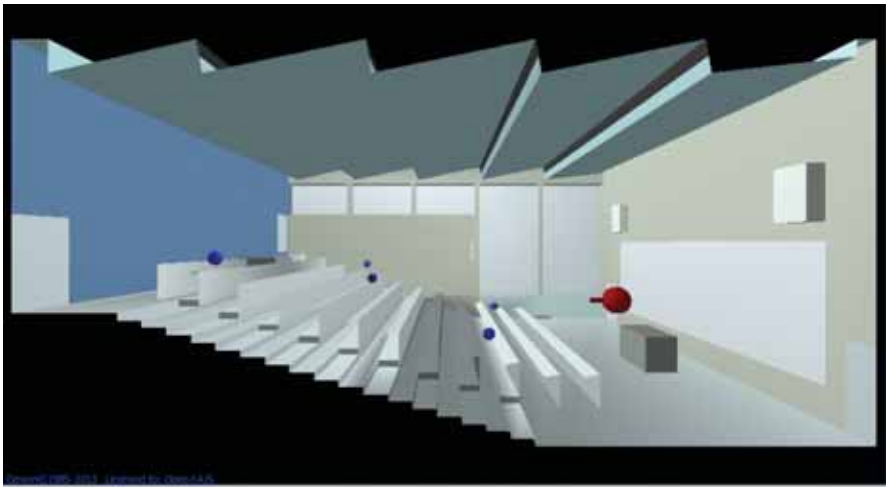

Fig. 7 : View into the 3D model of the auditorium. Blue spots mark the receiver positions and the red spot is one of the source positions.

derived directly from the backwards integrated curve with no corrections, 2) T_{30} derived from the curve with correction for truncation according to Eq. (3) and finally 3) T_{30} derived from the curve with correction for truncation, as well as correction for noise floor in the valid part of the impulse response.

In Figure 8 it can be seen that for long sweep lengths / high dynamic range all three methods agree that T_{30} is 1.89 *s*. When T_{30} is derived without compensation for truncation of the impulse response, the values derived are too high. If compensating for the truncation of the impulse response only, T_{30} tends to be too long. However, when the backwards integrated curve is compensated for background noise, the result is more stable even for rather short sweep lengths and closer to the "correct" value. This is the method implemented in ODEON 12.1.

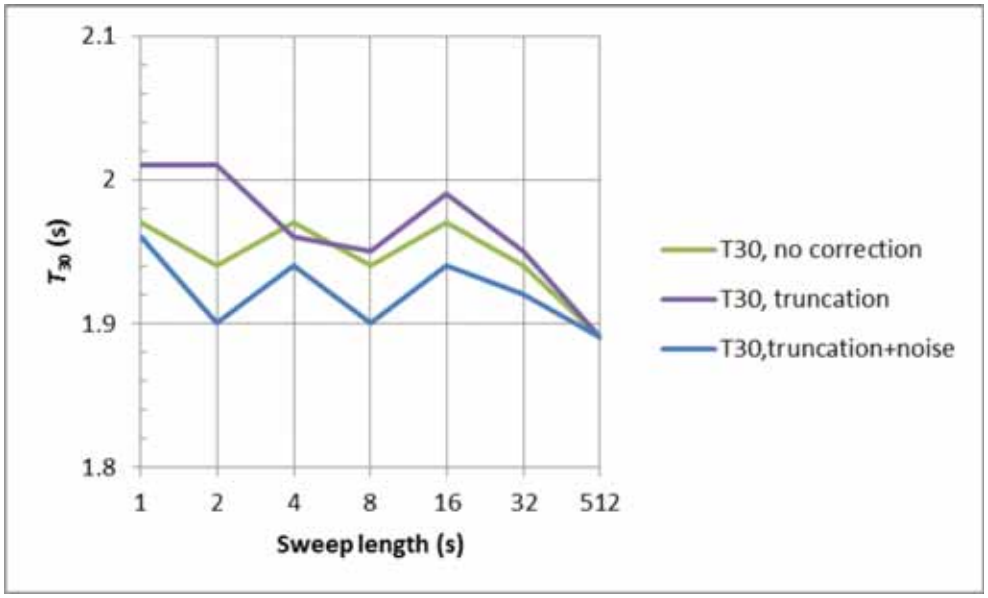

Fig. 8 : $T_{30,\ 1000\ Hz}$ derived from measured impulse responses with increasing sweep lengths and with and without correction for impulse response truncation and noise floor.

6.3 Comparison of measured and simulated results

In Figure 9 measured and simulated values of EDT, T_{30}, SPL (the G value with a source power level of 31 dB), T_S, C_{80} and D_{50} are displayed for source position P1 and five receiver positions at 1000 Hz. It should be noted that the absorption data in the model were adjusted in order to get close agreement in T_{30}, results. But it is interesting to look at the other room acoustic parameters.

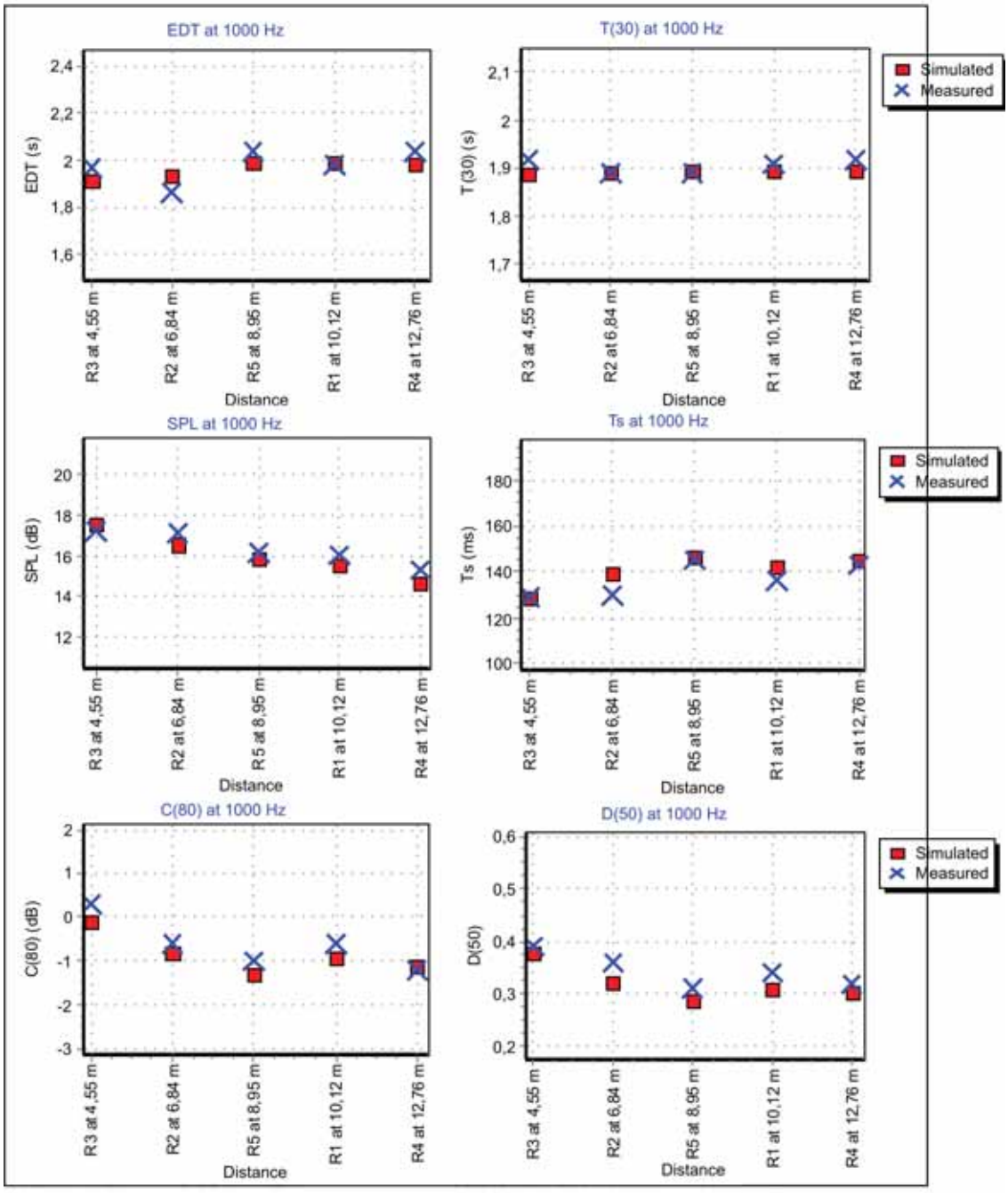

Fig. 9: Simulated and measured room acoustic parameters for the five receivers in audito-rium 21. Simulated parameters displayed with *red squares* and measurements with *blue crosses.*

The agreement between measured and simulated parameters at 1000 Hz is within 0.5 JND for most parameters, which is very satisfactory. The difference between measured and simulated EDT varies from 0.01 to 0.07 seconds with an average deviation of 0.52 JND. It is interesting to see that both measured and simulated values of EDT (1.98 and 1.96 seconds) are marginally higher that T_{30} (1.89 and 1.91 seconds) so this undesired feature of the room is detected in simulations as well as in the real room. Values of measured and simulated SPL, *T*s, C_{80} and D_{50} are all in good agreement - and measured and simulated values agree on the variation with position.

6.4 Uncertainty of receiver position

In practice it is not possible to position the microphone (nor the source) at an exact position when conducting room acoustic measurements. So, if reproducing the measurement at a later time slightly different results in terms of ISO3382-1 parameters should be expected. When a person is sitting in the auditorium the position will not be exact either. In order to give an idea of the uncertainty of measured parameters if the receiver position is not exact, measurements in a region close to receiver position 5 in the middle of the audience area were repeated with position offsets 30 cm right, 30 cm left, 15 cm front, 15 cm back, 10 cm up, and 10 cm down - a total of 7 positions including the original position. The graph below (Figure 10) shows statistics for the 7 positions for the parameter C_{80}, which is chosen as an example. Measured as well as simulated results are included for com-parison. As can be seen the simulated values in receiver positions that are close to each other only show minor deviations, much less than deviations between the measured results, probably because phase is not included in the simulation model.

At 1000 Hz *none* of parameters have a standard deviation larger than 0.7 when normalized to Just Noticeable Differences (JND) and even at 125 Hz all parameters except SPL have a standard deviation less than 1.2 JND's.

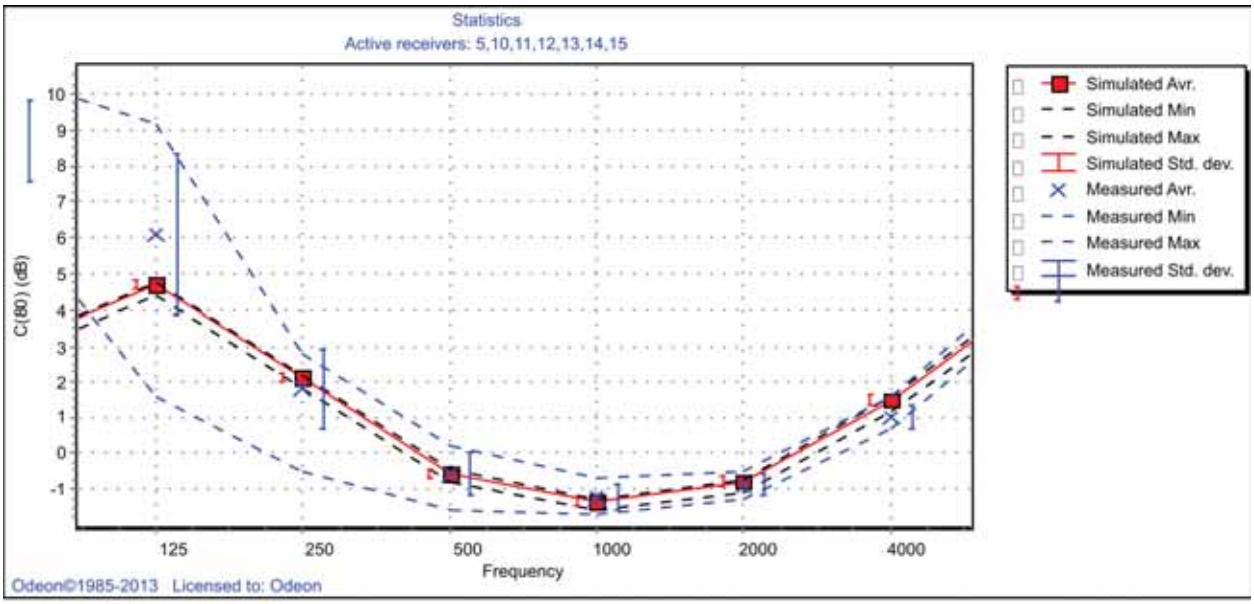

Fig. 10: Uncertainty due to receiver position, simulated and measured variation of the Clarity C80 in seven positions close to receiver 5 in the auditorium.

7. CONCLUSION

Both simulations and measurements have strengths and weaknesses. The most important reasons for uncertainty in simulations are the input data for absorption and scattering of the surfaces and the rough approximations of wave phenomena like diffraction and scattering.

The main reasons for unreliable measurements are due to the sound source; the dynamic range is limited and the loudspeaker may create distortion that have an unwanted influence on the measurements. At high frequencies (2 kHz and above) the commonly used dodecahedron source has a directivity that is far from omnidirectional. For some parameters like C_{80} the correct setting of the onset time in the impulse response is critical. Truncation of impulse responses and background noise in impulse responses may lead to systematic errors on T_{30} if not compensated for. However, if compensating for both errors, correct results may be achieved even with moderate signal to noise ratios.

Deviation was not larger than 0.7 JND for measurements of any of the ISO 3382-1 parameters tested at 1000 Hz when using 7 different positions within a volume of (w, l, h) = (0.6, 0.3, 0.2) metres around a central position in an auditorium – this indicates that the results can be reproduced even if the receiver position is not exact. For simulation results in ODEON it seems that small deviations at the position are negligible.

It is possible to simulate and measure accurately the room acoustic parameters according to ISO 3382-1 if care is taken in the implementation and use of simulation and measurement algorithms. In the auditorium example used here there is close agreement between measured and simulated values.

8. REFERENCES

[1] ISO 3382-1, 2009. *Acoustics - Measurement of room acoustic parameters - Part 1: Performance spaces*, International Organization for Standardization, Geneva.

[2] C.C.M. HAK, R.H.C. WENMAEKERS and L.C. LUXEMBURG, 2012. Measuring Room Impulse Responses: Impact of the Decay Range on Derived Room Acoustic Parameters, *Acta Acoustica united with Acustica*, **98**, 907-915.

[3] M.R. SCHROEDER, 1962. Frequency correlation functions of frequency responses in rooms, *J. Acoust. Soc. Am*, **34**, 1819-1823.

[4] C.L. CHRISTENSEN, 2013. *ODEON Room Acoustics Software, Version 12, User Manual*, Odeon A/S, Kgs. Lyngby.

[5] A. NASH, 2010. On the reproducibility of measuring random incidence sound absorption, Paper 2aAAp5, *162nd ASA Meeting*, 2010, San Diego.

[6] ISO 17497-1, 2004. *Acoustics - Sound-scattering properties of surfaces - Part 1: Measurement of the random-incidence scattering coefficient in a reverberation room*, International Organization for Standardization, Geneva.

[7] M.R. SCHROEDER, 1965. "New method of measuring reverberation," *J. Acoust. Soc. Am.*, **37**, 409-412.

[8] J.H. RINDEL, 2004. Evaluation of room acoustic qualities and defects by use of auralization. *148th Meeting of the Acoustical Society of America*, San Diego, Paper 1pAA1 (16 pages).

[9] M.C. VIGEANT, L.M. WANG and J.H. RINDEL, 2008. Investigations of orchestra auralizations using the multi-channel multi-source auralization technique. *Acta Acustica/Acustica*, **94**, 866-882.

[10] ISO 18233, 2006. *Acoustics - Application of new measurement methods in building and room acoustics*, International Organization for Standardization, Geneva.

[11] S. MÜLLER and P. MASSARANI, 2001. Transfer-Function Measurement with Sweeps, *J. Audio Eng. Soc.*, **49**, 443-471.

[12] A. TORRAS-ROSELL and F. JACOBSEN, 2011. A new interpretation of distortion artifacts in sweep measurements, *J. Audio Eng. Soc.*, **59**, (5), 283-289.

[13] D. CIRIC, M. MARKOVIC, M. MIJIC and D. SUMARAC-PAVLOVIC, 2013. On the effects of nonlinearities in room impulse response measurements with exponential sweeps, *Applied Acoustics*, **74**, 375-382.

[14] IEC 61260, 1995. *Electoacoustics - Octave Band and Fractional Octave Band Filters*, International Electrotechnical Commission, Geneva.

[15] A. LUNDEBY, T.E. VIGRAN, H. BIETZ and M. VORLÄNDER, 1995. Uncertainties of Measurements in Room Acoustics, *Acustica*, **81**, 344-355.

[16] C.L. CHRISTENSEN, 2001. Visualising acoustic surface properties, using colours, *Proceedings of 17th ICA*, Rome.

Journal of Acoustical Society of India : Vol. 42, No. 2, 2015 (pp. 112-117)

A General Approach to the Synthesis of Algorithms for Classification of Underwater Targests

Mashoshin Andrei
Concern Central Scientific and Research Institute "Elektropribor", JSC
30, Malaya Posadskaya str., Saint Petersburg 197046, Russia
**e-mail: aimashoshin@mail.ru*

[Received: 21.03.2014; Revised: 25.08.2014; Accepted: 27.11.2014]

ABSTRACT

Underwater target classification (UTC) based on the analysis of the acoustic field (primary or secondary) of underwater targets is one of the topical and the most challenging problems of applied underwater acoustics.

Underwater targets are classified using the target signature (TS) containing scalar or vector parameters of the target signal or echoes, which possesses information about the target class and can be measured at the sonar receiver output.

The purpose of the paper is to discuss the main features of the UTC problem and propose a general approach to the synthesis of optimal UTC algorithms which can be applied to both passive and active sonars.

The main problems concerned with obtaining a UTC are discussed. The properties of an optimal UTC algorithm are stated.

The main features of the UTC problem are the following:

– since an effective UTC is of particular interest at maximum detection ranges (i.e., at small signal-to-noise ratios (SNR)) where a TS does not possess much useful information (due to low accuracy of measurement), the desired effectiveness of classification can be reached by correct usage of all measured TS parameters;
– the information concentrated practically in each TS parameter depends on the current hydro acoustic conditions and SNR, which is why constructing UTC algorithms must be adaptive;
– practically all TS parameters are mutually dependent, which dictates the need for constructing the UTC algorithms on the basis of their mutual probability distribution function (PDF);
– different TS parameters are measured during different times, which is why constructing UTC algorithms must be dynamic.

The experience shows that the lack of knowledge about the above-mentioned features does not allow the UTC problem to be solved with the required quality. For example, the algorithms which do not consider current hydro acoustic conditions and also those in which the classification decisions are delivered with the use of separate TS parameters with subsequent weight summing of these decisions are ineffective.

The paper contains a procedure for substantiation of the synthesis of an optimal UTC algorithm. It is shown, that an optimal UTC algorithm must be Bayesian for the case of equal hypothesis. Taking in account the fact that the main procedure of the Bayesian algorithm is calculation of the mutual conditional PDF of TS parameters, we show how to calculate this PDF in the case of mutually dependent TS parameters.

A simple but important example is given to illustrate the use of an optimal UTC algorithm for classification of submarines and surface ships in the passive sonar.

1. INTRODUCTION

The underwater target classification (UTC) using their acoustic field (primary or second) is one of the actual and most difficult problems of the applied underwater acoustics [1,2].

For a long time the UTC was considered to be the skill of rumor operator to recognize noise and echoes. The need for the development of objective methods of the UTC arose in the end of the 50's of past century in connection with the appearance of the sonar in which the signal integration was realized. That has caused sharp decrease of the signal-to-noise ratio (SNR) threshold and growth of the target detection range. As a result the sonar operator began to experience difficulties with target classification at large detection distances. Classification as science appeared at the beginning of the 60's of past century.

The purpose of the paper is to discuss the main features of the UTC problem and as a result to propose the general approach to the synthesis of optimal UTC algorithms, which can be applied both to the passive and active sonar.

In section 2 the main features of the UTC problem are discussed. As a result of discussion the properties of the optimal UTC algorithm are stated.

Section 3 contains the procedure of the optimal UTC algorithm synthesis substantiation. It is shown that optimal UTC algorithm must be Bayesian for the case of equal hypothesis.

Taking in account that the main procedure of the Bayesian algorithm is the calculation of the mutual conditional probability distribution density (PDD) of the target signature (TS) parameters, in section 4 it is shown how to calculate this PDD for mutually dependent TS parameters.

Section 5 contains the conclusion and discussion.

2. MAIN FEATURES OF THE UNDERWATER TARGET CLASSIFICATION PROBLEM

The underwater target classification is fulfilled using the target signature (TS) containing scalar or vector parameters of target signal or echoes, which can be measured at the sonar receiver output and possesses information about the target class.

The UTC problem has some features, which must be considered when one begins the synthesis the UTC algorithm. The main of those features are the follows :

1. since the effective UTC has the greatest interest at the maximum detection ranges (*i.e.* at small SNR) where the utilized TS possess a little useful information (due to the low accuracy of their measurement), the desired classification effectiveness can be reached by correct usage of all measured TS parameters;
2. in practice, the information contained in each TS parameter depends on the current hydro acoustic conditions and SNR. That is why the construction of UTC algorithms must be adaptive;
3. practically all TS parameters are mutually dependent, which dictates the need of constructing the UTC algorithms based on their mutual probability distribution density (PDD);
4. the different TS parameters are measured during different time. That is why the construction of UTC algorithms must be dynamic.

3. PROCEDURE OF THE OPTIMUM UTC ALGORITHM SYNTHESIS

Let us state the formal formulation of the problem. Assume that they are assigned :

– the alphabet (the vector) Ω containing m target classes which form the full group of the events (*i.e.* each target which may be detected corresponds in the alphabet it's own class but only one):

$$\Omega = \{\omega_1, \omega_2, ..., \omega_m\} \quad (1)$$

– the vector $\mathbf{X}$ containing n TS parameters X_s:

$$\mathbf{X} = \{X_1, X_2, ..., X_n\} \quad (2)$$

It is necessary to synthesize the algorithm, which ensures the best target classification from the point of view of the selected statistical criterion.

It is known [3] that the full class of algorithms for the formulated problem (the class which contains all optimum algorithms of multi-class recognition) has the form

$$\omega_{opt} = arg \quad \min_{j} \quad \left\{ R\left(\omega_j, \hat{X}\right) \right\} \tag{3}$$

where:

ω_{opt} is a result of the classification (the optimal target class);

$\hat{\mathbf{X}}$ is the TS vector **X** estimate;

$\mathrm{R}\left(\omega_j, \hat{\mathrm{X}}\right)$ is the Bayesian risk function (BRF) which equals the loss of the decision in favor of the *j* th class (with the use of the vector $\hat{\mathbf{X}}$) :

$$\mathrm{R}\left(\omega_j, \hat{\mathrm{X}}\right) = \frac{\sum_{\substack{i=1 \\ i \neq j}}^{m} \mathrm{P}\left(\omega_i\right) \times \mathrm{C}_{i,j} \times \mathrm{g}_{\hat{\mathrm{X}}/\omega_i}\left(\hat{\mathrm{X}}\right)}{\sum_{i=1}^{m} \mathrm{P}\left(\omega_i\right) \times \mathrm{g}_{\hat{\mathrm{X}}/\omega_i}\left(\hat{\mathrm{X}}\right)} \tag{4}$$

$\mathrm{P}(\omega_1)$ is the apriori probability of *i* th class target detection;

$C_{i,j}$ is the cost of the false decision when the target of the *j* th class was classified as th class;

$g_{\hat{\mathbf{X}}/\omega_i}(\mathbf{x})$ is conditional PDD of the TS vector **X** estimate which converts into the likelihood function (LF) of the target class when the nonrandom argument **x** is changed by random TS vector **X** estimate $\hat{\mathbf{X}}$ [4].

According to the formula (3) the optimal class ω_{opt} minimizes the value of the LF which is calculated as the linear combination of $m-1$ alternative classes. The coefficients in the linear combination are multiplications of the apriori target detection probability and the cost of the false decision.

For the concrete definition of the class of algorithms (3) in our case let us take in consideration the fact that the parameters $P(\omega_1)$ and $C_{i,j}$ are unknown. Many attempts to motivate them failed without result due to the complexity of this task, caused by the need to take into account the large number of random factors. But it mustn't disturb the synthesis of the optimal classification algorithms because according to a well known postulate [3] in a real information systems the *apriori* determined parameters must not exert a substantial influence on the solutions. Taking into account that in practice the smaller the *apriori* target detection probability the larger the cost of its false classification (*i.e.* the less frequently the target is detected, the more it is available), it is possible to allow the validity of the condition

$$\mathrm{R}\left(\omega_j, \hat{\mathrm{X}}\right) = \frac{\sum_{\substack{i=1 \\ i \neq j}}^{m} \mathrm{P}\left(\omega_i\right) \cdot \mathrm{C}_{i,j} \cdot \mathrm{g}_{\hat{\mathrm{X}}/\omega_i}\left(\hat{\mathrm{X}}\right)}{\sum_{i=1}^{m} \mathrm{P}\left(\omega_i\right) \cdot \mathrm{g}_{\hat{\mathrm{X}}/\omega_i}\left(\hat{\mathrm{X}}\right)} \tag{5}$$

The substitution of (5) in (4) leads algorithm (3) to the form

$$\omega_{opt} = arg \quad \max_{j} \quad \left\{ P_{post}\left(\omega_j, \hat{\mathbf{X}}\right) \right\} \tag{6}$$

where $P_{apost}\left(\omega_j, \hat{\mathbf{X}}\right)$ is the aposteriori probability of belonging the target to *j* th class, which can be evaluated as follows [4]

$$P_{post}\left(\omega_j, \hat{\mathbf{X}}\right) = \frac{g_{\hat{\mathbf{X}}/\omega_j}\left(\hat{\mathbf{X}}\right)}{\sum_{i=1}^{m} g_{\hat{\mathbf{X}}/\omega_i}\left(\hat{\mathbf{X}}\right)} \tag{7}$$

Thus, the algorithm (6) is the optimal UTC algorithm. The probability weight of the optimal decision can be evaluated with help of formula (7) with the substitution $\omega_j = \omega_{opt}$.

Let us note that formula (7) is Bayes' formula for the case of the equal apriori target detection probabilities of each class, and algorithm (6) realizes the maximum likelihood method (ML-method) widely utilized in image recognition theory.

If one needs to introduce into the classification algorithm the zone of failure the algorithm (6) is converted to the form :

$$K = \begin{cases} \omega_{opt}, & if \quad P_{post}\left(\omega_{opt}, \hat{\mathbf{X}}\right) > P_{thresh} \\ refuse, & if \quad P_{post}\left(\omega_{opt}, \hat{\mathbf{X}}\right) \le P_{thresh} \end{cases} \tag{8}$$

where P_{thresh} is the threshold probability.

Let us view the organization of the target classification. From the moment of target detection the cyclical measuring process of target TS parameters starts. The time of measurement of each TS parameter is individual. Simultaneously with the TS parameters measuring process the cyclical process of making decisions according the algorithm (8) starts. The cycle time of this process, as a rule, coincides with the time of the very "rapid" cycle of TS parameters measurement. Since TS measurement and making of a decision realize asynchronously, the TS parameters amount utilized at the different cycles of decision can differ.

To increase the statistical regularity of the decisions the measurements of the similar TS parameters, obtained on the sequential cycles, are smoothed by one of the methods. The aposteriori probabilities, used in the algorithm (6), can also be smoothed. Usually this is achieved by the α -filter application:

$$P_{apost/smooth}\left(\omega_j\right) = \alpha \cdot P_{apost}\left(\omega_j, \hat{\mathbf{X}}\right) + (1-\alpha) \cdot P_{apost/smooth}\left(\omega_j\right), \quad j = 1,\ldots,m$$

where

$P_{apost}\left(\omega_j, \hat{\mathbf{X}}\right)$ is the aposteriori probability of belonging the target to *j* th class, evaluated with help of formula (7) at current decision cycle;

$P_{apost/smooth}\ (\omega_j)$ is the smoothed aposteriori probability of belonging the target to *j* th class;

α is the constant which controls the smoothing time $(0 < \alpha < 1)$.

4. PROCEDURE OF THE MUTUAL CONDITIONAL PDD ALGORITHM SYNTHESIS OF THE TS PARAMETERS ESTIMATES

From the revue of formulas (5)…(8) it follows that the only nontrivial operation in the procedure of UTC algorithm synthesis is the calculation of the conditional (depending on the target class) PDD $g_{\hat{\mathbf{X}}/\omega_i}(\mathbf{x})$ of the TS vector estimate **X**. Therefore let us pay more attention to this question.

For the PDD $g_{\hat{\mathbf{X}}/\omega_i}(\mathbf{x})$ calculation the following procedure was developed.

(1) For each TS parameter X_s, belonging to the vector **X**, the stochastic model is created in the form:

$$\hat{X}_s = \varphi_s\left(\mathbf{Z}_s\right) + \Delta X_s \tag{9}$$

where $\hat{X}_s$ is an estimate of TS parameter X_s (scalar or vector);

$\varphi_s(Z_s)$ is the nonrandom function connecting the TS parameter X_s true value with the target sound emission (or reflection) parameters, the target coordinates and moving parameters and the signal channel propagation parameters, *i.e.*,

$$X_s = \varphi_s(Z_s) \tag{10}$$

Functions $\varphi_s(Z_s)$ make it possible to incorporate the effects of hydroacoustic conditions into the classification algorithm;

ΔX_s is an estimation error of TS parameter X_s. The error statistical characteristics (for example, the variance) allow inclusion of noise conditions into classification algorithms.

The Z_s vectors for different TS can contain the different quantity of parameters.

(2) The vector **Z**, which includes all parameters belonging at least to one vector, is formed.

(3) The mutual conditional (depending on the target class and **Z** vector) PDD of all TS parameters $\hat{X}_s$ is calculated. Since the TS parameters estimation errors ΔX_s, as a rule, are independent, all TS parameters estimates $\hat{X}_s$ become independent too. Therefore their mutual conditional PDD equals to the multiplication of conditional PDD of every TS [5], *i.e.*

$$g_{\hat{\mathbf{X}}/\omega_j,\mathbf{Z}}(\mathbf{x}) = \prod_{s=1}^{n} g_{\hat{X}_s/\omega_j,\mathbf{Z}}(x_s) = \prod_{s=1}^{n} g_{\Delta X_s}\left(x_s - \varphi_s\left(\mathbf{Z}_{s/\omega_j}\right)\right) \tag{11}$$

The mutual conditional (depending only on the target class) PDD of all TS parameters estimates $\hat{X}_s$, united in the vector $\hat{\mathbf{X}}$, is calculated [3] :

$$g_{\hat{\mathbf{X}}/\omega_j}(\mathbf{x}) = \iiint_{\mathbf{z}} g_{\mathbf{Z}/\omega_j}(\mathbf{z}) \cdot g_{\hat{\mathbf{X}}/\mathbf{z}}(\mathbf{x}) \cdot d\mathbf{z} \tag{12}$$

where $g_{z/\omega_j}(z)$ is mutual conditional PDD of the parameters, forming the vector **Z**. Since the majority of these parameters are mutually independent, the PDD $g_{z/\omega_j}(z)$ is calculated as the multiplication of the PDD of each vector **Z** element.

5. SUMMARY

The article contains the brief revue of general approach to the underwater target classification (UTC) algorithm syntheses. This approach is based on the main features of UTC problem and can be used to design the modern passive and active sonar.

6. ACKNOWLEDGEMENTS

This work is supported by the Russian Foundation for Basic Research (RFBR) (projects 12-08-00511-? and 11-08-01097-?).

7. REFERENCES

[1]. S. DIVYA, M.H. SUPRIYA and P.R. SASEENDRAN PILLAI, 2010. Underwater Signal Classification based on VQ Analysis, Proceedings of the 4th European Conference on Underwater Acoustics (ECUA), Istanbul, Turkey.

[2]. H. Midelfart and Ø., 2011. Midtgaard. Robust template matching for object classification, Proceedings of the 4th International Conference and Exhibition on Underwater Acoustic Measurements: Technologies & Results, Kos island, Greece.

[3]. V.G. REPIN and G.P. TARTAKOVSKII, 1977. Statistical Synthesis at an *a priori* Indeterminacy and the Adaptation of Information Systems. Sovetskoe radio, Moscow.

[4]. M.G. KENDALL and A. STUART, 1967. The Advanced Theory of Statistics. London: Charles Griffin, **2**.

[5]. E.S. VENTCEL and L.A. OVCHAROV, 1988. Probability Theory and its Engineering Applications. Nauka, Moscow

[6]. S.K. KADASHNIKOV and A.I. MASHOSHIN, 1998. Statistical description of a signal propagation channel with application to hydroacoustic classification. *Acoustical Physics*, 44(4), 394-400.

INFORMATION FOR AUTHORS

ARTICLES

The Journal of Acoustical Society of India (JASI) is a refereed publication published quarterly by the Acoustical Society of India (ASI). JASI includes refereed articles, technical notes, letters-to-the-editor, book review and announcements of general interest to readers.

Articles may be theoretical or experimental in nature. But those which combine theoretical and experimental approaches to solve acoustics problems are particularly welcome. Technical notes, letters-to-the-editor and announcements may also be submitted. Articles must not have been published previously in other engineering or scientific journals. Articles in the following are particularly encouraged: applied acoustics, acoustical materials, active noise & vibration control, bioacoustics, communication acoustics including speech, computational acoustics, electro-acoustics and audio engineering, environmental acoustics, musical acoustics, non-linear acoustics, noise, physical acoustics, physiological and psychological acoustics, quieter technologies, room and building acoustics, structural acoustics and vibration, ultrasonics, underwater acoustics.

Authors whose articles are accepted for publication must transfer copyright of their articles to the ASI. This transfer involves publication only and does not in any way alter the author's traditional right regarding his/her articles.

PREPARATION OF MANUSCRIPTS

All manuscripts are refereed by at least two referees and are reviewed by the Publication Committee (all editors) before acceptance. Manuscripts of articles and technical notes should be submitted for review electronically to the Chief Editor by e-mail or by express mail on a disc. JASI maintains a high standard in the reviewing process and only accept papers of high quality. On acceptance, revised articles of all authors should be submitted to the Chief Editor by e-mail or by express mail.

Text of the manuscript should be double-spaced on A4 size paper, subdivided by main headings-typed in upper and lower case flush centre, with one line of space above and below and sub-headings within a section-typed in upper and lower case understood, flush left, followed by a period. Sub-sub headings should be italic. Articles should be written so that readers in different fields of acoustics can understand them easily. Manuscripts are only published if not normally exceeding twenty double-spaced text pages. If figures and illustrations are included then normally they should be restricted to no more than twelve-fifteen.

The first page of manuscripts should include on separate lines, the title of article, the names, of authors, affiliations and mailing addresses of authors in upper and lowers case. Do not include the author's title, position or degrees. Give an adequate post office address including pin or other postal code and the name of the city. An abstract of not more than 200 words should be included with each article. References should be numbered consecutively throughout the article with the number appearing as a superscript at the end of the sentence unless such placement causes ambiguity. The references should be grouped together, double spaced at the end of the article on a separate page. Footnotes are discouraged. Abbreviations and special terms must be defined if used.

EQUATIONS

Mathematical expressions should be typewritten as completely as possible. Equation should be numbered consecutively throughout the body of the article at the right hand margin in parentheses. Use letters and numbers for any equations in an appendix: Appendix A: (A1, (A2), etc. Equation numbers in the running text should be enclosed in parentheses, i.e., Eq. (1), Eqs. (1a) and (2a). Figures should be referred to as Fig. 1, Fig. 2, etc. Reference to table is in full: Table 1, Table 2, etc. Metric units should be used: the preferred from of metric unit is the System International (SI).

REFERENCES

The order and style of information differs slightly between periodical and book references and between published and unpublished references, depending on the available publication entries. A few examples are shown below.

Periodicals:

[1] S.R. Pride and M.W. Haartsen, 1996. Electroseismic wave properties, *J. Acoust. Soc. Am.*, **100** (3), 1301-1315.

[2] S.-H. Kim and I. Lee, 1996. Aeroelastic analysis of a flexible airfoil with free play non-linearity, *J. Sound Vib.*, **193** (4), 823-846.

Books:

[1] E.S. Skudzryk, 1968. *Simple and Comlex Vibratory Systems*, the Pennsylvania State University Press, London.

[2] E.H. Dowell, 1975. *Aeroelasticity of plates and shells*, Nordhoff, Leyden.

Others:

[1] J.N. Yang and A. Akbarpour, 1987. Technical Report NCEER-87-0007, Instantaneous Optimal Control Law For Tall Buildings Under Seismic Excitations.

SUMISSIONS

All materials from authors should be submitted in electronic form to the JASI Chief Editor: B. Chakraborty, CSIR - National Institute of Oceanography, Dona Paula, Goa-403 004, Tel: +91.832.2450.318, Fax: +91.832.2450.602,(e-mail: bishwajit@nio.org) For the item to be published in a given issue of a journal, the manuscript must reach the Chief Editor at least twelve week before the publication date.

SUMISSION OF ACCEPTED MANUSCRIPT

On acceptance, revised articles should be submitted in electronic form to the JASI Chief Editor (bishwajit@nio.org)

ISSN 0973-3302

JOURNAL OF ACOUSTICAL SOCIETY OF INDIA

Volume 42 Number 3 July 2015

A Quarterly Publication of the JASI
http://www.acousticsindia.org

Journal of Acoustical Society of India

Volume 42 Number 3 July 2015 pp 119-180

JASI

Journal of Acoustical Society of India

The Refereed Journal of the Acoustical Society of India (JASI)

The Journal of Acoustical Society of India is a refereed journal of the Acoustical Society of India **(ASI)**. The **ASI** is a non-profit national society founded in 31st July, 1971. The primary objective of the society is to advance the science of acoustics by creating an organization that is responsive to the needs of scientists and engineers concerned with acoustics problems all around the world.

Manuscripts of articles, technical notes and letter to the editor should be submitted to the Chief Editor. Copies of articles on specific topics listed above should also be submitted to the respective Associate Scientific Editor. Manuscripts are refereed by at least two referees and are reviewed by Publication Committee (all editors) before acceptance. On acceptance, revised articles with the text and figures scanned as separate files on a diskette should be submitted to the Editor by express mail. Manuscripts of articles must be prepared in strict accordance with the author instructions.

All information concerning subscription, new books, journals, conferences, etc. should be submitted to Chief Editor:

B. Chakraborty, CSIR - National Institute of Oceanography, Dona Paula, Goa-403 004,
Tel: +91.832.2450.318, Fax: +91.832.2450.602, e-mail: bishwajit@nio.org

Annual subscription price including mail postage is Rs. 2500/= for institutions, companies and libraries and Rs. 2500/= for individuals who are not **ASI** members. The Journal of Acoustical Society of India will be sent to **ASI** members free of any extra charge. Requests for specimen copies and claims for missing issues as well as address changes should be sent to the Editorial Office:

ASI Secretariat, C/o Acoustics, Ultrasonics & Vibration Section, CSIR-National Physical Laboratory, Dr. KS Krishnan Road, New Delhi 110 012, Tel: +91.11.4560.8317, Fax: +91.11.4560.9310, e-mail: asisecretariat.india@gmail.com

ISSN 0973-3302

Printed at Alpha Printers, WZ-35/C, Naraina, Near Ring Road, New Delhi-110028 Tel.: 9810804196. JASI is sent to ASI members free of charge.

JASI

Journal of Acoustical Society of India (JASI)

A quarterly publication of the Acoustical Society of India

Volume 42, Number 3, July 2015

ARTICLES

INFORMATION

Journal of Acoustical Society of India : Vol. 42, No. 3, 2015 (pp. 119-125)

Energy pumping by cavitation cloud in low-frequency horn-type devices

Bertrand Dubus and Christian Granger
Institut d'Electronique de Microélectronique et de Nanotechnologie, département ISEN, UMR CNRS 8520, 41 boulevard Vauban, 59046 Lille cedex, France
**e-mail: bertrand.dubus@isen.fr*

[Received: 22.12.2013; Revised: 10.05.2014; Accepted: 15.08.2014]

ABSTRACT

To optimise sonochemistry devices and develop scale-up strategies, it is important to predict how cavitation bubbles are spatially distributed when they are generated by high intensity ultrasonic transducers. The cavitation field generated by an ultrasonic horn transducer at low frequency and high power is known to self-organize into a conical bubble structure. The spatial distribution of bubbles results from bubble motion due to primary Bjerknes force: bubbles nucleate at horn surface, move parallel to the surface and finally leave it along streamers that constitute the cone. Recently published results suggest that this bubble structure behaves as a non linear resonator. As such device couples linear (transducer) and non linear resonators (bubble structure), the mechanism of irreversible energy transfer from linear to non linear resonator called "energy pumping" could take place when the adequate excitation amplitude is reached.

A one-dimensional theoretical model is proposed to analyse the two lowest coupled non linear modes of the transducer-bubbly layer system. Sound speed in the bubbly layer is assumed to vary with pressure amplitude according to published experimental results. Frequency-energy curves show that the first mode, which corresponds mainly to transducer resonance, gets off-balance above a given energy. A new equilibrium, involving both resonance modes and energy dissipation by the cavitation cloud, is found with much lower sound speed in the bubbly layer and much smaller energy stored in the system. Energy pumping could be associated to this mode of operation.

Experiments are performed on a horn transducer radiating in a water tank driven by a pulsed sinusoidal excitation (20 kHz). Horn surface velocity is monitored by laser vibrometry and acoustic pressure is measured in the cavitation field using an hydrophone. Images of the cavitation bubble structure are obtained with a high speed camera at 7000 frames per second. When the electrical excitation is stopped, horn vibration amplitude decreases whereas the pressure amplitude remains constant and bubble structure unchanged. When horn vibration vanishes, pressure amplitude starts decreasing and bubble structure disappears. This result, which shows that the cavitation cloud pumps irreversibly energy from the transducer, opens the field up to new strategies in high power sonoreactors optimization and scale-up.

1. INTRODUCTION

For sonochemistry device optimisation and scale-up strategies, it is important to predict how cavitation

bubbles are spatially distributed when they are generated by high intensity ultrasonic transducers [1]. To improve the understanding of this phenomena, the stable bubble structure of conical shape observed at the vicinity of the horn surface of a cylindrical horn-type transducer is an extensively studied test case [2-9]. Physical models of the cavitation field at high intensity can thus be compared to experimental results on acoustic pressure field, fluid streaming or spatial distribution of bubbles. Recent results suggest that the bubble structure behaves as a nonlinear resonator constituted by moving cavitation bubbles. It has been shown theoretically and verified experimentally that a resonant bubble layer trapped at horn surface can explain nonlinear acoustic effects associated to the cone-like bubble structure [8].

As ultrasonic cavitation fields are usually generated using piezoelectric transducers which are linear resonators, the device includes two coupled resonators: a linear resonator, the transducer, which provides mechanical energy and a nonlinear resonator, the bubble structure. Systems coupling linear and nonlinear resonators have been extensively studied in mechanics [10] and more recently in acoustics [11], revealing that an irreversible passive energy transfer from the linear resonator to the nonlinear resonator can appear above a threshold amplitude. In this paper, the occurrence of this phenomenon, called "energy pumping", is investigated in horn-type cavitation devices at high intensity.

2. THEORY OF CRLH METAMATERIALS

2.1 Problem geometry and set of equations

A one-dimensional system constituted by a piezoelectric resonant transducer, a resonant bubbly layer and an acoustic load is considered. Classical electro-mechanical and electro-acoustical analogies are used to describe the system [12]. The transducer dynamics is described by the lumped constant equivalent electrical circuit given using

$$(k - \omega^2 m)U = F_d - F \tag{1}$$

where U and F are respectively the displacement and the force at transducer radiating surface. F_d is the driving force applied to the mechanical part of the transducer due to piezoelectric effect, k and m are respectively the effective stiffness and the dynamic mass of the transducer. $e^{+j\omega t}$ time dependency is considered ω is the angular frequency, t the time and $j^2 = -1$. The resonance frequency of the isolated transducer is $f_0 = \sqrt{k/4\pi^2 m}$. The resonant bubbly layer of thickness τ is represented by a transmission line relating forces and displacements on its surfaces [12]:

$$\rho_b c_b \omega\left[\left(\cos\beta\tau\right)U - U_{\text{int}}\right] = \left(\sin\beta\tau\right)\frac{F}{S} \tag{2}$$

$$\rho_b c_b \omega\left(\sin\beta\tau\right)U = \frac{F_{\text{int}}}{S} - \left(\cos\beta\tau\right)\frac{F}{S} \tag{3}$$

where F_{int} and U_{int} are respectively the pressure and the displacement at the interface between the resonant layer and the acoustic load. ρ_b and c_b are the effective density and effective speed of sound in the bubbly layer which is assumed homogeneous. $\beta = \omega/c_b$ is the acoustic wavenumber in the bubbly layer and S is the transducer radiating surface area. To simplify the analysis, the interface is assumed to be a free surface described by setting Z_{load} i.e. $F_{int} = 0$ in equation (3).

Non-linearity of the bubbly layer is associated to the variations of ρ_b and c_b (and therefore β) with pressure at horn surface $p = F/S$. If bubble volume fraction δ verifies $\delta << 1$ and frequency is far below bubbles resonance frequency, these variations are written as [13]:

$$\rho_b \approx \rho_f \tag{4}$$

$$\frac{1}{c_b^2} \approx \frac{1}{c_f^2} + \frac{\delta\rho_f}{\gamma P_0} \tag{5}$$

where ρ_f and c_f are liquid density and speed of sound respectively, P_0 the static pressure and γ the ratio of specific heats for bubble gas. By combining equations (1) to (3) the set of equations is written as:

$$\left[\rho_f c_b S\omega(\cos\beta\tau)+\left(k-\omega^2 m\right)(\sin\beta\tau)\right]U-\rho_f c_b S\omega\, U_{\text{int}}=F_d \tag{6}$$

$$\left[\rho_f c_b S\omega(\sin\beta\tau)-\left(k-\omega^2 m\right)(\cos\beta\tau)\right]U=-(\cos\beta\tau)F_d \tag{7}$$

2.2 Results

Resonance frequencies of this system are obtained by setting $F_d = 0$ in equations (6) and (7). The two lowest resonance frequencies are numerically computed for $0.036\ c_f \le c_b \le c_f$ with the following data: $k = 2.984\ 10^{10}$ N.m^{-1}, m = 1.89 kg, f_0 = 19998 Hz, ρ_f = 1000 kg.m^{-3}, c_f = 1500 m.s^{-1}, γ = 1.4, $P_0 = 1.065\ \ 10^5$ Pa, $\tau = 1.525\ 10^{-3}$ m and $S = \pi R^2$ with R = 0.035 m.

Variation of resonance frequencies versus cb is displayed in Figure 1.

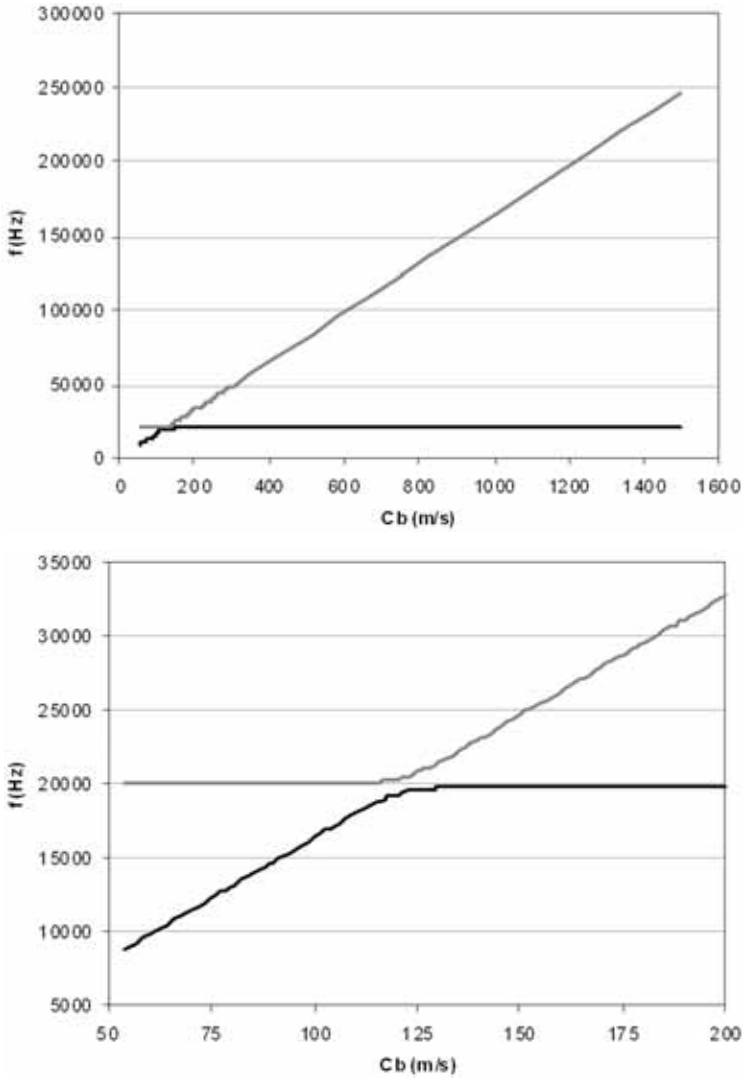

Fig. 1. Ultrasonic transducer coupled to a fluid layer. Computed two lowest resonance frequencies (black line: first mode; red line: second mode) versus fluid speed of sound: (a) in the 54-1500 m.s^{-1} range; (b) in the 54-200 m.s^{-1} range.

- As long as c_b > 150 m.s^{-1}, resonances are not coupled. The lowest resonance frequency remains quasi-constant at 19960 Hz. This mode is similar to the resonance mode of the transducer loaded by the added mass of the liquid layer which produces a slight frequency down-shift with respect to f_0. The second resonance frequency exhibits a linear decrease with c_b. This resonance mode is a quarter of wavelength thickness resonance of the fluid layer having zero-velocity boundary conditions on one side (horn-fluid interface) and zero pressure on the other side (fluid-acoustic load interface).
- In the range 100 < c_b < 150 m.s^{-1}, the two aforementioned resonance frequencies get closer and interaction takes place between resonance modes. New coupled modes are obtained as a combination of previous modes. Both kinetic and strain energies are stored in the transducer and the fluid layer for coupled modes, contrary to previous cases where the fluid layer (for lowest mode) or the transducer (for highest mode) behaves as an added mass and stores only kinetic energy. This modal interaction can lead to energy pumping when one resonator is nonlinear.
- When c_b < 100 m.s^{-1}, uncoupled resonances are recovered. The lowest resonance frequency is associated liquid layer resonance frequency. The highest resonance frequency is associated to transducer resonance frequency with a slight frequency up-shift due to fluid layer which behaves as a negative added mass.

To compute frequency-energy plots, an additional relationship is introduced between bubble density and acoustic pressure $p = F/S$. It is extracted from published measurements realized at 15.4 kHz on a ring transducer [14]

$$\delta = \begin{cases} 0 & if \quad |p| \le p_t \\ b\left(|p| - p_t\right)^3 & if \quad p_t \le |p| \le p_{sat} \\ \delta_{sat} & if \quad |p| \ge p_{sat} \end{cases} \tag{8}$$

with p_t = 1.7 10^5 Pa, P_{sat} = 2.1 10^5 Pa, δ_{sat} = 0.125, b = 1.953 10^{-15} Pa^{-3}. Coupled nonlinear resonance frequencies are plotted versus total energy in a log scale in Figure 2. When the transducer is driven near its resonance frequency with increasing amplitude, the system remains linear as long as the cavitation threshold is not reached in the fluid layer. The resonance frequency remains constant while energy stored in the system

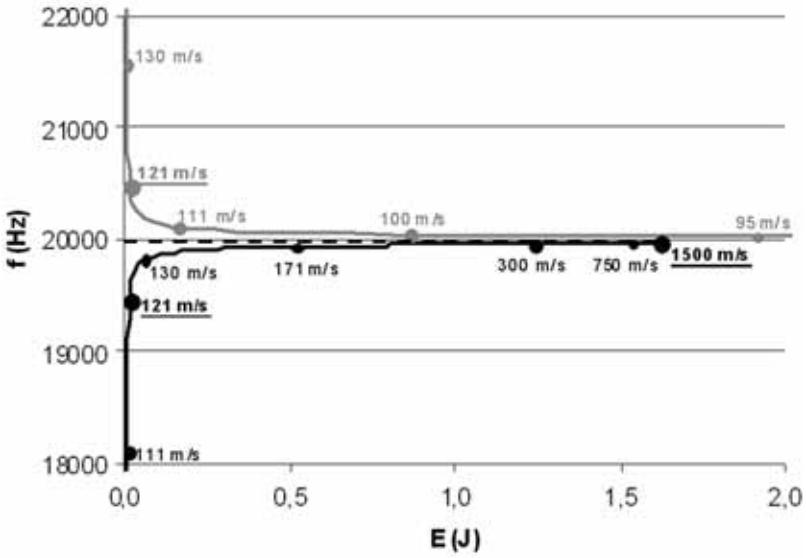

Fig. 2. Ultrasonic transducer coupled to a fluid bubbly layer. Computed frequencies versus total energy of the two lowest resonance frequencies (black line: first mode; red line: second mode).

increases (dashed line of Fig. 2). Once cavitation threshold is reached (circle corresponding to 1500 m/s in Fig. 2), additional increase of driving amplitude leads to the appearance of cavitation bubbles in the fluid layer and therefore to a decrease of speed of sound. The system gets off-balance as the increase of input energy in the system produces a decrease of energy of the nonlinear mode. No harmonic solution can be found in that case but a new quasi-periodic state consisting of a combination of two coupled nonlinear resonance modes may be reached for a sound speed of approximately 121 m/s. Both coupled resonance modes have similar total energy and resonance frequencies separated by 1 kHz (19460 Hz and 20460 Hz). A previously published work has demonstrated that irreversible energy pumping of the linear resonator by the nonlinear resonator takes place in these conditions [11].

3. EXPERIMENTS

3.1 Set-up

Ultrasonic vibration is generated by a sandwich piezoelectric transducer coupled to a mechanical amplifier and a 70 mm diameter horn. It is driven by a pulsed sinusoidal excitation with a typical pulse length of 2000 periods at 20900 Hz with 3 Hz repetition rate. The horn surface velocity is monitored indirectly by measuring the radial velocity at half-height of the horn and using a preliminary measurement of the longitudinal (surface)/radial (half height) velocity ratio. The horn is partially immersed (approximately 1 cm deep) in a tank is filled with tap water. Acoustic pressure is measured on the symmetry axis, 1 cm below horn surface, using a Bruel & Kjaer (B&K) 8103 hydrophone. Images of the cavitation bubble structures are obtained with a high speed camera at 7000 frames per second. To synchronize high speed images and hydrophone measurement, an ultra-fast light emitting diode is used to generate a very short flash when the electrical drive is stopped. The duration of the flash is calibrated at a value of 200 μs to illuminate only one picture taken by the high speed camera.

3.2 Results

A first set of experiments is performed at moderate amplitude drive, when cavitation takes place in the tank without formation of the cone bubble structure. In that case, the effective speed of sound in the fluid remains close to 1500 $m.s^{-1}$. According to theoretical analysis, the system is expected to be driven on the mechanical mode of the transducer / amplifier / horn system loaded by the fluid. Energy pumping should not be observed. Variation of measured acoustic pressure and horn surface velocity after electric drive switch off is characterized by a simultaneous exponential decrease of acoustic pressure and horn velocity immediately after switch off. Pictures of cavitation field and particularly of bubbles streamers at horn surface shows an important decrease of cavitation bubble activity after switch off: energy pumping does not take place at moderate drive level.

Experiments are also conducted at high drive levels for which cone-like bubble structure is observed below horn surface. Variation of measured acoustic pressure and horn surface velocity after electric drive switch off as well as pictures of cone-like bubble structure at specific times are displayed in Figure 3. A large

(a) **(b)**

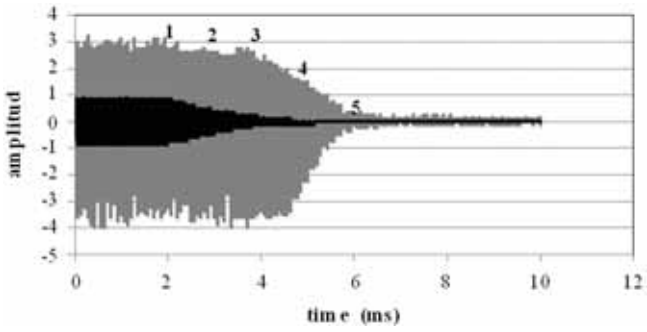

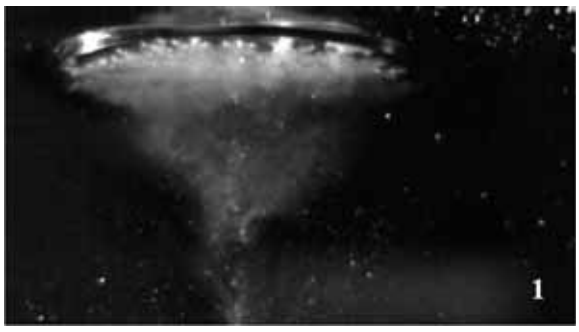

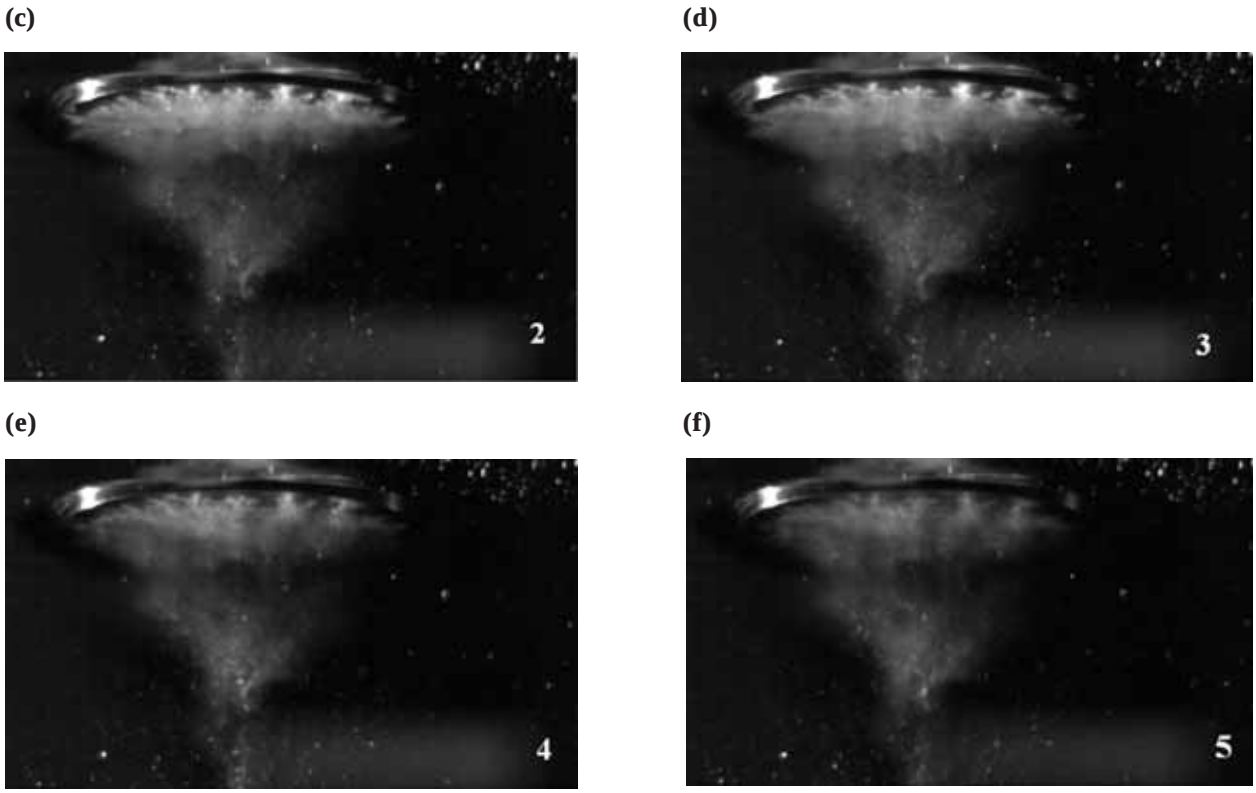

Fig. 3. Case of a high drive level (conical bubble structure is observed). (a) variation of measured acoustic pressure (grey line) and surface velocity (black line) (in arbitrary units) versus time when the electrical drive is stopped; (b) to (f) Pictures of bubble structure at different times.

time delay of 1.813 ms (*i.e.* 38 periods of driving frequency) is found between the start of velocity decrease (which coincide with electrical switch off) and the start of pressure decrease. During that period of time (times 1 to 3), no change is observed in cone-like bubble stru-ture and in streamers at horn surface. Vibrational energy of the transducer is pumped by cone-like bubble structure which remains unchanged as does the associated pressure field. Interestingly, it can be noted that, during this energy pumping, pressure field remains asymmetrical suggesting that inertial cavitation is also maintained. At later times (times 4 and 5), structure vibrational energy is drained and energy pumping is stopped leading to an important decrease of bubble activity.

4. CONCLUSION

The results presented in this paper demonstrate that energy pumping takes place in horn-type devices at high intensity *i.e.* that the cone-like bubble structure acts as a non linear resonator which pumps horn vibrational energy. Therefore, horn-type devices driven at high level should no more be considered as linear resonators radiating energy in a fluid which converts part of this energy into cavitation bubbles (which is the working mode at moderate drive level), but as a system coupling a mechanical resonator (the horn transducer) and a nonlinear acoustic resonator (the cone-like bubble structure) in which irreversible energy transfer from horn towards bubbles structure takes place. This phenomenon appears when the resonance frequency of the cone bubble structure is close enough to the driving frequency (and therefore to the horn transducer frequency). It requires to reach a given bubble density threshold and therefore a given drive amplitude threshold, a phenomenon which has been observed experimentally [2, 5, 8].

6. REFERENCES

[1] F.J. KEIL and K.M. SWAMY, 1999. Reactors for sonochemical engineering - Present status, *Rev. Chem. Eng.,* **15**, 85-155.

[2] A. MOUSSATOV, C. GRANGER and B. DUBUS, 2003. Cone-like Bubble Formation in Ultrasonic Cavitation Field, *Ultrason. Sonochem*. **10**, 191-195.

[3] A. MOUSSATOV, R. METTIN, C. GRANGER, T. TERVO, B. DUBUS and W. LAUTERBORN, 2003. Evolution of Acoustic Cavitation Structure near Larger Emitting Surface, *Ultrasonics World Congress 2003 Proceedings*, Paris, France.

[4] P. KOCH, R. METTIN and W. LAUTERBORN, 2004. Simulation of Cavitation Bubbles in Travelling Acoustic Waves, *Proceedings of the joint congress CFA/DAGA'04,* Strasbourg, France.

[5] C. CAMPOS-POZUELO, C. GRANGER, C. VANHILLE, A. MOUSSATOV and B. DUBUS, 2005. Experimental and theoretical investigation of the mean acoustic pressure in the cavitation field, *Ultrason. Sonochem*. **12**, 79-84.

[6] V.N. SKOKOV, V.P. KOVERDA, A.V. RESHETNIKOV and A.V. VINOGRADOV, 2005. 1/f fluctuations under acoustic cavitation of liquids, *Physica A* **364**, 63-69.

[7] A. MANDROYAN, R. VIENNET, Y. BAILLY, M.-L. DOCHE and J.-Y. HIHN, 2009. Modification of the ultrasound induced activity by the presence of an electrode in a sonoreactor working at two low frequencies (20 and 40 kHz). Part I: Active zone visualization by laser tomography, *Ultrason. Sonochem.* **16**, 88-96.

[8] B. DUBUS, C. VANHILLE, C. CAMPOS-POZUELO and C. GRANGER, 2010. On the physical origin of conical bubble structure under ultrasonic horn, *Ultrason. Sonochem*. **17**, 810-818.

[9] O. LOUISNARD, 2012. A simple model of ultrasound propagation in a cavitating liquid. Part II: Primary Bjerknes force and bubble structures, *Ultrason. Sonochem.* **19**, 66-76.

[10] D.M. MCFARLAND, L.A. BERGMAN and A.F.VAKAKIS, 2005. Experimental study of non-linear energy pumping occurring at a single fast frequency, *Int. J Nonlinear Mech.* **40**, 891-899.

[11] R. BELLET, B. COCHELIN, P. HERZOG and P.-O. MATTEI, 2010. Experimental study of targeted energy transfer from an acoustic system to a nonlinear membrane absorber, *J. Sound Vib.* **329**, 2768-2791.

[12] O. B. WILSON, 1985. *Introduction to Theory and Design of Sonar Transducers*, Peninsula Publishing.

[13] M.F. HAMILTON, YU.A. IL'INSKII and E.A. ZABOLOTSKAYA, 1998. *Nonlinear Acoustics* edited by M.F. Hamilton and D.T. Blackstock, Academic Press, 151-175.

[14] V.A. AKULICHEV, 1969. Experimental investigation of an elementary cavitation zone, *Sov. Phys. Ac.* **14**, 284-289.

Journal of Acoustical Society of India : Vol. 42, No. 3, 2015 (pp. 126-131)

Polymer Embedded Novel Flexible Acoustic Sensor Arrays for Underwater Surveillance

Rahna K. Shamsudeen, V. G. Jayakumari, S. Kusumakumari, R. Rajeswari, Subhash Subramoniam, K. E. Nissar and T. Mukundan*

Naval Physical and Oceanographic Laboratory,Thrikkakara, Kochi- 682 021, Kerala, India

**e-mail: ms_npol@yahoo.com*

[Received: 16.04.2013; Revised: 29.05.2014; Accepted: 08.08.2014]

ABSTRACT

Conventional towed type underwater sensor array modules consist of acoustic sensors, elec-tronics and allied accessories housed in a polyurethane tube, filled with oil as the coupling fluid. This system is vulnerable to puncture damages which result in oil leakage leading to total loss of performance of the array and result in ecological issues. In order to overcome these issues, an alternative, which is unaffected by puncture damages, was developed. This novel sensor array when fully made, acquires a monolithic solid form encompassing the sensors, electronics etc. in a new design and is devoid of oil and the outer polyurethane tube. A fully functional solid linear acoustic sensor array in Seabed Array configuration for stationary applications was developed and proved. Linear arrays in towed array configuration were also developed and the performance compared with conventional type of oil filled arrays. The results of ambient noise level pick up by array sensors, influence of wake on array performance and signal detection levels in stationary and towed condition are presented.

1. INTRODUCTION

Underwater acoustic transducers are the primary surveillance tool for ships and submarines in the naval scenario. Among the different types of underwater acoustic surveillance tools, '*Seabed deployed sensor array*', a passive variety, is used as a stationary surveillance tool. Another class of surveillance tools is a *towed sensor array* that is towed in a linear array behind towing vessels or platforms like ships or submarines. Conventionally, these sensor arrays comprise long flexible housings filled with an acoustically coupling fluid, embedding the sensors and allied electronics arranged on a strength member. The present study relates to the design, development and comparison of performance of a novel solid polymer embedded linear flexible acoustic sensor arrays in *Seabed deployed* as well as towed array configuration and its performance comparison with otherwise similar fluid filled array. Solid arrays, wherein the coupling fluid is replaced by a solid material, are important advancements in underwater scenario and are better in terms of reliability and ruggedness, ease of transportation, environment friendliness and they are unaffected by puncture damages while maintaining the acoustic performance of the existing technology[1-7].

The polymer selected for embedding the sensor assembly and the electronics was a two component polyurethane. A performance comparison of the solid array designed for seabed deployment, with the fluid filled version using channel-wise frequency spectra and target tracking analysis proved that this indigenously developed technology could be used as an efficient tool for coastal surveillance. Three

independent modules, containing sensor units in three different environments were developed for towing evaluation. Extensive acoustic evaluation and performance comparison was performed by the following studies, (i) ambient noise level pick up by each array sensors, (ii) effect of wake on hydrophones in different environments and (iii) signal detection levels of each array by pulsed transmission of half sine wave and 3 kHz CW pulse. It was also proved that the solid array is very flexible enabling easy winding over a winch before deployment for towing. The improved and more consistent acoustic performance of these arrays suggests that these are highly beneficial towards the development of futuristic thin line passive underwater acoustic surveillance tools.

2. SOLID LINEAR FLEXIBLE ACOUSTIC SENSOR ARRAY FOR STATIONARY APPLICATIONS

A 16 channel sensor array was designed and developed by embedding acoustic sensor assemblies, allied electronics and power supply capsules in a flexible matrix. The acoustic signals are amplified by a pre amplifier of certain gain. The pre amplified signal is further converted into a proportional current form using a voltage to current converter. The important design features of the array are as follows.

- A paradigm shift from conventional oil-filled linear acoustic sensor arrays
- Fabricated using *in situ* polymerization of a liquid PU resin fill material
- Monolithic solid structure that embeds all sensors and electronics in the solid matrix
- Devoid of the outer PU tube and other housings and supports for sensor PCB assemblies
- Devoid of housings for hydrophone-PCB assembly
- Hydrophones premoulded using PU and PCBs and power supply unit premoulded using thermally conducting silicone
- Remedies the problems of cracks, damages and leakage and resultant total loss of performance
- Fabrication can be up scaled for bulk production

The hydrophones used for underwater applications are to be protected from water permeation by proper encapsulation with a suitable material. The matrix material chosen for fabricating the solid linear array in stationary configuration for seabed array application (hereafter referred as Solid Array 1) is an indigenous two component polyurethane material. This has suitable mechanical, electrical and physical properties for the projected applications. The important material properties are mentioned in Table 1.

Table 1. Physico-chemical and acoustic properties of the matrix material used for fabrication of solid linear flexible acoustic sensor arrays

Property	Value/ Remarks	Property	Value
Colour	transparent pale yellow	Hardness (Shore A)	65 ± 5
Specific gravity	1.1	Ultimate tensile strength, MPa	12
Tear strength, N / cm	372	Flexural modulus, MPa	8.6
Compressive strength	27 N / mm^2	Elongation at break, %	400
Water absorption, % (stabilized)	0.5	Compression set, %	46
Water absorption, % (20 kg / cm^2, 10 days):	0.22	(ASTM D 395, method B): Volume resistivity, &!-cm, 500 V, 27°C	1.2 x 10^{12}
Insertion loss, dB	< 1	Echo Reduction, dB	< 1

3. SOLID LINEAR FLEXIBLE ACOUSTIC SENSOR ARRAYS FOR TOW APPLICATIONS

The present work is extended to design and develop solid linear acoustic sensor arrays for towing applications also. An important application of the solid array technology that emerged was to remedy the left-right (LR)

ambiguity of targets. The idea is to arrest the misalignment of the sensors due to twist and roll which, in turn, creates errors in LR resolution. Towards this, three independent array modules were fabricated which contained sensor modules as triplet units in three different environments. The first one is the array with completely solid PU moulded triplets (hereafter referred as Solid Array 2), the second is a hybrid one in which hydrophones are in an oil environment in a leak proof compartment and the mounting is compliant (hereafter referred as Hybrid Array). The third one is a conventional oil filled triplet sensor array (Oil filled array) for comparison with the other two. The triplet sensor units are shown in Fig. 1 and array modules are shown in Fig. 2. Each array consists of 9 triplet units, heading sensors, depth sensors and allied electronics. The modules are interconnectable through electro mechanical connectors. The total array is a 27 triplet sensor array and 15 m long. Data from the array was received through an FOM cable. Extensive acoustic performance evaluation was performed for the array, both in stationary and towed configurations.

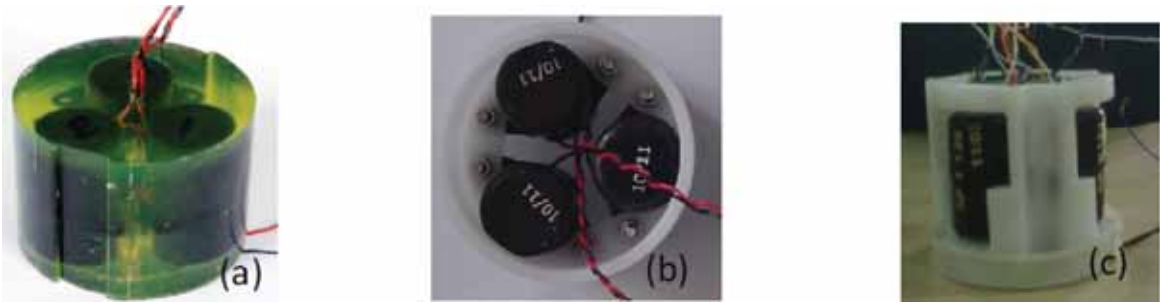

Fig. 1. (a) PU moulded LR triplet hydrophones (b) triplet hydrophone arranged in delrin compartment for hybrid array (c) triplet hydrophone for oil filled module

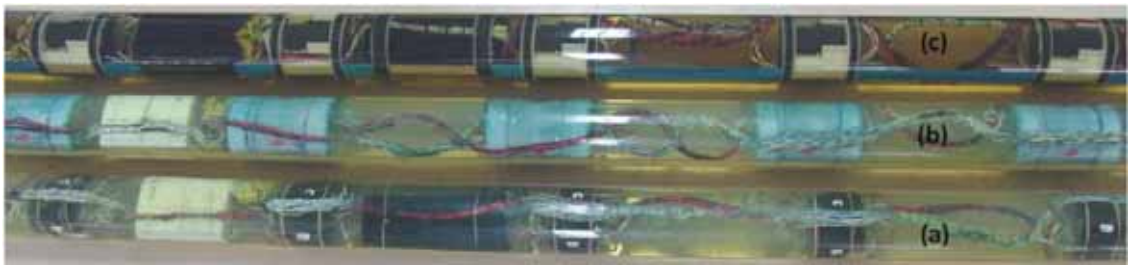

Fig. 2. (a) Solid array 2 (b) Hybrid array (c) Oil filled array modules

4. RESULTS AND DISCUSSIONS

4.1 Acoustic evaluation of solid linear sensor arrays in seabed configuration for stationary applications (Solid array 1)

A schematic of Solid array 1 is shown in Fig 3.

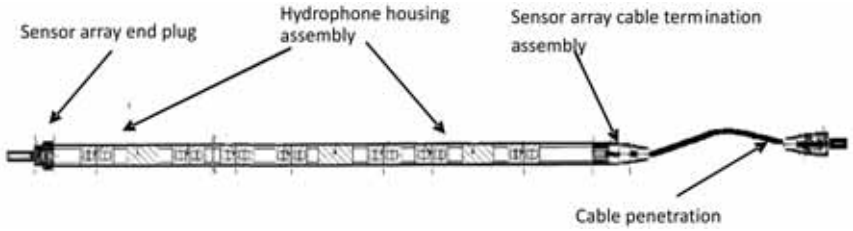

Fig. 3. Schematic of solid linear acoustic sensor array and its major components

Acoustic evaluation of Solid array 1 was performed by monitoring the time domain signals and frequency spectrum of individual channels and multi channel signals and was compared with a similar oil filled array (OFA). A 1.5 kHz transmission signal from a projector was used as input. The time- bearing tracks processed by the signals received at the hydrophones of both the arrays was performed by target tracking experiments in a lake. Representative channel wise frequency spectrum amplitude of both the arrays are shown in Fig. 4a and beam forming results for target tracking are given in Fig. 4b

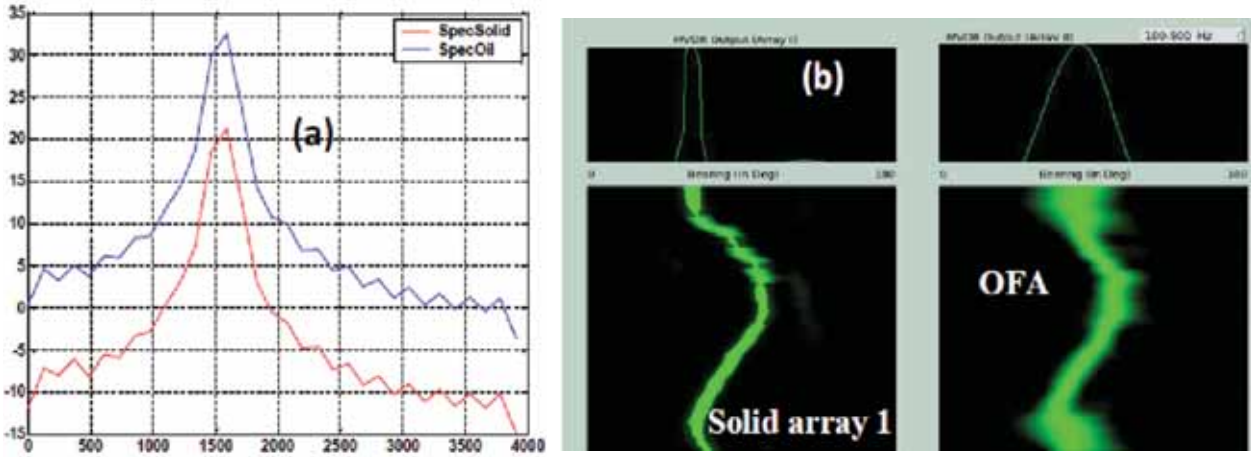

Fig. 4.(a) Representative channel wise frequency spectrum of Solid array 1 and OFA
(b) target tracking result of Solid array 1 and OFA

The signals are better and the beam width is sharper for Solid array 1, whereas those of OFA are diffused. Solid array 1 has no outer plastic tube and the acoustic signals are transferred directly from water to the sensors inside through the acoustically transparent matrix material. In OFA, the sensors are placed in an oil filled tube by means of a polyacetal casing. Hence, the acoustic signals have to encounter more interfaces such as water / outer tube, tube / oil, oil / casing, etc. and the loss of acoustic energy due to these interfaces are obviously more, which leads to the inferior performance for OFA, when compared to Solid array 1.

4.2 Acoustic evaluation omf solid linear sensor arrays in towed array configuration (Solid array 2, Hybrid array and Oil filled array)

Acoustic performance evaluation results for the three arrays shown in Figure 2a, 2b and 2c was carried out both in stationary and towed conditions in underwater lake facility. Ambient noise level of each sensor channel and its power spectral density and the beam output noise level were measured for the individual array modules in stationary condition. The same experiments were also repeated in generated wake condition. A comparison of the influence of wake on the performance of the individual array modules was made. Signal detection levels in stationary condition were measured both when the arrays were inside the wake and not inside the wake. The position of the arrays were so adjusted that the effect of position was nullified. The loss of performance by the influence of wake was compared. The arrays were towed at two different speeds and similar experiments were carried out to compare the performance of the arrays in towed condition.

Noise level measurements for each sensor channel as well as the beam output noise levels show that wake noise was minimum for the hybrid array compared to the oil filled and the solid arrays (Fig. 5a). The performance comparison for signal transmission experiments (continuous wave, 3 kHz) in static condition is given in Fig. 5 b. Maximum signal pick up and SNR was obtained for the hybrid array compared to the oil filled and the Solid array 2 in wake. Adverse effect of wake towards signal pick up was minimum for the Hybrid array. The reduction in signal level for each array due to wake is given in Table 2.

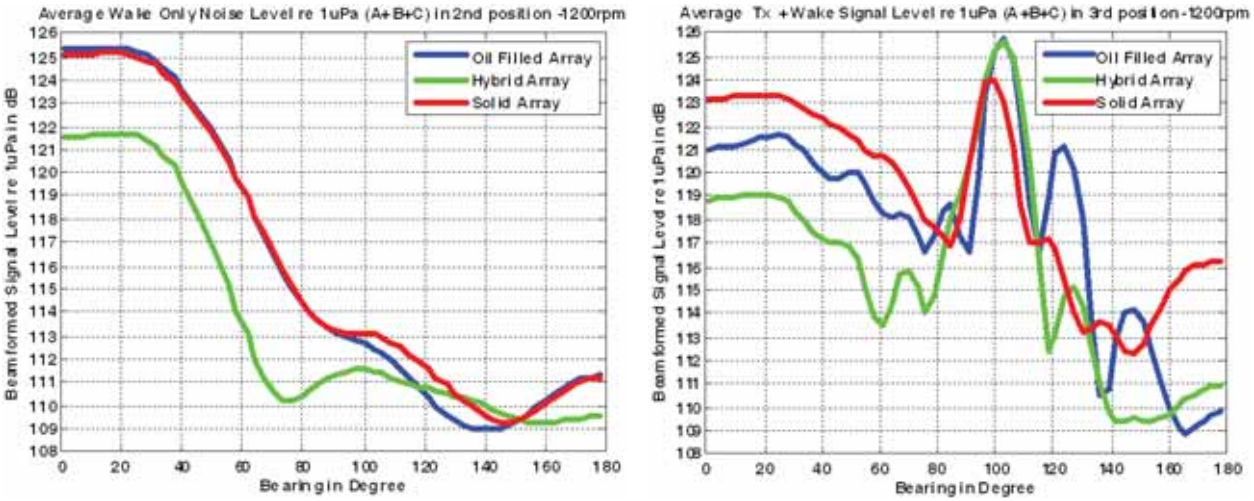

Fig. 5. (a) Noise level data for the three arrays in presence of wake (propeller speed, 1200 rpm), (b) beam formed signal level output for the three arrays in presence of wake for an input of 3 kHz CW

Table 2. Reduction signal levels when the arrays in wake (compared with 'no wake' condition)

Array positions	Reduction in signal level when arrays are in wake (dB)		
	Oil Filled array	Solid array	Hybrid array
Position 1	18	12.5	4.6
Position 2	15.3	11.3	6.7
Position 3	13.7	8.5	4.2

The arrays were towed at two speeds 8 km / h & 11.5 km / h. The noise levels (Fig 6 a & b) are lowest for the Hybrid array during towing also. Signal pick up for 3 kHz CW (Fig. 7 a.) was found to be higher for Hybrid array along with minimum no. of side lobes. The corresponding waterfall display (Fig. 7b) is also shown.

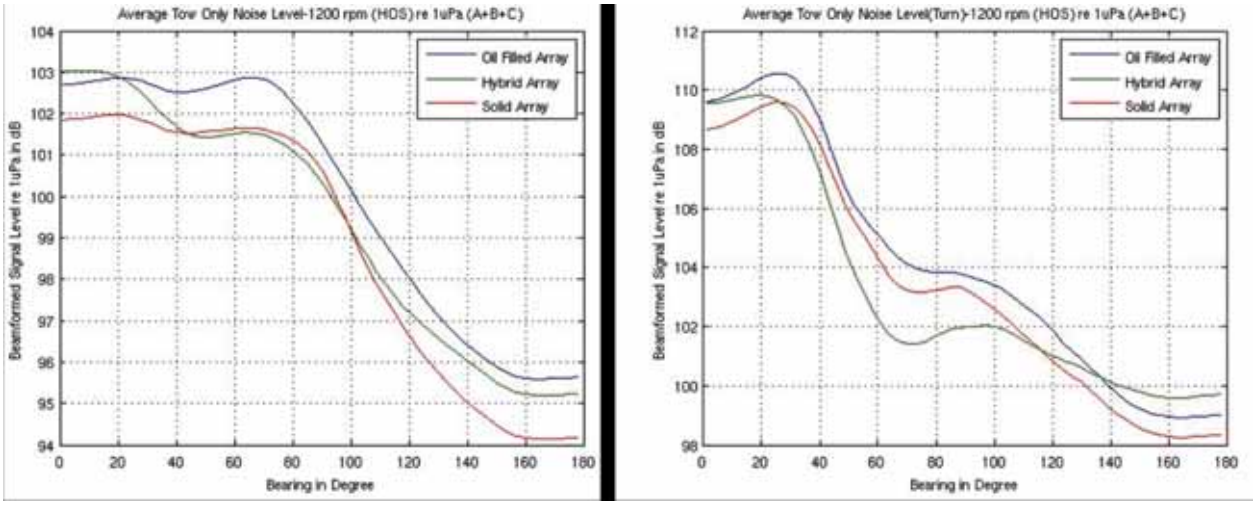

Fig. 6. Noise levels during straight run (a) & during turn (b) while towing

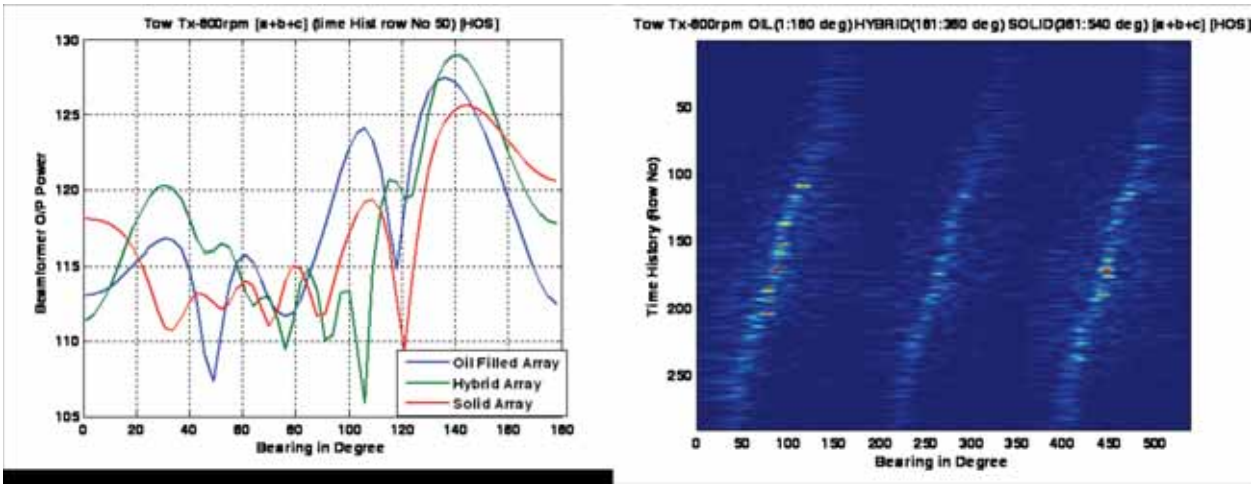

Fig. 7. (a) signal pick up by the arrays on towing & (b) corresponding waterfalls display

The influence of wake on all the arrays in the absence and presence of signal transmission was also studied. The signal level obtained by the three modules with 3 kHz continuous wave signal transmissions and the performance in wake studies showed that the Hybrid array was least affected by the presence of wake, whereas the wake affected the performance of the oil filled array considerably and the that of solid array to a lesser extent, as shown in Table 2. The signal pick-up by the solid and hybrid array modules are better than oil filled array in the presence of wake.

5. CONCLUSIONS

A novel solid polymer embedded linear acoustic sensor in stationary configuration for seabed sensor array application was designed and developed. It is established that this can be used successfully as an acoustic sensor array for geophysical and military applications. The solid array route for developing flexible linear sensor arrays was extended to develop towed arrays also. The performance of these arrays were compared with that of a conventional oil filled array by extensive acoustic evaluation performed, both in stationary and towed configurations. The influence of wake was also studied. The results indicated that the solid arrays are suitable, and better compared to conventional oil filled arrays, for passive underwater acoustic surveillance. The study is highly beneficial towards development advanced sensor arrays.

6. REFERENCES

[1] T. L. MCKEY and A. STENZEL A., 2008. Fluid filled sensor mount for gel filled streamer and streamer made therewith, *US Patent* 0186803 A1, 10.

[2] A. HALVORSEN, R. RUSTAD and E. AKER, 2005. Gel-filled seismic streamer cable, *US Patent*, 6879546 B2.

[3] ZHANG XIANG, LI SHU-QIU, 2011. Performance analysis of solid towed array, *American Journal of Engineering and Technology Research*, **11**(9), 1626-1631.

[4] ANDREW KNIGHT, 1996. Flow noise calculations for extended hydrophones in fluid and solid filled towed arrays, *Journal of Acoustical Society of America*, **100**(1), 245-251.

[5] PGS Solid streamer: RDH-S, Tech link, PGS Geophysical, **5**(7) 2005.

[6] P.J. WELTON, A. D. MEYER, J. K. ANDERSON, 2001. Solid fill acoustic array, *US Patent* 6262944

[7] RAHNA K. SHAMSUDEEN, V. G. JAYAKUMARI, S. SUBHASH SUBRAMONIAM and T. MUKUNDAN. A Prototype Solid Flexible Acoustic Sensor Array Module Patent solid array, *Indian Patent*, Filed, 1211/DEL/2009

Journal of Acoustical Society of India : Vol. 42, No. 3, 2015 (pp. 132-138)

Long-Range Passive Localization of Marinemammals with a Dense Towed Horizontal Receiver Array

Zheng Gong[1], Duong Tran[1], Nicholas Makris[2] and Purnima Ratilal[1]
[1]Department of Electrical and Computer Engineering, Northeastern University, Boston, Massachusetts 02115,
[2]Department of Mechanical Engineering, Massachusetts Institute of Technology, Cambridge, Massachusetts 02139
**e-mail: purnima@ece.neu.edu*

[Received: 26.12.2013; Revised: 10.05.2014; Accepted: 15.09.2014]

ABSTRACT

Approaches for instantaneous long-range passive localization of marine mammals using a single densely-sampled towed horizontal receiver array in a random range-dependent ocean waveguide have been examined[21]. They include (1) moving array triangulation (MAT), which combines measurements made on adjacent or widely separated finite apertures of a single towed receiver array and employs the conventional triangulation ranging algorithm for localizing sources located in the near- or far-field of the receiver array; (2) array invariant(AI), a technique that exploits the dispersive modal arrival structure of the acoustic field in an ocean waveguide to estimate the source range for sources located off the broadside beam of the receiver array; (3) the bearings-only target motion analysis in modified polar coordinates implemented using the extended Kalman filter (MPC-EKF) where the bearing and range components of the source location and velocity state vector are decoupled, and (4) bearings-migration minimum mean square error (MMSE), which is also based on triangulation but combines sequential bearing measurements in a global inversion for the mean source position over the measurement time interval. The passive source localization methods are calibrated by applying them to localize and track a vertical source array deployed in the far-field of a towed horizontal receiver array during the Gulf of Maine 2006 experiment[21,2,3]. The source transmitted intermittent broadband pulses in the 300-1200 Hz frequency range and was located between 1 to 20 km from the receiver array. A nonlinear matched-filter kernel designed to replicate the acoustic signal measured by the receiver array is applied to enhance the signal-to-noise ratio (SNR). The performance of the passive source localization methods are determined by comparing the estimated source position with the true positions obtained from Global Positioning System (GPS) measurements of source and receiver locations. Finally, passive localization of marine mammals from their vocalizations received on a dense towed horizontal array employing the approaches investigated here is discussed.

1. INTRODUCTION

Current approaches for passive localization and motion tracking of marine mammals[1-3] in an ocean waveguide include hyperbolic ranging[4-5] with measurements from two or more widely separated single hydrophones

or vertical receiver arrays, and triangulation[6-7] from measurements made on two or more horizontal receiver arrays. Some other passive acoustic methods for localizing sperm whales from their click signals use either hyperbolic ranging with a small network of single hydrophones,[8] or combine multipath time-delay measurement of click reflections from ocean boundaries acquired with a single hydrophone or two-element array.[9-1] The hyperbolic ranging approach is limited to localizing marine mammals present within or close to the near-field of the sensor configuration. So the localization range in practical applications is often limited to ten kilometers or less.

Here, four distinct approaches for instantaneous passive localization and tracking of acoustic sources over long ranges with measurements made on a single high-resolution towed horizontal receiver array in a random range-dependent ocean waveguide are examined[21]. Towed horizontal receiver arrays are employed in a wide range of applications in the ocean, such as naval operations for detecting and tracking underwater vehicles;[11] active and/or passive sensing of marine life,[1-3] oceanography[12] and ocean geology;[13] and for oil and natural gas exploration.[14] An advantage of sensing with a horizontal array of hydrophones is that the bearing of the sound source can be directly obtained by beamforming the received signals so that only the range of the source to the receiver has to be determined. The passive source localization methods investigated here are calibrated by applying them to localize and track a vertical source array deployed in the far-field of a towed horizontal receiver array during the Gulf of Maine 2006 experiment (GOME'06).[2-3] The localization errors are determined by comparing the estimated source position with the true positions obtained from Global Positioning System (GPS) measurements of source and receiver locations.

2. PASSIVE SOURCE LOCALIZATION METHODS WITH TOWED RECEIVER ARRAY

2.1 Moving Array Triangulation

The MAT[21] method combines bearing measurements from spatially separated apertures of a towed horizontal receiver array and employs the conventional triangulation ranging algorithm[15-16] for localizing a source that may be in the near- or far-field of the array. At each time instance , the source range is determined as the third point of a triangle from the intersection of the straight lines from pairs of source bearing estimates. This process is repeated for every adjacent pair of source bearing estimates. Finally, the sequential source range estimates are mapped onto a Cartesian grid to predict the source trajectory.

Consider the geometry shown in Fig. 1, where the origin of the coordinate system is placed at the receiver array center at the start of a tow track at time $t = 0$. The x coordinate points East and the y coordinate points North. The angular course of the array center $\theta(t)$ is measured clockwise from true North, and the corresponding receiver array center positions $\mathbf{r}_r(t) = (x_r(t), y_r(t))$ are determined from the ship-board GPS. With a high-resolution horizontal line-array,[3] the bearing of the source can be estimated by conventional plane-wave beamforming.[3,17] Let $\hat{\mathrm{B}}_0 = [\hat{\beta}_0(\mathrm{t}_1), \hat{\beta}_0(\mathrm{t}_2), \cdots, \hat{\beta}_0(\mathrm{t}_N)]$ be the sequential source bearing estimates measured clockwise from true North. The projected source range $\hat{R}_0$, tangent to the receiver tow track as shown in Fig. 1, at each time t has the following relationship

$$\int_{t-\Delta t}^{t} v_r(\tau)d\tau = \hat{R}_0(t)\left\{\cot\left[\hat{\beta}_0(t-\Delta t)-\theta(t)\right]-\cot\left[\hat{\beta}_0(t)-\theta(t)\right]\right\} \tag{1}$$

where $v_r(\tau)$ is the corresponding GPS-measured receiver array velocity. Taking the time-derivative on both sides of Eq. (1), we can obtain

$$\hat{R}_s^{MAT}(t) = \frac{\hat{R}_0(t)}{\sin\gamma(\mathrm{t})} = \frac{\overline{v}_r(t)\cdot\sin\gamma(t)}{\dot{\hat{\beta}}_0(t)} \tag{2}$$

in terms of the time-derivative of source bearing estimates $\dot{\hat{\beta}}_0(t) = d\hat{\beta}_0(t)/dt$ *(rads · s^{-1})* and mean receiver array velocity $\overline{v}_r(t) = \sqrt{\left[x_r(t)-x_r(t-dt)\right]^2+\left[y_r(t)-y_r(t-dt)\right]^2}\,/dt$ *(m· s^{-1})*. Then the source horizontal location $\hat{r}_s^{MAT}(t) = \left(\hat{x}_s^{MAT}(t), \hat{y}_s^{MAT}(t)\right)$ is obtained from :

$$\hat{x}_s^{MAT}(t) = x_r(t) + \hat{R}_s^{MAT}(t)\cos\phi(\mathrm{t})$$
$$\hat{y}_s^{MAT}(t) = y_r(t) + \hat{R}_s^{MAT}(t)\sin\phi(\mathrm{t}) \tag{3}$$

where $\phi(\mathrm{t}) = \pi/2 - \hat{\beta}_0(t)$.

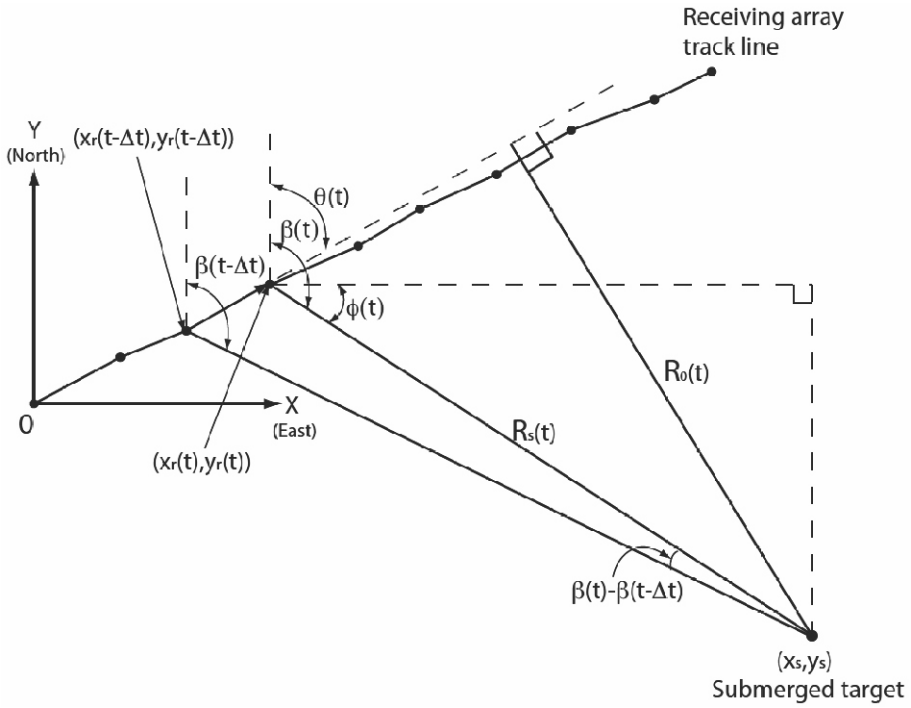

Fig. 1. Typical source-receiver geometry for two-dimensional source localization in the horizontal ocean plane using moving array triangulation method, given that the source is relatively stationary in space between adjacent bearing estimates.

The MAT can be implemented either by directly using pair of source bearing estimates $\hat{\beta}_0(t-\Delta t)$ and $\hat{\beta}_0(t)$ or by using bearing derivative $\dot{\hat{\beta}}_0(t)$ instead. In the case when there is a constant bias in source bearing estimates or the source bearing estimation error is large, the source localization results obtained by MAT using bearing derivatives are more accurate than those obtained using pair of source bearings. The MAT method is applicable for localizing and tracking a stationary source. For a non-stationary source with velocity $v_s(t)$, MAT can still provide accurate and robust source localization if the condition $v_s(t) << v_r(t)$ is satisfied, and, if the source is at or near the broadside direction of the receiver array.

2.2 Array Invariant

The array invariant (AI) method[18] provides instantaneous source range estimation by exploiting the multi-modal dispersive behavior of guided wave propagation in a dispersive ocean wave-guide. The AI is applied to passive beam-time intensity data obtained after conventional plane-wave beamforming and matched filtering of acoustic measurements received on a horizontal array of hydrophones. It has been shown in Ref. 18 that the migration angle of maximum beam-time intensity, defined as the array invariant χ_h, is invariant to environmental parameters but follows a known and unique dependence on source-receiver range.

Here, we apply Eqs. (28) and (27) of Ref. 18 to estimate the array invariant $\hat{\chi}_h$ and the source range $\hat{R}_s^{AI}$ respectively from beam-time intensity data $L_{bt}(s, t)$ collected in the Gulf of Maine continental-shelf waveguide.

Similar to MAT, the AI-estimated source positions $\hat{\mathbf{r}}_s^{\mathbf{AI}}(t) = \left(\hat{x}_s^{AI}(t), \hat{y}_s^{AI}(t)\right)$ can be calculated using Eq. (3), given the known receiver array position $\bar{R}_i = [\hat{R}_s^{MAT} + \hat{R}_s^{AI}]/2$ and $\phi(t)$.

2.3 Recursive nonlinear filters for bearings-only TMA

There are many existing recursive type nonlinear filters in Bayesian framework available for bearings-only source localization and tracking with a single moving observer. Here the modified polar coordinate extended Kalman filter (MPC-EKF) is employed to estimate source horizontal trajectory because (1) it is computationally efficient, (2) it can provide asymptotically unbiased source state estimates,[19] and (3) it automatically decouples the observable bearing from the unobservable range component of the estimated source state and prevents error covariance matrix ill-conditioning.[19] Detailed formulation of the MPC-EKF is given by Eqs. (6.47) to (6.55) in Sec. (6.4.1.1) and Eqs. (6.110) to (6.116) in Sec. (6.7) of Ref. 20, and Eqs. (B1) to (B13) in Appendix B of Ref. 19.

Accurate initialization of the source state vector and error covariance matrix are essential for the MPC-EKF to achieve reliable tracking performance.[19-20] The initialization procedure is described by Eqs. (6.56) to (6.78) in Sec. (6.4.1.1) of Ref. 20. Here we use the averaged initial range estimates from the MAT method and the AI method, $\bar{R}_i = [\hat{R}_s^{MAT} + \hat{R}_s^{AI}]/2$, and the first bearing estimate $\hat{\beta}_0(\mathrm{t}_1)$ as inputs to initialize the MPC-EKF in scenarios where the source is located off the endfire beam of the receiver array.

2.4 Bearings-migration Minimum Mean Square Error method

The MMSE[21] method is derived for estimating the mean source position over a measurement time interval when multiple source bearing measurements are available. For a towed horizontal receiver array and a spatially stationary source, the sequential source bearing measurements will follow a unique, unambiguous, and nonlinear migration route over time. Taking advantage of the one-to-one mapping between the source position and the bearing-migration path for the statistically stationary source, the expected mean source position

$$\hat{\bar{\mathbf{r}}}_s^{\mathrm{MMSE}} = \arg\min_{\hat{\bar{\mathbf{r}}}_s \in \mathbf{S}} \mathrm{MSE}(\hat{B}(\hat{\bar{\mathbf{r}}}_s)) = \arg\min_{\hat{\bar{\mathbf{r}}}_s \in \mathbf{S}} \mathrm{E}\left[\left(\hat{B}(\hat{\bar{\mathbf{r}}}_s) - \hat{B}_0\right)^2\right] \quad \textbf{(4)}$$

is determined by minimizing the mean square error of sequential source bearing estimates, where $\hat{B}(\hat{\bar{\mathbf{r}}}_s)$ is a sequence of theoretical source bearings for the source position $\hat{\bar{\mathbf{r}}}_s$ within the search space **S** of all source positions, $\forall \hat{\bar{\mathbf{r}}}_s \in \mathbf{S}$, and $\hat{B}_0$ is the measured source bearing from the receiver array obtained by conventional beamforming.

3. LOCALIZATION AND MOTION TRACKING OF A VERTICAL SOURCE ARRAY

We apply the (1) MAT, (2) AI, (3) MPC-EKF, and (4) MMSE methods to localize and track the horizontal trajectory of a vertical source array using measurements made on a towed horizontal linear receiver array during GOME'06.[2-3] A total of 42 tracks of the towed receiver array with relative source bearing spanning from broadside to endfire of the towed receiver array were analyzed and the localization accuracy quantified in terms of a normalized bias of the mean source position estimate and the fractional root mean-square error of the instantaneous source range estimates along a track (see Fig 2 for an example). The AI was found to be the most consistent in its performance maintaining a roughly 7% normalized bias in mean source position estimate and 8% fractional RMS error in source horizontal trajectory tracking over a wide range of tracking scenarios. The performance of the MAT and MMSE varied widely depending on the tracking scenario. The MAT led to as small as 2-3% normalized bias and 3-5% fractional RMS error when localizing moored sources, but was not reliable for localizing sources located within or near the endfire beam of the receiver array or for fast moving sources. The MPC-EKF was shown to be the most favorable approach for localizing moving sources with less than 6% normalized bias when the source range estimates from the MAT and AI are used to initialize the Kalman filter. It also provided the best mean source position estimates with roughly 6%

normalized biases averaged over all tracking scenarios, and yielded relatively small (roughly between 7 and 12%) fractional RMS errors, slightly larger than those of the AI (<9%). The most reliable technique for localizing sources within or near the the endfire beam of the towed receiver array was the AI regardless of whether the source was moving or moored.

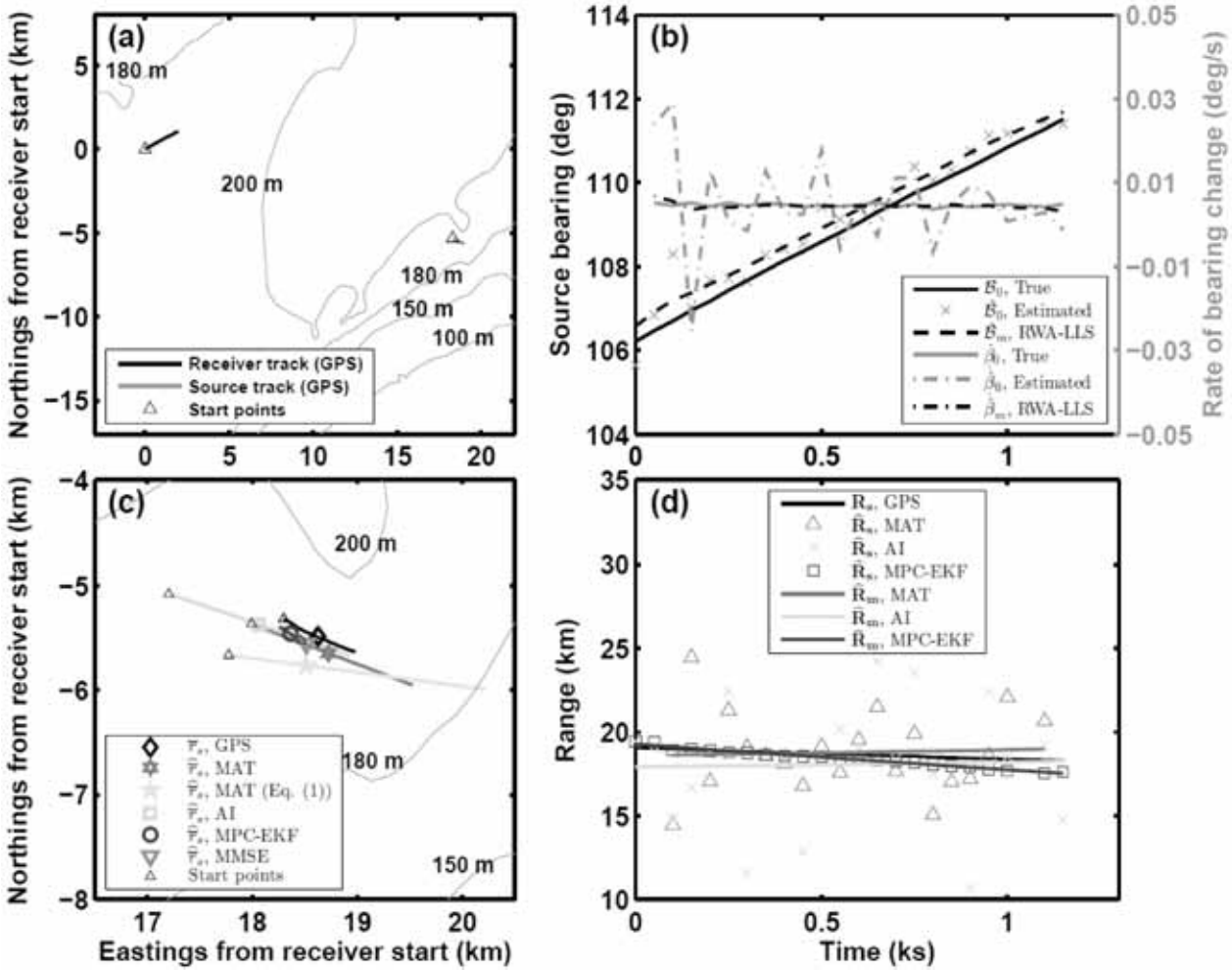

Fig. 2. Passive localization and tracking of a vertical source array using a high-resolution towed horizontal receiver array during Gulf of Maine 2006 Experiment. (a) Source-receiver geometry; (b) true (GPS) and beamformed source bearings, (c) estimated source horizontal trajectories and corresponding mean source positions estimated using the MAT and AI methods match well with the GPS-measured true source horizontal trajectory and mean position; (d) Instantaneous source range estimates and the linear-least-squares (LLS) fitted results from the MAT and AI methods are compared to the GPS-derived true source ranges.

4. LOCALIZATION AND TRACKING OF MARINE MAMMALS

The four passive source localization methods discussed here have been applied to localize and track numerous humpback whale *(Megaptera novaeangliae)* individuals from their vocalizations in the 200 Hz to 800 Hz range received on a towed horizontal receiver array during their Fall 2006 feeding season in the Gulf of Maine. The farthest whale localized extended roughly 100 km range from the receiver array. The MAT method has also

been applied to localize and track several sperm whales *(Physeter macrocephalus)* in the shallow Gulf of Maine and deeper continental slope region south of Cape Cod in the US East Coast from the low frequency component of their vocalizations in the 300 to 2500 Hz range comprising of echolocation and social clicks received on a towed horizontal receiver array. The approach and results presented here can be applied to address the feasibility of monitoring marine mammals from long ranges with other low frequency towed receiver array systems, such as those used in naval and geophysical applications, where it may be important and necessary to remotely sense marine mammal activity from long ranges.

5. CONCLUSIONS

Four methods for passive localization and motion tracking of a source located in the far-field of a towed horizontal receiver line array have been examined. They are (1) moving array triangulation, (2) array invariant, (3) bearings-only target motion analysis in modified polar coordinates via the extended Kalman filter, and (4) bearings-migration minimum mean-square error. The methods were calibrated by applying them to localize and track a vertical source array deployed in the far-field of a towed horizontal receiver array during the Gulf of Maine 2006 experiment (GOME'06). The four methods have also been applied to instantaneously localize and track both baleen and toothed whales in the US Northeast Coast using a dense towed horizontal receiver array from their received vocalizations.

6. REFERENCES

[1] N. C. MAKRIS, P. RATILAL, D. T. SYMONDS, S. JAGANNATHAN, S. LEE and R. W. NERO, 2006. "Fish population and behavior revealed by instantaneous continental shelf-scale imaging", *Science* **311**, 660-663.

[2] N. C. MAKRIS, P. RATILAL, S. JAGANNATHAN, Z. GONG, M. ANDREWS, , I. BERTSATOS, O. R. GØDO, R.W. NERO and J. M. JECH, 2009. "Critical population density triggers rapid formation of vast oceanic fish shoals", *Science* **323**, 1734-1737.

[3] Z. GONG, M. ANDREWS, S. JAGANNATHAN, R. PATEL, J. M. JECH, N. C. MAKRIS and P. RATILAL, 2010. "Low-frequency target strength and abundance of shoaling Atlantic herring (Clupea Harengus) in the Gulf of Maine during the Ocean Acoustic Waveguide Remote Sensing 2006 Experiment", *J. Acoust. Soc. Am.* **127**, 104-123.

[4] J. L. SPIESBERGER and K. M. FRISTRUP, 1990. "Passive localization of calling animals and sensing of their acoustic environment using acoustic tomography", *Am. Nat.* **135**, 107-153.

[5] S. MITCHELL and J. BOWER, 1995. "Localization of animal calls via hyperbolic methods", *J. Acoust. Soc. Am.* **97**, 3352-3353.

[6] E. J. HILLIARD and R. F. PINKOS, 1979. "An analysis of triangulation ranging using beta density angular errors", *J. Acoust. Soc. Am.* **65**, 1218-1228.

[7] Y. D. HUANG and M. BARKAT, 1991. "Near-field multiple source localization by passive sensor array", IEEE Trans. *Antennas Propag*. **AP-39**, 968-975.

[8] P. M. BAGGENSTOSS, 2011. "An algorithm for the localization of multiple interfering sperm whales using multi-sensor time difference of arrival", *J. Acoust. Soc. Am.* **130**, 102-112.

[9] D. MATHIAS, A. M. THODE, J. STRALEY, J. CALAMBOKIDIS, G. S. SCHORR and R. D. ANDREWS, 2012. "Acoustic and diving behavior of sperm whales (Physeter macrocephalus) during natural and depredation foraging in the Gulf of Alaska", *J. Acoust. Soc. Am.* **132**, 518-532.

[10] D. MATHIAS, A. M. THODE, J. STRALEY and R. D. ANDREWS, 2012. "Acoustic tracking of sperm whales in the Gulf of Alaska using a two-element vertical array and tags", *J. Acoust. Soc. Am*. **134**, 2446-2461.

[11] S. G. LEMON, 2004. "Towed-Array History, 1917-2003", *IEEE J. Ocean. Eng.* **29**, 365-373.

[12] W. STEVEN HOLBROOK, P. PARAMO, S. PEARSE and R. W. SCHMITT, 2003. "Thermohaline fine structure in an oceanographic front from seismic reflection profiling", *Science* **301**, 821-824.

[13] M. SIDERIUS, P. L. NIELSEN and P. GERSTOFT, 2002. "Range-dependent seabed characterization by inversion of acoustic data from a towed receiver array", *J. Acoust. Soc. Am.* **112**, 1523-1535.

[14] N. R. CHAPMAN, J. F. GETTRUST, R. WALIA, D. HANNAY, G. D. SPENCE, W. T. WOOD and R. D. HYNDMAN, 2002. "High-resolution, deep-towed, multichannel seismic survey of deep-sea gas hydrates off western Canada", *Geophysics*, **67**, 1038-1047.

[15] G. C. CARTER, 1981. "Time delay estimation for passive sonar signal processing", *IEEE Trans*. **ASSP ASSP-29**, 463-470.

[16] J. C. HASSAB, 1989. *Underwater signal and data processing*, 205-308 (CRC Press, Boca Raton, FL).

[17] D. H. JOHNSON and D. E. DUDGEON, 1993. *Array Signal Processing: Concepts and Techniques*, 111-198 (Prentice Hall Inc, Upper Saddle River, New Jersey).

[18] S. LEE and N. C. MAKRIS, 2006. "The array invariant", *J. Acoust. Soc. Am.* **119**, 336-351.

[19] V. J. AIDALA and S. E. HAMMEL, 1983. "Utilization of Modified Polar Coordinates for bearings-only tracking", *IEEE Trans. Automat. Contr.* **AC-28**, 283-294.

[20] B. RISTIC, S. ARULAMPALAM and N. GORDON, 2004. *Beyond the Kalman Filter: Particle Filters for Tracking Applications*, 1-153 (Artech House, Norwood, MA).

[21] Z. GONG, D. TRAN and P. RATILAL, 2013. "Comparing passive source localization and tracking approaches with a towed horizontal receiver array in an ocean waveguide", *J. Acoust. Soc. Am.* 134.

Journal of Acoustical Society of India : Vol. 42, No. 3, 2015 (pp. 139-155)

Acoustics of Chants, Conch-shells, Bells and Gongs in Hindu Worship Spaces

M.G. Prasad and B. Rajavel
Noise and Vibration Control Laboratory, Department of Mechanical Engineering, Ste-vens Institute of Technology, Hoboken, New Jersey, 07030, USA
e-mail: mprasad@stevens.edu

[Received: 26.12.2013; Revised: 10.05.2014; Accepted: 15.09.2014]

ABSTRACT

Sound plays a very important role in Hindu worship spaces both at homes and temples. In Hindu temples the two chambers that have reverberant acoustic characteristics are the Garbha-Griha where the deity is consecrated and the Ardha-Mantapa which is a chamber in front of Garbha-Griha. The Vedic chants and prayers are recited and the sacred instruments such as conch-shells, bells, and gongs are played in these chambers. The Vedas, which are the foundational literature of Hinduism, are the collection of mantras chanted with precise acoustical characteristics. It is for this reason oral tradition has been very efficient in transmitting the Vedic chanting from master to disciple. The use of Vedic chants in Hindu worship is well known. In addition to Vedic chants, conch-shells, bells and gongs are also very commonly used to enhance the spiritual experience of the devotees during the worship. The sounds from these acoustically well designed conch-shells, bells and gongs are considered as sacred when they are used during worship. These sacred sounds help devotees in their concentration during worship in the sacred space. The sounds of conch-shell, bell and gong are used at various times during the worship. However, all of these sounds are simultaneously used at the end of the worship when camphor flame is offered to the deity. This acoustical experience is significant to the devotees in the worship. The conch-shell when unwound on an axis can be seen as a French horn. The sound from a conch-shell has very high quality factor indicating the sharpness of its resonance. The conch-shell is generally used at the beginning of the worship. Given the tonal quality of its sound, it captures the attention of the devotees and helps in focusing the mind to the worship. Similarly the bell is also used at the beginning of the worship. The sound of well-designed bell has a ringing sound that sustains for considerable duration. It is also noted that both the conch-shell and bell sounds acoustically resembles the chant of sacred sound of OM. The gong is generally played during the end of the worship along with bell and conch-shell. The gong is played as a percussion instrument with a nice rhythm. Generally the rhythmic gong sound is loud. When all these three instruments are played together at the end along with the chanting, one can experience the synergy of the various sounds adding to the spiritual experience of the devotees. The Hindu worship is seen as a celebration of the devotees having communion with God. This paper presents acoustical studies of chants and also of these instruments. The paper also discusses the importance of these sounds in their contributions to the acoustics of the worship spaces.

1. INTRODUCTION

Worship is the pinnacle of communication between God and human beings in many religions. Worship can be individualistic or communal. Individual worship can happen anywhere and anytime. However, the communal worship usually requires dedicated spaces such as temples, gurdwaras, churches, synagogues and mosques. Communication during the worship can take several forms. Praying mentally and contemplation can be silent whereas other forms of worship such as chants, songs and music all will involve sound [1-3]. Acoustics plays an important role in worship spaces in all cultures and religions of the world. This is natural as acoustics deals with sound, one of the senses of perception [4]. In Hinduism, acoustics is of major importance in various aspects of life namely spirituality, religion, culture, science, art etc. It is well known that sound plays a very important role in Hindu worship spaces namely homes, community halls and temples. The Vedas, which are the foundational literature of Hinduism, are the collection of mantras chanted with precise acoustical characteristics [5-8]. It is for this reason oral tradition has been very efficient in transmitting the Vedic chanting from master to disciple [7]. The use of Vedic chants in Hindu worship is well known. In addition to Vedic chants (vocal), conch-shells, bells and gongs are also very commonly used to enhance the spiritual experience of the devotees during the worship [9]. This paper presents acoustical studies of chants and of these instruments sounding individually as well as collectively. Figure 1 shows typical Conch-Shell, Bell and Gong instruments used for the study. The paper also discusses the importance of these instruments and their contributions to the acoustics of the Hindu worship spaces.

Fig. 1. Conch-Shell, Bell and Gong used in this study.

2. VEDIC PERSPECTIVES ON SOUND

Vedas are categorized into four namely Rig-Veda, Yajur-Veda, Sama-Veda and Atharvana-Veda. Vedas refer to the body of the knowledge that deals with physical, psychological and spiritual aspects of life and cosmos. The word “Veda” is etymologically related to a verbal root “Vid” meaning “to know”. In addition it is interesting to know that Vedas are collection of very large number of “mantras”, which are referred as Vedic chants. These Vedic chants have phonetic characteristics such as pitch, duration, emphasis, uniformity and juxta-position [7]. These Vedic chants are orally transmitted with extraordinary acoustic precision from master to disciples from ancient times to present times. It is well known that the acoustic precision in the oral transmission of Vedic chants, music and speech cannot be surpassed through writing [5, 7]. In 2003, UNESCO proclaimed that the oral tradition of the Vedic chanting as an intangible cultural heritage of the world. The proclamation recognizes that *“..To ensure that the sound of each word remains unaltered, practitioners are taught from childhood complex recitation techniques that are based on tonal accents, a unique manner of pronouncing each letter and specific speech combinations”* [7].

The art and science of acoustics have received a high importance in the Vedic literature. The chants along with both vocal and instrumental music are playing major role in Hindu tradition from ancient times to the present. This is noted by Sir C.V. Raman that *"it would form a fascinating chapter of history to try and trace the gradual development of musical instruments and musical knowledge, from the rhythmic chanting of the Rig-Veda in the ancient home of Aryan race to the Indian music of the present day"* [8]. In Vedic literature the production of human speech is emphasized. This could be due to the importance of acoustical aspects of Vedic chants. The speech production according to Vedic view can be described through four stages. These four stages are called as Para, Pashyanti, Madhyama and Vaikhari. These four stages are integrally connected to the yoga aspects of Vedic tradition. Among these four stages the last stage namely Vaikhari refers to fully manifested speech sounds from the human speaker propagated to the listener. The other three stages namely Para, Pashyanti and Madhyama refers to the stages internal to the human speaker. The fourth stage of Vaikhari encompasses various types of acoustic expressions in human life. They can be represented (as shown in Fig. 2) by speech, music, literature and spirituality. This model for four stage development of speech sounds can also be generalized conceptually to production of sound [10].

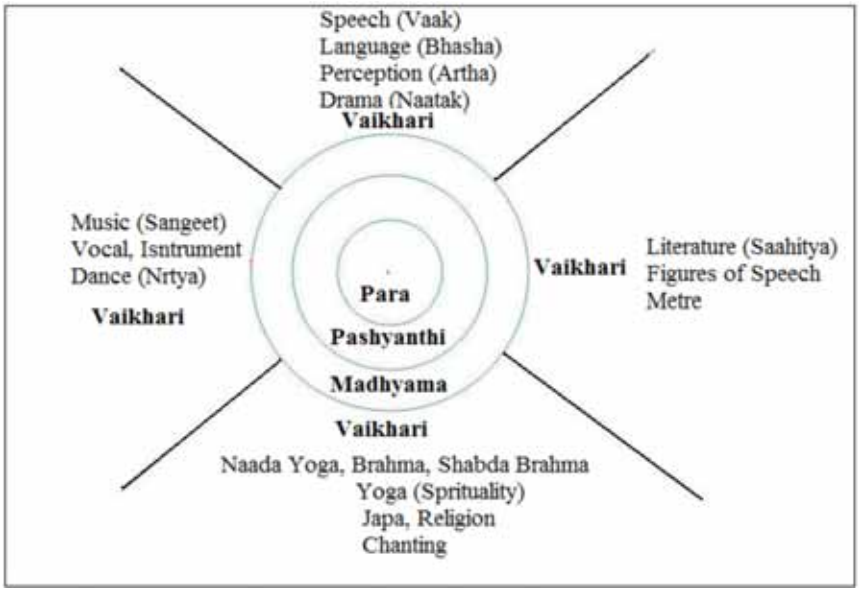

Fig. 2. Representation of the four fields of sound at Vaikhari level.

The philosophical and spiritual aspects of sound are also very much emphasized in Vedic Hindu tradition. It is interesting to note that the commonly referred five basic elements in Vedic literature namely space, air, fire, water and earth are related to corresponding senses of perception [5, 11]. The subtle to gross order of correspondence according to the Vedic tradition is shown in Table 1. It is interesting to note that the spatial experience is solely related to the sense of sound perception.

Table 1. The order of correspondence according to the Vedic tradition

Space	Sound
Air	Touch, Sound
Fire	Form, Touch, Sound
Water	Taste, Form, Touch and Sound
Earth	Smell, Taste, Form, Touch and Sound

3. ACOUSTICAL ASPECTS OF HINDU WORSHIP SPACES

Temples (devaalayas or mandirs) as worship spaces have been an integral part of Hindu religion from ancient times. Hindu temples in India and around the world are marvels of art and architecture. Hindu temples play a major role in not only performing various sacraments and celebrating festivals but also a resource for spiritual development. In addition to Hindu temples as worship spaces, Hindus also use spaces such as community halls and specified space in their homes as spaces of worship. The worship practice in general consists of a priest performing the worship on behalf of the congregation. However, at some stages of worship devotees chant together mantras and recite prayers along with the priest. Devotees also sing together songs as prayers and they are known as bhajans and kirtans. In addition to the mantras and bhajans, instruments such as bells, gongs and conch-shells are also used in the worship.

The most important space in a Hindu temple is the space where the deity is installed. This space is known as "Garbha-Griha" in Sanskrit, which means a "womb-chamber". This is also referred as sanctum-sanctorum. The dimensions of this chamber are based on the size of the deity. This chamber has only a door and no windows. Only the priest is allowed in this chamber for worship through chants and prayers. Generally the priest also rings a hand-bell during the worship along with chants. Generally this chamber is built of walls made of stones. The interesting acoustical fact is that this chamber is highly reflective and has a high reverberation time. In addition, this womb-chamber is generally connected to another space through its door opening. This attached second space is generally called as "Ardha-Mantapa" which means "half-chamber" to indi-cate that this space is about half the floor size of the Garbha-Griha. The Ardha-Mantapa is also made of stones and is highly reflective with high reverberation time. The scriptures called *Agama Shastras* on temple design prescribe that the whole temple is designed based on the size of the deity installed in the Garbha-Griha. The acoustical importance of Ardha-Mantapa is that a number of priests in addition to the main priest in the Garbha-Griha chant in unison and also the instruments such as conch-shells, bells and gongs are sounded. Generally the Ardha-Mantapa leads to a "main hall" referred as "Maha-Mantapa". It is in this Maha-Mantapa where a large number of devotees assemble and participate in the worship [12-14]. The Narayanaswami temple at Melkote, near Mysore city, Karnataka, India is a well-known temple dated back to 11th century A.D. Figure 3 shows the floor plan of the temple. The spaces noted as 1, 2 and 3 in Fig. 3 are the Garbha-Griha, Ardha-Mantapa and Maha-Mantapa respectively. The dimensions of the Garbha-Griha are 7 ft 10 in. x 8 ft 2 in. (2.39 m x 2.49 m) with a height of 10 ft (3.05 m). The dimensions of the Ardha-Mantapa are 13 ft x 6 ft 9 in. (3.96 m x 2.06 m) with a height of 10 ft (3.05 m) [15].

The two temples in which acoustical measurements were made are Sri Venkateswara Temple of the *Hindu Temple and Cultural Society* in the Bridgewater, New Jersey, USA shown in Figure 4(a) and The Sri Lakshmi- Sri Narayana Temple of the *Hindu Temple Society of Capital District* in Albany, New York, USA shown in Fig. 5(a). Figure 4(b) shows the details of Ardha-Mantapa and Garbha-Griha of the deity Sri Venkateswara and the corresponding main hall. The details of Ardha-Mantapa and Garbha-Griha of the deities of Sri Lakshmi and Sri Narayana and the corresponding main hall are shown in Fig. 5(b). In both temples there are many other deities. In both temples the sound pressure level recordings were made outside but near the Ardha-Mantapa in the main hall. The priest chanted in the Ardha-Mantapa and also the conch-shell, bell and gong sounds were produced in the Ardha-Mantapa. Similarly sound recordings were made in a community hall environment and an anechoic chamber. The sound pressure level increases at the position outside the Ardha-Mantapa of each temple. This is due to reverberation effects of combined Garbha-Griha and Ardha-Mantapa in comparison with the corresponding position in the free field. The increase in sound pressure level can be predicted using the following room acoustic equations.

(a) if we model the entire Garbha-Griha and Ardha-Mantapa space as highly reflective and diffuse field then the sound pressure level (SPL) at any given point,

$$L_{P1} = L_w + 10\log\left[\frac{4}{R}\right] \tag{1}$$

(b) However, If we assume the room (such as Garbha-Griha and Ardha-Mantapa) space as entirely

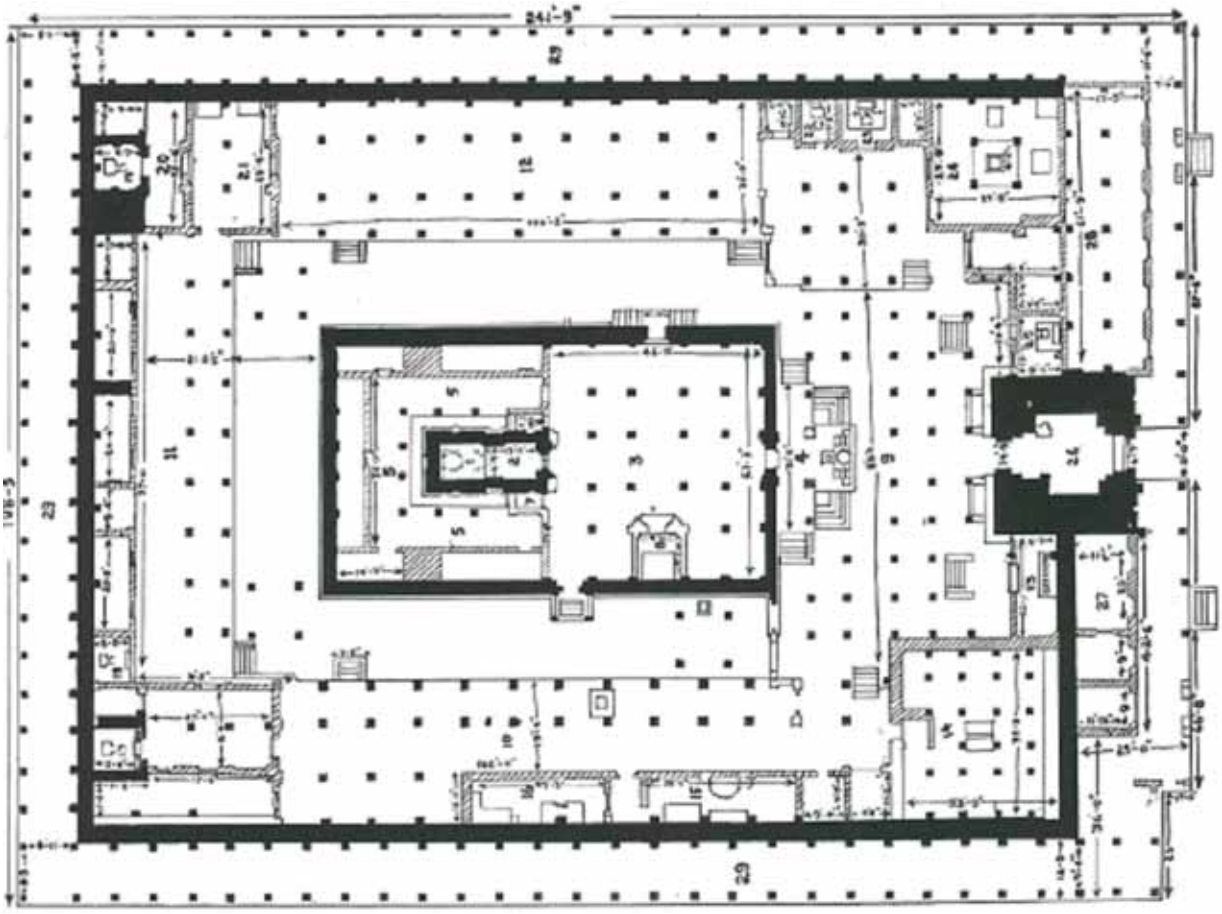

Fig. 3. Floor plan of The Narayanaswami Temple at Melkote, Karnataka, India.

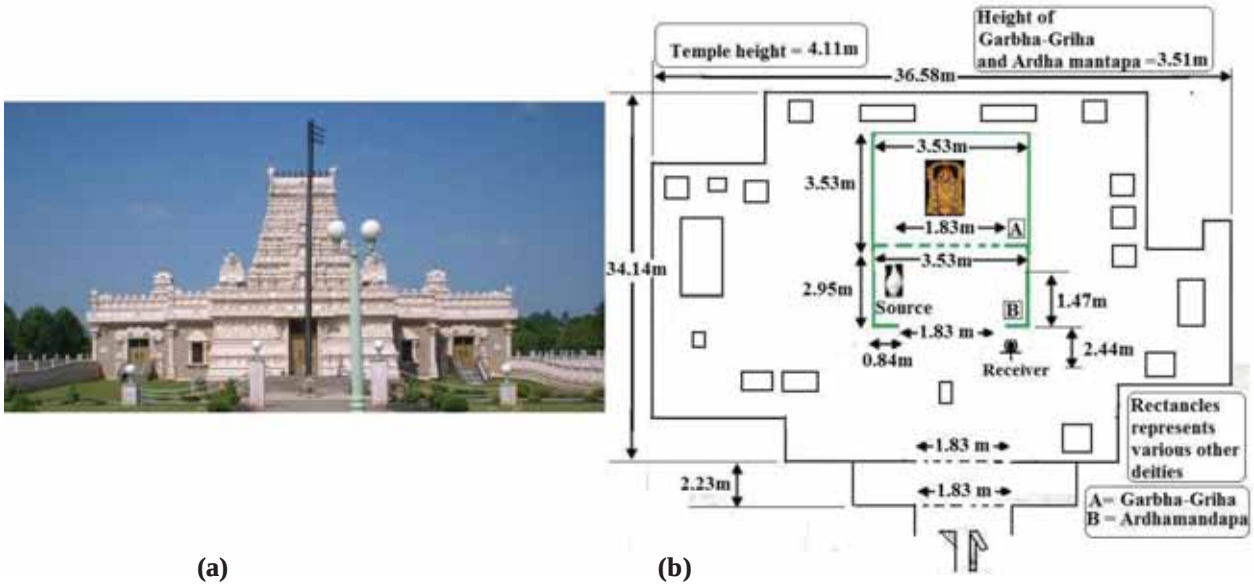

Fig. 4. (a) Sri Venkateswara Temple, Bridgewater, NJ, USA (b) Floor Sketch View.

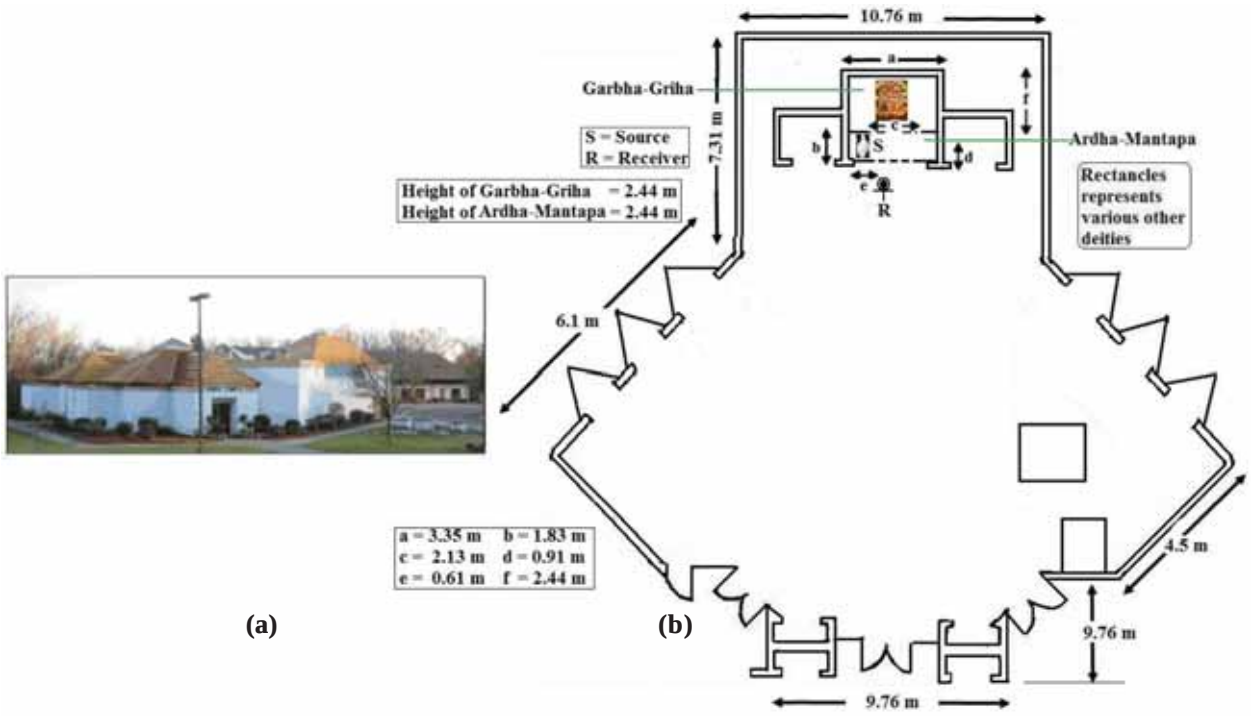

Fig. 5. (a) The Hindu Temple Society of Capital District, Albany, NY, USA (b) Floor Sketch View.

free field then the sound pressure level at the corresponding point, close to Ardha-Mantapa for a given source of sound power level (L_w) can be written as,

$$L_{P2} = L_w + 10\log\left[\frac{1}{4\pi r^2}\right] \tag{2}$$

Subtracting Eqn. (2) from (1), we can obtain the increase in SPL of the room space as,

$$\Delta L = L_{P1} - L_{P2} = 10\log\left[\frac{16\pi r^2}{R}\right] \tag{3}$$

where, $R = S\bar{\alpha} / (1-\bar{\alpha})$ is the room constant, S is the surface area of the room and $\bar{\alpha}$ is the average absorption coefficient of the room. Here, *'r oom'* represents Ardha-Mantapa, Garbha-Griha as well as combined space of Ardha-Mantapa and Garbha-Griha. The volume (m_3), theoretical estimation of reverberation time T_{60} (in sec) and increased sound pressure level (?L in dB) calculated using the Eqn. 3 for all these three temples are given in Table. 2. The estimated theoretical reverberation times (T_{60}) for the combined Ardha-Mantapa

Table 2. Estimated reverberation time and sound pressure level of various Hindu temples

	Temple (Bridgewater, NJ)			Temple (Albany, NY)			Temple (Melkote, India)		
	Volume	T_{60}	ÄL	Volume	T_{60}	ÄL	Volume	T_{60}	ÄL
Ardha-Mantapa	36.18	1.09	22.93	10.87	0.58	13.9	24.84	0.92	21.9
Garbha-Griha	43.86	1.14	22.32	19.93	0.68	14.5	18.11	0.61	21.5
Combined	80.02	1.12	19.62	30.80	0.63	11.2	42.95	0.76	18.7

and Garbha-Griha for the Sri Venkateswara temple, Bridgewater, NJ, USA and the Sri Lakshmi - Sri Narayana temple, Albany, NY, USA are 1.12 sec and 0.63 sec respectively. The theoretically estimated reverberation times for the Maha-Mantapa for the above two temples are 1.25 sec and 1.1 sec respectively. The theoretically estimated reverberation time (T_{60}) as in Table 2 for the combined Garbha-Griha and Ardha-Mantapa for the Sri Narayanaswami temple in Melkote, Mysore, India is 0.76 sec. The reverberant field in this highly reflective combined space and its propagation to the Maha-Mantapa can be pictorially represented in Figs. 6(a) and (b) for the cases of sound sources in Garbha-Griha and Ardha-Mantapa respectively.

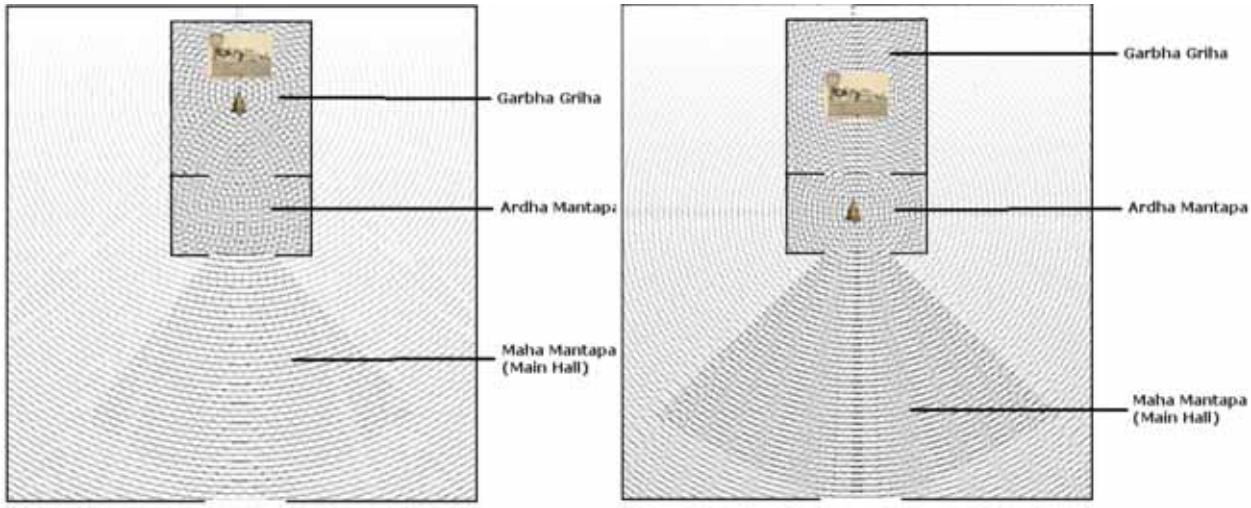

Fig. 6. Reverberant sound fields with sound source in (a) Garbha-Griha and in (b) Ardha-Mantapa.

4. CHANTING THE MANTRAS IN HINDU WORSHIP SPACES

Vedas, the foundational literature of Hinduism refers to infinitely large collection of mantras. These mantras describe the various facets of knowledge dealing with life and cosmos [4]. The chants from Vedas are extensively used in worship and sacrament rituals at homes and temples. Sounds of the Veda mantras chanted in Hindu worship spaces would carry the listeners to spiritual experiences. The acoustical characteristics, in addition to the clear phonetic articulation of chants, have deep impact on the devotees [4, 16, 17]. The Vedas are recited by a single priest or a number of priests collectively throughout the rituals or worship. Sometimes devotees also join the recitation of Vedas. In this study, a single priest recitation is measured and sound spectral analysis is carried out for an anechoic room, a community hall and an Ardha-Mantapa of a temple. The observed frequencies are given in Table 3. The measured sound spectra of the vocal (Vedic chanting) are given in Fig. 7. It is noted that the observed fundamental frequency of the Vedic chanting spectra (V1) is 147 Hz. The recoded audio (.mp3) files of typical Vedic chanting recorded in anechoic room, community hall and Ardha-Mantapa of temple (Bridgewater,NJ) are also embedded in Fig. 7.

5. SOUNDING OF *CONCH-SHELLS* IN HINDU WORSHIP SPACES

Conch-shell (*Turbinella pyrum or Indian Conch*) is a musical wind instrument that is made from a seashell, one of several different kinds of very large sea snail. It is also sometimes referred to as "conch-shell trumpet" and it is thought to have been the original horn-trumpet. The clear and hauntingly beautiful sound when blowing the conch-shell trumpet was an integral part of daily life in many societies, where it was used for communication and religious rituals. The recent excavation of twenty conch-shells (Strombus Galeatus marine shell trumpets) referred as chavin pututus in Peru was reported [18]. In Hindu religion, conch-shell is of great importance and symbolizes luster, brilliance, purity. Its tonal sound provides auspicious beginning of an event. In many Hindu temple rituals, conch-shells are sounded to announce the beginning

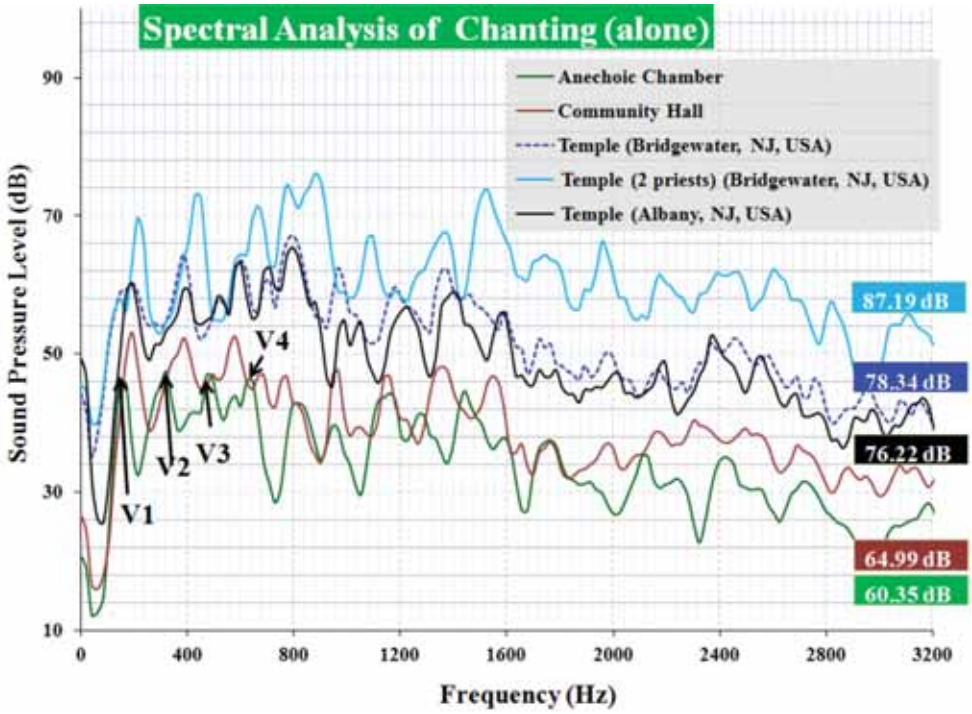

Fig. 7. Spectra of Vedic-chanting (V) alone. *(**Not**e: All the audio recordings were made at a distance of 2 ft (0.61m) in the anechoic chamber, community hall; 15 ft (4.6m) in Temple (Bridgewater) and 5 ft (1.52m) in Temple (Albany). However, all the graphs have been corrected for the distance of 15 ft (4.6m).)*

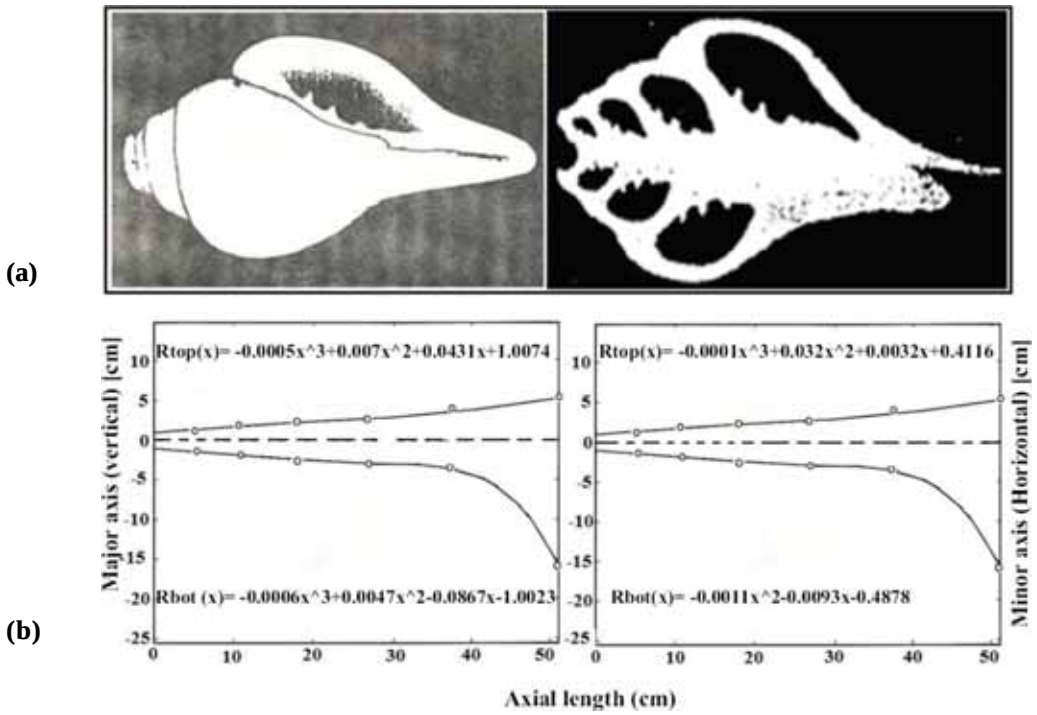

Fig. 8. (a) X-Ray tomography and (b) Straightened conch-shell cavity profile (major and minor axis) [20]

and the ending of a worship and also arrival of the deity. It is used both as a musical instrument and as a container for holy water. It is also used to drive away the evil spirits [13]. It is interesting to note that sound from conch-shell has a loud and sharp tonal quality that can be recognized while listening. Figure 8 (a) shows the X-ray tomography view of the conch-shell. The Fig. 8(b) shows the equivalent horn of the conch-shell based on unwinding it with reference to the major and minor axes of the elliptical cavity. It is seen from Fig. 9 that the conch-shell has a very high Q-factor.

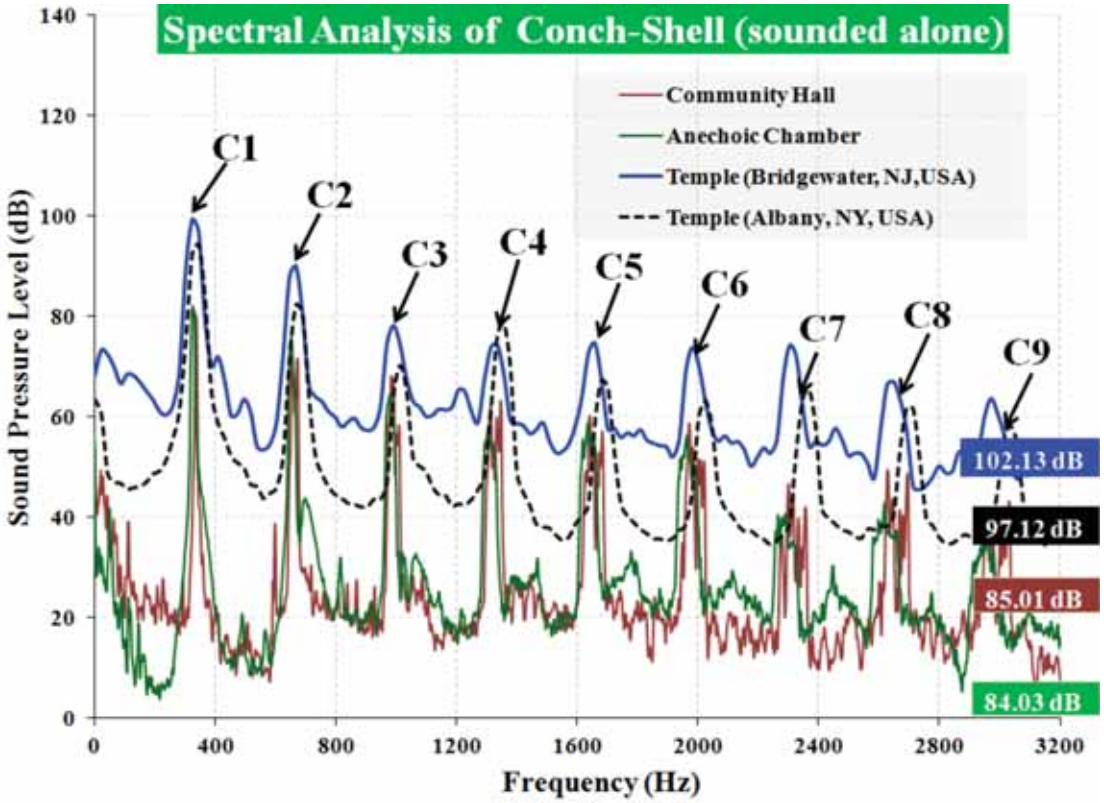

Fig. 9. Spectra of a conch-shell sounded alone.

It is not possible to sound or play the naturally available conch-shell in their original form. In order to play the conch-shell, a pointed tip of its closed end is cut off to open the cavity, and then it is played by blowing into that end through vibrating lips. When the frequency of the lip vibrations matches a resonance frequency of the conch shell cavity, a clear tone is produced. By adjusting lip tension and blowing speed, different frequencies can be produced by skilled players, as like on any brass wind instruments. The spectrum of sound produced on an end blown Indian conch-shell trumpet was studied initially by Bhat et al [19, 20]. Recent studies of acoustical characteristics of conch-shell have been carried out by Rath *et al.* [21] and Prasad et al [22]. In this study a conch-shell was blown in an anechoic chamber, a community hall that can be used as a worship space and in the Ardha-Mantapa of the two Hindu temples. The corresponding spectral analyses were carried out. The measurement was carried out using LabView Sound and Vibration software suite. The measurement was carried out for conch-shell alone and also along with other musical instruments. The observed fundamental tones of conch shell are given in Table 3 and in Fig. 9. The measured frequencies of conch-shell in an anechoic chamber are 327.5 Hz as fundamental and its harmonics. *(Note: click on the audio symbol which is embedded in Fig. 9 to listen to the sound of a conch-shell).*

Table 3. Observed frequencies of Vedic chants, Conch-Shell, Bell and Gong.

Type of Instrument	Observed Frequency (Hz)
Vedic chant (alone)	147.5, 302, 440
Conch-Shell (sounding alone)	327.5, 655, 980, 1302.5, 1637, 1965, 2292.5
Bell (sounding alone)	1262.5, 2877.5
Gong (sounding alone)	392, 762, 1437, 1792, 2070, 2350, 2675, 3002
Simultaneous sounding of Vedic chant, Conch-Shell, Bell and Gong	327.5, 392, 440, 655, 762, 980, 1262.5, 1437, 1792, 2070, 2350, 2675, 2877.5, 3002

5.1 Finger-in effect of sound spectrum in Conch-shell

Measurements were also carried out to study the effect of player inserting the fingers at the mouth (large open end) of the cavity of a conch-shell as similar to hand-in condition of French horn. The measured spectra of with maximum finger-in and no finger-in conditions in an anechoic chamber are shown in Fig. 10. It is observed from the measured spectra that inserting the finger in mouth of conch-shell shifts the fundamental frequency to lower value as expected [20]. The shifting of fundamental frequency is due to increase of effective duct length of the cavity of conch shell. The recorded audio (.mp3) files of no finger-in, with maximum finger-in and gradual finger-in conditions of conch-shell blown in an anechoic room are embedded in Fig. 10.

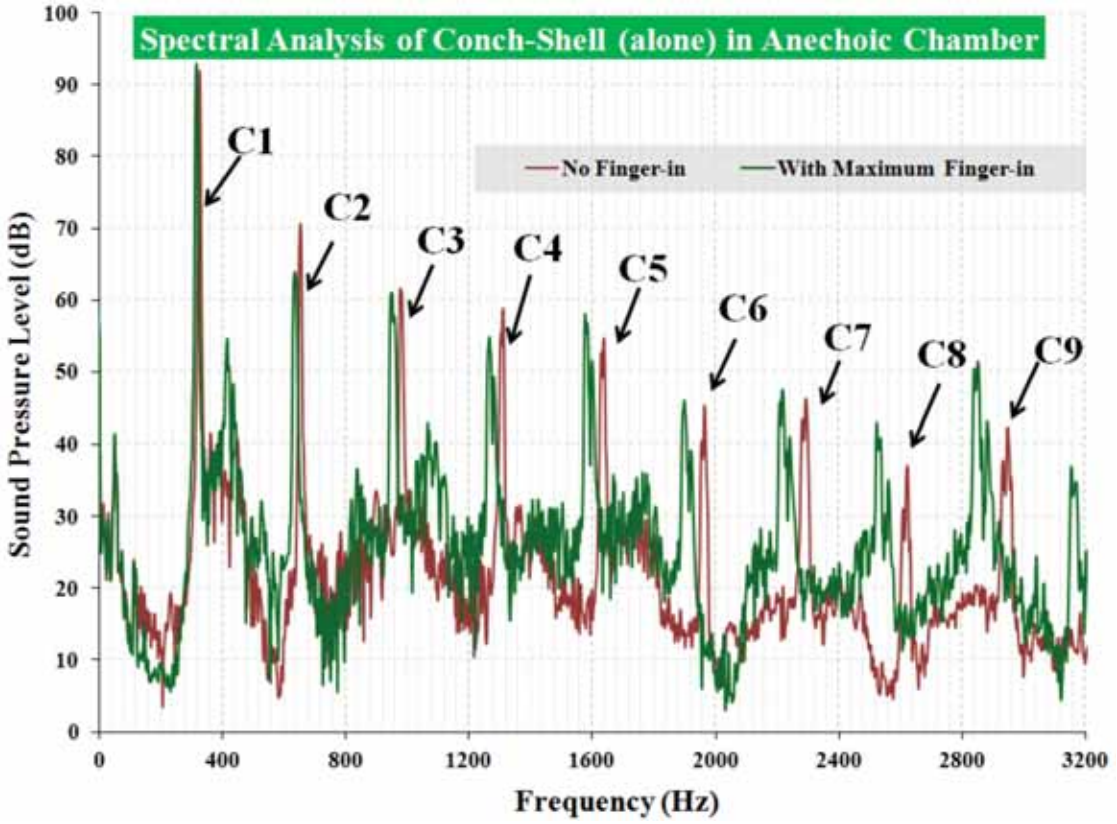

Fig.10. Finger-in effect for a conch-shell (C) sounded in an anechoic chamber.

6. SOUNDING OF BELLS IN HINDU WORSHIP SPACES

According to *Agama-Shastra* [23] which is the text for temple design and rituals, ringing of *bells* in temples and in other Hindu worship spaces during rituals is to ward off evil spirits. A verse in Sanskrit is recited when ringing the bell at the beginning of the worship. The meaning of the verse is that the bell is rung to invite the sacred vibrations and to drive away the evil vibrations.

A well designed bell is an indispensable and an important part in most Hindu worship (pooja) and prayers. It is also observed that a well-designed bell would produce long strains of the sound 'OM.' Usually the bell is sounded before the actual pooja begins. A bell is also rung in a Hindu worship, during the waving of camphor light in front of the deity, while bathing the deity and while offering food.

The sound made from a well-designed bell is uninterrupted, reverberating, deep and sonorous. The bells used in Hindu temples are usually made of five metal alloys or panchaloha. The five met-als used are gold (Au), silver (Ag), copper (Cu), iron (Fe) and lead (Pb). A typical hand-bell used in Hindu worship rituals is shown in Fig. 1. The spectra of the hand-bell are shown in Fig. 11 and the observed frequencies of the bell are given in Table. 3. It is noted that the fundamental frequency of the bell analysed for the study is 1292 Hz and it also noted that the second higher tone is not an integer multiple unlike conch-shell. The recorded audio (.mp3) file of ringing a hand bell in anechoic chamber, community hall and temple (Bridgewater, NJ) is also embedded in Fig. 11.

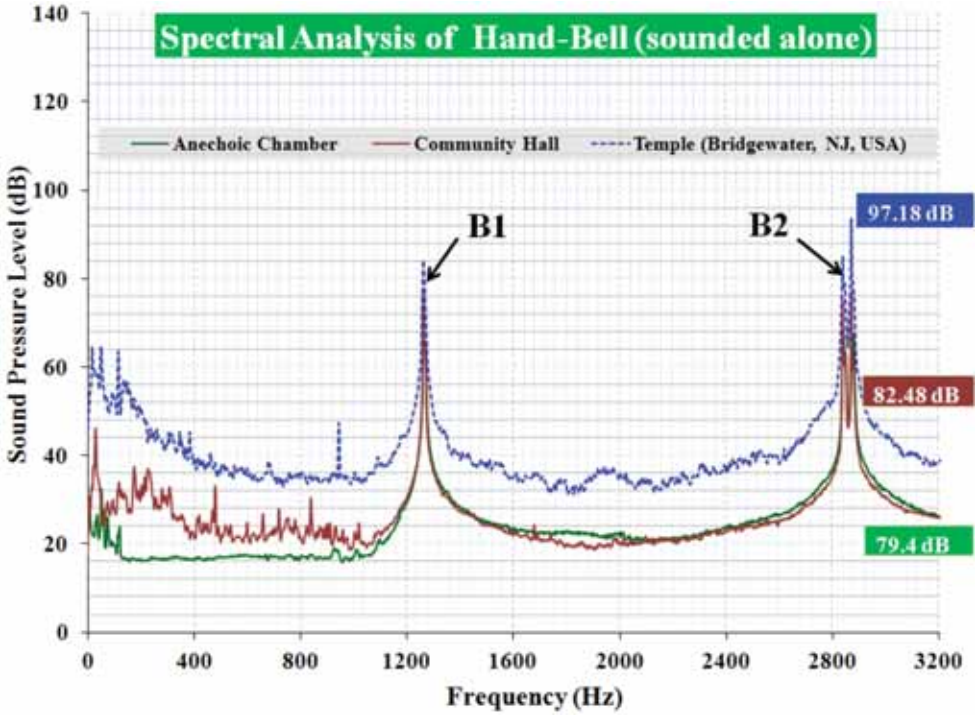

Fig.11. Spectra of a hand-bell (B) sounded alone.

6.1 Comparison of Hand-Bell and Hanging-Bell

In Hindu worship spaces especially in temples, there are large bells suspended at the entrance and in some temples also inside the Ardha-Mantapa. When the devotees enter or leave the temple premises they ring the bell. Also in temples, hanging (suspended) bells are rung when the pooja is offered. In this study the sound spectrum of hanging-bell (the same hand-bell was suspended) is measured and analysed in an Anechoic chamber. The frequency spectrum shown in Fig. 12 indicates that fundamental and second higher

tones are coincides with the hand bell spectra. However, the measured sound pressure level of hand-bell is higher than the hanging-bell. The ob-served higher value in hand-bell is due to the pendulum striking at two places in very short time period compared to the hanging-bell. The recorded audio (.mp3) files of striking the hand-bell and hanging-bell are embedded in Fig. 12. The spectral plot of time-decay of a hand-bell is shown in Fig. 13. The audio file of the time-decay is also embedded in Fig. 13. The time decay sound

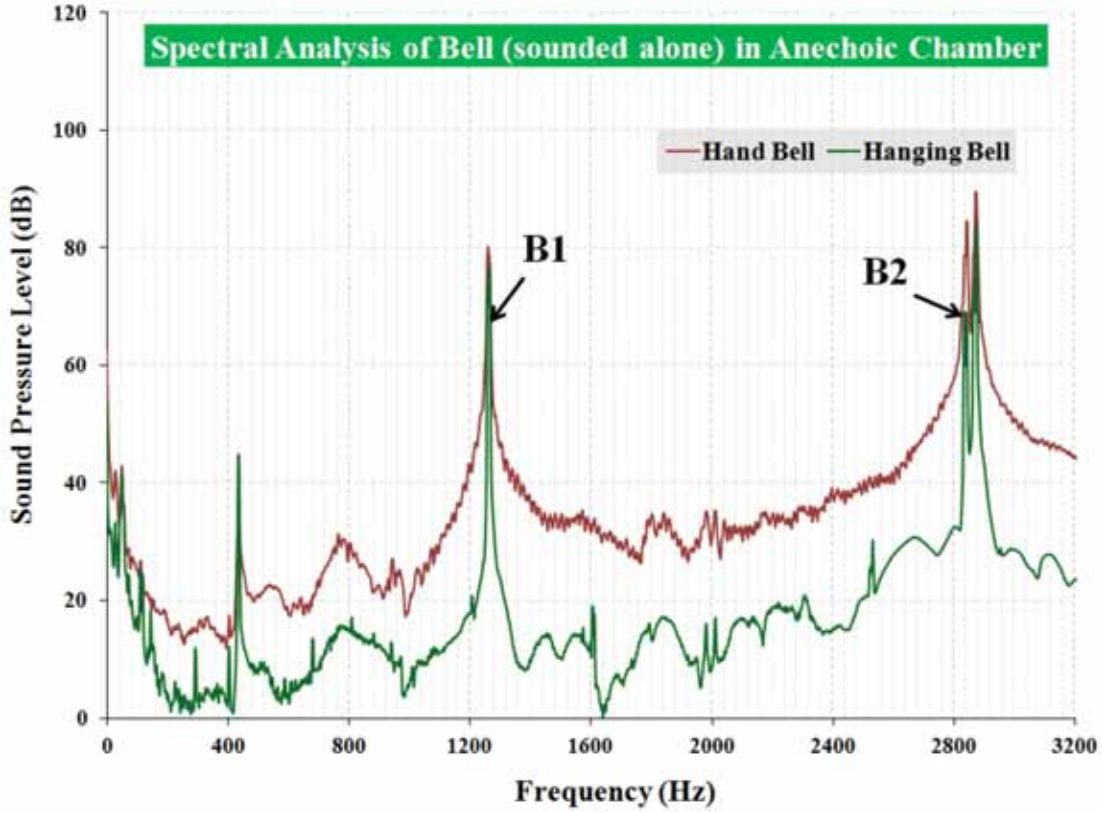

Fig. 12. Spectra of hand and hanging-bells.

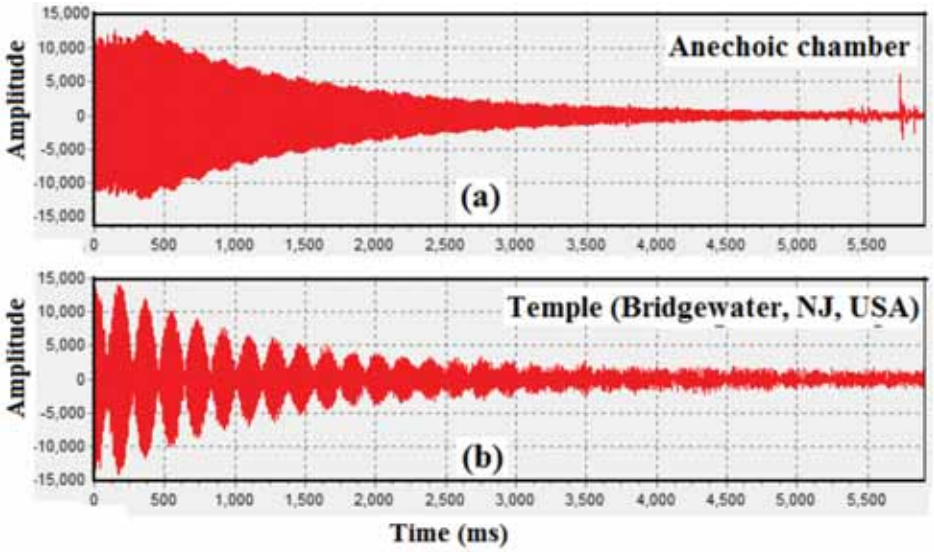

Fig. 13. Impulse response of (a) Anechoic chamber and (b) Ardha-Mantapa.

indicates that the bell analysed for the spectrum studies is well made because the resonance tone amplitude gradually reduces than a sudden stop.

7. SOUNDING OF *GONGS* IN HINDU WORSHIP SPACES

A *gong* is a musical instrument that takes the form of a flat, circular metal disc which is struck with a mallet. Gongs are broadly of three types. Suspended gongs are more or less flat, circular discs of metal suspended vertically by means of a cord passing through holes near to the top rim. Bossed or nipple gongs have a raised centre boss and are often suspended and played horizontally. Gongs are made mainly from bronze or brass but there are many other alloys also in use. Gongs are fabricated by a metal (iron) or wooden hammer after repeated intervals to get sound of same pitch. Sharavage et al [24] studied in detail the vibrational properties and the modes of vibration of the gong. They [24] carried out the spectral analysis and time average holography on the gong. They also [24] observed that the vibrational properties of gongs will depend on the point of actuation and found the modes of vibration and its mathematical equation. In Hindu temples, gongs are sounded during the worship and they are sounded along with other musical instruments such as conch shells and bells. The sizes of the gongs are usually small and they are sounded using wooden mallets. They are made of brass and circular in nature. A typical gong used in Hindu worship spaces is shown in Fig. 1. For this study the gong is excited at the center and spectral analysis is carried out. The measured fundamental frequency is 392 Hz. It is noted that unlike the conch-shell, the higher frequencies observed in gong are not exact integer multiples. The measured sound spectra are shown in Fig. 14. It is also observed that the fundamental frequency and its higher tones are not shifted when the measurement is taken at reflective room which is similar to the observation made for Bell ringing. The recorded audio (.mp3) files of gong struck at center in an anechoic chamber, community hall and in Ardha-Mantapa of Hindu temple are also embedded in Fig. 14.

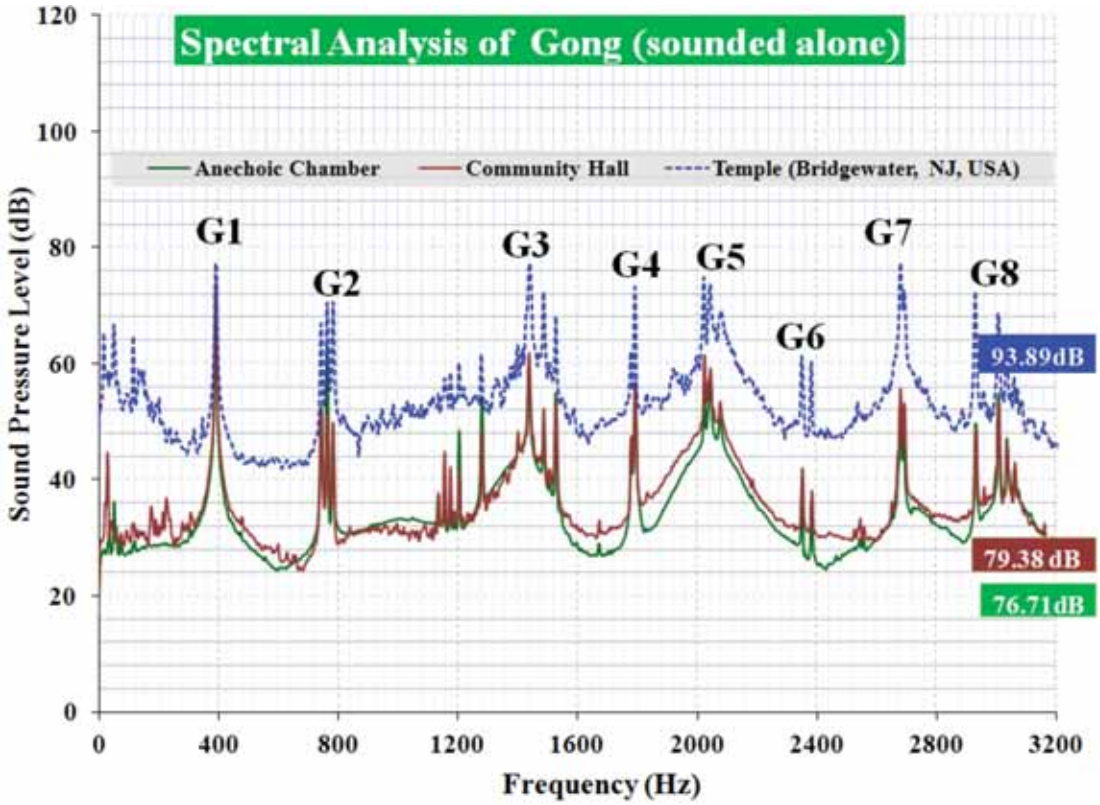

Fig. 14. Spectra of a gong sounded alone.

7.1 Effect of striking the Gong at different places

In this study the gong is hit at three different places and the corresponding sound spectra are analysed. The spectral analysis are carried out for striking the gong at the center (r=0), middle (r=R/2) and at the edge (r=R). The spectra are shown in Fig. 15. The spectra indicate that the striking at three different places does not have any effect on the fundamental frequency. The audio (.mp3) files of striking the gong at three different places recorded in anechoic room are also embedded in Fig. 15.

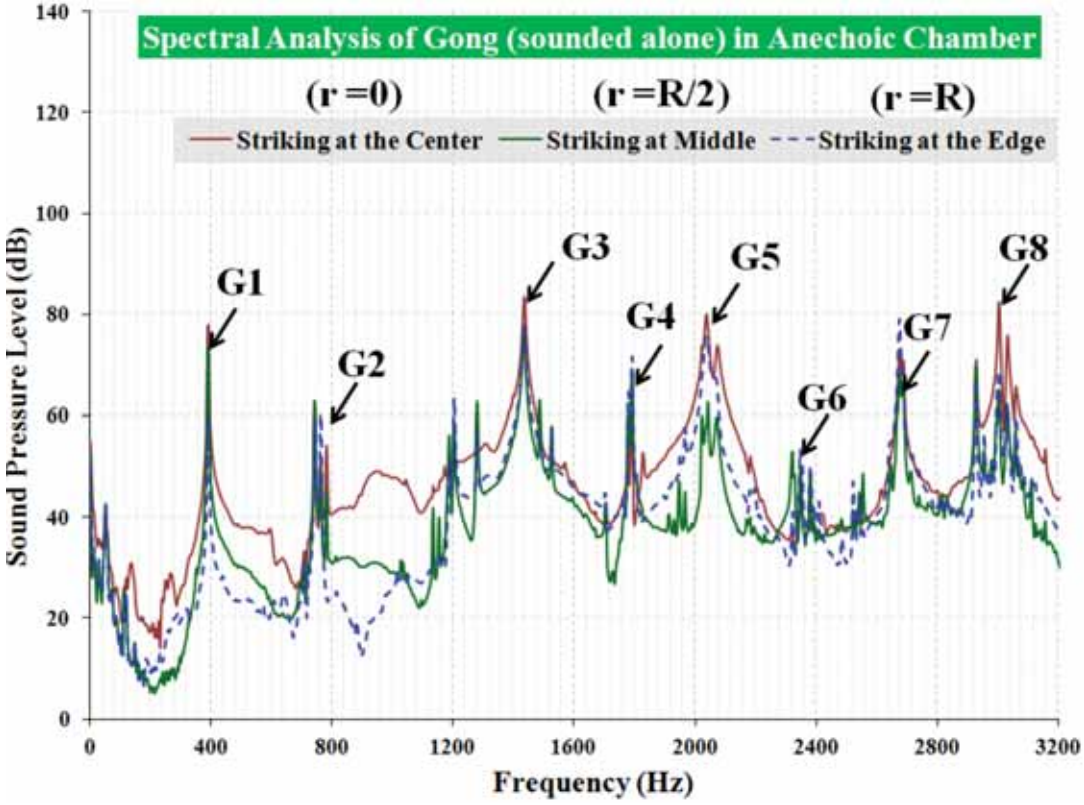

Fig. 15. Spectra of a gong when stroked at different places.

8. SIMULTANEOUS SOUNDING OF CONCH-BELL-GONG AND CHANTING IN HINDU WORSHIP SPACES

In worship rituals at a Hindu temple, in a community hall and in a worship room at individual homes, usually all the instruments described above are simultaneously sounded along with Vedic chanting during the pooja. In this study we have measured the sound spectra of all the three instruments played along with Vedic chanting. The measurement was carried out in anechoic chamber, community hall and Ardha-Mantapa of a temple. The measured frequencies are given in Table 3 and the sound spectra are shown in Fig. 16. It is observed that the measured spectra of all the three instruments and vocal chanting are combination of individual frequencies of the Conch-Shell, Bell, Gong and Chanting frequencies. The recorded audio (.mp3) files of playing three instruments and Vedic chanting simultaneously in an anechoic chamber, Ardha-Mantapa and community hall are also embedded in Fig. 16.

9. RESULTS AND DISCUSSIONS

It is seen from the Table 2 that both theoretically estimated and measured increase in sound pressure levels in the main hall outside the Ardha-Mantapa agree well for the temples in USA. Generally a traditional

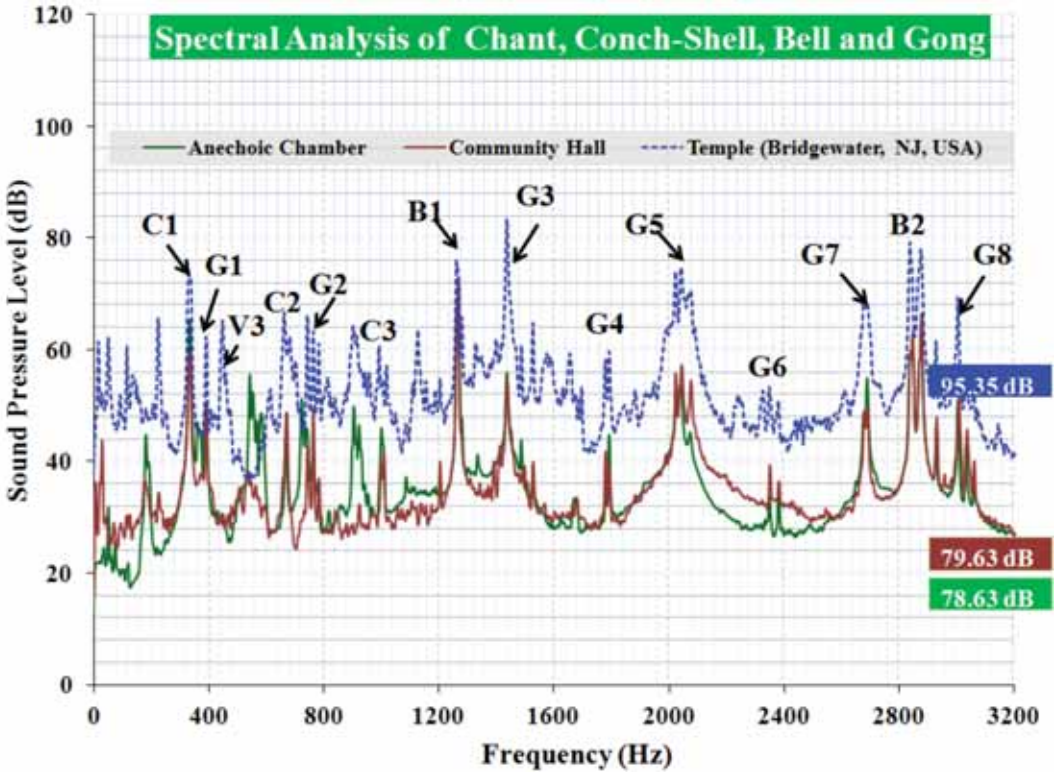

Fig. 16. Spectra of Chant (V), Conch-Shell (C), Bell (B) and Gong (G) when simultaneously sounded.

Hindu temple has both a Garbha-Griha and an Ardha-Mantapa. Thus the acoustically reverberant environment in the Garbha-Griha and the Ardha-Mantapa not only enhances the spiritual experiences for the devotees but also adds to the devotional environment of the temple. Figures 6(a) and 6(b) show the sound propagations due to the placement of the acoustical source in Garbha-Griha and Ardha-Mantapa respectively. The acoustical enhancement of the environment is seen clearly in both cases. However during the celebrations of the festivals in a temple, the priests will be in both Garbha-Griha and Ardha-Mantapa. This will further amplify and enhance the acoustical environment in the temples.

Figures 7, 9, 11 and 14 show the spectra respectively of the four sources namely chants, conch-shell, hand-bell and gong sounded individually. In each figure is also shown the spectra in three spaces namely a temple, a community hall and an anechoic chamber. The spectra details of sounds from these sources and the various spaces clearly show that various dominant resonance frequencies are spread out in the active hearing range. In particular, the high amplitude sharp tonal frequencies of conch-shell, bell and gong are distinct. The Fig. 16 and the embedded audio of the combined sounds of all sources show this effect clearly.

The perception of pitch is known to depend on both spectral and temporal characteristics [25]. The presence of tones in chants and various musical instruments have deep impact on devotees in Hindu worship spaces. It is to be noted that chants and musical instruments are also commonly used in worship spaces of other religions [26-29]. Although it is observed that there are positive and beneficial effects of chants and music on human beings [30-32], further research is needed in this interesting field.

10. CONCLUSIONS

In Vedic Hinduism sound has received major emphasis through mantras, music, religion and spirituality. It is well known that sound plays a very important role in Hindu worship spaces both at homes, community halls and temples. It is observed that both Garbha-Griha and Ardha-Mantapa significantly contribute to

the acoustical enhancement of the spiritual experience of the devotees. The effects of Vedic chants in Hindu worship are well known. In addition to Vedic chants musical instruments such as conch-shells, bells and gongs are also very commonly used to enhance the spiritual experience of the devotees during the worship. It is known that sounds of these instruments along with Vedic chanting during the prayer would enable the wandering mind of the devotees to focus on the worship rituals. In this study, evaluations of acoustical characteristics of these instruments have been carried out by sounding individually as well as collectively. Measurements are carried out in an anechoic chamber, community worship hall and temple. The observed sound spectra indicate that the measured frequencies are collection of all individual frequencies. Also the frequencies are distinct and are spread across from low to high frequencies in the active hearing range, which contribute to the spiritual experience of the devotees.

11. ACKNOWLEDGEMENT

The first author (MGP) gratefully acknowledges the inspiration of his guru Yogi Sriranga Sadguru for the author's interest and efforts in conducting research on acoustical studies in Vedic literature. The authors thank Sri Vivek Vasanth, Sri Sunil Iyengar and Prof. Robert Harari (at Stevens Institute of Technology, Hoboken, NJ) for their help and discussions. Also, the authors thanks Sri Siva Lakshmanarao Kakarala, Sri Naidu Bonthu and the priests Vidwan Pramod Acharya and Vidwan Sriram Acharaya of the Hindu Temple and Cultural Society in Bridgewater, New Jersey and Sri Mattur Balakrishna of the Hindu Temple Society of Capital District in Albany, New York for their help in making acoustic measurements.

12. REFERENCES

[1] M. KLEINER, D. L. KLEPPER and R.R. TOREES, 2010. Worship Space Acoustics, *J. Ross Publishing,* USA.

[2] M.G. PRASAD and L.B. WEISS, 2012. *Sacred Spaces*, An inter-faith journey, *Taranga,* New Jersey.

[3] G.L. BECK, 2010. Sacred Sound: Experiencing music in world religions, *Motilal Banarsidass,* New Delhi.

[4] M.G. PRASAD, 2004. Mantras to Music: Acoustics in Hinduism, *147th Acoustical Society of America Meeting,* New York, USA. (www.acoustics.org/press/147th/prasad.htm)

[5] M.G. PRASAD, 2009, Vedic Perspectives on Acoustics, Workshop on Exploring Vedic Sciences organized by the Center for Indic Studies, The Center for Indic Studies, *The University of Massachusetts at Dartmouth.* http://vimeo.com/32063009.

[6] T.V.ANANTHAPADMANABHA, K. SILVERMAN and M.G. PRASAD, 1989. Vedic Chanting and Vowel Intrinsic Pitch Evidence from an Ancient Source", *117th meeting of the Acoustical Society of America,* Syracuse, NY, USA.

[7] M. G. PRASAD, 2013, Oral Tradition in Indian Civilization, Chapter 6, Perspectives on the Origin of Indian Civilization, edited by A. MARCANTONIO and G.N. JHA, *Center for Indic Studies and D K Printworld,* New Delhi.

[8] C.V. RAMAN, 1922, The Acoustical Knowledge of the Ancient Hindus, *Ashutosha Mukherji Silver Jubilee*, **2**, 179-185.

[9] SANGITA AND STOTRA, 1991. Lectures of Sriranga Sadguru, *Ashtanga Yoga Vijnana Mandiram*, Volume 7 of Amaravani, (http://www.ayvm.in), Mysore, India.

[10] M.G. PRASAD, 2012, Four Fold Description of Sound: A Vedic view, Chapter 4, Science and technology in Ancient Indian Texts, Edited by BAL RAM SINGH, GIRISH NATH JHA, UMESH KUMAR SINGH and DIWAKAR MISHRA, *D K Printworld,* New Delhi, India.

[11] B. SARASWATI, 1999. Thinking About Sound in Traditional Science, in *Dhvani: Nature and Culture of Sound,* (editor: S.C. Malik), *Indira Gandhi national Centre for the Arts,* New Delhi.

[12] S. K. RAMACHANDRARAO, 2010. Art and Architecture of Indian Temples, *Kalpataru Research Academy*, Bengalooru, India.

[13] SADHU SHANTIPRIYADAS, 1995. Mandir: Traditions and Beliefs, *Swaminaryayan Aksharpith*, Amdavad, India.

[14] K. R. SRINIVASAN, 1985, Temples of South India, *National Book Trust*, New Delhi, India.

[15] R. VASANTHA, 1991. The Narayanaswami Temple at Melkote: An Archaeological and Historical Study, *Directorate of Archaeology and Museums*, Karnataka, India.

[16] S. MUKHOPADHYAYA, 1999. Importance of Sound in the Tradition of Vedic Chanting, in *Dhvani: Nature and Culture of Sound*, (editor: S.C. Malik), *Indira Gandhi National Centre for the Arts*, New Delhi.

[17] M. G. PRASAD and B. RAJAVEL, 2010. On the Role of Acoustics in the Vedic Hindu Tradition and Philosophy, *The Journal of Acoustical Society of America*, **127** (3), 1983.

[18] P. R. COOK, J. S. ABEL, M. A. KOLAR, P. HUANG, J. HUOPANIEMI, J. W. RICK, C. CHAFE and J. M. CHOWNING, 2010. Acoustic Analysis of the Chavín Pututus (*Strombus Galeatus* Marine Shell Trumpets), *The Acoustical Society of America*, 128 (4), 2359.

[19] R. B. BHAT, 1992. Acoustics of conch shells, *Journal of Sound and Vibration*, 157(1), 190–191.

[20] L. R. TAYLOR, M. G. PRASAD and R. B. BHAT, 1994. Acoustical characteristics of a conch shell trumpet, *The Journal of Acoustical Society of America*, **95**, 2912.

[21] S. K. RATH, S. K. and P. C. NAIK, 2009. A study on acoustics of conch shell, *Current Science*, **97**, 521-528.

[22] M. G. PRASAD and B. RAJAVEL, 2010. Acoustical Studies on Conch-Shells, *The Journal of Acoustical Society of America*, **127**(3), 1983.

[23] C .V. S. SARMA, 2009. The Temple Pooja Rituals as per Agama Shastras, *Narmadha Pathippagam*, Chennai, India.

[24] P. SHRAVAGE, S. PARMESWARAN and KEITH deSa, 2005. Vibration study of Indian Gong hung at One Point Near the Edge, *The Journal of Acoustical Society of America*, **117**(4), 2567.

[25] W.A. YOST, 2009. Pitch Perception, Attention, *Perception and Psychophysics*, **71**(8), 1701-1715.

[26] T. IRVINE, 2007. Shofar Acoustics, *Newsletter of Vibration data* (www.vibrationdata.com).

[27] E. YONNETTI, 2011. Like the Roar of Thousand Thunders: Instrumental Music and Creativity in Tibetan Buddhist Ritual, *Independent Study Project Collection*, 1065, (http://digitalcollections.sit.edu/isp_collection/1065).

[28] J. JACKSON, 1978. On Good Health and Gregorian Chant; An Interview With Dr.Alfred Tomatis, Colorado, USA. (www.saintpeterorthodox.org/files/gregorian-health.pdf)

[29] M. R. ISMAIL, 2013. A Parametric Investigation of the Acoustical Performance of Contemporary Mosques, *Frontiers of Architectural Research*, **2**, 30-41.

[30] B. M. THOMPSON and S. R. ANDREWS, 2000. An Historical Commentary on the Physiological Effects of Music: Tomatis, Mozart and Neuropsychology, *Integrative Physiological and Behaviorial Sciences*.

[31] A. BENNET and D. BENNET, 2009. The Human Knowledge System : Music and Brain Coherence, *The Journal of the Monroe Institute*, Virginia, USA.

[32] J. J. PILCH, 2004. Music and Trance, *Music Therapy Today*, **2**, 1-19. (http://musictherapyworld.net)

Journal of Acoustical Society of India : Vol. 42, No. 3, 2015 (pp. 156-161)

Incorporating Laboratory Measurements in Models Based on Statistical Energy Analysis to Predict Sound Insulation in Heavy weight Buildings

Carl Hopkins[1]* and Mahavir Singh[2]

[1]Acoustics Research Unit, School of Architecture, University of Liverpool, Liverpool, L69 7ZN, UK

[2]Acoustics, Ultrasonics & Vibration Section, CSIR-National Physical Laboratory, New Delhi

**e-mail: carl.hopkins@liverpool.ac.uk or mahavir.acoustics@gmail.com*

[Received: 10.04.2013; Revised: 26.05.2014; Accepted: 21.11.2014]

ABSTRACT

The prediction of sound insulation *in situ* is important at the design stage as well as in the diagnosis of problems once a building has been built. In building acoustics it is common to use Statistical Energy Analysis (SEA) and the version of first-order path analysis based on SEA which is incorporated into European / International Standards to predict airborne and impact sound insulation in buildings. This paper discusses the implications of incorporating measured sound reduction indices or structural coupling parameters in SEA and SEA-based models when predicting direct and flanking transmission in heavyweight buildings. The inclusion of the sound reduction index for solid heavyweight walls requires an additional measurement of the structural reverberation time. However, the transmission paths for heavyweight cavity walls are sufficiently complex that this correction is not feasible and it is concluded that laboratory measurements are of limited practical value. For structural coupling parameters, SEA and FEM indicate that the approach used in EN 12354 / ISO 15712 to incorporate measured data from isolated junctions may be problematic for transmission across several rooms in large

1. INTRODUCTION

In the field of building acoustics, prediction models that are commonly used to estimate the *in situ* performance tend to use Statistical Energy Analysis (SEA) [1] or SEA-based models such as those described in the series of Standards EN12354 / ISO 15712 [1,2]. Due to the complexity of many modern building elements it is often necessary to incorporate laboratory measurements into these models. This paper uses examples with basic heavyweight building elements such as homogeneous isotropic plates to discuss the implications.

2. INCORPORATING SOUND REDUCTION INDICES

Prediction models that are based on the framework of SEA are fairly well-suited to the inclusion of laboratory measurements of the sound reduction index. This approach can be useful when direct transmission across an element is too complicated to model and the element itself does not affect any important flanking transmission paths. This section considers solid and cavity heavyweight walls.

2.1 Solid heavyweight walls

Transmission suites are often used to measure the airborne and impact sound insulation of heavyweight test elements such as masonry walls. However, the measured structural reverberation time for the test element is essential for the comparison of sound insulation results from different laboratories, and for predicting the sound insulation *in situ*.

Above the critical frequency of a non-porous, solid, homogeneous plate, there is a direct relationship between the sound reduction index and the total loss factor of the plate. Consider the situation where such a plate has been measured in laboratory A and has a sound reduction index, R_A, with a total loss factor, η_A. The same plate is then measured in laboratory B where the total loss factor is η_B. Assuming that all measurement errors are negligible, we can convert R_A to the sound reduction index, R_B, that would be measured in laboratory B using

$$R_B = R_A + 10\lg\left(\frac{\eta_B}{\eta_A}\right) \tag{1}$$

An example is shown in Fig. 1 for a masonry wall with a high mass per unit area and a low critical frequency. In the mid and high-frequency ranges, the conversion adequately accounts for the difference

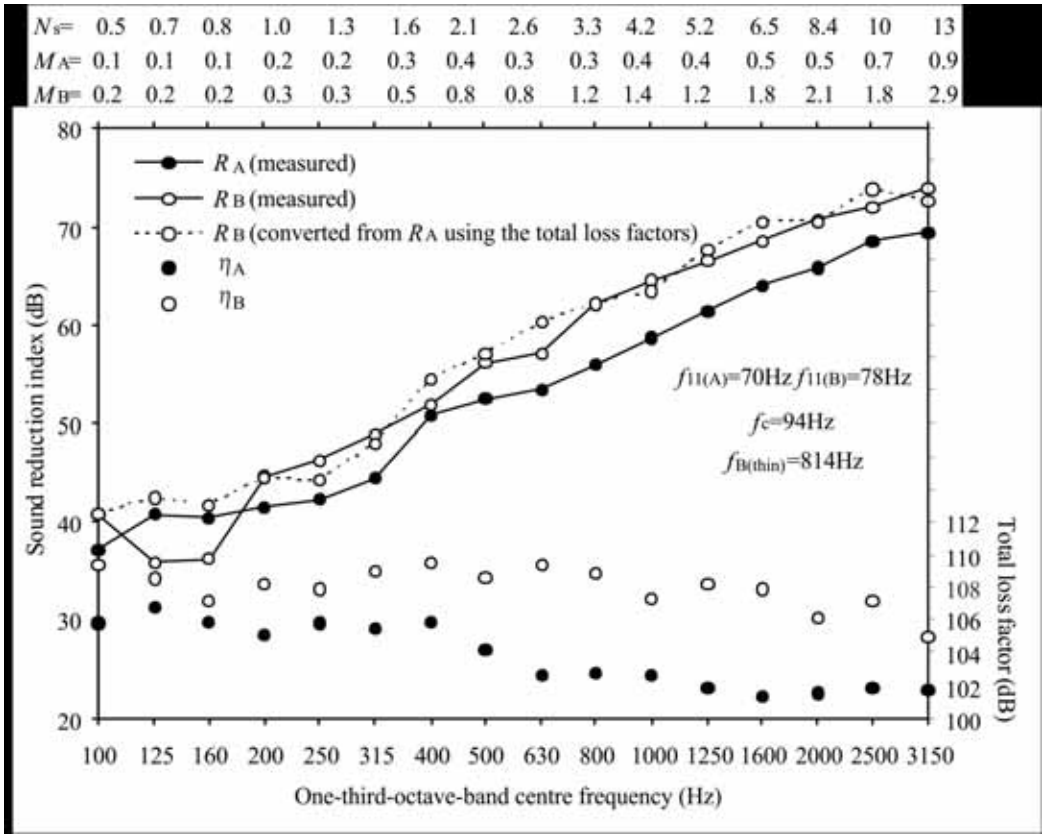

Fig. 1. Converting the sound reduction index measured in laboratory A to the result expected in laboratory B, where the measured total loss factor of the test element is different in each laboratory. Test element: 215 mm solid masonry wall with a 13 mm plaster finish (each side). Wall areas are 9.3 and 8.6 m^2 in laboratories A and B respectively. Upper x-axis labels show the predicted statistical mode count (average value of both walls is shown) and the modal overlap factor for each wall A and B in each frequency band.

between the measured sound reduction indices. It is not appropriate in the low-frequency range where the plate has very low modal overlap and only two or three bending modes in the entire low-frequency range. These bending modes vary between the two different sized walls; hence the conversion is not able to account for the measured difference in the sound reduction index.

Below the critical frequency, the theory for airborne sound insulation of an infinite plate with mass, stiffness and damping implies that there will only be non-resonant (mass law) transmission, and that the total loss factor plays no role in airborne sound transmission. For many solid masonry / concrete plates this is not the case; resonant transmission may dominate below, at and above the critical frequency. In order to carry out the conversion below the critical frequency using Eq. 1, it is necessary to estimate the non-resonant transmission. If this is negligible compared to the resonant transmission the conversion can be made in the same way. If not, the non-resonant component of the sound reduction index needs to be removed so that the conversion can be carried out on the resonant component. The non-resonant component can then be re-introduced after the conversion.

Despite the accepted importance of the total loss factor, it is rare for commercial laboratories to measure the structural reverberation time. This is partly because of perceived difficulties in evaluating and measuring fast structural decays with standard equipment, but also due to a desire to reduce testing costs. Recent work by Hopkins and Robinson [1] has used Transient Statistical Energy Analysis (TSEA) to predict structural decay curves used to determine structural reverberation times. Good agreement is shown between decay curves measured on concrete / masonry walls and floors in a large building and those predicted using TSEA. A series of numerical experiments are then performed with TSEA to quantify the error in the estimate of the total loss factor when using different evaluation ranges to calculate the structural reverberation time. The intention was to reconcile the three main issues that have historically caused problems when measuring structural reverberation times on heavyweight walls and floors. These issues are: (1) the evaluation range that is needed to ensure that the total loss factor calculated from the decay curve is representative of the true total loss factor, (2) the errors in the total loss factor when placed in the context of the other errors that occur due to energy flow between the test element and the connected structure, and (3) the signal processing that is necessary to measure and evaluate short decays. The outcome is a proposal for an evaluation procedure to determine structural reverberation times that maximises the part of the early decay which can be used in the evaluation range and identifies when a structural decay curve is and is not significantly affected by energy returning from the rest of the structure.

2.2 Heavyweight cavity walls

Section 2.1 indicates that solutions exist to measure solid heavyweight walls and floors in a transmission suite and make use of these data in prediction models. However, this is not the case for heavyweight cavity walls. This is illustrated by considering a masonry cavity wall in three different scenarios. Scenario (A) has no structural connections between the plates so that all sound transmission occurs via the cavity, scenario (B) has wall ties connecting the plates, and scenario (C) has wall ties and a foundation connecting the plates [1]. The predicted sound reduction indices using the SEA matrix solution are shown in Fig. 2 for scenarios A, B and C. Path analysis is shown for scenarios A and C to help assess the strength of different paths by comparing with the matrix solution in the lower two graphs in Fig. 2.

Scenario A has a mass-spring-mass resonance frequency that is well-below 50 Hz and outside of the building acoustics frequency range such that below the resonance frequency the cavity wall effectively acts as a single solid wall. As all transmission paths involve the cavity, the sound reduction index will change when the cavity total loss factor is changed; hence the addition of absorption in the cavity will increase the sound reduction index (and vice versa). Below the first cross-cavity mode the sound field in the cavity is two-dimensional so absorption could either be placed around the perimeter of the cavity, or the cavity could be partially or fully-filled with absorbent material across its depth. In a transmission suite the absorption around the cavity perimeter may vary between laboratories unless specific material is introduced around the perimeter as part of the test element.

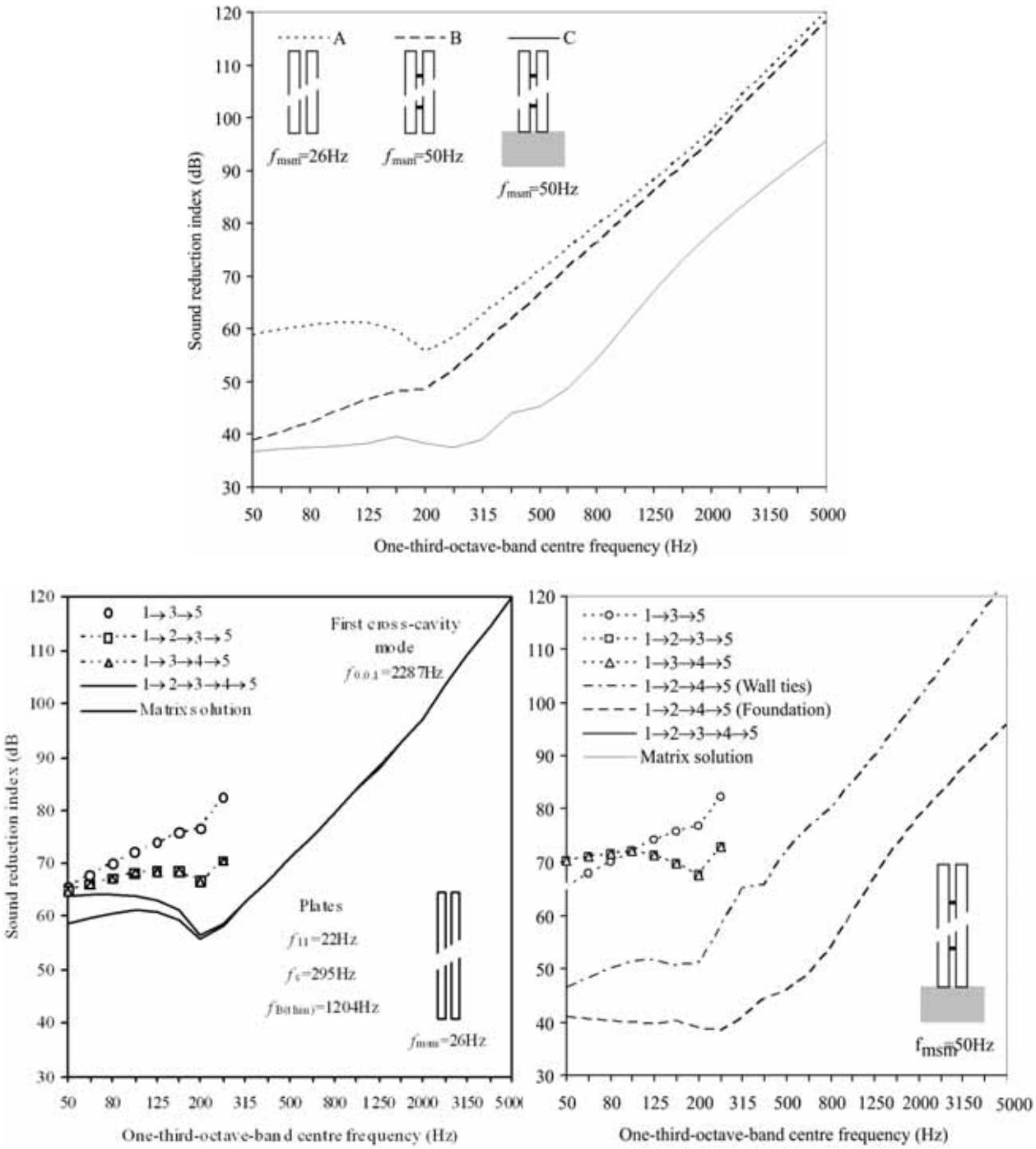

Fig. 2. SEA model of a masonry cavity wall. (a) matrix solution, (b) path analysis for comparison with the matrix solution. Plate properties: L_x=4m, L_y =2.5m, h=0.1m, ρ_s=140 kg / m^2, c_L=2200m / s, ν=0.2, radiation efficiency uses method No. 3, total loss factor η=0.01+0.3f $^{-0.5}$+$\Sigma\eta_{ij}$ (Note that $0.3f^{-0.5}$ is being used here to represent the sum of the structural coupling losses to connected walls and floors that are not included in the model). Cavity properties: Empty cavity, L_x=4m, L_y=2.5m, L_z=0.075m, T=0.3s. Wall ties: 2.5 ties / m^2, k=2 × 106N / m. Foundation: 0.25m × 0.6m, ρ=2000 kg / m^3, s_{soil}=1.96 × 109N / m^3, η_{soil}=0.96.

Scenario A gives an unrealistically high sound reduction index because there are no structural connections or flanking transmission. Note that above the critical frequency, the matrix solution gives the same sound reduction index as path 1→2→3→4→5. The addition of wall ties gives scenario B where the sound reduction index is now significantly reduced in the low-frequency range. Scenario C is created by adding a common foundation (concrete) where the earth is stiff clay with stones [1]. This reduces the sound reduction index across the entire building acoustics frequency range. This foundation detail has deliberately been chosen to give strong foundation coupling so that scenarios A and C are indicative of the extremes.

Measurements on masonry cavity walls in the laboratory are very difficult to interpret in terms of their performance *in situ*. We recall that with solid homogeneous walls we could convert a result from one laboratory to another laboratory by using the measured total loss factor. With cavity walls there is more than one path involving resonant transmission; hence there are no simple conversions. The engineer is caught between a rock and a hard place; laboratory measurements are important because 'exact' theoretical models do not exist, yet it is difficult to apply the laboratory measurement without the aid of a theoretical model. Various tactics have been used to try and overcome this difficulty. One possibility is to establish rule-of-thumb conversions from a specific mounting condition in the laboratory to a specific situation in buildings. This may be possible when masonry cavity walls are not rigidly connected to the foundations; they are sometimes built off resilient materials so the transmission path via the foundations may not be as important. In addition, structural coupling via the foundations may dominate on the ground floor of a multi-storey building but not several floors above it. In some transmission suites it is possible to build foundations below the aperture. Otherwise, if the aperture is sufficiently high a foundation can be built within the aperture and shielded with linings [1]. Another approach is to use a flanking laboratory to test the combination of the separating cavity wall and some of the flanking walls and floors to try and simulate the actual building. Note that transmission via the foundations can be affected by the underlying soil; hence there are limitations to building representative foundations in a transmission suite or a flanking laboratory.

3. INCORPORATING STRUCTURAL COUPLING PARAMETERS

The prediction model in EN 12354 / ISO 15712 was introduced to standardize the estimation of *in situ* sound insulation. Whilst these Standards contain some theoretical and empirical data these requirements it was essential for manufacturers to be allowed to use measured structural coupling data for their products. This required a new series of measurement Standards ISO 10848 [1] to determine the vibration reduction index, K_{ij}. Although EN 12354 / ISO 15712 was originally intended for adjacent rooms in heavyweight

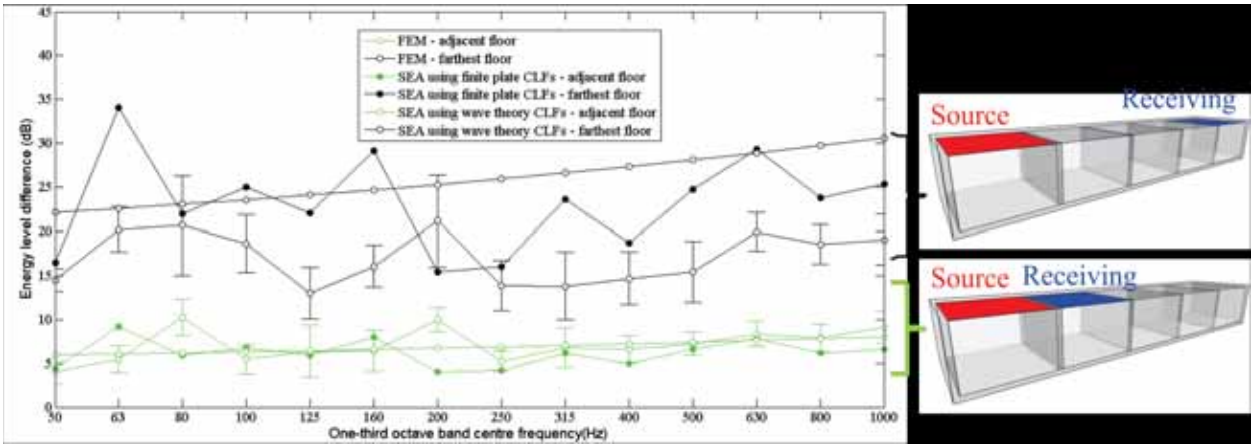

Fig. 3. Energy level difference between source and receiving floors predicted using FEM and SEA either using coupling loss factors from wave theory or from a finite plate approach.

buildings it has subsequently been shown that problems occur as it uses only first-order SEA path analysis [1,2,3]. In practice there are so many higher-order paths of collective significance that matrix SEA tends to be needed for accurate prediction. However, it is questionable whether the inclusion of measured coupling parameters from isolated junctions that are built in the laboratory improves predictions when there are many similar plate junctions in a building. An example is shown in Fig. 3 for five adjacent rooms formed from masonry / concrete walls and floors which compares predictions from Finite Element Methods (FEM) and SEA. As there will be natural variation in the material properties, FEM is used to run a Monte Carlo simulation with uncertainty in the Young's modulus for each plate. This is then compared against two different SEA models. The first SEA model uses coupling loss factors calculated from angular average wave theory which assumes a diffuse field on each plate. The second SEA model uses coupling loss factors that are calculated from analytical models for finite plates that form the isolated L- and T-junctions.

The results indicate that when the receiving plate is directly connected to the source plate, both SEA models are close to the FEM ensemble average. However, when the receiving plate is farthest from the source plate, SEA wave theory tends to underestimate the transmission but the improvement by using SEA using coupling loss factors from a finite plate approach is marginal. The reason for lower energy level differences with FEM compared to SEA is partly due to the effect of spatial filtering across successive junctions which is not accounted for in SEA. This indicates that the approach used in EN 12354 / ISO 15712 to incorporate measured data from isolated junctions may be problematic for transmission across several rooms in large buildings.

4. CONCLUSIONS

This paper highlighted the implications of incorporating measured sound reduction indices or structural coupling parameters in SEA and SEA-based models when predicting direct and flanking transmission in heavyweight buildings. The inclusion of the sound reduction index for solid heavyweight walls requires an additional measurement of the structural reverberation time. However, the transmission mechanisms for heavyweight cavity walls are sufficiently complex that this correction is not feasible and it is concluded that laboratory measurements are of limited practical value. For structural coupling parameters, SEA and FEM indicate that the approach used in EN 12354 / ISO 15712 to incorporate measured data from isolated junctions may be problematic for transmission across several rooms in large buildings.

5. ACKNOWLEDGEMENT

The author is grateful to David Wilson in the Acoustics Research Unit for providing Figure 3.

6. REFERENCES

[1] C. HOPKINS, 2007. Sound insulation. Butterworth Heinemann, ISBN 978-0-7506-6526-1.

[2] EN 12354:2000 / ISO 15712:2005 Building acoustics – Estimation of acoustic performance of buildings from the performance of elements – Parts 1 and 2.

[3] C. HOPKINS and M. ROBINSON, 2013. On the evaluation of decay curves to determine structural reverberation times for building elements. *Acta Acust. Acust.* **99**, 226-244.

[4] J. PARMANEN, R. HEINONEN and V. SIVONEN, 1988. Kaksinkertaisen tiiliseinän ääneneristävyys. Äänen sivutiesiirtymä perustuksen kautta, Research Note 919, VTT, *Technical Research Centre of Finland*. (9513832392).

[5] ISO 10848-1:2006 Acoustics – Laboratory measurement of the flanking transmission of airborne and impact sound between adjoining rooms.

[6] R.J.M. CRAIK, 2001. The contribution of long flanking paths to sound transmission in buildings, *Appl. Acoust.* **62**(1), 29-46.

[7] L. GALBRUN, 2008. The prediction of airborne sound transmission between two rooms using first-order flanking paths. *Appl. Acoust.* **69**(12), 1332-1342.

Journal of Acoustical Society of India : Vol. 42, No. 3, 2015 (pp. 162-167)

Acoustic Probing of Elasticity in the Bulk of Tilted Granular Layers - Precursors of Avalanches

Mickaël Duranteau[1]*, Renaud Delannay[1], Vincent Tournat[2], Vladimir Zaitsev[3] and Patrick Richard[4]

[1]Institut de Physique de Rennes, UMR CNRS 6251, Université de Rennes 1, 1-263 av. General Leclerc, 35042, Rennes, France

[2]LUNAM Université, LAUM, UMR CNRS 6613, Université du Maine, Av. O. Messiaen, 72085, Le Mans, France

[3]Institude of Applied Physics, Russian Academy of Sciences, Uljanova St. 46, 603950 Nizhny Novgorod, Russia

[4]GPEM, LUNAM Université, IFSTTAR, site de Nantes, route de Bouaye, 44344 Bouguenais cedex, France

**e-mail: mickael.duranteau@gmail.com*

[Received: 05.04.2013; Revised: 28.05.2014; Accepted: 19.12.2014]

ABSTRACT

Earthquakes, avalanches and landslides have a shearing nature. The related mechanisms that take place are strongly complex due to heterogeneities of geometry as well as internal and applied stresses. Analogue experiments in laboratories are often designed with granular media to mimic the mechanical behaviors of the crust at a much larger scale. For tridimensional granular materials, the use of acoustic waves is a way to probe modifications in the bulk where the shearing process develops. Here, we conduct experiments with monodisperse glass beads of 2 mm in diameter where humidity and temperature are controled. We experimentally study by both linear and nonlinear acoustic methods the destabilization of tilted granular layers where precursors of avalanches occur pseu-do-periodically. The quasi-periodicity of the avalanche precursors as a function of the tilt angle still remains poorly understood. These precursors can be observed on the free surface of the layer as collective motions of grains which increase exponentially in intensity until avalanche. A few important parameters influence the precursor dynamics: the surface features of grains and the moisture. Both of them are related to the cohesion between grains in the medium. The acoustic measurements for probing the bulk elasticity of the granular layer are conducted at frequencies of a few kHz with two piezoelectric transducers embedded in the sidewalls and thus working non-invasively. A linear acoustic method allows to probe elastic relaxations to, which follows each precursor event. In transmitting single gaussian pulses through the medium, it is also possible to observe an elasticity softening effect. The method allows the measuring of the acoustic transfer function of the granular layer and the acoustic wave phase velocity. When working in the frequency region where the acoustic transfer function is significantly modified during the tilt, we show important variations of the elasticity of the medium. This frequency region is in the low frequencies (under ~ 10 kHz), that is for wave lengths much larger than the grain size. The granular assembly is thus seen as an effective medium. The measurement of the phase velocity allows to estimate the Young moduli which is found to slowly decrease during the tilting process. For each precursor softening occurs leading to a loss of rigidity of the medium, and then hardening follows. This work may bring an interesting train of thought on catastrophic events in geophysical processes.

1. INTRODUCTION

When a granular packing is slowly tilted until its maximal angle of stability, precursors of avalanche are noted. These precursors correspond to collective events which occur quasi-periodically until the avalanche. They are identified by imaging the rearranged grains on the free surface of the packing by particle tracking [1-6]. The surface which moves during a precursor increases exponentially until avalanche. The smallest rearrangements follow a power law distribution, contrary to the precursors which have a quasi-periodic nature, a behavior still misunderstood. Their occurrence depends mainly on the history of the packing and cohesion forces between grains. Precursors of avalanches have also been studied in the bulk with a nonlinear acoustic method [4, 7, 8] which is sensitive to the modifications of the weak contacts network. The observations show strong perturbations of the weakest contacts for each precursor. It is also possible to detect precursors by listening to the the acoustic emission by the packing [9, 10].

Recently, with optical diffusive wave spectroscopy, Amon *et al.* [11] have shown that successive precursors occur at a depth which increases with each consecutive event. This work brings to light the existence of micro-failure planes during a precursor. We also developed a theoretical approach [6] which faithfully reproduces the experimental dependency of precursors by assuming hydrostatic and isotropic pressure and with the introduction of a failure criterion for the reaction force on the front wall. A precursor is seen as the rupture of the upper part of the packing (the slab) which slides in a shear motion. After each precursor hardening occurs, the depth for the next involved slab increases.

In this study we probe the elasticity of a tilted granular packing constituted of beads of millimetric size. After describing the experimental setup, the acoustic method employed is explained. Then, the results are presented and finally discussed.

2. EXPERIMENTAL SETUP

The experimental setup (Fig. 1) consists of quasi-statically tilting a 3D granular packing until avalanche. We work with monodisperse glass beads of 2 ± 0.1 mm in diameter which are contained into a vessel of 30 cm in length, 10 cm in width, and 11 cm in height. The packing fraction is controlled at 0.596 ± 0.005 with

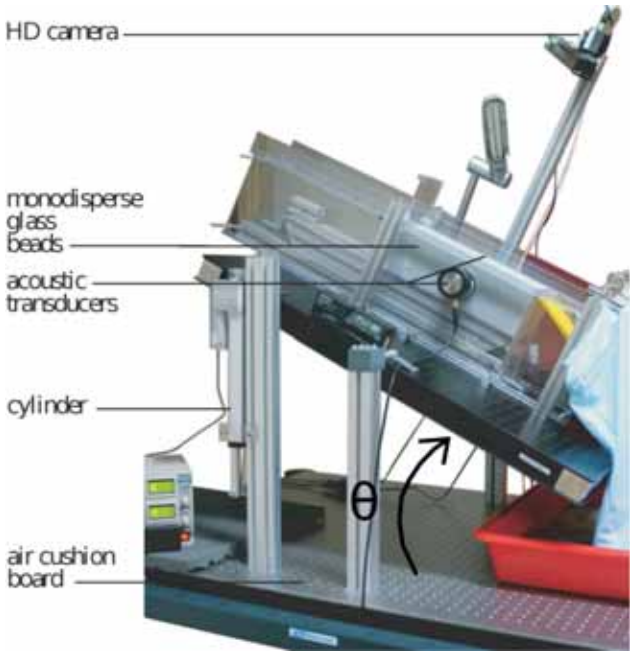

Fig. 1. Experimental setup. A 3D granular medium into a vessel is quasi-statically tilted at the angle θ.

the following method. Firstly, a metallic grid is placed at the bottom of the vessel. Then, the beads are poured into this vessel. A scraper smoothes the surface in order to remove the excess of beads at the top of the vessel. Finally, the grid is removed carefully and a last smoothing is done to plane the free surface of the packing. The control of the packing fraction is important to obtain reproducible results.

The system is placed on a cushion board to minimize external vibrations which tend to decrease the granular activity [5]. An electric jack allows to tilt a second board on which is placed the vessel. The velocity of inclination is approximately 2.5°/min. A camera placed above the packing permits to image the rearrangements on the free surface with a 0.1 mm resolution corresponding to 1 pixel. Each image is later processed in the same way as described in [5] by particle tracking in order to measure the rearranged area according to the angle of inclination θ. Two piezoelectric transducers of 4 cm in diameter are placed in each lateral wall of the vessel to probe the medium with longitudinal acoustic waves. One transducer works as an emitter, and the second works as a receiver. These transducers are in contact with grains and they allow to probe the bulk with a few millisecond time resolution (less than 10^{-2}° of inclination).

Measurements are conducted under constant temperature of 22 ± 1° and moisture of 50 ± 3%. These atmospheric conditions are controlled by air conditioning, humidifier and dehumidifier. Measurements are performed for freshly prepared mediums until avalanche to avoid relaxation effects after preparation.

3. ACOUSTIC METHOD

By transmitting longitudinal acoustic waves we aim to measure the variations of the packing elasticity. We generate single Gaussian pulses of 250 μs in duration every 10 ms. The received signal is processed by Fourier transform in order to evaluate the acoustic transfer function. The acoustic transfer function under these conditions (air saturated, low static pressure) mainly exhibits two propagation regimes [12]. For the lowest frequencies, the acoustic waves propagate essentially by the solid skeleton formed by the beads contacts network. For frequencies higher than a cut-off frequency, the acoustic propagation is mainly controlled by the fluid which saturates the beads assembly (here the air). The cut-off frequency between these two regimes is here observed to be ~ 10 kHz.

Measurements of the acoustic transfer function were already performed for compaction processes [12] where showed strong modifications for lower frequencies have been observed when the compacity grows. Here, we also show important modifications for the propagation of low frequencies during packing inclination.

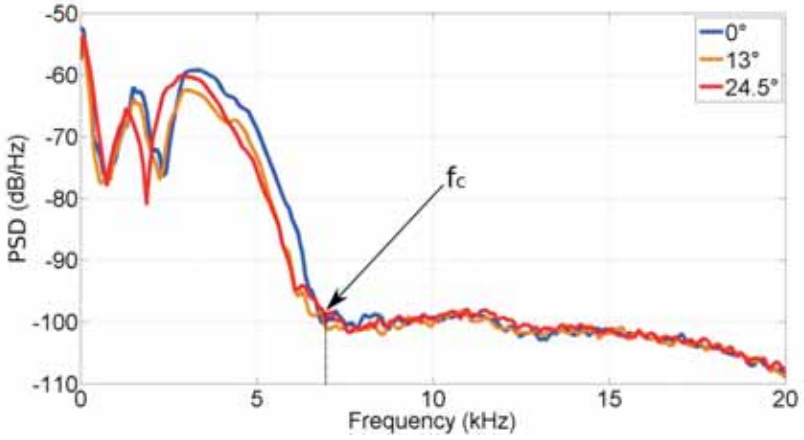

Fig. 2. Acoustic transfer functions estimated by a power spectral density for three angles of inclination: at the start (0°), before the precursors regime (13°), before the avalanche (24.5°). The cut-off frequency f_c between the solid and the fluid propagation is close to 7 kHz (f_c should not be confused with the central frequency Fc which is a barycentre frequency).

4. RESULTS

Different acoustic transfer functions are measured for different tilting angles (Fig. 3). The cut-off frequency is nearly 7 kHz. We can observe important modifications for the low frequency range. They correspond mainly to the shift of resonances and anti-resonances. In order to characterize this shift, we compute also the central frequency F_c of this transfer function between 1 and 5 kHz during the tilt (Fig. 4). F_c decreases from the start of the tilting to the occurrence of the first precursor at $\theta = 14°$. For each precursor F_c drops and then increases and decreases until the next precursor.

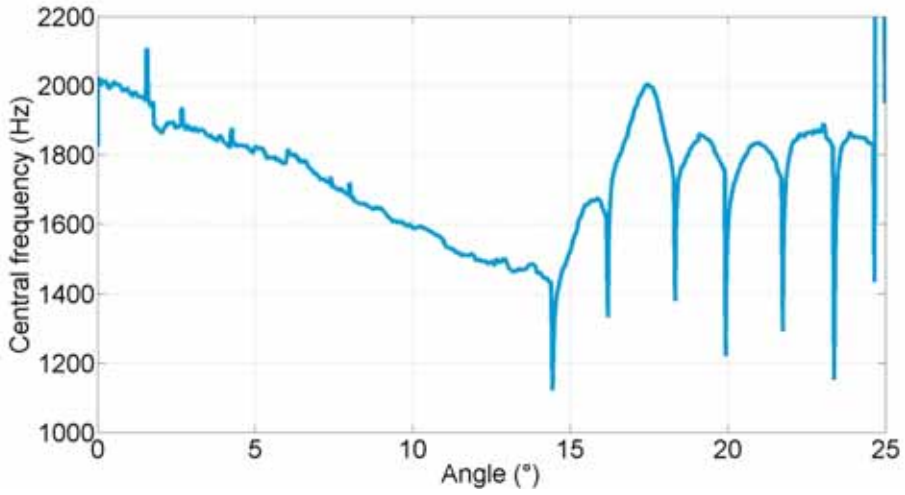

Fig. 3. Central frequency F_c measuring in the range of 1-5 kHz during a tilting process until avalanche.

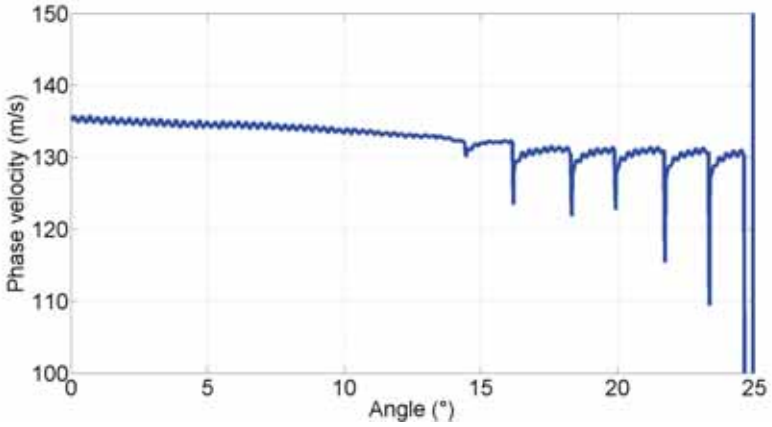

Fig. 4. Phase velocity c_φ measuring during a tilting process until avalanche

In the same time we measure the time of flight of the transmitted pulses in order to evaluate the phase velocity c_φ of the acoustic waves. For low frequencies, the granular packing can be considered as an effective medium because the wave-length λ is greater than ten bead diameters, that is comparable to the distance between both transducers (*ie.* the width of the packing). The result obtained for the phase velocity (Fig. 5) shows large regular drops from $\theta = 14°$ (which correspond to the occurrence of the first precursor) to the avalanche. From the start (0°) to the occurrence of the first precursor (14°), the phase velocity slowly decreases,

and then for each precursor c_φ suddenly decreases to finally slowly increase until the next precursor. c_φ decreases of 4% during the tilting, which corresponds to a decrease of 7% of the Young moduli ($2.76.10^7$ Pa $\rightarrow 2.56.10^7$ Pa) if we use the approximation for an effective medium [12] :

$$E = \rho_{eff} c_\varphi^2 \quad (1)$$

ρ_{eff} is the effective density of the medium which depends of the beads density ñ and of the packing fraction ($\rho_{eff} = \rho$), supposed constant.

5. DISCUSSION

The decrease of both the central frequency and the phase velocity as soon as the tilting motion starts, shows slow softening of the granular packing. The occurrence of the precursors of avalanches implies large drops of these parameters. The drops correspond to the loss of rigidity of the beads assembly. These drops become larger when approaching the angle of avalanche, that suggests precursors involve more and more of the bulk. This interpretation is consistent with the results of Amon *et al.* [11] who show that the depth implied by a precursor grows with the tilting angle. Between each precursor, F_c and c_φ grow, which is consistent with hardening, and then, F_c decreases proving softening just before the next precursor. During the tilting process the probed elastic modulus decreases dramatically (7%).

The linear acoustic method employed allows to precisely probe the elasticity variations of a 3D granular medium. The destabilization of such materials shows a global softening effect. The precursors regime consists in intermittent phases of hardening and softening. This characteristic is typical of plasticity. It would be interesting to know if the precursors of avalanches have the same behavior as simple stick-slip motions for granular materials.

6. ACKNOWLEDGEMENTS

This research is supported by the ANR grant “STABINGRAM” No. 2010-BLAN-0927-01. We thank Y. Le Gonidec for helpful discussions, A. Faisant and P. Chasle for experimental support.

7. REFERENCES

[1] M. BRETZ, J.B. CUNNINGHAM, P.L. KURCZYNSKI and F. NORI, 1992. Imaging of avalanches in granualr materials. *Physical Review Letters*, **69**(16), 2431–2436.

[2] N. NERONE, M.A. AGUIRRE, A. CALVO, D. BIDEAU and I. IPPOLITO, 2003. Instabilities in slowly driven granular packing. *Physical Review E*, **67**, 011302.

[3] T. SCHELLER, C. HUSS, G. LUMAY, N. VANDEWALLE and S. DORBOLO, 2006. Precursors to avalanches in a granular mono-layer. *Physical Review E*, **74**, 031311.

[4] S. KIESGEN DE RICHTER, V. ZAITSEV, P. RICHARD, R. DELANNAY, G. LE CAËR and V. TOURNAT, 2010. Experimental evidence of ageing and slow restoration of the weak-contact configuration in tilted 3d granular packings. *Journal of Statistical Mechanics: Theory and Experiment*, **11**, 11023.

[5] S. KIESGEN DE RICHTER, G. LE CAËR, and R. DELANNAY, 2012. Dynamics of rearrangements during inclination of granular packings: the avalanche precursor regime. *Journal of Statistical Mechanics: Theory and Experiment*, 04013.

[6] M. DURANTEAU, R. DELANNAY, P. RICHARD, and V. TOURNAT, 2013. Avalanches and quasi-periodic events in slowly tilted granular media. *Physcical Review Letters*, submitted.

[7] V.Y. ZAITSEV, P. RICHARD, R. DELANNAY, V. TOURNAT and V.E. GUSEV, 2008. Pre-avalanche structural rearrangements in the bulk of granular medium: experimental evidence. *Europhysics Letters*, **83**, 64003.

[8] M. DURANTEAU, V. TOURNAT, V. ZAITSEV, R. DELANNAY and P. RICHARD, 2013. Identification of avalanche precursors by acoustic probing in the bulk of tilted granular layers. *Proceedings of the 7th International Conference on Micromechanics of Granular Media*, Sydney, Australia, 8-12 July, (2013).

[9] V. GIBIAT, E. PLAZA and P. DE GUIBERT. Acoustic emission before avalanches in granular media, 2009. *Journal of the Acoustical Society of America*, **123**(5).

[10] J.L. THIROT, Y. LE GONIDEC and B. KERGOSIEN, 2012. Acoustic emissions in multiscale granular structures under gravitational destabilization. *In International Congress of Ultrasonics Proceedings*.

[11] A. AMON, R. BERTONI and J. CRASSOUS, 2013. Experimental investigation of plastic deformations before granular avalanche. *Physical Review E*, **87**, 012204.

[12] J-B. LEGLAND, V. TOURNAT, O. DAZEL, A. NOVAK and V.E. GUSEV, 2012. Linear and nonlinear biot waves in a noncohesive granular medium slab: transfer function, self-action, second harmonic generation. *Journal of the Acoustical Society of America*, **131**(6), 4292–4303.

Journal of Acoustical Society of India : Vol. 42, No. 3, 2015 (pp. 168-173)

New Theory for the Low Frequencies Non Linear Acoustic Radiation of Beams at Large Vibrations Amplitudes

Hanane M. Abdelali[1], Mohamed Ichchou[2], Rhali Benamar[1] and Mahavir Singh[3]

[1]EMI, EGT, LERSIM, Université Mohammed V- Agdal; Rabat, Morocco

[2]LTDS, Ecole Centrale de Lyon; Lyon, France

[3]CSIR-National Physical Laboratory, New Delhi, India

e-mail: hanane@emi.ac.ma & mahavir.acoustics@gmail.com

[Received: 11.12.2013; Revised: 19.06.2014; Accepted: 09.01.2015]

ABSTRACT

In many practical situations, the sound radiation from vibrating structures is of great importance and major environmental concern. Due to obvious security and comfort reasons, engineers in various industrial fields, such as loudspeakers manufacturing; road, rail, marine and airborne vehicles design, need to be provided with efficient tools in order to obtain reasonably accurate estimates of the noise radiation due to the vibration of the structural components involved. In many practical modern situations, geometrically non-linear structural vibrations occur, making the classical analytical and numerical tools, developed within the frames of linear theories, unable to predict properly the corresponding sound radiation parameters.

In this paper, a new approach is presented for the estimation of the non-linear acoustic radiation of beams exhibiting geometrical non linear behavior at low frequencies, corresponding to the structure considered first modes of vibration. The explicit analytical expression for the beam non-linear forced response in the neighborhood of a given mode, obtained in previous works, is substituted in the classical expressions for the acoustic indicators, such as pressure, velocity, impedance, and efficiency. This has led to new expressions for these indicators involving the effect of the geometrical non-linearity on the beam acoustic radiation indicators. Then, the indicators have been computed numerically and comparisons have been made with the corresponding classical linear ones. The results allowed the estimation of the effect of non-linearity on the classical acoustic parameters and showed a higher increase in the acoustic indicators, compared with those predicted by the linear theory. This confirms the necessity of taking into account the geometrical non-linearity in order to get an accurate estimate of the beams sound radiation at large vibration amplitudes.

1. INTRODUCTION

In many practical situations, the sound radiation from vibrating structures is of great importance and major environmental concern. Due to obvious security and comfort reasons, engineers in various industrial fields, such as loudspeakers manufacturing; road, rail, marine and airborne vehicles design, need to be provided with efficient tools in order to obtain reasonably accurate estimates of the noise radiation due to the vibration

of the structural components involved. In many practical modern situations, geometrically non-linear structural vibrations occur, making the classical analytical and numerical tools, developed within the frames of linear theories, unable to predict properly the corresponding sound radiation parameters.

The purpose of this work is to develop an easy practical tool to calculate the acoustic radiation indicators, such as pressure, velocity, impedance, and efficiency of a simply supported beam subjected to large vibration amplitudes in the neighborhood of one of its modes of vibration. To do so, the explicit analytical expression for the beam non-linear forced response in the neighborhood of the mode considered, obtained in previous works, is first substituted in the classical expressions for the acoustic indicators mentioned above. This leads to new expressions for these indicators involving the effect of the geometrical non-linearity on the beam acoustic radiation. Finally, the indicators are computed numerically and plotted in order to enable comparisons to be made with the corresponding classical linear ones.

The sound radiation from beams of finite length has been considered by several authors. Radiation associated to the transverse steady state vibrations of beams was considered by exact and approximate theories in [1-2]. In 1962, Maidanik [6] proposed approximate formulae for the modal radiation efficiency in different frequency regions of simply supported rectangular vibrating beams and panels set in an infinite rigid baffle. In 1972, Wallace [7] presented integral expressions for the modal radiation efficiency at arbitrary frequencies based on the far field acoustic intensity. Simply supported unbaffled beams of circular [8-9] or elliptical [10-11] cross sections have been analyzed. In an extensive analytical and experimental study of the radiation of beams of slender elliptical cross section, Blake [9] has obtained expressions for the radiated power for baffled and unbaffled beams in air and water and studied the effects of fluid loading. Using a thorough mathematical description of the modal radiation efficiency, Leppington [16] obtained approximate expressions in the large wave number region, especially in the neighborhood of high critical frequencies. Li [17] obtained an analytical solution for the self and mutual radiation resistances in the form of power series of the non-dimensional acoustic wave number, which appeared to be extremely efficient in comparison with the traditional numerical integration scheme. Also, the effect of the baffle on the modal radiation efficiency was presented by Laulagnet [18].

2. GEOMETRICALLY NON-LINEAR STEADY STATE HARMONIC RESPONSE OF SIMPLY-SUPPORTED BEAMS

The purpose of the present section is to make a brief review of the theory, previously developed by Benamar and his co-authors, for the geometrically non-linear steady state harmonic response of simply-supported beams in the neighborhood of one of its mode shapes [1-2]. This is made in order to introduce the analytical expressions for the non-linear beam response substituted in the present work into the integrals used to calculate the non-linear acoustic indicators. For a complete presentation of the theory, the reader can be turned for example to the references mentioned above.

The transverse vibrations a simply supported beam set in an infinite rigid baffle and radiating into the fluid in a semi-infinite space are examined. The beam has the following characteristics: L, b, S: length, width and area of the beam cross section; x-y: beam coordinates in the length and the width directions; H beam thickness; E, ν : Young's modulus and Poisson's ratio; D, ρ: beam bending stiffness and mass per unit volume. The beam is supposed to be subjected to a harmonic force in such a manner to excite predominantly a given non-linear mode. For example, if the excitation concentrated dimensionless force of amplitude f* is harmonic, with a frequency ω chosen in the vicinity of the beam fundamental frequency, and is applied at the beam middle span, it has been sown that the corresponding non-linear frequency response function may be presented by [2]:

$$(\omega^* / \omega_L^*)^2 = 1 + \frac{3}{2}(b_{1111}^* / k_{11}^*)a_1^2 - (1 / k_{11}^*)f_1^* / a_1 \qquad (1)$$

In which: $\omega_L^{*2} = k_{11}^*$ and m_{11}^*; k_{11}^* and b^*_{1111} are the dimensionless mass, rigidity and non-linear rigidity terms corresponding to the first mode respectively defined in reference [1] as :

$$b^*_{ijkl} = \alpha ijkl \frac{\pi^4}{4} \delta_{ij}\delta_{kl}; \qquad k^*_{ij} = i^2 j^2 \frac{\pi^4}{2}\delta_{ij}; \qquad m^*_{ij} = \frac{1}{2}\delta_{ij}$$

Where δ_{ij} is the Kronecker symbol, defined by δ_{ij} =0 if $i \neq j$ and δ_{ij} =1 if $i = j$.

$\alpha = S\frac{H^4}{4I}$, where I is the second moment of area of cross-section. For a uniform beam with a rectangular cross-section, $\alpha = 3$.

For the first mode, ω^2 can be written as :

$$\omega^2 = \frac{EI\pi^4}{\rho SL^4}[1 + \frac{9}{4}a_1^2 - 2f_1^* / \pi^4 a_1] \tag{2}$$

3. EXPRESSIONS FOR THE BAFFLED BEAM RADIATION INDICATORS

The classical expressions for the acoustic radiation indicators, which will be used here in the non-linear case, may be found for example in reference [3]. Before presenting the modifications made, these are summarised below.

The spatially averaged mean square velocity of the beam is given by :

$$\left\langle \dot{V}^2 \right\rangle = \frac{1}{2S}\int_S \dot{W}(x,z,t)\dot{W}^*(x,z,t)dxdz. \tag{3}$$

where $\dot{W}(x,z,t)$ and $\dot{W}^*(x,z,t)$ are the normal velocity distribution over the surface of the beam and its conjugate. For a simply supported beam, the mode is orthogonal and then the expression for the spatially averaged mean square velocity of beam can be written as :

$$\left\langle \dot{V}^2 \right\rangle = \frac{\omega^2}{2L}\sum_{i=1}^{n} |ai|^2 N_i. \tag{4}$$

N_i is the norm of the i^{th} mode and is given by :

$$N_i = \int_0^L W_i^2(x)dx = \frac{L}{2}.$$

The sound pressure radiated in the far-field for a baffled beam using the simplified Kirchhoff–Helmholtz integral is given by :

$$P(r) = \frac{\rho_0}{2\pi}\iint_{(S_0)} \ddot{W}(r_0)G(r/r_0)dS(r_0). \tag{5}$$

where ρ_0 is the density of the surrounding medium, S_0 the area of the structural surface, r_0 the point on structural surface, r the field point expressed in spherical coordinates as $r = (R, \theta, \varphi)$, k the sound wave number, $k = \omega/c_0$, with c_0 the sound speed in the medium, and $G(r/r_0) = \frac{1}{2\pi}\frac{e^{-Jk|r-r_0|}}{|r-r_0|}$ is the Green function. The above expression constitutes the basic relation between the structural response and the sound pressure radiated. In the far field, the distance between the field point r and the beam is large compared to the characteristical dimension of the beam. That allowed approximating the distance in the denominator of the Green's function by R. Then : $|r - r_0| \approx |r| = R$.

Using the spherical coordinates, the expression for the far-field acoustic pressure distribution can be written as :

$$P(R,\theta,\varphi) = -\rho_0\omega^2 . \left(2\frac{\sin(\frac{\beta b}{2})}{\beta} \right) . \frac{e^{-jkR}}{2\pi R} . \sum_{i=1}^{n} a_i \left[\frac{\frac{L}{\pi i}((-1)^i e^{j\alpha L} - 1)}{\left(\frac{\alpha L}{\pi i}\right)^2 - 1} \right] \tag{6}$$

With: $\alpha = k.\sin\theta.\cos\varphi$ and $\beta = k.\sin\theta.\sin\varphi$

The integral of the average acoustic intensity over the hemisphere in the far field yields the total acoustic power radiated by the beam, are given by :

$$\Pi(\omega) = \frac{1}{2\rho_0 c_0} \int_0^{2\pi} \int_0^{\pi/2} R^2 \left| p(R,\theta,\varphi) \right|^2 \sin\theta d\theta d\varphi. \tag{7}$$

The radiation efficiency can be written as:

$$\sigma = \frac{\Pi(\omega)}{\rho_0 c_0 s_0 (V^2)} \tag{8}$$

Where: $\Pi(\omega)$is the sound power radiated, ρ_0 is the density of the fluid (air in the present case), c_0 is the speed of sound, S_0 is the beam surface area and $\langle \dot{V}^2 \rangle$ is the spatially averaged mean-square normal velocity of the beam.

4. ANALYTICAL DETAILS AND NUMERICAL RESULTS

Substituting the expression for ω^2 given in equation (2), which corresponds to the geometrically non-linear vibration of the beam considered, into equations (4) and (6) leads to the new expressions for the non-linear acoustic radiation indicators:

$$\left\langle \dot{V}^2 \right\rangle = \frac{EI\pi^4 \left[1 + \frac{9}{4}\alpha_1^2 \ -2f_1 / \pi^4 \alpha_1 \right]}{4\rho S L^4} |a_1|^2 \tag{9}$$

$$P(R,\theta,\varphi) = -\frac{EI\rho_0\pi^4}{\rho S L^4} \left[1 + \frac{9}{4}\alpha_1^2 \ -2f_1^* \ / \pi^4 a_1 \right] . \left(2\frac{\sin(\frac{\beta b}{2})}{\beta} \right) . \frac{e^{-jkR}}{2\pi R} . a_1 \left[\frac{\frac{L}{\pi}\left(-e^{jaL} - 1\right)}{\left(\frac{aL}{\pi}\right)^2 - 1} \right] \tag{10}$$

Using the above equations, numerical results have been obtained in the case of a beam having the following parameters: L = 0.39 m, b = 0.038 m, h = 0.00634 m.ρ = 7800 Kg/m^3, E = 210 10^9 N/m^2. The external fluid: Air: ρ_0 = 1.29 kg/m^3, c_0 = 343 m/s. f* = 350.

In figure 1 (a), the nonlinear frequency response function of the beam, *i.e.* equation (1) is plotted, showing the hardening non-linear behavior. In figures (1 (b), 2), the acoustic radiation indicators, *i.e.* the velocity, the pressure, and the radiated acoustic power are plotted in each figure for the same value of the dimensionless excitation force f*= 350 using both the classical linear expressions and the corresponding non-linear ones established here. It can be seen that the geometrical non-linearity induces a visible difference in the curves, indicating that the non-linearity has to be taken into account, especially as this effect is expected to increase if the amplitude of vibration increases.

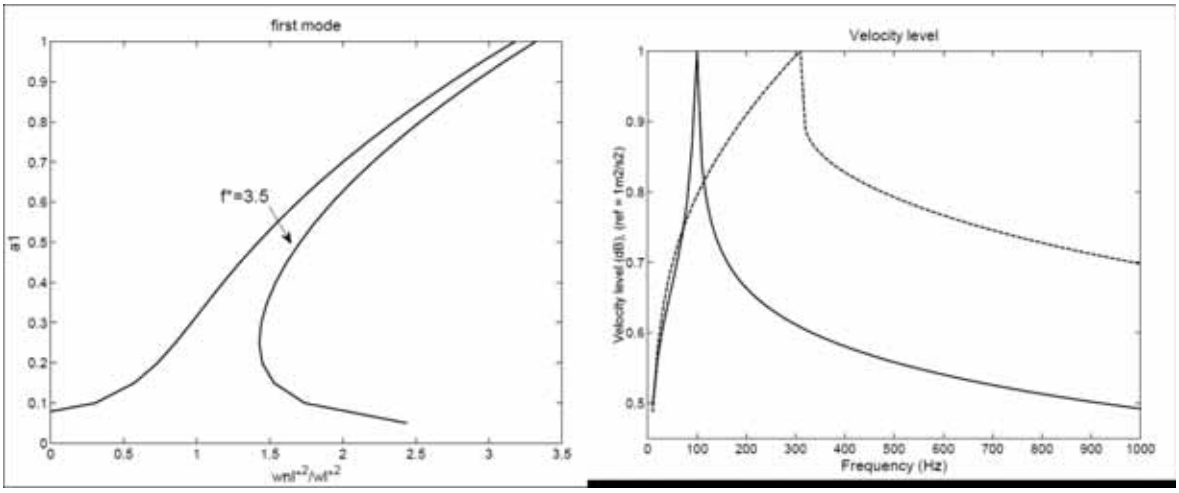

(a) (b)

Fig. 1. (a) The nonlinear frequency response; (b) Normalized mean square velocity level in the neighborhood of the first non-linear mode for f* = 350._____Linear; - - - - - - Nonlinear

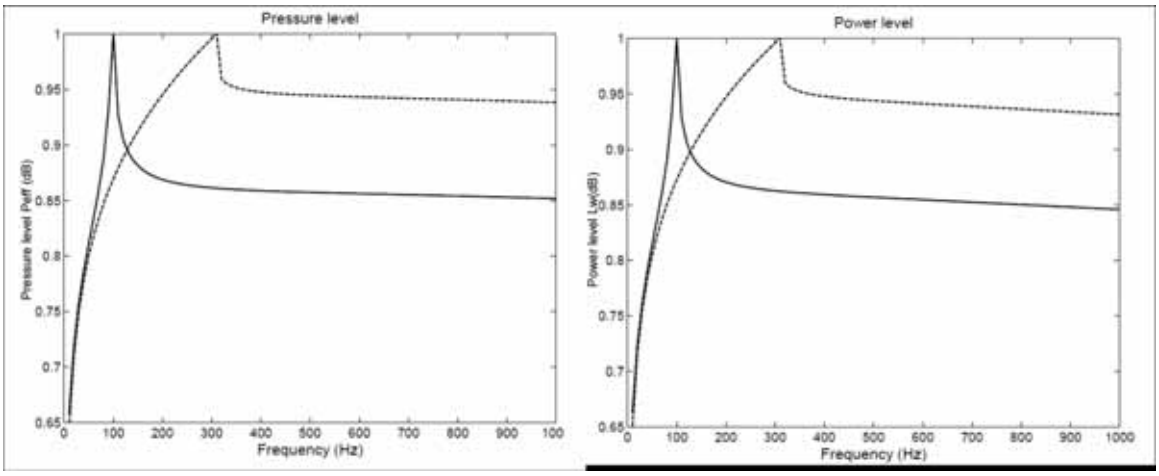

(a) (b)

Fig. 2. (a) Normalized pressure for f*=350; (b) power level in the first mode for f* = 350._____Linear; - - - - - - Nonlinear

5. CONCLUSION

The above results are typical of what occurs when the non linear frequency response function is used in the expressions for the velocity, the pressure, and the radiated power level of a simply supported rectangular beam in the neighborhood of the non-linear first mode. It can be noticed that both the values of the sound radiation indicators and their distributions predicted by the present non-linear theory can be different from those usually obtained by the classical linear approaches. Consequently, it appears that the extension of the present works to higher modes and to other structures, such as beams with other end conditions and plates, may be useful to the engineers working in the field of sound control.

6. REFERENCES

[1] R. BENAMAR, M.M. K. BENNOUNA and R. G. WHITE, 1991. The effects of large vibration amplitudes on the mode shapes and natural frequencies of thin elastic structures. Part I: simply supported and clamped-clamped beams. *Journal of Sound and vi bration,* **149**, 179-195.

[2] L. AZRAR, R. BENAMAR and R. G. WHITE, 1999. A semi-analytical approach to the non-linear dynamic response. Problem of SS and CC beams at large vibration amplitudes. Part I: general theory and application to the single mode approach to free and forced vibration analysis. *Journal of Sound and vibration*. **224**, 377-395.

[3] H. ZHENG and C. CAI, 2004. Minimization of sound radiation from baffled beams through optimization of partial constrained layer damping treatment. *Applied Acoustic,* **65**, 501–520.

[4] AKAY, 1978. A review of impact noise. *Journal of the Acoustical Society of America,* **64**, 977-987.

[5] R.H. LYON and G. MAIDANIK, 1962. Power flow between linearly coupled oscillators. *Journal of the Acoustical Society of America,* **34**, 623-639.

[6] MAIDANIK, 1962. Response of ribbed panels to reverberant acoustic fields. *Journal of the Acoustical Society of America*, **34**, 809–826.

[7] C. E. WALLACE, 1972. Radiation resistance of a baffled beam. *Journal of the Acoustical Society of America,* **51**, 936-945.

[8] J.R. BAILEY and F.J. FAHY, 1972. Radiation and response of cylindrical beams excited by sound. *Journal of Engineering for Industry*, **94**, 139-147.

[9] S.N. YOUSRI and F.J. FAHY. 1973. Sound radiation from transversely vibrating unbaffled beams. *Journal of Sound and Vibration,* **26**, 437-439.

[10] M.C. JUNGER, 1972. Sound radiation by resonances of free-free beams. *Journal of the Acoustical Society of America*, **52**, 332-334.

[11] R.A. JOHNSTON and A.D.S. BARR, 1969. Acoustic and internal damping in uniform beams. *Journal Mechanical Engineering Science,* **11**, 117-127.

[12] W.K. BLAKE, 1974. The radiation from free-free beams in air and in water. *Journal of Sound and Vibration,* **33**,427-450.

[13] L.E. KINSLER and A.R. FREY, 1962. New York: John Wi ley and Sons, Inc. *Fundamentals of Acoustics,*

[14] R.K. JEYAPALAN and E.J. RICHARDS, 1979. Radiation efficiencies of beams in flexural vibration. *Journal of Sound and Vibration,* **67**, 55-67.

[15] G. XIE, D.J. THOMPSON and C.J.C. JONES, 2005. The radiation efficiency of baffled plates and strips. *Journal of Sound and Vibration,* **280**, 181–209.

[16] F.G. LEPPINGTON, E.G. BROADBENT F.R.S and K.H. HERON, 1982. The acoustic radiation efficiency of rectangular panels. *Proceedings of the Royal Society London,* **A 382**, 245– 271.

[17] W.L. LI., 2006. Vibroacoustic analysis of rectangular plates with elastic rotational edge restraints. *Journal of the Acoustical Society of America,* **120** (2), 769–779.

[18] B. LAULAGNET, 1998. Sound radiation by a simply supported unbaffled plate. *Journal of the Acoustical Society of America,* **103**(5), 2451–2462.

[19] M.C. JUNGER and D. FEIT, 1993. Sound, Structures and their Interaction. *Acoustical Society of America,*

Journal of Acoustical Society of India : Vol. 42, No. 3, 2015 (pp. 174-179)

Audio Novelty-based Segmentation of Music Concerts

Dalia El Badawy, Patrick Marmaroli* and Hervé Lissek
[1]Laboratory of Electromagnetism and Acoustics (LEMA),
Swiss Federal Institute of Technology in Lausanne (EPFL) - Station 11, 1015 Lausanne
**e-mail: patrick.marmaroli@epfl.ch*

[Received: 16.12.2013; Revised: 17.08.2014; Accepted: 26.04.2015]

ABSTRACT

The Swiss Federal Institute of Technology in Lausanne (EPFL) is in the process of digitizing an exceptional collection of audio and video recordings of the Montreux Jazz Festival (MJF) concerts. Since 1967, five thousand hours of both audio and video have been recorded with about 60% digitized so far. In order to make these archives easily manageable, ensure the correctness of the supplied metadata, and facilitate copyright management, one of the desired tasks is to know exactly how many songs are present in a given concert, and identify them individually, even in very problematic cases (such as medleys or long improvisational periods). However, due to the sheer amount of recordings to process, it is a quite cumbersome and time consuming task to have a person listen to each concert and identify every song. Consequently, it is essential to automate the process. To that end, this paper describes a strategy for automatically detecting the most important changes in an audio file of concert; for MJF concerts, those changes correspond to song transitions, interludes, or applause. The presented method belongs to the family of audio novelty-based segmentation methods. The general idea is to first divide a whole concert into short frames, each of a few milliseconds length, from which well-chosen audio features are extracted. Then, a similarity matrix is computed which provides information about the similarities between each pair of frames. Next, a kernel is correlated along the diagonal of the similarity matrix to determine the audio novelty scores. Finally, peak detection is used to find significant peaks in the scores which are suggestive of a change. The main advantage of such a method is that no training step is required as opposed to most of the classical segmentation algorithms. Additionally, relatively few audio features are needed which leads to a reduction in the amount of computation and run time. It is expected that such a pre-processing shall speed up the song identification process: instead of having to listen to hours of music, the algorithm will produce markings to indicate where to start listening. The presented method is evaluated using real concert recordings that have been segmented by hand; and its performance is compared to the state-of-the-art.

1. INTRODUCTION

At EPFL, the *Montreux Jazz Digital Project*aims at digitizing the archives of the Montreux Jazz Festival (MJF) concerts. A few figures: since 1967, 5000 hours of audio and video are stored on 10000 magnetic tapes. These archives contain approximately 40000 songs. The safeguarding of this heritage has begun in 2010 and will continue until early 2015 when 100% of the archives (1.2 Petabytes) will be processed and stored. In order to improve these archives, make them easily manageable, facilitate copyright management and help with quality control, several applications are desired such as the detection of audio events. In particular,

it is required to know exactly which songs were sung in a given concert and even songs in a medley. However, due to the sheer amount of recordings available, it is quite cumbersome and time consuming to listen to each concert and note down the songs; it is therefore required to automate the process.

Detection of song changes using stochastic models is described in [1]; however, it is assumed that there are pauses between the songs which is not always the case for the MJF concerts. Related methods for semantic audio segmentation which deals with finding the constituents of a song like the intro, chorus, and bridge are described in [2], [3], [4], and[5]. Inthis paper, we describe a methodology to automatically segment MJF audio file concerts in order to aid human listeners and speedup the process of songs identification. Audio novelty scores presented in [4] are used for detection of song changes instead of structures within the same song.

The proposed approach is described in Section 2. Section 3 presents the experiments we carried out and the performance results. Finally, the conclusion and suggestions for future work are presented in Section 4.

2. CONCERT SEGMENTATION

A concert recording generally contains several acoustic events including the songs, applause, and interludes. The first step in segmenting aconcert into those separate events is to represent the audio recording in a format suitable for analysis. This is done by extracting the so-called audio features from the raw audio signal. Then, these audio features which describe the signal are used by the segmentation module to generate a proper segmentation.

2.1 Audio features

Audio feature vectors are computed from small successive frames ofsize N_f (in samples) with an overlap of N_0 (in samples). The number of frames M contained in a signal of length N is given by the formula:

$$\mathrm{M} = \left\lfloor \frac{\mathrm{N} - \mathrm{N_f}}{\mathrm{N_f} - \mathrm{N_o}} \right\rfloor + 1 \tag{1}$$

where $\lfloor . \rfloor$ stands for the floor function. In order to avoid edge effects when transforming it to the frequency domain, each frame is weighted by a Hann window (defined in[6] p. 397 for instance).

2.2 Segmentation

Once the audio is reduced to feature vectors (one per frame); the segmentation process can begin. The method used here follows [4]. The idea is to calculate the similarity between two successive frames; if they are different,then a change is possibly detected. So first, a distance measure is required.

2.2.1 *Distance Measure*

A distance measure is used to quantify the similarity (or dissimilarity) between two feature vectors. One such measure is the cosine similarity, which for two feature vectors $\mathbf{X}_i$ and $\mathbf{X}_j$ is calculated as follows:

$$d_{ij} = \frac{< \mathbf{x}_i , \mathbf{x}_j >}{\left\| \mathbf{x}_i \right\| \left\| \mathbf{x}_j \right\|} \tag{3}$$

where <.,.> denotes the inner product and$| |.| |$ the Euclidean norm. The values range between [–1, 1] with 1 for parallel vectors and –1 for anti parallel. It is a suitable measure because it is not affected by the energy levels where if the energy is low in two feature vectors, they can still have a high similarity score [4].

2.2.2 *Similarity Matrix*

Using the distance measure, the similarity between each pair of frames can be computed and placed in a similarity matrix **S** of size $M \times M$ where :

$$\mathbf{S}[i, j] = d_{ij}, \forall (i, j) \in \{1, 2, ..., M\}^2 \tag{4}$$

Figure 1 shows an audio excerpt and its corresponding similarity matrix. As indicated on the figure, the excerpt contains the ending and beginning of two different songs separated by applause.The checkerboard patterns where the changes occur are visible in the center of the similarity matrix.

2.2.3 *Novelty Score*

A novelty score is computed at each frame where the frames with high scores indicate a change and thus the audio should be segmented there. To calculate the score, a "checkerboard kernel" $\mathbf{H}_K$ of size, $K \times K$, $\forall K \in \{2, 3, ...M\}$ is used. An example of such a kernel when $K = 4$ is provided below:

$$\mathrm{H}_4 = \begin{pmatrix} 1 & 1 & -1 & -1 \\ 1 & 1 & -1 & -1 \\ -1 & -1 & 1 & 1 \\ -1 & -1 & 1 & 1 \end{pmatrix} \tag{5}$$

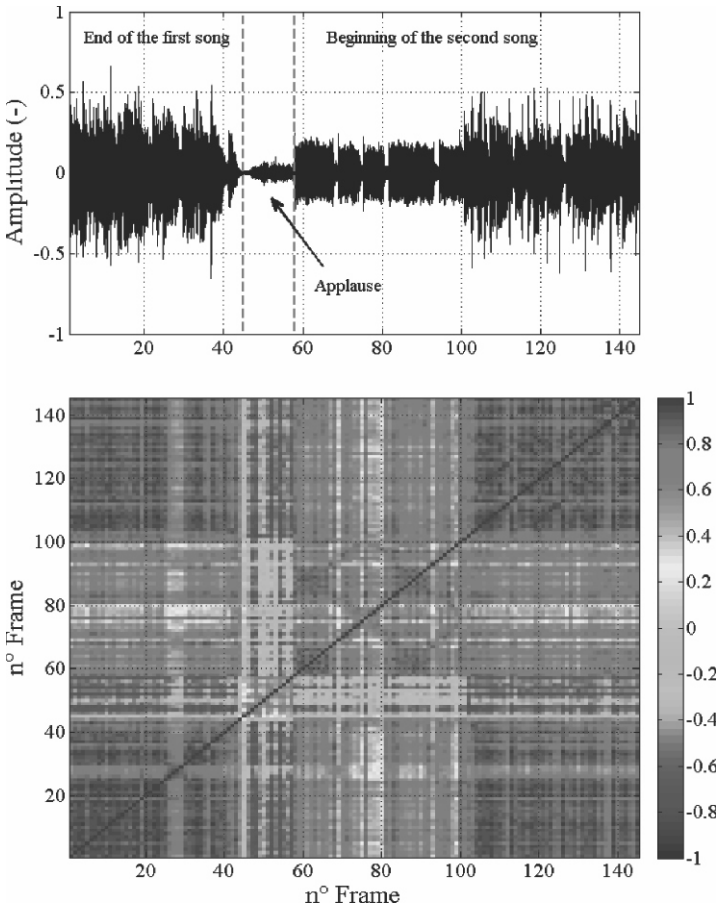

Fig. 1. top: waveform of a song change, bottom: corresponding similarity matrix.

Then, the 2D cross-correlation, r, between the kernel and the similarity matrix at each frame is calculated as follows :

$$r(m) = \mathrm{corr}\left(\mathbf{H}_K, \mathbf{S}_K^m\right) \tag{6}$$

where $\mathbf{S}_K^m$ is the part of the similarity matrix with the same size of the kernel and centered at coordinates (m, m) :

$$\mathbf{S}_m^K = \mathbf{S}\left(\left[m - \frac{K}{2} + 1, ..., m + \frac{K}{2}\right], \left[m - \frac{K}{2} + 1, ..., m + \frac{K}{2}\right]\right) \tag{7}$$

Thus, r is high at locations where the checkerboard patterns of the matrix match up with those of the kernel *i.e.* the positive and negative parts of the kernel multiply their respective positive and negative parts on the matrix.

Note that *K* here determines the extent of boundary detection: smaller kernels detect changes on a lower level like individual musical notes. The kernel is correlated only along the diagonal of the similarity matrix to get a score along the time dimension. Then, the scores are normalized to between 0 and 1. Using the generated novelty score at each frame, peak detection is used (with a threshold value) to find the local maxima and thus determine the positions of change.

Only peaks above a threshold areconsidered as song changes. In our algorithm, the threshold is adjusted automatically to the data. The hypothesis is that when a change occurs, the indicative peak is much higher than the other scores or weaker peaks in the same audio window. Therefore, the threshold Λ is chosen according to the standard deviation of the scores in that window:

$$\Lambda = \mu = \lambda\sigma \tag{9}$$

where μ, respectively σ, are the mean and standard deviation of the cross-correlation values, *r = [r(1), r(2), ..., r(M)*], in the audio file, and λ is a scalar.

2.2.4 Evaluation

In order to evaluate the performance of the segmentation, two measures canbe used: recall and precision. Given the ground truth *i.e.* correct segmentation, *recall* is the ratio of the number correctly detected boundaries to the number of boundaries inthe ground truth (it measures how good the system is at finding the required boundaries and equals 1 if all the correct boundaries have been found). Whereas *precision*is the ratio of the number of correctly detected boundariesto all detected boundaries regardless they are right or wrong (it equals 1 if only correct boundaries were found) :

$$recall = \frac{\text{number of correct boundaries}}{\text{number of ground truth boundaries}} \qquad precision = \frac{\text{number of correct boundaries}}{\text{number of all boundaries}}$$

3. EXPERIMENT

The dataset consists of 50 MJF concerts. All wave files are mono and sampled at 48 kHz. The total duration is of 60 hours 43 minutes 32 seconds. There was a total of 1132 manually placed segments (song, applause, interlude) that served as the ground truth for evaluating the system.A subset of this dataset was used for tuning the parameters (frame size, kernel size, detection threshold, audio features). It consisted of 5 randomly chosen concerts of total duration 6 hours 29 minutes 1 second with 99 manual segments.Audio features that have been compared are the spectrum, MFCC, chroma features, and their combinations; however, the spectrum gave the best results. Finally, the parameters giving us the best results are summarized in Table 1.

Table 1: Parameter values for the experiment.

Frame size (in samples)	N_f	8192 (170 ms)
Overlap (in samples)	N_0	0
Threshold parameter	λ	4.5
Kernel size (in number of frames)	K	64
Audio features	$\mathbf{x}$	Lower spectrum (50 first coeffi cients) by using the MIRToolbox [7].

Note that in [2], the checkerboard kernel was tapered using a Gaussian function. From our experience, not using a Gaussian weighting provides a slightly better result.

The segmentation results were evaluated with atolerance of $\pm$ 10 second saround the manual ground truth segmentation. We get a recall of 78.7%which is more than 8% higher than reported in [1]; while the precision is 23.3%. On inspecting some of the manual segmentations, it could be argued that some segments should actually start earlier or later since it is subjective; this affects the recall. However, for the precision, when listening to the extra added segments, it is usually the case that the beat stopped and started; or there is a sudden silence; or even a short impulse sound like a whistle.

4. CONCLUSION

This study was concerned with song change detection for the Montreux Jazz Festival concerts. The algorithm that has been developed is based on audio novelty detection. Several audio features were tried; the best was found to be the lower frequency spectrum. Other parameters like the frame size and whether to weight the checkerboard kernel were optimized. Finally, the algorithm was tested on 50 MJF concerts and achieved a recall value of 78.7%.

Suggestions for further improvement include overlapping the windowsfrom which frames are extracted since it could be the case that a change between the windows is missed; also, over lapping the frames them selves could be useful. Moreover, for MJF concerts, it is interesting to note that thereare 3 main audio events: music, speech, and applause which may occur between songs or even during a song. This extra knowledge can by all meansbe leveraged to improve the song change detection system. For instance,salient features for speech or applause can be used to detect their respective events which usually occur before or after songs and thus improve the song detection accuracy.

Future work includes matching the detected segments in the end to their respective events. And also, if a database of songs is available, each songcan be matched to get its title and other meta data. Further more, it is also possible to utilize the video as well where during a song; the camera is most likely focused on the performers then switches to the audience at the endduring the applause; so the scene changes can be a useful addition.

5. REFERENCES

[1] T. PLOTZ, G.A. FINK, P. HUSEMANN, S. KANIES, K. LIENEMANN, T. MARSCHALL, M. MARTIN, L. SCHILLINGMANN, M. STEINRUCKEN and H. SUDEK, 206. Automatic detection of song changes in music mixes using stochastic models. In *Proceedings of the International Conference on Pattern Recognition (ICPR)*, **3**, 665–668.

[2] P. ROMANO, G. PRANDI, A. SARTI and S. TUBARO, 2009. Musical audio semantic segmentation exploiting analysis of prominent spectral energy peaks and multi-feature refinement. In *Proceedings of the IEEE International Conference on Acoustics, Speech and Signal Processing (ICASSP)*, 1965–1968.

[3] M. LEVY, M. SANDLER and M. CASEY, 2006. Extraction of high-level musical structure from audio data and its application to thumbnail generation. In *Proceedings of the IEEE International Conference on Acoustics, Speech and Signal Processing (ICASSP)*, **5**, V–V.

[4] J. FOOTE, 2000. Automatic audio segmentation using a measure of audio novelty. In *Proceedings of the IEEE International Conference on Multimedia and Expo (ICME)*, **1**, 452–455.

[5] SAMER ABDALLAH, KATY NOLAND, MARK SANDLER and S. MARK, 2005. Theory and evaluation of a bayesian music structure extractor. In *Proceedings of the Sixth International Conference on Music Information Retrieval (ISMIR)*, 420–425.

[6] S. SALIVAHANAN, A. VALLAVARAJ and C. GNANAPRIYA, 2007. *Digital signal processing*. Tata McGraw-HIll Education.

[7] OLIVIER LARTILLOT and PETRI TOIVIAINEN, 2007. A Matlab toolbox for musical feature extraction from audio.In *Proceedings of the 10thInternational Conference on Digital Audio Effects (DAFx)*, 237-244.

INFORMATION FOR AUTHORS

ARTICLES

The Journal of Acoustical Society of India (JASI) is a refereed publication published quarterly by the Acoustical Society of India (ASI). JASI includes refereed articles, technical notes, letters-to-the-editor, book review and announcements of general interest to readers.

Articles may be theoretical or experimental in nature. But those which combine theoretical and experimental approaches to solve acoustics problems are particularly welcome. Technical notes, letters-to-the-editor and announcements may also be submitted. Articles must not have been published previously in other engineering or scientific journals. Articles in the following are particularly encouraged: applied acoustics, acoustical materials, active noise & vibration control, bioacoustics, communication acoustics including speech, computational acoustics, electro-acoustics and audio engineering, environmental acoustics, musical acoustics, non-linear acoustics, noise, physical acoustics, physiological and psychological acoustics, quieter technologies, room and building acoustics, structural acoustics and vibration, ultrasonics, underwater acoustics.

Authors whose articles are accepted for publication must transfer copyright of their articles to the ASI. This transfer involves publication only and does not in any way alter the author's traditional right regarding his/her articles.

PREPARATION OF MANUSCRIPTS

All manuscripts are refereed by at least two referees and are reviewed by the Publication Committee (all editors) before acceptance. Manuscripts of articles and technical notes should be submitted for review electronically to the Chief Editor by e-mail or by express mail on a disc. JASI maintains a high standard in the reviewing process and only accept papers of high quality. On acceptance, revised articles of all authors should be submitted to the Chief Editor by e-mail or by express mail.

Text of the manuscript should be double-spaced on A4 size paper, subdivided by main headings-typed in upper and lower case flush centre, with one line of space above and below and sub-headings within a section-typed in upper and lower case understood, flush left, followed by a period. Sub-sub headings should be italic. Articles should be written so that readers in different fields of acoustics can understand them easily. Manuscripts are only published if not normally exceeding twenty double-spaced text pages. If figures and illustrations are included then normally they should be restricted to no more than twelve-fifteen.

The first page of manuscripts should include on separate lines, the title of article, the names, of authors, affiliations and mailing addresses of authors in upper and lowers case. Do not include the author's title, position or degrees. Give an adequate post office address including pin or other postal code and the name of the city. An abstract of not more than 200 words should be included with each article. References should be numbered consecutively throughout the article with the number appearing as a superscript at the end of the sentence unless such placement causes ambiguity. The references should be grouped together, double spaced at the end of the article on a separate page. Footnotes are discouraged. Abbreviations and special terms must be defined if used.

EQUATIONS

Mathematical expressions should be typewritten as completely as possible. Equation should be numbered consecutively throughout the body of the article at the right hand margin in parentheses. Use letters and numbers for any equations in an appendix: Appendix A: (A1, (A2), etc. Equation numbers in the running text should be enclosed in parentheses, i.e., Eq. (1), Eqs. (1a) and (2a). Figures should be referred to as Fig. 1, Fig. 2, etc. Reference to table is in full: Table 1, Table 2, etc. Metric units should be used: the preferred from of metric unit is the System International (SI).

REFERENCES

The order and style of information differs slightly between periodical and book references and between published and unpublished references, depending on the available publication entries. A few examples are shown below.

Periodicals:

[1] S.R. Pride and M.W. Haartsen, 1996. Electroseismic wave properties, *J. Acoust. Soc. Am.*, **100** (3), 1301-1315.

[2] S.-H. Kim and I. Lee, 1996. Aeroelastic analysis of a flexible airfoil with free play non-linearity, *J. Sound Vib.*, **193** (4), 823-846.

Books:

[1] E.S. Skudzryk, 1968. *Simple and Comlex Vibratory Systems*, the Pennsylvania State University Press, London.

[2] E.H. Dowell, 1975. *Aeroelasticity of plates and shells*, Nordhoff, Leyden.

Others:

[1] J.N. Yang and A. Akbarpour, 1987. Technical Report NCEER-87-0007, Instantaneous Optimal Control Law For Tall Buildings Under Seismic Excitations.

SUMISSIONS

All materials from authors should be submitted in electronic form to the JASI Chief Editor: B. Chakraborty, CSIR - National Institute of Oceanography, Dona Paula, Goa-403 004, Tel: +91.832.2450.318, Fax: +91.832.2450.602,(e-mail: bishwajit@nio.org) For the item to be published in a given issue of a journal, the manuscript must reach the Chief Editor at least twelve week before the publication date.

SUMISSION OF ACCEPTED MANUSCRIPT

On acceptance, revised articles should be submitted in electronic form to the JASI Chief Editor (bishwajit@nio.org)

ISSN 0973-3302

JOURNAL OF ACOUSTICAL SOCIETY OF INDIA

Volume 42 Number 4 October 2015

A Quarterly Publication of the JASI
http://www.acousticsindia.org

Journal of Acoustical Society of India

Volume 42 Number 4 October 2015 pp 181-238

JASI

Journal of Acoustical Society of India

The Refereed Journal of the Acoustical Society of India (JASI)

The Journal of Acoustical Society of India is a refereed journal of the Acoustical Society of India **(ASI)**. The **ASI** is a non-profit national society founded in 31st July, 1971. The primary objective of the society is to advance the science of acoustics by creating an organization that is responsive to the needs of scientists and engineers concerned with acoustics problems all around the world.

Manuscripts of articles, technical notes and letter to the editor should be submitted to the Chief Editor. Copies of articles on specific topics listed above should also be submitted to the respective Associate Scientific Editor. Manuscripts are refereed by at least two referees and are reviewed by Publication Committee (all editors) before acceptance. On acceptance, revised articles with the text and figures scanned as separate files on a diskette should be submitted to the Editor by express mail. Manuscripts of articles must be prepared in strict accordance with the author instructions.

All information concerning subscription, new books, journals, conferences, etc. should be submitted to Chief Editor:

B. Chakraborty, CSIR - National Institute of Oceanography, Dona Paula, Goa-403 004,
Tel: +91.832.2450.318, Fax: +91.832.2450.602, e-mail: bishwajit@nio.org

Annual subscription price including mail postage is Rs. 2500/= for institutions, companies and libraries and Rs. 2500/= for individuals who are not **ASI** members. The Journal of Acoustical Society of India will be sent to **ASI** members free of any extra charge. Requests for specimen copies and claims for missing issues as well as address changes should be sent to the Editorial Office:

ASI Secretariat, C/o Acoustics, Ultrasonics & Vibration Section, CSIR-National Physical Laboratory, Dr. KS Krishnan Road, New Delhi 110 012, Tel: +91.11.4560.8317, Fax: +91.11.4560.9310, e-mail: asisecretariat.india@gmail.com

ISSN 0973-3302

Printed at Alpha Printers, WZ-35/C, Naraina, Near Ring Road, New Delhi-110028 Tel.: 9810804196. JASI is sent to ASI members free of charge.

JASI

Journal of Acoustical Society of India (JASI)

A quarterly publication of the Acoustical Society of India

Volume 42, Number 4, October 2015

ARTICLES

INFORMATION

Journal of Acoustical Society of India : Vol. 42, No. 4, 2015 (pp. 181-187)

Urban Sound Quality Assessment with Mobile Technology: The Cart_Asur Project

Lavandier Catherine[1]*, Delaitre Pauline[1], D'Hondt Ellie[2], Gonzalez Boix Elisa[2] and Kambona Kennedy[2]

[1]Laboratoire MRTE, Université de Cergy Pontoise, F-95000 Cergy-Pontoise

[2]Software Languages Lab, Vrije Universiteit Brussels, B-1050 Brussels

**e-mail: catherine.lavandier@u-cergy.fr*

[Received: 09.12.2013; Revised: 29.06.2014; Accepted: 27.12.2015]

ABSTRACT

The aim of the Cart_ASUR project is to propose urban sound quality indicators based on acoustic and perceptive data. In order to collect the data, a mobile application has been especially developed by the BrusSense Team of the Vrije Universiteit Brussel. The Cart_ASUR application is based on the NoiseTube one which makes it possible to record noise levels after relevant calibration of the mobile microphone. This new application proposes to collect, in addition to noise levels, perceptive data in specific places (parks, squares, thoroughfares, streets, schools, markets, pedestrian streets, etc.). 60 mobiles have been distributed to 60 persons in Paris for conducting the measurements and the evaluations. Each person has to assess about 20 locations at four or five homogeneous periods (day, evening, night, summer, winter etc.). After a year of experiment, it is expected to collect 6 000 measurement data. Each measurement corresponds to a 10-minute recording of sound pressure level. Following this recording, participants have to answer a short questionnaire. The first questions are related to the sound environment characterization with semantic scales. The next questions concern the perceived loudness assessment of some special sources. Finally, the last questions regard the presence time ratio assessment of other sources. Participants are also asked to take as many photographs of the locations as they want in order to study the influence of the visual setting. The data are automatically uploaded online on a dedicated server. With these 6000 data, it is expected to propose indicators of urban sound quality with the help of mathematical models such as regressions or artificial neural networks. Different types of variables will be considered as the input of the models: (1) perceptive variables collected through the questionnaires, (2) acoustic variables calculated from the sound level evolution recording such as equivalent sound level, percentile levels, standard deviation, dynamic indicators, and (3) non acoustic variables which could be extracted from the photographs or collected through already archived data from city maps such as the presence of public seats or the type of shops in a street, or the number of bus stops, etc. To conclude, the final aim of this research is to provide new solution towards noise pollution maps, focusing not only on noise levels, but also on other aspects such as visual settings, urban planning settings or assessments dedicated to special identified sources which lead towards urban sound quality.

1. INTRODUCTION

The study presented in this paper is part of a French project (Cart_ASUR) which aims at developing new

indicators of urban sound quality and proposing new types of sound maps. In France, noise mapping is regulated by a European Directive [1]. Large cities over 100 000 inhabitants have to present the average noise levels LDEN (Day Evening Night Level) due to traffic noise through noise maps. These noise levels, excluding many sound sources such as e.g. voices or mopeds, do not correspond to the real loudness perceived by citizens and do not match their experience thereof. It would be much better to represent the sound quality of urban situations instead of the average traffic noise level. In the short term, it is necessary to better understand what is behind the perceived sound quality. In the long run, it should also be interesting to be able to predict urban sound quality.

During the last four years, a study has been carried out in two large cities in France, focusing on variables which have an impact on sound quality. 320 passers-by were asked to assess their environment mainly from an acoustic point of view but also from other perspectives (visual context for example).

Table 1. Measured variables

<table>
<tr><td>Pleasantness</td><td colspan="2">(1) Sound pleasantness
(2) Global pleasantness
(3) Visual pleasantness
(4) Air quality pleasantness</td></tr>
<tr><td>Soundscape global characteristics</td><td colspan="2">(5) Quiet / Noisy
(6) Stable / Changing
(7) Lifeless / Lively
(8) Enveloping / Not Enveloping
(9) Surprising / Familiar
(10) Unsuitable / Suitable</td></tr>
<tr><td rowspan="8">Sound Sources

PL
=
Perceived
Loudness

TP
=
Time ratio
of presence</td><td>(11) PL.LV
(12) TP.LV</td><td>Cars / Motorbikes
(Light Vehicles)</td></tr>
<tr><td>(13) PL.Mop
(14) TP.Mop</td><td>Mopeds</td></tr>
<tr><td>(15) PL.TB
(16) TP.TB</td><td>Trucks/Buses</td></tr>
<tr><td>(17) PL.H
(18) TP.H</td><td>Horns</td></tr>
<tr><td>(19) PL.Act
(20) TP.Act</td><td>Activities</td></tr>
<tr><td>(21) PL.HP
(22) TP.HP</td><td>Human Presence</td></tr>
<tr><td>(23) PL.Bir
(24) TP.Bir</td><td>Birds</td></tr>
<tr><td>(25) PL.Nat
(26) TP.Nat</td><td>Nature</td></tr>
</table>

The investigation involved 8 different kinds of typical sound environments: park, pedestrian street, boulevard, street and urban transitions such as that between park and boulevard. In each location, 40 passers-by had to evaluate 26 subjective variables (Table 1) on 10-point scales between 2PM and 8PM. The collected data was analyzed according to two methods: multiple linear regressions and artificial neural networks [2]. For both methods, it was possible to link sound quality (sound pleasantness variable) to 13 dependent variables (Table 2). Moreover, the correlation coefficient between the sound pleasantness measured and that calculated was highly significant (over 0.8 for the test database).

Table 2. Variables chosen to explain the sound pleasantness

	Measured perceptive variables
Dependent variable	Sound pleasantness
	Visual pleasantness
	Quietness
	Liveliness
	Envelopment
	Familiarity
	Time ratio of light vehicle presence
	Perceived loudness of mopeds
Independent variables	Perceived loudness of trucks & buses
	Perceived loudness of Horns
	Time ratio of activities
	Time ratio of human presence
	Time ratio of bird presence
	Time ratio of nature sound presence

Questioning passers-by was time consuming (about six months in each city) even for the limited number of data considered. So these first results have to be validated with a much larger set of data. Moreover, it was not possible to record the sound environments in parallel with the interviews. Therefore it has been decided to take advantage of mobile technology to continue the work on sound pleasantness indicators, questioning participants through their mobile. At the same time, the evolution of noise levels is recorded with the microphone of the mobiles, in order to store acoustic measures in parallel to the perceptive data. With the synchronized data, it will be then possible to correlate perceptive data with acoustic measures directly.

2. MOBILE APPLICATION FOR THE CART_ASUR PROJECT

In order to collect the data, a mobile application has been specifically developed by the Brus-Sense Team of the Vrije Universiteit Brussel. The Cart_ASUR application is based on the NoiseTube one which makes it possible to record noise levels after relevant calibration of the mobile phone's microphone [3]. This new application proposes to collect, in addition to noise levels, perceptive data in specific places (parks, squares, thoroughfares, streets, schools, markets, pedestrian streets, *etc*.). 60 mobiles have been distributed to 60 persons living or working in the 13th or 14th districts of Paris for conducting the measurements and the evaluations. Each person has to assess about 20 locations in these two districts, each at four or five homogeneous periods (day, evening, night, week ends, summer, winter *etc.*). After a year, it is expected to collect 6 000 measurements. Each measurement corresponds to a 10-minute recording of sound pressure levels (stored each second). Following this recording, participants have to answer a short questionnaire.

The questions have been designed to cover three categories of perceptive variables. The first questions are related to the characterisation of the environment: climatic conditions and overall feelings on semantic scales. These scales correspond to variables which have a significant impact on the sonic pleasantness such as quietness, liveliness, envelopment and familiarity feeling (Table 2). In addition to these questions about the sound environment, a question is dedicated to the visual pleasantness (Figure 1).

Fig. 1. Screens of the mobile application for global evaluation

Looking at Table 2, it can be seen that the variables connected to perceived loudness concern only sources whose sounds emerge from the background noise such as mopeds, trucks, buses or horns, whereas variables connected to the time ratio of presence concern sources whose sounds disappear in the background. It has been decided to differentiate these two kinds of sources. For those which emerge from the background

Fig. 2: Screens of the mobile application for sound evaluation of sources and photographs

noise and thus can be evaluated as "events", perceived loudness assessment is rated on an intensity scale (weak / loud). In the chosen districts in Paris, metros (sometimes passing overground) as well as some urban activities can be considered as events. On the Figure 2, the presence of non-event sources (voices, steps, birds, water and wind) is assessed on a time ratio scale (rarely / continually).

Some sound sources can be heard as events or as background. For example, cars can be considered as events during the night, when only few are passing, but can be considered as background when there is heavy traffic. As such, this particular source appears in the two categories.

Participants are also asked to take as many photographs of the locations as they want in order to study the influence of the visual context on the soundscape.

3. ACOUSTIC MEASUREMENTS

Before calculating any acoustic indicator, the microphone of the mobile has to be calibrated.

3.1 Calibration

Several types of mobiles were tested in order to choose the one which can measure sound levels typical in an urban environment. Actually, while phone performance with respect to sound intensity varies, we have not yet encountered a phone model with a linear response between 20 dB(A) and 90 dB(A). The HTC One X mobile has been chosen for two reasons: (1) all mobiles are sensitive to noise level ranges between 50 dB(A) and 90 dB(A), even extending to between 40 dB(A) and 90 dB(A) in some cases (Figure 3.) and (2) this mobile is trendy which helps in motivating the 60 participants who are offered the telephone subscription for a year in addition to the mobile.

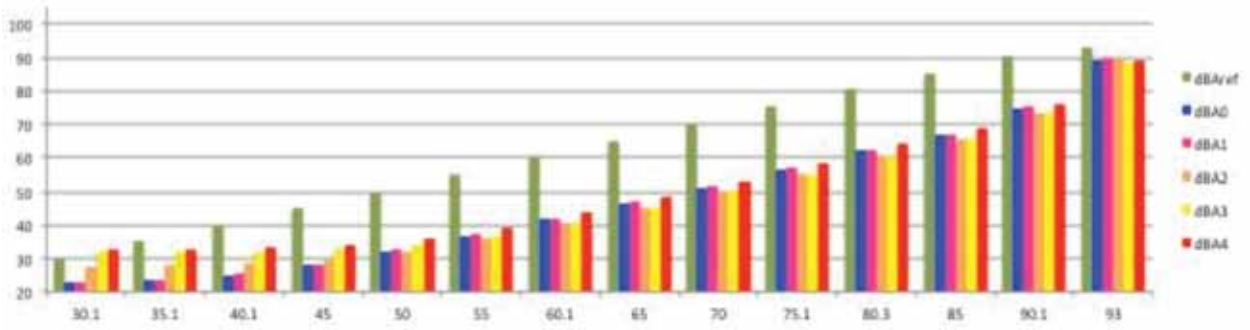

Fig. 3. Responses of 5 mobiles HTC One X compared to the reference (green curve)

As it is not possible to implement individual calibration in each mobile, an average of the behaviour of 5 phones have been set, which then of course is not perfect for each individual phone. Then, after calibration settings were included, the mobiles perform very well between 50 dB(A) and 90dB(A) but not completely below 50 dB(A). One reason is that phone behaviour varied more below 50 dB than beyond. This is not a problem because a previous campaign showed that in Paris, equivalent sound levels $L_{Aeq,10\ min}$ are never measured below 50 dB(A) even during the night (except for parks where $L_{Aeq,10}$ min can reach 45 dB(A)). On the opposite, the maximum equivalent sound levels are measured along boulevards during the day and can reach 80 dB(A) [4]. Moreover, note the averaging over many different measurements for a chosen locations and time further decreases random errors due to the difference in individual mobiles.

3.2 Acoustic indicators

In order to avoid participants opting out of the experiment prematurely, it is important to minimize duration of the experiment. Therefore, the duration of the sound level recording is limited to 10 minutes. This duration is long enough to characterize the acoustic environment of an urban situation [4].

Two kinds of indicators are calculated (Table 3.): on one hand energy indicators, such as the sound equivalent level L_{Aeq} or percentile levels, and on the other hand indicators related to the number of events. Unfortunately, it is not yet possible to identify sources automatically. Indeed automatic source recognition is a field of active study [5] but not yet mature enough to be implemented in the mobile application. So it is not possible to measure neither the level of a source nor the real number of events for a source. Moreover, no stimuli are recorded to preserve privacy, so it is not possible to identify the sources afterwards. Only the sound level in dB(A) is stored every second.

Table 3. Definition of the indicators calculated for each measurement

Indicator	Definition
$L_{Aeq,10\ min}$	"A" weighted equivalent sound level, calculated from 1s measurements $_{LAeq,1s}$ over 10 minutes.
$L_{Amax,\ 1\ s}$	Maximum "A" weighted equivalent sound level, extracted from 1s measurements $L_{Aeq,1s}$
L_{A10}, L_{A50}, L_{A90}	"A" weighted sound level exceeded respectively 10%, 50% and 90% of the time
L_{Amin}	Minimum "A" weighted equivalent sound level, extracted from 1s measurements $L_{Aeq,1s}$
α	Standard deviation of the $L_{Aeq,1s}$
L_{A10} - L_{A90}	Difference of percentile levels L_{A10} and L_{A90}
NNEL>Lα	Number of noise events exceeding the Lα level. Lα : 70 dB(A), 75 dB(A), 80 dB(A), L_{A10}, $L_{Aeq,10\ min}$ + 10 dB(A) and $L_{Aeq,10\ min}$ + 15 dB(A)

4. CONCLUSION

With 6000 measurements, it is expected to propose indicators of urban sound quality with the help of mathematical models. These models will try to predict the dependent variable (the sound pleasantness variable) with independent variables. Different types of independent variables will be considered as the input of the models: (1) perceptive variables collected through the questionnaires, (2) acoustic variables calculated from the sound level evolution recording and (3) non-acoustic variables which can be extracted from the photographs or collected through already archived data from city maps such as the presence of public seats, the type of shops in a street, the number of bus stops, etc. It has already been shown that it is possible to predict the sound pleasantness variable with other perceptive data, but in the long term, it would be interesting to test the models, excluding perceptive data, in order to be able to predict the urban sound quality through sound monitoring and/or through other geo-referenced city data. To conclude, the final aim of this research is to provide a new solution towards noise pollution mapping, focusing not only on noise levels, but also on other aspects such as visual context, urban planning settings or assessments dedicated to specific sources identified which lead towards a different experience of urban sound quality.

5. ACKNOWLEDGMENT

This research is part of a program funded by a PREDIT contract. It is supported by the French Agency ADEME.

6. REFERENCES

[1] EUROPEAN PARLIAMENT and COUNCIL, 2002. Directive 2002/49/EC relating to the assessment and management of environmental noise. *Official Journal of the European Communities* **L 189.45**, 12–26.

[2] L. BROCOLINI, C. LAVANDIER, C. MARQUIS-FAVRE, M. QUOY and M. LAVANDIER, 2012. “Prediction and explenation of sound quality indicators by multiple linear regressions and artificial neural networks”, IOA/CFA Congress, *Acoustics 2012 Nantes*, France.

[3] E. D'HONDT, M. STEVENS and A, JACOBS, 2013. "Participatory noise mapping works! An evaluation of participatory sensing as an alternative to standard techniques for environmental monitoring". *Journal on Pervasive and Mobile Computing: Special Issue on Pervasive Urban Applications.* **9**(5), 681-694.

[4] L. BROCOLINI, C. LAVANDIER, M. QUOY and C. RIBEIRO, 2013. "Measurements of acoustic environments for urban soundscapes: choice of homogeneous periods, optimization of durations and selection of indicators", *Journal of the Acoustical Society of America*, **134** (1), Pt. 2, 813-821.

[5] X. VALERO, A. FRANCESC, D. OLDONI and D. BOTTELDOOREN, 2012. "Support vector machines and self-organizing maps for the recognition of sound events in urban soundscapes", in Proc. *Internoise*, New York City, USA.

Journal of Acoustical Society of India : Vol. 42, No. 4, 2015 (pp. 188-194)

Coarticulation in Young Children: F2 Locus Equation as a Metric

E. Sreedevi N[1], Irfana M.[2] and Alphonsa Mathew[3]
Department of Speech Language Sciences
All India Institute of Speech & Hearing, Mysore - 570 006
[1]Reader in Speech Sciences, [2] Research Officer, [3] Speech Language Pathologist

[Received: 13.02.2014; Revised: 26.05.2014; Accepted: 27.05.2015]

1. INTRODUCTION

Speech rarely involves production of one sound in isolation, but rather is a continuous, dynamic sequencing of vocal tract movements produced in rapid succession. Though it might be convenient to consider phonemes as independent, invariant units that are simply linked together to produce speech, this simplistic approach does not really fit the facts. When sounds are put together to form syllables, words, phrases, and sentences, they interact in complex ways and sometimes appear to lose their separate identity. The influence that sounds exert on one another is called coarticulation, which means that the articulation of any one sound is influenced by a preceding or following sound. For any given target sound, the phoneme immediately preceding and the one immediately following will influence the articulatory posture of the vocal tract. We make articulatory adjustments to both phonemes at the same time and in fact we are articulating more than one phoneme at one time. This phenomenon of simultaneously articulating more than one phoneme is called coarticulation.

Coarticulation is majorly divided into two types: anticipatory (Right to left) and carryover (Left to right). For example in the words "snoozed" and "sneezed" the contrast shows that the /sn/ cluster acquires lip rounding only if it is followed by a rounded vowel /u/ and it is unrounded when followed by unrounded vowel /i/. This is because of anticipatory coarticulation where the following vowel influences the preceding phonemes. In contrast, in carryover coarticulation, the feature of the preceding phoneme will spread to the following sound. For example in the word "me" vowel /i/ becomes nasalized because of the preceding nasal sound /m/.

Appropriate coarticulation indicates the maturation of oral speech motor control. So the development of coarticulation provides knowledge about the maturational pattern of articulators with age. The influences of coarticulation often extend well beyond the boundaries of a particular segment and appear to be the influence of both spatial and temporal linking of articulatory gestures. Child's language learning process skillfully develop from the simple articulatory patterns of babble to the complex patterns of connected speech and articulates an endless number of sound combinations, using necessary co-articulatory adjustments to accommodate neighboring sounds. Children's pronunciation in the first 50 word stage appears to be constrained by their physiology, ambient language, and child specific factors (Vihman, 1992). Kent and Bauer (1985) reported that children who are in the first fifty word stage are able to produce combinations of vowel (V) and consonant (C) such as V, CV, VCV, and CVCV structures which will be accounted for appropriately 94 % of all syllables produced.

Acoustic based theories describe anticipatory coarticulation, in which the vowel influences the preceding consonant, in children's speech as more segmental (Kent, 1983) or more holistic (Nittrourer, Studdert-Kennedy & Neely, 1996) than adult's coarticulation patterns. The segmental theory predicts that children initially

produce phonetic segments with less coarticulation than an adult's production of the same segment, suggesting children learn patterns of individual components of the CV segment. In this case, the vowel of the CV sequence has less influence on the articulatory movements of the preceding consonant and coarticulation increases and their speech becomes more efficient or adult like (Kent, 1983). In contrast, the holistic theory projected that babbling patterns of reduplicated, variegated syllables and syllable strings are holistic, undifferentiated gestures of consonants and vowels and later the holistic gestures of early word productions are narrowed to smaller phonetic units (Goodell & Studdert-Kennedy, 1993) weakening consonant and vowel interdependencies and coarticulation decreases with age and motor practice (Nittrouer *et al.*, 1996).

Though there are studies supporting segmental/ holistic theories, there are also findings which show mixed results pointing to further complexities, such as coarticulation varying with the syllable type, meaningfulness, and types of context (Sussman, Minifie, Buder, Stoel Gammon, & Smith, 1996; Katz and Bharadwaj, 2001; Gibson & Ohde, 2007). Goodell *et al.* (1993) and Gibson *et al.* (2007) noted age-related changes in coarticulation which mainly depend on the places of articulation.

Coarticulation can be studied perceptually, physiologically and acoustically. For measuring coarticulation in individuals with speech disorders, most researchers have used relatively more indirect techniques such as acoustic analysis, mainly because of the practical difficulties associated with the types of invasive physiological techniques. Using acoustic analysis, the transition between the consonant and vowel will provide information about coarticulation. Many acoustic studies have addressed that F2 locus equation can be used as a quantitative measure for CV coarticulation (Lindblom, 1963; Sussman, McCaffrey, & Matthews, 1991).

The locus equation plots F2 at vowel onset against the target frequency of the same vowel at a so-called steady-state location. The plots are compiled mainly for voiced stops across different vowel contexts (/i, a, u/) and the slope is said to be related to the degree of coarticulation (Krull, 1987). Minimum coarticulation is where the locus equation has a relatively fixed F2 onset frequency across vowel contexts and maximum coarticulation is where the F2 onset frequency varies systematically with F2 vowel target frequency. Fig. 1

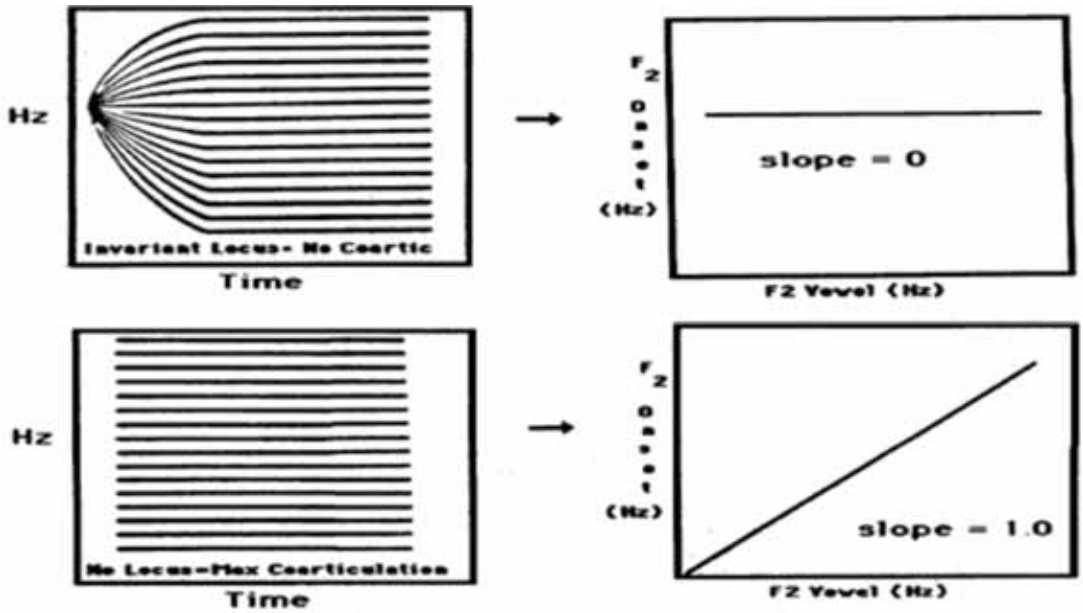

Fig.1. Hypothetical extremes of locus equation slopes. The upper panel illustrates a situation that would occur with an invariant consonantal locus when no coarticulation is present between consonant and vowel. The lower panel reflects a condition of no consonantal locus and maximum coarticulation between consonant and vowel (Sussman *et. al.*, 1996).

depicts maximum and minimum coarticulation. The regression equation parameters (slope, intercept) provide insight into the magnitude of coarticulation depending on the consonant's place of articulation. A steep slope of 1.0 is evidence for a high degree of coarticulation between C and V. On the other hand, a low slope indicates that at the onset of the vowel F2 shows a smaller change for each 1 Hz change in the vowel, an indicator of a smaller degree of coarticulation. Experimental work has shown that the magnitude of the slope characterizing CV coarticulation differs according to consonant place of articulation (Sussman et al., 1998).

Acoustical analysis is one of the most feasible measurements in younger children since the speech sample is elicited through natural play situations. Sreedevi, Smitha, Irfana and Nimisha (2012) studied coarticulation in hearing impaired population using F2 locus equation as a metric and the slope of the regression lines provided a numerical index of coarticulation which showed variation across hearing aid users, cochlear implantees and normal controls among places of articulation. Velars showed higher degree of coarticulation and bilabials and dentals revealed weaker coarticulation effect. Normals articulated more effectively and were highly positively correlated with the F2 locus equation measures. Among children with hearing impairment, as expected, the hearing aid users showed comparatively poorer performance than cochlear implantees particularly for velar coarticulation. As per the literature, there are no reported studies on coarticulation in typically developing young children in Indian languages. In this perspective the present study attempts to investigate the coarticulatory changes across places of articulation in children in the age range of 12 to 24 months in Malayalam.

2. METHOD

Participants : Sixteen typically developing native Malayalam speaking children in the age range of 12-24 months were considered for the study. The participants were divided into two groups; 12-18 months and 18-24 months. Each group comprised of 8 toddlers including 4 males and 4 females. None of the participants had any known disorders and normal developmental milestones were ensured.

Data recording Procedure : The speech samples recorded consisted of imitated as well as spontaneous speech. Recordings were carried out by using a video recorder (Sony Handycam, Model No DRC DVD 908 E) with an inbuilt microphone and each session lasted for about 30- 45 minutes. The recording was conducted until a sample containing 50-60 speech like utterances were obtained from each participant.

Data Analysis : The recorded data was subjected to data reduction. CV syllables constituted 33.07% of the total corpus. To select the target production from the recorded sample, imitated and spontaneous CV productions including voiced stop consonants like /b/, /d/, /g/ in the context of vowels /a/, /i/, /u/ were identified and subjected to acoustical analysis using PRAAT software (Version 5.1.14). PRAAT software is easily and freely downloadable with options for general acoustic analysis. Locus equation estimation

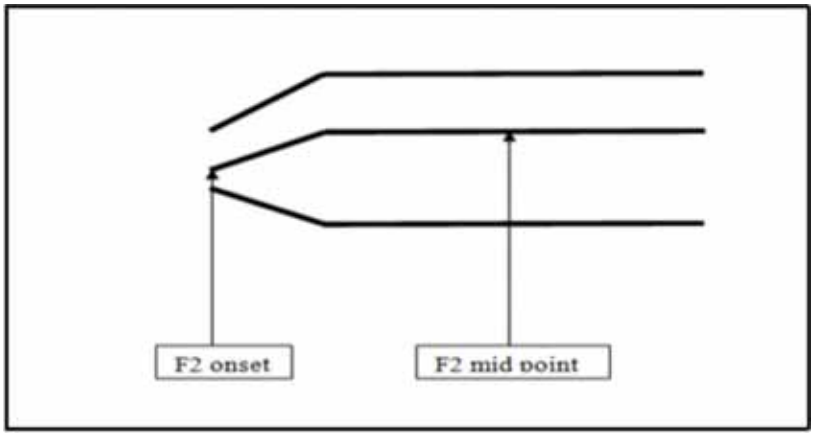

Fig. .2 Spectrogram depicting F2 onset and F2 mid point

required onset and midpoint of the vowel F2. F2 represents the second formant of the vocal tract and is considered to be a significant cue for place of articulation. For data analysis, F2 vowel onset and midpoint of each CV utterance was identified. Vowel onset was identified as the onset of voicing in the second formant of the vowel following consonant release and the formant value at the temporal midpoint of the vowel was also selected. Spectral measures were taken from wide-band spectrograms, schematic representation is shown in Figure 2. These obtained data was statistically analyzed using regression analysis.

10 percent of each participant's data was subjected to intra judge and inter judge reliability. The overall intra judge and inter judge reliability index were 95% and 88% respectively.

3. RESULTS

Regression analyses were carried out to ensure the relationship between F2 onset and F2 midpoint of the vowel using SPSS (Version 17) package. This statistics has been used to evaluate how closely data points cluster around the regression lines. The obtained slope, y-intercept, R2 and standard error (SE) values are presented in Table 1.

Table 1. Shows the Slope, y-intercept, R2 and standard error (SE)

Groups	Target	Slope	y-intercept	R2	SE
12-18 months	ba	0.65	279	0.56	78.75
	da	0.11	875	0.05	51.56
	ga	0.81	114	0.21	167.21
18-24 months	ba	0.72	473	0.57	86.83
	da	0.26	1401	0.07	53.78
	ga	0.84	189	0.47	170.44
Combined	ba	0.42	214	0.83	90.85
(12-24 months)	da	0.05	481	0.18	77.1
	ga	0.71	96	0.51	179.13

Here the slope, y-intercept, standard error (SE) and R^2 functions of regression equations on the F2 onset and F2 vowel frequencies were calculated for the sixteen participants for the 3 different places of articulation. The slope function described degree of coarticulation and places of articulation for each participant; it means that for every 1 Hz change in the vowel midpoint, there is a corresponding 1 Hz change in the CV transition onset. The y- intercept also provides the variations of coarticulation. The SE value indicates goodness of fit around the regression line, and the R^2 described extent of variability of F2 onset and F2 vowel target. The smaller the SE, the more the scatter plot takes on a linear or a straight line appearance. Small SEs, often near to 100 Hz on the scatter plot along the liner regression line indicates adequate coarticulation.

Regression functions for voiced bilabial, dental and velar stop consonants pooled across participants are shown in Figures 3, 4 and 5 respectively where vowel onset and midpoint are depicted in X and Y-axis . The regression lines revealed that the goodness of fit increased in all three places of articulation as age increased. The slopes for /b/, /d/ and /g/ were 0.65, 0.11 and 0.81 for the younger age group (12-18 months) and 0.72, 0.26 and 0.84 for the older age group (18-24 months) respectively. Hence based on the slope, the coarticulation was maximum for velar /g/ followed by bilabial /b/ and dental /d/. As evident in Figure 4, the slope is almost flat for dental /d/ indicating minimal effect of the vowel on the consonant. Y-intercepts, R2 and SE also showed variation across groups though it was trivial.

Based on the combined data also the same trend of coarticulation was evident; velars /g/ > bilabials /b/ > dentals /d/. The combined slopes for /b/, /d/ and /g/ were 0.42, 0.05 and 0.71 respectively. Bilabial and velar stops had R2 value of 0.83 and 0.5 respectively, indicating slopes that represent coarticulation well by the co-variation of F2 onset and F2 vowel target. Dentals had a small R2 of 0.18 indicating very less coarticulation. The SEs for /b/, /d/ and /g/ were 90.85 Hz, 77.1 Hz and 179.13 Hz.

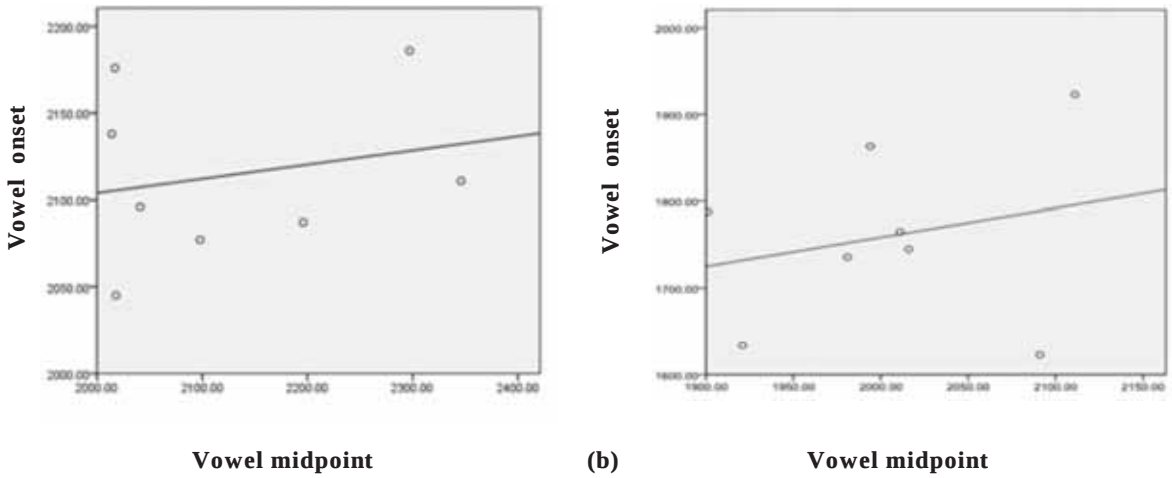

Fig. 3. The locus equation of bilabial stop /b/ in children aged 12-18 (a) and 18-24 (b) months.

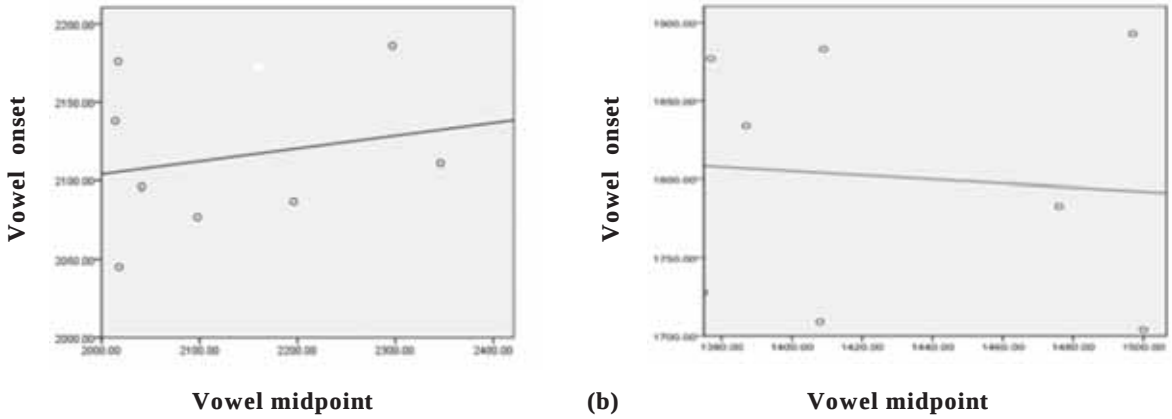

Fig. 4. The locus equation of dental stop /d/ in children aged 12-18 (a) and 18-24 (b) months.

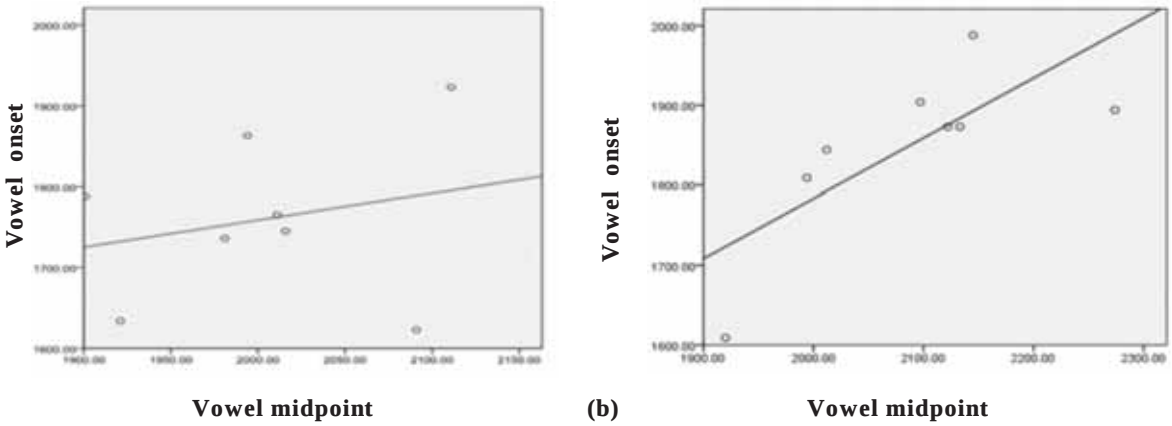

Fig. 5. The locus equation of velar stop /g/ in children aged 12-18 (a) and 18-24 (b) months.

4. DISCUSSION

In the present study, the LE metric was used to describe coarticulation patterns in voiced stop CV productions of children aged 12-24 months. Results indicated that velars had maximum coarticulation followed by bilabial and dental places of articulation. Vowel in CV syllables moderately influenced velars /g/ and bilabial /b/ and with a minimal vowel influence for dental /d/. Also voiced velar stop revealed moderate goodness of fit around the regression line followed by voiced bilabial and dental stops. As reasoned by Gibson and Ohde (2007), the toddlers must learn to simultaneously and independently implement the appropriate tongue position for the vowel and lip closure for the bilabial stop reducing the anticipatory coarticulatory effect of the following vowel. The production of dental sound in CV requires the child to implement two separate gestures for the same articulator. That is the child has to move tongue tip for dental sound production and tongue body for the vowel. A different production strategy exists for velars in that both C and V are produced by the tongue body itself. The variability across participants were also reduced for velars compared to dentals and bilabials indicating degree of velar coarticulation was produced more consistently, possibly because of the single gesture for one articulator. Similar trends were revealed in other studies (Goodell & Studdert-Kennedy, 1993; Sussman et al, 1996; Sreedevi et al, 2012).

Results of this study also support earlier studies (Goodell et al 1993; Gibson et al, 2007) in English speaking children. This signifies the similarity of coarticulatory pattern across languages. The present study including very young children showed coarticulatory patterns similar to adults as reported by Sussman et al, 1996. To conclude, it can be stated that, coarticulatory influence of vowel in CV contexts is different across places of articulation, velars showing the maximum effect.

5. ACKNOWLEDGEMENTS

We extend our sincere gratitude to Prof. S.R. Savithri, Director, and Prof. Y V Geetha, Head, Department of Speech Language Sciences, All India Institute of Speech and Hearing for permitting us to carry out this study. We also thank all the participants for their kind cooperation.

6. REFERENCES

[1] T. GIBSON and R.N. OHDE, 2007. F2 locus equations: phonetic descriptor of coarticulation in 17 to 22 month old children, *Journal of Speech, Language, and Hearing Research,* **50**, 97-108.

[2] E.W. GOODELL and M. STUDDERT-KENNEDY, 1993. Acoustic Evidence for the Development of Gestural Coordination in the Speech of 2-Year-Olds: A Longitudinal Study, *Journal of Hearing Research,* **36**, 707-727.

[3] P. GRUNWELL, 1982. *Clinical Phonology*. Croom Helm, London.

[4] W.F. KATZ and S. BHARADWAJ, 2001. Coarticulation in fricative-vowel syllables produced by children and adults: a preliminary report, *Clinical Linguistics and Phonetics*, **15**(1), 139-143.

[5] R. KENT, 1983. The origin of coarticulation. In W. J. Hardcastle and N. Hewlett (eds) *Coarticulation: theory, Data & Technique*, 7-30, Cambridge: Cambridge University Press.

[6] R. D. KENT and H.R. BAUER, 1985. Vocalizations of one-year-olds, *Journal of Child Language*, **12**(3), 491-526.

[7] D. KRULL, 1987. *Second formant locus patterns as a measure of consonant vowel coacrticulation.* Perilus, Institute of Linguistics: University of Stockholm.

[8] B. LINDBLOM, 1963. Explaining phonetic variation: a sketch of the H & H theory. In W. J. Hardcastle and A. Marchal (eds) *Speech production and speech modeling*, 403-439, Kluwer Academic Publisher.

[9] S. NITTROUER, M. STUDDERT-KENNEDY and S.T. NEELY, 1996. How children learn to organize their speech gestures: Further evidence from fricative-vowel syllables, *Journal of Speech and Hearing Research,* **39**, 379-389.

[10] N. SREEDEVI, K.N. SMITH, M. IRFANA and R. NIMISHA, 2012. F2 locus equation: As an index for measuring coarticulation in cochlear implantees and hearing aid users, *In proceedings of the national seminar on speech synthesis and its applications.* July 9-11, Organized by Dept of Linguistics, University of Kerala, LDC-Il, CIIl, Mysore and Kerala State IT Mission, Govt. of Kerala, Thiruvananthapuram.

[11] H.M. SUSSMAN, D. FRUCHTER, J. HILBERT and J. SIROSH, 1998. Linear correlates in the speech signal the orderly output constraint, *Behavior Brain Science,* **21**, 241-259.

[12] H.M. SUSSMAN, H.A. McCAFFREY and S.A. MATTHEWS, 1991. An investigation of locus equations as a source of relational invariance for stop place categorization, *Journal of Acoustic Society of America,* **90**(3), 1309-1325.

[13] M.M. VIHMAN, 1992. The Construction of a Phonological System: speech and face processing in the first year of life, *Developmental Neurocognition,* **69**, 411-419.

Journal of Acoustical Society of India : Vol. 42, No. 4, 2015 (pp. 195-201)

Compact and Robust Real Time Passive Acoustic 3D Tracking: Application to Whales and Bats Survey

Ales Mishchenko[1,2]*, Hervé Glotin[1,3,4] and Pascale Giraudet[1]
[1]LSIS-DYNI, University of the South, Toulon-Var,
Avenue de l'Université, BP 20132, 83957 La Garde, PACA, France
[2]SATT Sud Est; 8 rue Sainte Barbe, 13001 Marseille
[3]IUF, Institut Universitaire de France
[4]Aix Marseille University; CNRS, ENSAM, LSIS, UMR 7296 13397 Marseille, France
**e-mails: alesmichtchenko@mail.ru*

[Received: 13.04.2014; Revised: 22.08.2014; Accepted: 24.04.2015]

ABSTRACT

This paper presents method for tracking animals moving in 3D (bats, whales) using 4 microphones at different spatial locations. Like many acoustic source localization algorithms, our method is based on grouping all microphones into pairs, estimating the TDOA of each pair, then finding a set of distances to microphones, consistent with the observed TDOAs. The novelty of our method is filtering the set of acquired TDOAs using coherency equations, reflecting consistency between different TDOAs, as well as typical animal sounds and trajectories. This allows eliminating echoes and distortions of sound trajectory due to water layers, or any kind of reflections.

1. INTRODUCTION

Tracking of wildlife movements has been widely studied since the 1960s [1-2]. For the majority of these studies, an operator monitors received signal strength while changing the orientation of a directional receiving antenna. The problem of localizing an acoustic source from Time-Differences-of-Arrival (TDOAs) is received recently a lot of scientific attention with a number of different solution approaches (the review can be found in [3]) and many military, bioacoustic and surveillance applications. However, most of these methods assume known and constant propagation speed, reliable only under controlled conditions where the air / water temperature can be monitored. The effects of a wrongly assumed propagation speed is surveyed in [4]. One of the most successful approach to overcome the problem of variable propagation speed, echoes, etc, in the field of bioacoustics is the algorithm is based on the principle of transitivity of TDOAs, computed from correlation of each couple of microphones [5-8]. We apply this approach to the whales and bats tracking (figure 1).

System of microphones in case of whale tracking was the short base (2 meters square) hydrophone array. For this purpose, we used the Nemo Onde platform (from INFN, CIBRA and the NEMO Collaboration) that was distributed within the 2009 DCL challenge organized by Gianni Pavan. In case of bats tracking we used 4 microphones, organized in a tetrahedron with 1,6m edge.

Recordings from such systems of microphones are processed by our technique, developed in [5-8] to robustly estimate the flying bats and whales trajectories from TDOAs. Such an estimate can be used to enhance the localization by filtering all possible TDOAs to provide consistency between TDOAs of different

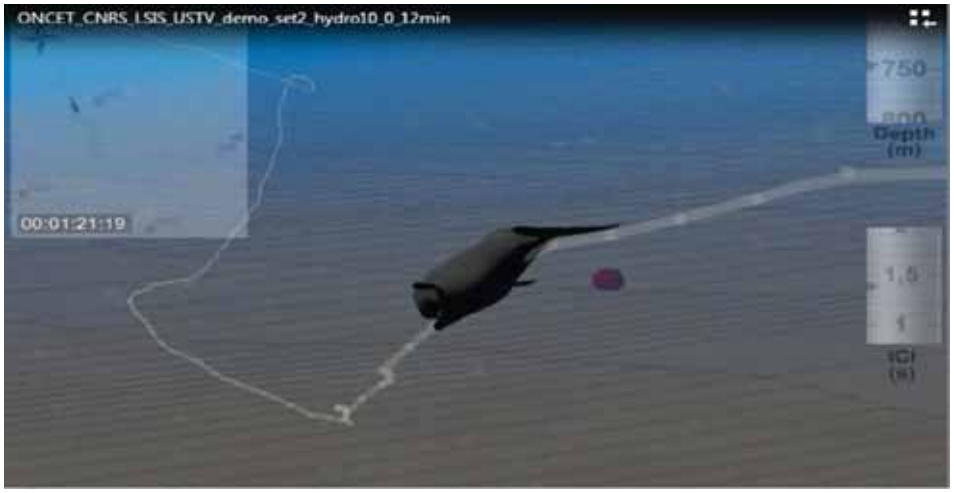

Fig. 1. The snapshot of the video of our fine tracking results computed on the DCL 2005 challenge Bahamas set with only one whale. (available online at http://sabiod.univ-tln.fr/tv).

microphones as well as typical animal sounds and trajectories. The TDOAs were computed on a teagerkaiser detector or an SMF in order to get more precise detections.

The problem of non-robustness of automatic animal tracking is present in both bats and whales recordings. It is confirmed by application of statistical measures (Likehood, Fisher information, Cramer-Rao bounds and other) which show that real commercial antennas (such as 4 microphones, organized in a tetrahedron with 1,6m edge) do not provide robust localisation.

2. BIOACOUSTIC DATA OPTIMIZATION

Real-world recordings of different species of bats and whales recordings are used to validate our method. The typical signal recording and corresponding spectrogram are shown in a Figure 2.

Correlation of sounds, arrived to pair of sensors results in cross-correlation-functions, showing shifts at which signals are more similar (best shifts) or more different (worst shifts) - see figure 3. TDOAs between two microphones are calculated as peaks of correlation of recordings of these microphones.

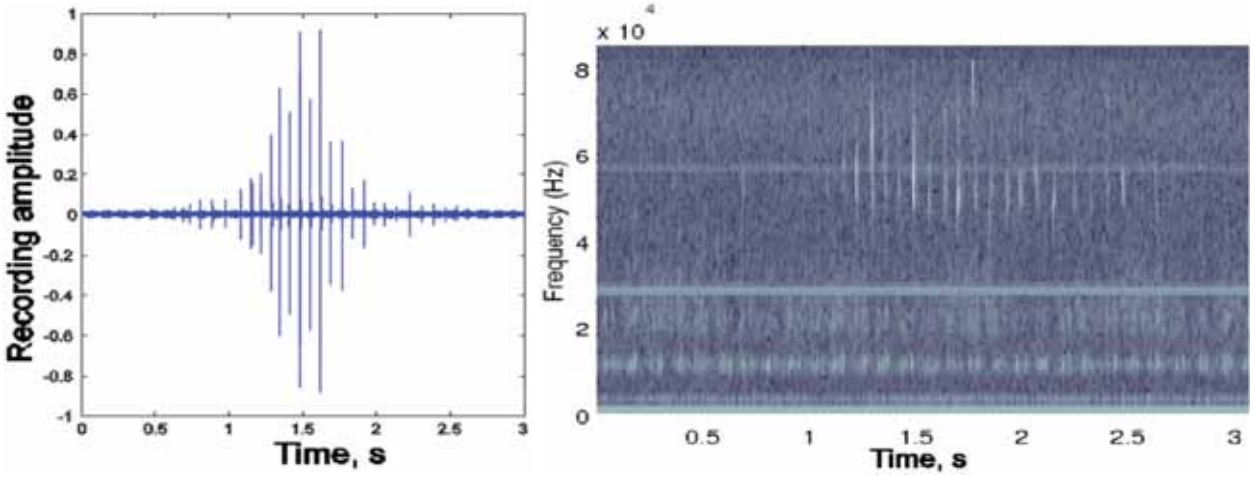

Fig. 2. Left: The typical bat-recording. Right: The corresponding spectrogram

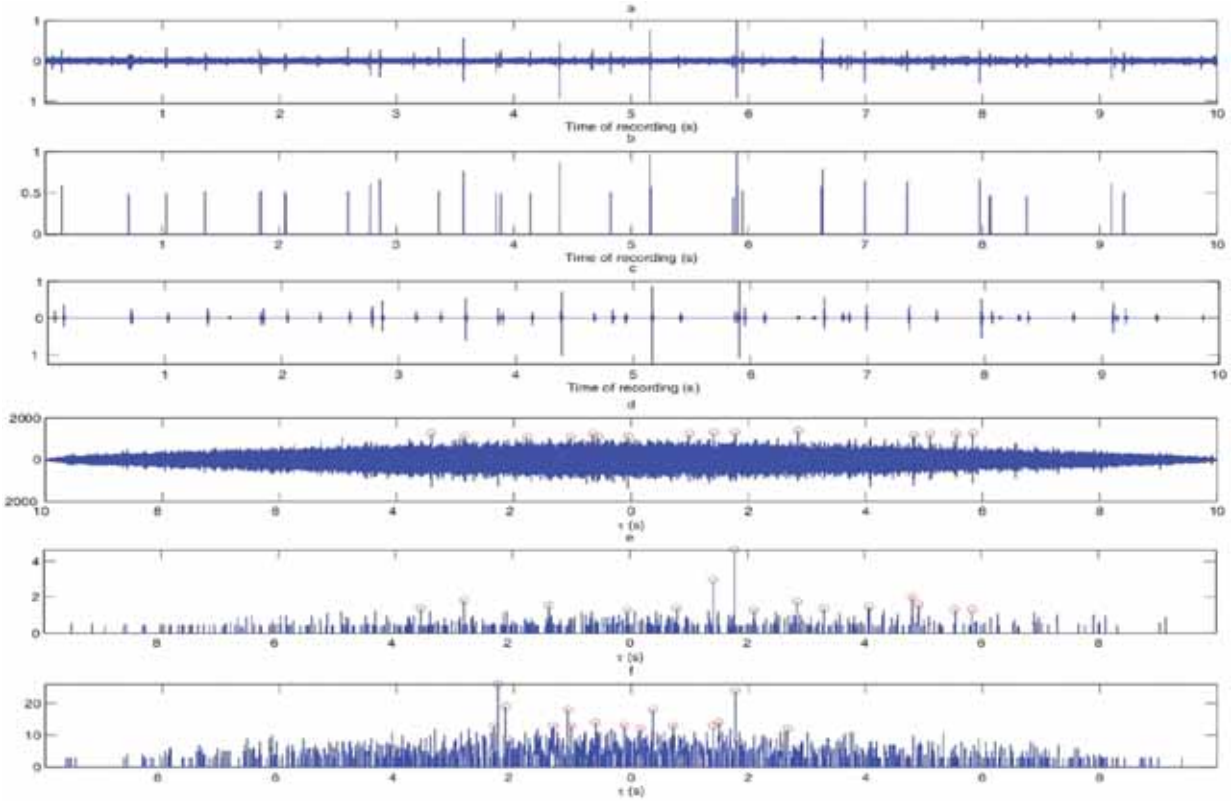

Fig. 3. (a): ten seconds of raw signal of the Bahamas set with four emitting whales (b): (a) after TKM filtering. (c): (a) after the SMF. (d): CC between (a) and corresponding raw signal (e): idem than (d) but with (b). (f): idem than (d) but with (c). Circles on the top of some peaks correspond to the 15 maximum peaks that are used for localization. This shows the difference between TK and SMF.

Refinement of TDOAs by coherence formulas is used to filter the set of TDOA by application of the following coherence equations, developed in [5-8] (4 sensors case) :

$$\left|TDOA_{ij}^{m} + TDOA_{ik}^{m} - TDOA_{ik}^{m}\right| < \varepsilon$$

$$\left|TDOA_{ij}^{m} + TDOA_{ih}^{m} - TDOA_{ih}^{m}\right| < \varepsilon$$

$$\left|TDOA_{ik}^{m} + TDOA_{kh}^{m} - TDOA_{ih}^{m}\right| < \varepsilon$$

$$\left|TDOA_{ik}^{m} + TDOA_{kh}^{m} - TDOA_{ih}^{m}\right| < \varepsilon$$

Here indices i, j, k, h are microphone numbers, whereas index m is the rank of the maximum. ε is the maximum possible overall system error, depending on microphone sensitivity, noise level, sound quality, *etc.* This way the equations will serve as a filters for TDOAs, selecting the coherent TDOA, producing smooth TDOA and correct tracking.

Optimization of parameters of TDOA calculation is used to automatically adapt the algorithm for a particular animal. Optimization includes time-step, correlation-window, number of maximums and percentage of TDOA to filter with coherence condition formulas.

Due to the difference in sounds, emitted by different species, as well as difference in antennae geometry and media of sound-propagation, we adapt the time steps and correlation windows to the sonar rate.

3. RESULTS OF TDOA CALCULATION AND REFINEMENT

The refinement results in more smooth and more coherent TDOAs, removing less false outbursts of TDOAs, caused by noise and echoes in recordings, as illustrated in a figure 4.

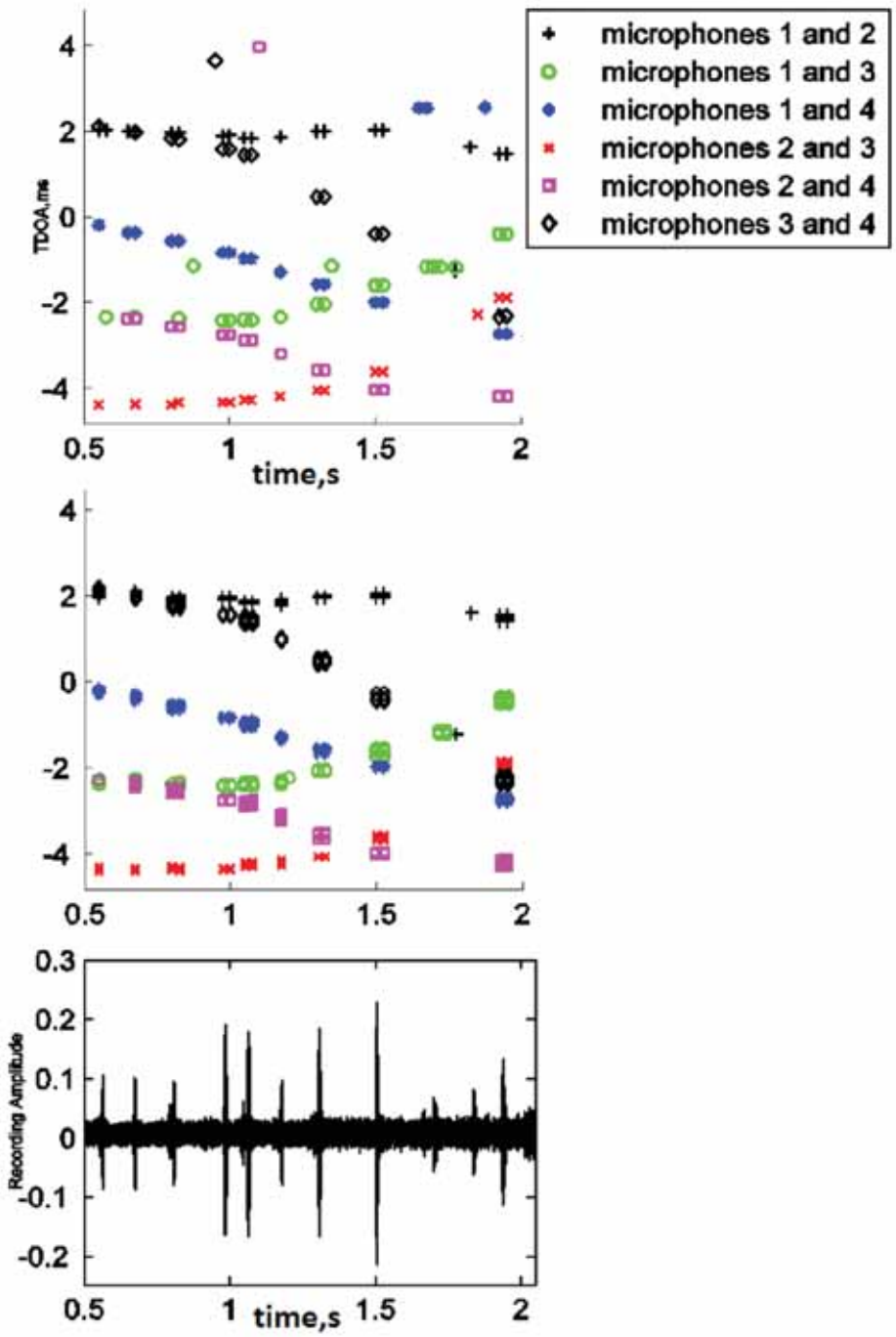

Fig. 4. Upper: highest-correlation TDOAs (before refinement), Middle: 10 TDOAs with highest correlation calculated, 5% (most coherent) shown. Lower: Signal, recorded by 4microphones (1.6m-tetrahedron).

The resulting trajectories in case of whales tracking are shown in a following figures. The figure 5 shows the result of our algorithm processing 4 simultaneously clicking whales (corresponding to the autocorrelation, shown in a figure 3, Bahamas set 1).

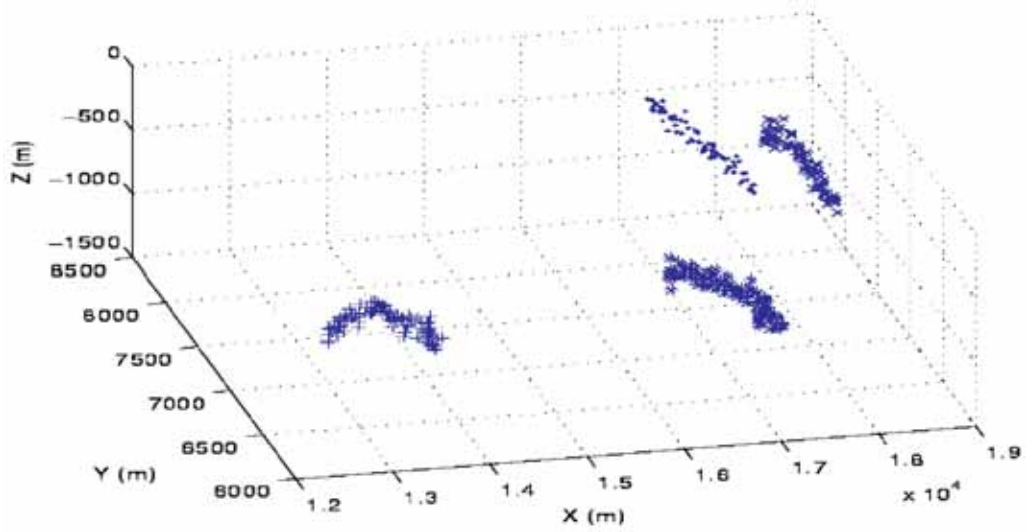

Fig. 5. Result on Bahamas set 1 with the SMF method. Each symbol corresponds to one whale, clearly and continuously tracked in 3D. Video is available at http://sabiod.org, with SMF detectors and 3D view.

Our algorithm is capable of processing many types of microphones arrays. The following figure 6 shows the result of the same system but running on a short base (2 meters square) hydrophone set, 96kHz, data from NEMO, courtesy of INFU, G. Riccobene and G. Pavan.

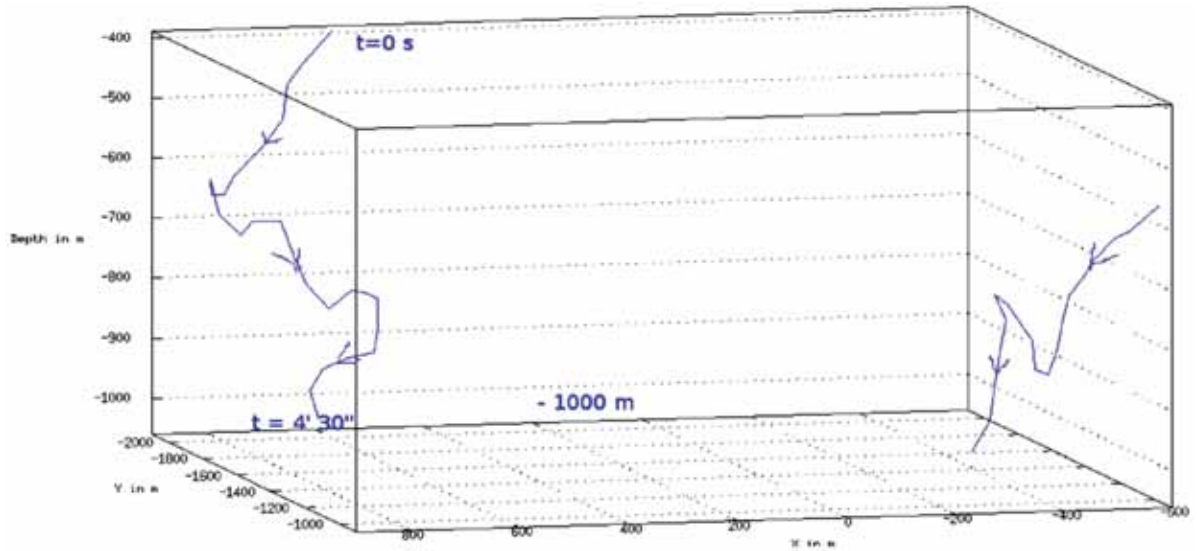

Fig. 6. Our 3D tracking results from the recordings of the 15th of august 2005, 15h00 Est. We see clearly the 2 Physeter catodon diving together from -400m to -1000 m in 5 minutes. We acknowledge Gianni Pavan and Giorgio Riccobene for NEMO recordings from INFN & CIBRA.

4. CONCLUSIONS AND FUTURE WORK

This paper presents the application of our method of calculation and refinement of TDOA, followed by 3D trajectory reconstruction [5-8] to bats and whales tracking. In both cases, our system is designed to eliminate echoes, noise and run in the case of multiple simultaneously recorded animals.

Line-detection in spectrograms remains optional. This step allows to stress clicks (verical lines in spectrogram), characteristic for some bats and whales.

Difference in sound of approaching bat and the bat flying away from the microphones can be seen from the correlation amplitude, the sound emitted by approaching bat is less coherent than the sound from the flying away animal. This may be caused by more complex amplitude modulations of the frontal direction of the sound. This causes that frontal emissions are incoherent from one microphone to another, which may be due to the head function transfer of the bat.

Distinction between stationary/non-stationary sound sources can be improved further. The typical recordings (as presented in a figure 1) represent not only the bat sound (high frequency bursts between 1 second and 2, 5 seconds of recording), but also the static sound sources, such as, for example, night insects (low frequency bursts during all the recording).

Such static sound sources provide a very high degree of correlation between pairs of microphones and a very high degree of coherence. Therefore, static sound sources contribute into the highest coherent TDOA. In order to remove the static sound sources from the consideration, 2 methods can be applied: (1) filtering by frequency (using a frequency range for a spectrogram, characteristic for the recorded animals) and (2) using non-zero time-variations of TDOA, characteristic for the moving object like the flying bat.

Physical constrains, such as different propagation properties of different frequencies represent another direction of future method improvement.

Biological constrains, such as range of operation, are possible to estimate, based on theoretical analysis of general biology and physics of a considered system. Different theories of functional organization of cochlea agree in different integration segments in different frequency-ranges and this can be used in adjusting the spectrogram according to biological frequency integration principles. Another adaptation of the system to biological properties of bat echolocation system is using different sensibilities to different frequencies, as well as evolutionary adaptation of the bat to the difficulty with location of objects, those sizes is less than sound wavelength.

All these biological constraints, optimized by evolution, resulted in a very particular temporal pattern of sound used by bats, as well as its frequency distribution. We can use the same constrains to optimize the operation of our system.

5. ACKNOWLEDGMENTS

We thank SATT and Institut Universitaire de France (IUF). We thank the 'Mission Interdisciplinaire' of the French National Research Center which supports the Scaled Acoustic Biodiversity SABIOD project (Pi Glotin, http://sabiod.univ-tln.fr). We thank Didier Mauuary (CYBERIO, 6 bis chemin des prés - Inovalle, 38240 Meylan - France) for the bats data recording.

6. REFERENCES

[1] C.D. LEMUNYAN, W. WHITE and E. NYBERT, 1959. "Design of a miniature radio transmitter for use in animal studies," *J.Wildl. Mgmt.*, **23**(1), 107-110.

[2] W.W. COCHRAN and R.D. LORD, 1963. "A radio tracking system for wild animals," *J. Wildl. Mgmt.*, **27**(1), 9-24.

[3] P. STOICA and J. LI., 2006. Lecture notes - source localization from range-difference measurements. Signal Processing Magazine, *IEEE*, **23**(6), 63-66.

[4] P. ANNIBALE and R. RABENSTEIN, 2010. Accuracy of time-difference-of-arrival based source localization algorithms under temperature variations. In Proc. of 4th Int. Symposium on Communications, Control and Signal Processing, (ISCCSP), Limassol, *Cyprus. IEEE*.

[5] GIRAUDET P. and GLOTIN H., 2006. Real-time 3D tracking of whales by echo-robust precise TDOA estimates with a widely-spaced hydrophone array. Int. Jour. Applied Acoustics, Elsevier Ed., **67**(11-12), 1106-1117.

[6] GLOTIN H., CAUDAL F. and GIRAUDET P., 2008. Whales cocktail party: a real-time tracking of multiple whales, in Internat Journal Canadian Acoustics, 36, 139-145. ISSN 0711-6659.

[7] GLOTIN H., GIRAUDET P. and CAUDAL F., 2007. Patent, Real time multiple whale tracking by passive acoustics, **07** / 06162, PCT Europe, in PCT extension 2009 Canada, USA, Australie, New Zeeland.

[8] BÉNARD F., GLOTIN H. and GIRAUDET P., 2010. Whale 3D monitoring using astrophysic NEMO ONDE two meters wide platform with state optimal filtering by Rao-Blackwell Monte Carlo data association, in Journal of Applied Acoustics, **71**, 994-999.

Journal of Acoustical Society of India : Vol. 42, No. 4, 2015 (pp. 202-208)

The Optimization Design of Microphone Array Layout for Wideband Noise Sources

Pengxiao Teng[1]*, Jianfei Shen[1], Ying Xiao[1], Yichun Yang[1] and Mahavir Singh[2]
[1]*Key Laboratory of Noise and Vibration Research, Chinese Academy of Sciences, North 4th Ring West Road, Beijing, 100190,China*
[2]*Acoustics, Ultrasonics & Vibration Standards, CSIR-National Physical Laboratory, New Delhi, India*
**e-mail: px.teng@mail.ioa.ac.cn*

[Received: 18.12.2013; Revised: 27.07.2014; Accepted: 21.01.2015]

ABSTRACT

Acoustic source localization has been hot topics in microphone array signal processing in the last decades and widely applied in various fields including radar, sonar, ultrasound imaging, seismic, and machinery trouble shooting and diagnosis, *etc.* Up to now, phased microphone array system has been an important tool to identify main noise sources from mixed acoustic field emitted from running machines. The performance of localization is affected by several parameters such as the microphone array layout, the number of microphone, weights and the array aperture. Usually the array aperture and the number of microphone are restricted in practical applications, and therefore array layout design and weights are the most crucial parameters to improve localization performance characterized by the array beam pattern. To reduce cost and complexity it is desirable to employ as few microphones as possible in the array. Therefore, it is reasonable to optimize array layout to remove some elements and form the desirable beam pattern with narrow main-lobe width (MLW) and low side-lobe level (SLL) which is in agreement with high spatial resolution and strong capability of interference rejection, while still maintaining a satisfactory imaging performance. Most research interest has focused on linear and planar arrays under the narrow band or single frequency condition. However, array layout optimization design is highly related to noise frequency bandwidth. Therefore, a new array layout optimization method is presented in this paper for wide-band noise sources to generate low side-lobe level beam patterns based on particle swarm optimization (PSO) which has proven to be very efficient in optimal layout design. In this paper, we present a general framework to consider the overall performance based on the narrow main-lobe width and low side-lobe level criterion using the particle swarm optimization method. In low frequency band we place more emphasis on the main-lobe width, and place more emphasis on the side-lobe level within high frequency band. In the presented paper, both weights and layout can be optimized simultaneously. Finally, simulations and experiments are carried out to demonstrate that the proposed.

1. INTRODUCTION

Microphone array has been an important research field in acoustic source localization and source separation for acoustic camera in the last decades. The performance of localization is determined by the array beam

pattern characterized by main-lobe width (MLW) and low side-lobe level (SLL), which is affected by several parameters such as the microphone array layout, the number of micro-phone, weights and the array aperture. The larger array aperture can lead to narrower main-lobe width which means higher spatial resolution, and the more microphones can allow low side-lobe level in higher frequency band, which means high imaging dynamic range. However, the array aperture size and the number of microphone are usually restricted in practical application or by product cost. Therefore, array layout design and weight are two crucial parameters which we can employ to improve localization performance. Recently, most of work in the literature has focused on optimal design of sparse linear or planar array [1-6]. Although statistical analysis method was used to suggest the possible performance of sparse arrays [5], it can not represent a design methodology to optimize the array geometry. Holm analyzed two optimization methods of weights and both the layout and weights [6]. The optimization algorithm is based on linear programming and minimizes the peak side-lobe level lower than the mean of side-lobe of the array. However, only a single frequency is assumed in this paper and array layout optimization design is highly related to noise frequency bandwidth. In [3], the design of wideband array based on simulated annealing was proposed by summing the frequency band. As a general result, the side-lobe level increases with frequency bandwidth and a fraction of frequency bandwidth was used in the paper.

In this paper, we present a general framework to consider the overall performance based on the narrow main-lobe width and low side-lobe level criterion using the particle swarm optimization method [7]. In low frequency band we place more emphasis on the main-lobe width, and place more emphasis on the side-lobe level within high frequency band. Thereafter, the array geometry is optimized by the criterion of narrow main-lobe width for low frequency and that of low side-lobe level for high frequency band based on the particle swarm optimization method. In the presented paper, both weights and layout can be optimized simultaneously. An alternate PSO is proposed to improve the optimization process.

This paper is organized as follows. In Sect.2, we give the array configuration model .A modified PSO method is proposed to optimize the array layout. In Sect.3, an optimization design frame-work of microphone array layout for wideband sources is proposed, which implements the geometry optimization for low frequency band and for high frequency band respectively. Then weights optimization is also further optimized to balance the main-lobe and side-lobe level. Simulations are carried out and results are demonstrated in Sect.4. The conclusions are drawn in Sect.5.

2. ARRAY MODEL

As is known that acoustic source localization is highly related to the array beam pattern. The beam pattern formula is given for the planar array, and then an modified PSO method is proposed to improve optimization process in array configuration both according to MLW and SLL in this section.

Assume that a source signal propagates from the direction (θ,φ) and the coordinate of micro-phone p_m is $[r_m \cos \phi_m, r_m \sin \phi_m]$ illustrated in Fig.1. The time delay of m th microphone is represented as:

$$\tau(m) = \frac{r_m}{c}\left(\cos\phi_m \sin\theta\cos\varphi + \sin\phi_m \sin\theta\sin\varphi\right) \tag{1}$$

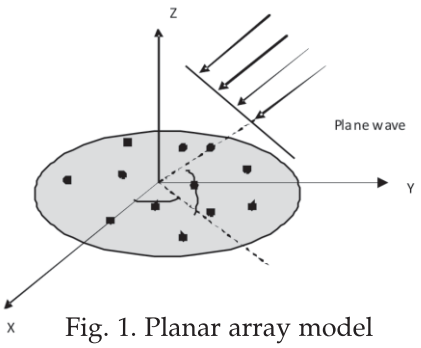

Fig. 1. Planar array model

Using Eqation (1) , one may obtain the beam pattern as :

$$B(\theta,\varphi)=\sum_{m=1}^{M} w_m \exp\left[j\frac{\omega r_m}{c}\left(\cos\phi_m \sin\theta\cos\varphi+\sin\phi_m \sin\theta\sin\varphi\right)\right] \tag{2}$$

The MLW is defined as Θ which is the angular interval of the first pair nulls of $|B(\theta, \varphi)|$ for a given φ and the side-lobe level is represented as :

$$\mathrm{SSL}=20\log_{10}\frac{\left|B_{\notin\Theta}(\theta,\varphi)\right|}{\left|B(\theta,\varphi)\right|_{\max}} \tag{3}$$

where $\notin\Theta$ means side-lobe which is the angular interval outside the main-lobe. Based on the narrow MLW and low SLL criterion, an array configuration can be optimized by

$$\begin{aligned} &\min\ \{\mathrm{MLW}, \max\{\mathrm{SLL}\}\} \\ &s.t.\ \ r_{\min}\le r_m \le r_{\max} \end{aligned} \tag{4}$$

where $[r_{\min}, r_{\max}]$ being the range of array elements. In this paper, we employ PSO method to implement the optimization. In order to implement optimization, a fitness value is designed to evaluate the updated particles.

$$F=\int_{\theta_0}^{\theta_{lim}}\int_{-\pi}^{\pi}\left(B_{\notin\Theta}(\theta,\varphi)-\xi(\theta,\varphi)\right)\delta(\theta,\varphi)d\theta d\varphi \tag{5}$$

where the integral lower limit θ_0 is the first null of $B(\theta, \varphi)$ outside the main-lobe and the integral upper limit θ_{lim} is the angle boundary limit. $[\theta_0, \theta_{lim}]$ is angle volume where we pay more attention to side-lobe. In Equation(5), δ(θ, φ) is defined as :

$$\delta(\theta,\varphi)=\begin{cases}1, B_{\notin\Theta}(\theta,\varphi)>\xi(\theta,\varphi)\\ 0, B_{\notin\Theta}(\theta,\varphi)\le\xi(\theta,\varphi)\end{cases} \tag{6}$$

3. THE MODIFIED PARTICLE SWARM OPTIMIZATION

The aim of employing PSO method [7] to implement equation (4) is to exploit possible microphone positions in order to find a set of optimal position which obtains both narrow MLW and low SLL. Consider a swarm with particles, each of which *N* represents an array configuration.

$$\mathbf{X}=\left[\boldsymbol{x}_1,\boldsymbol{x}_2,\cdots\boldsymbol{x}_n\cdots\boldsymbol{x}_N\right]^{\mathrm{T}} \tag{7}$$

where each particle can be denoted as :

$$x_n=[x_{n1}, x_{n2}, \ldots x_{nd}, \ldots x_{nD}] \tag{8}$$

where *D* is the dimension of optimization. We represent the best individual solution for each particle in the iteration process as :

$$\mathbf{P}=\left[\boldsymbol{p}_1,\boldsymbol{p}_2,\cdots\boldsymbol{p}_n\cdots\boldsymbol{p}_N\right]^{\mathrm{T}} \tag{9}$$

where $p_n = [p_{n1}, p_{n2}, \ldots p_{nd}, \ldots p_{nD}]$ is the best individual solution for the *n*th particle, and the best swarm solution is represented as:

$$\boldsymbol{g}=[g_1,g_2,\cdots g_d,\cdots g_D] \tag{10}$$

With Equation(7) through (10), the particles are updated according to the following equations:

$$\begin{aligned} v_{nd}^{t} &= w\cdot v_{nd}^{t-1}+c_1r_1\left(p_{nd}-x_{nd}^{t-1}\right)+c_2r_2\left(g_d-x_{nd}^{t-1}\right)\\ x_{nd}^{t} &= x_{nd}^{t-1}+v_{nd}^{t} \end{aligned} \tag{11}$$

where c_1 and c_2 are two positive constants (typically $c_1 = c_2 = 2$), r_1 and r_2 are two random variables, and *w* is inertia weight. The *t* and *t*-1 represent newly updated variable and previous one, respectively. From Equation (11), we can see that the new velocity is determined by three terms. The first term represents how

much the previous velocity is kept. The second term related to the distance between the best individual solution and its current one allows each particle to approach closely to best individual solution. Last term related to the distance between the best global swarm solution and its current one allows each particle to approach closely to best swarm solution. A large inertia weight w tends to explore global area while a small one tends to search local area. Shi [8]suggested a way to determine the inertia weight written in Equation(12) to make a balance in exploring global and local area .

$$w_t = w_{\max} - \frac{w_{\max} - w_{\min}}{T} t \tag{12}$$

where $w_{\max}$ and $w_{\min}$ are maximum and minimum weight respectively, and T is the total iteration number, t is current iteration index.

In this paper, we proposed a modified PSO procedure which alternately optimizes the main-lobe and side-lobe level. As a result, the can be summarized as follows :

STEP 1 : Initialize PSO parameters including the number of particle N , the optimization dimension D, particles $\mathbf{X}$, best individual solution $\mathbf{P}$, and best global solution $\boldsymbol{g}$, inertia weight $w_{\min}$, $w_{\max}$. Set a preliminary SLL and MLW θ_0.

STEP 2 : All particles are updated using Equation (11) through (12).

STEP 3 : Calculate the fitness value using Equation (5) to evaluate new particles, and judge if $\mathbf{P}$ and $\boldsymbol{g}$ are replaced by newly updated particles.

STEP 4 : Judge if the fitness value is zero. If so, decrease the θ_0 in a small amount and go to step 2, and then repeat step 2 through step 4. Otherwise, go to step 5.

STEP 5 : Judge if the iteration number reaches the maximum T. If not, repeat step 2 through step 4. Otherwise, go to step 6.

STEP 6 : Terminate and obtain the final result $\boldsymbol{g}$.

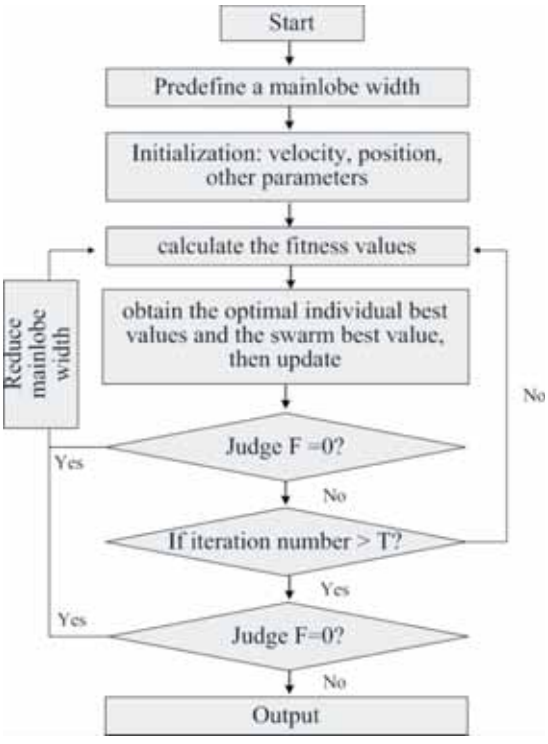

Fig. 2. Modified PSO flow chart

4. ARRAY GEOMETRY AND WEIGHTS OPTIMIZATION

In this paper, we present a general framework to optimize array layout considering narrow main-lobe width and low side-lobe level criterion. On one hand, in low frequency band we use modified particle swarm optimization presented in Sect. 3 to optimize half of microphones to obtain higher spatial resolution according to narrow main-lobe criterion. On the other hand, we employ modified particle swarm optimization to optimize the left half of microphones to obtain lower side-lobe level in higher frequency band according to low side-lobe level criterion. Therefore, we place more emphasis on the main-lobe width within low frequency band and place more emphasis on the side-lobe level within high frequency band when optimizing array geometry. Afterward, once the array geometry is determined, weights are optimized to balance the main-lobe and side-lobe at each frequency bin. When the array geometry and weights are determined, the beam pattern can be calculated.

Figure3-Figure5 show the simulation results of array optimization. The number of microphone is 128 and array radius is 0.5 m. [r_{min} , r_{max}] is [0,0.25] for higher frequency band and [0.25,0.5] for lower frequency band. We compare three typical array layouts: optimized array, random array and circle array. The circle array represents an extreme case which has very narrow main-lobe and high side-lobe level. Fig. 3 shows the position of array elements. In Fig. 4, it can be shown that circle array has narrowest main-lobe but has highest side-lobe level. The optimized array has narrower main-lobe and lower side-lobe level. Fig. 5 shows the similar results at the frequency of 9000Hz.

Therefore, the proposed method allows to have ability to balance the main-lobe and side-lobe level flexibly by adjusting the weights when the array geometry is fixed.

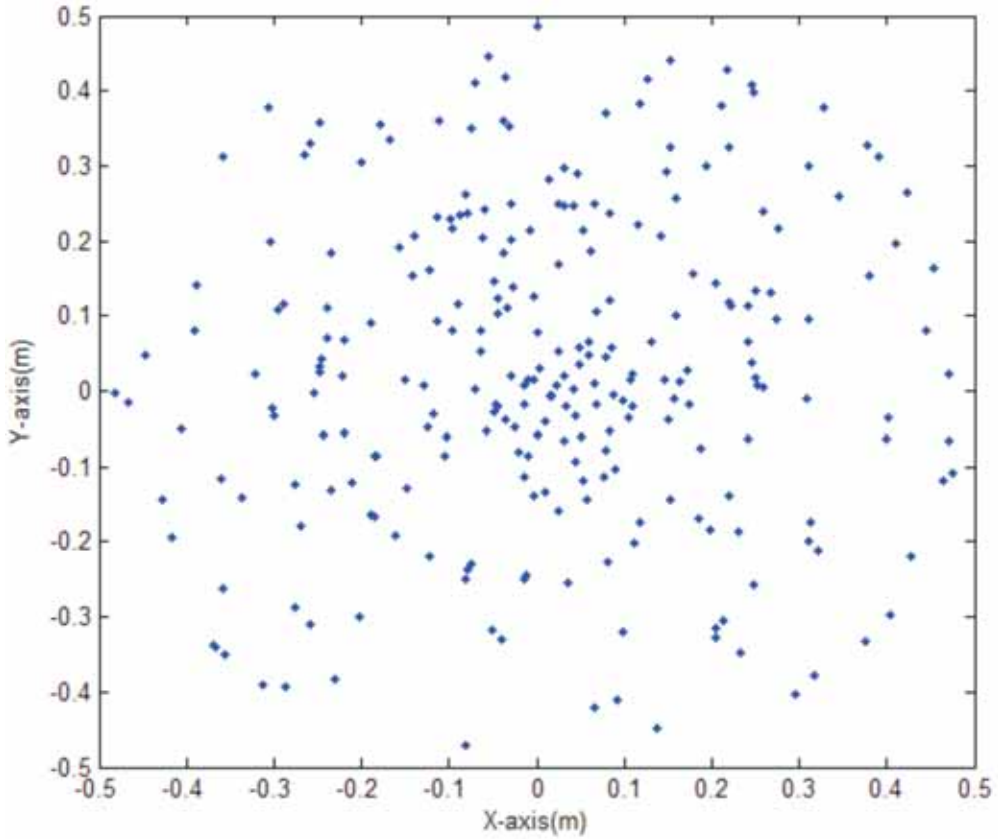

Fig. 3. Optimized array layout

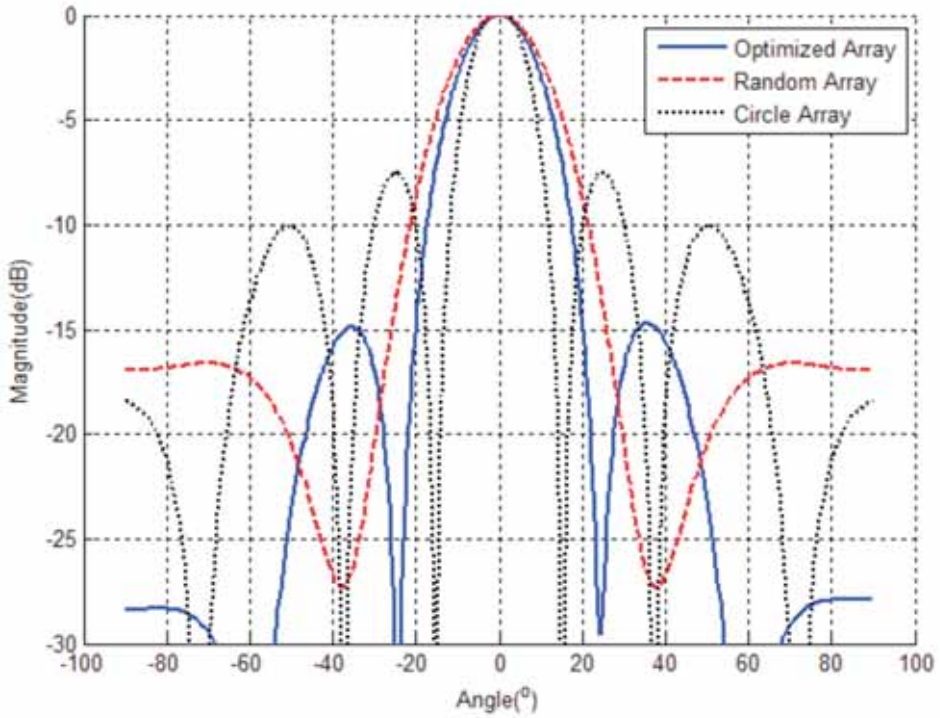

Fig. 4. Beampatterns of three arrays at 1000Hz
(Optimized Array, Random Array,Circle Array)

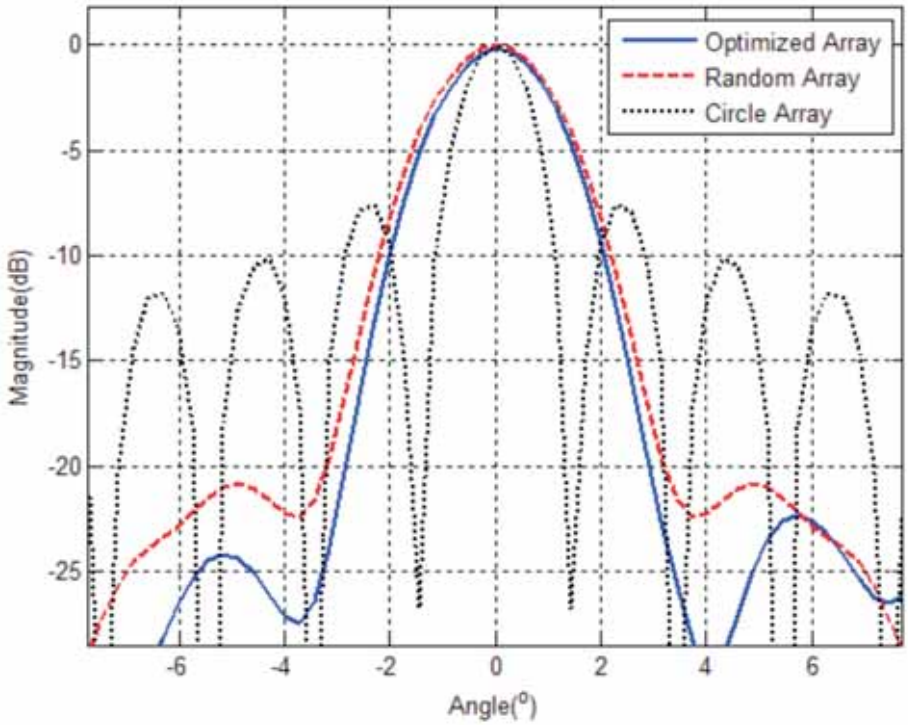

Fig. 5. Beampatterns of three arrays at 9000Hz
(Optimized Array,Random Array,Circle Array)

5. CONCLUSIONS

In this paper, we present a general framework to control the narrow main-lobe width and low side-lobe level based on the particle swarm optimization method. In low frequency band we place more emphasis on the main-lobe width, and place more emphasis on the side-lobe level within high frequency band. In the presented paper, both weights and layout can be optimized simultaneously. Simulations are carried out to demonstrate that the proposed scheme can improved localization performance of wideband noise sources.

6. REFERENCES

[1] M.J. WILSON, 2007. Sparse-periodic Hybrid Array Beam former, *IET Radar Sonar Navig*.,**15**(2), 116-123.

[2] J.E. KIRKEBO and A. AUSTENG, 2008. Sparse Cylindrical Sonar Arrays. *IEEE Journal of Oceanic Engineering*, **33**(2), 224-231.

[3] G. CARDONE and G. CINCOTTI, 2002. Design of Wideband Arrays for Low Sidelobe Level Beam Patterns by Simulated Annealing. *IEEE Transactions on Ultrasonics,Ferroelectrics,and Frequency Control*, **49**(8), 1050-1059.

[4] P. TENG and R. CHEN, 2012. A Hybrid Scheme for Localization and Separation for Multiple Noise Sources using a Microphone array. *International Congress and Exposition on Noise Control Engineering,* New York, USA, 19-22.

[5] B. STEINBERG,1972. The Peak Sidelobe of the Phased Array Having Randomly Located Elements: Antennas and Propagation. IEEE Trans.Antenna.Propag., **20**(2),129-136.

[6] S. HOLM, B. ELGETUN and G. DAHL, 1997. Properties of the Beampattern of Weight- and Layout-Optimized Sparse Array. *IEEE Trans. Ultrason.,Ferroelect.Contr.* **44**(5), 983-991.

[7] J. KENNEDY, 1997. The PSO: Social Adaptation of Knowledge. *Proc IEEE Int. Conf. on Evolutionary Computation*, 303-308.

[8] Y. SHI and R. EBERHART, 1998. Parameter Selection in Particle Swarm Optimization. *Proceedings of the 7th International Conference on Evolutionary Programming*.

Journal of Acoustical Society of India : Vol. 42, No. 4, 2015 (pp. 209-216)

Modification of Flat Plates to Increase Radiation Efficiency

S.S. Pathan[1] and Dhanesh N. Manik[2]
[1]Government Engineering College, Palanpur, Gujarat, 385001, India,
[2]Indian Institute of Technology Bombay, Powai, Mumbai, India,
e-mail: pathan_ss@yahoo.co.in, dnmanik@iitb.ac.in

[Received: 19.02.2014; Revised: 18.07.2014; Accepted: 22.02.2015]

ABSTRACT

Flat plates of large surface area are commonly used in constructing machinery and since they are efficient radiators of sound due to their vibration, the best way of reducing noise in machines is to reduce the radiation efficiency of flat plates. Sometimes the sound radiation may be due to lower transmission loss of the plate that can be increased by using a double walled construction. Adding external damping to plates is another possibility to reduce sound radiated by it. However, both these methods cannot be used in many cases as they would reduce the extent of heat transfer that may have to be allowed in some machines, for example, transformers. Stiffening of the plate is a possibility that would not interfere with heat transfer, but the radiation efficiency cannot be reduced in proportion to the extent of stiffeners. Therefore, in the present study, the flat nature of the plates is modified by adding stiffening elements over a large area that would change the flat nature of the outer surface of flat plates. This modification is expected to change the nature of bending vibrations of the plate that would interact with the sound waves and would thus reduce its overall radiation efficiency. The effect of these modifications are predicted and verified through experiments based on SEA and BEM modelling. The stiffeners that were used are in the form of angle sections of various included angles and thickness. Nine different combinations of these angle sections and thickness were used in the simulation and experiment. The use of these angle sections resulted in additional acoustic modes in the cavity and their contribution was reduced by using acoustic absorption material. Experiments were conducted by giving a standard impulse excitation and then measuring the resulting vibration and noise. A significant difference in sound radiation has been observed between plates of some types of angle stiffeners and the bare plate. The same set of structures was used to determine their transmission loss to determine whether the advantage of higher transmission loss and lower radiation efficiency can be simultaneously obtained. Experiments confirm that the same set of stiffened plates that had least radiation efficiency also have the maximum transmission loss.

1. INTRODUCTION

Sound radiating from vibrating structures is the main source of noise in most machines. Therefore, accurate prediction of sound radiation from such structures has been a challenging task for a long times. Most of the structural components of machines are generally constructed from an assemblage of flat plates; examples include casings of machineries, car body shells, ship hulls and decks etc. Hence, due to the wide use of flat

plates, it has been the consistent approach of researchers to model such complex structures using analytical or numerical approach—by simplifying them as simple plate like structures and studying their sound radiation mechanism. The study of a representative sample of a plate provides the basic understanding of the interaction between the flexural vibration behaviour of a structure and its sound radiation. This paper presents an attempt to minimize sound radiation from flat plates in a wider frequency range by using specifically designed stiffeners.

2. LITERATURE

W Maidanik [1] determined the radiation resistance of a baffled plate for a broadband excitation in terms of a frequency band average. Leppington*et al.* [2] have proposed an asymptotic formula for the radiation resistance at the critical frequency as Maidanik's prediction overestimated the radiation resistance by a factor of about 2, for a large plate aspect ratio. Wallace [3] studied the radiation efficiency of a finite, simply supported rectangular plate in an infinite baffle. Bonilha and Fahy [4] proposed a model of sound radiation from a baffled flat plate in multimodal response, with an assumption of large modal density of a plate to include the effect of number of resonant modes contributing within a frequency band. Onsay*et al.* [5] have analysed vibro-acoustics behaviour of bead stiffened flat panels byvarying design parameters such as bead orientation, depth and periodicity. Xie*et al*. [6] have investigated the effects of boundary conditions on the mode count and modal density of beams and plates using the wave number integration method. It is found that at low frequency there is an effect of boundary condition on modal density but at high frequencies modal density is constant irrespective of boundary conditions. The vibro-acoustic behaviour of aluminium extrusions is presented by Xie*et al*. [7]. An extruded panel is represented by a single global mode subsystem and three subsystems representing local modes of various strips which occur for frequencies above 500 Hz.. Using stiffeners in order to strengthen the structure and avoid undue vibrations generally modifies flat plates. Sometimes the behaviour of stiffened plate becomes that of a bare plate at high frequencies [5]. This means that increasing stiffness does not guarantee reduction in radiation efficiency.

3. STATISTICAL ENERGY ANALYSIS MODEL

In order to precisely evaluate the dynamic behaviour and acoustic properties at high frequencies, the space and frequency averaged responses of energy values are required to be estimated. Statistical Energy Analysis (SEA) is a method evolved basically to solve such problems.In case of BEM, only first few modes of a plate appear to involve global behaviour of the structure. At higher frequencies, the mode shapes become complicated and local motion of stiffeners begins to dominate the modes. Global modes may be considered

Table 1. Corrugated plate parameters used for experimental work.

Plate No.	Overall size of corrugated plate X × Y × Z (m)	Included angle of attachment	Thickness of attachment (mm)
1	0.48 × 0.3 × 0.0035	Bare plate	
2		70°	1.5
3		70°	2
4		70°	3
5		90°	1.5
6		90°	2
7		90°	3
8		120°	1.5
9		120°	2
10		120°	3

as those in which the energy is distributed over the whole system, involving the motion of the whole plate, whereas local modes involve motion of one or more members without much motion of the whole plate. The vibration energy of modified plates is distributed in the global modes of the whole plate and local modes that are dominated by individual stiffeners. For the present work, a bare plate is stiffened with different types of stiffeners as shown in Table 1; each stiffener has a different thickness and angle. There are nine such combinations of thickness and angles. The bare plate is designated as number 1 and the stiffened plates, called as corrugated plates, are designated as shown in Table 1. The photographs of plates 2 and 5 are shown in Fig. 1.

The material properties are: Young's modulus of 210 GPa, mass density 7850 kg / m^3 and Poisson's ratio as 0.3.

(a)

(b)

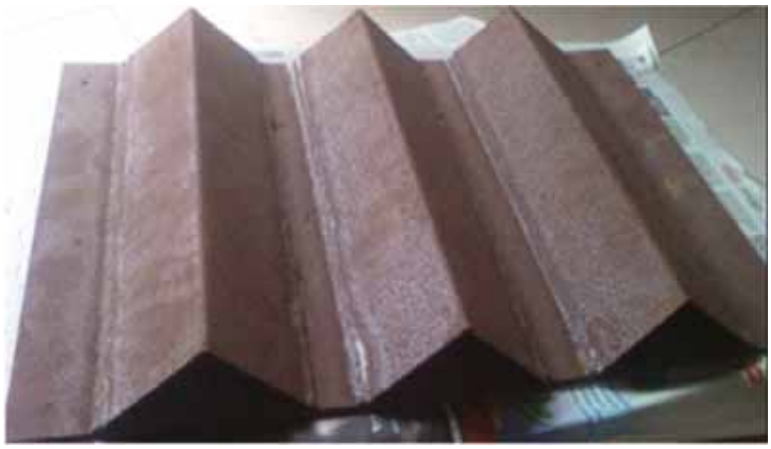

Fig. 1: Corrugated plates : (a) Plate 2 and (b) Plate 5.

4. SIMULATION OF MODAL DENSITY

Modal density is a very important parameter required to define a subsystem within an SEA model. In order to represent a corrugated plate using a simple SEA model, it is necessary to determine its modal density first. For some basic structures such as a rod, a beam or a plate, analytical expressions are available as given by Lyon [8] and Cremer, Heckl and Ungar [9]. However, for complicated structures like corrugated plates, there is no theoretical expression available to calculate their modal densities. The modal density of

corrugated plates can be considered as the sum of the modal density of the global and local modes. Details are presented in [7].

$$n(\omega) = n_g(\omega) + n_l(\omega) \text{ modes/rad} \quad (1)$$

where n_g (w) and n_1 (w) represent the modal densities of global and local modes, respectively.

The global modes can be considered on the basis of an equivalent uniform plate. The modal density of the local modes can be estimated from that of a large plate, having an area equal to the combined area of all the stiffeners with a number of line constraints applied [7]. It has been shown by Xieet al. [6] that boundary conditions and intermediate constraints on a plate have systematic effects on the mode count and modal density of the structures.

The modal densities of corrugated plates are predicted based on equation 1. The simulation results of modal densities for plates 2-10 are shown in Fig. 2. It can be seen that the modal densities are flat below 800 Hz for all the plates coinciding with those of a bare plate. Depending on the type of stiffener, the modal densities increase with frequency. For the plates 8 and 9 that have 1200 included angle, the modal densities are far higher than most of the other plates. It is interesting to note that these plates (8 & 9) turn out to be those with the least vibration and sound for impulse excitation. For different thickness values of stiffeners, the separation of modal density occurs at 1600 Hz for plates 2-4, at 1250 Hz for plates 5-7 and at 800 Hz for plates 8-10.

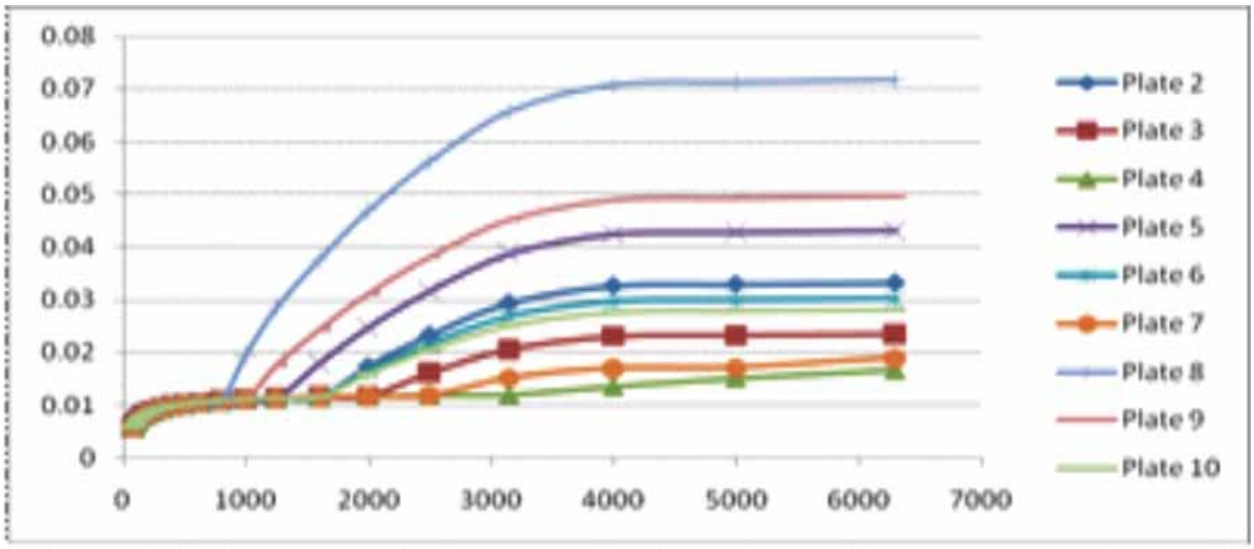

Fig. 2. Predicted modal densities of corrugated plates

5. EXPERIMENT

A series of plates as described in Table 1 were used for conducting experiments. The experimental setup is shown in Fig. 3. Each plate was freely suspended by hanging on two hooks and free to respond without any boundary conditions. A ball attached to the end of a rod was used to give a standard impulse input for the plates at their center, by swinging the rod from a specific height. The impulse excitation results in vibration in these plates that is radiated as sound. The experiment was repeated for each plate and the corresponding space averaged vibration corresponding to 25 locations and the sound pressure level at a distance of 1.6 m from the plate at a height corresponding to the height of the plate center is measured. A Pulse Brüel&Kjær FFT analyzerwas used for collecting the data.

(a) (b)

Fig. 3. Experimental setup

6. COMPARISON OF MODAL DENSITIES

Based on the vibration data of the corrugated plates, by counting the number of resonances within 1/3 octave bands, the modal densities were determined. First, the predicted modal densities are compared with those of experimental for a bare plate as shown in Fig. 4.

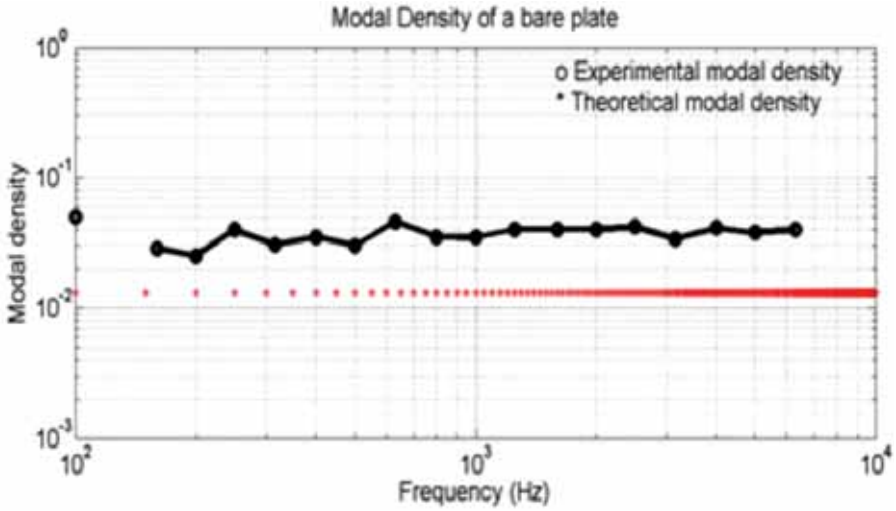

Fig. 4. Comparison of predicted and experimental modal densities of a bare plate (Plate-1).

Comparisons are made for all the plates between predicted and experimental modal densities but only a few cases (a bare plate, plate 6 and plate 9) are discussed here, as the trends are similar for rest of the plates.

The stiffeners actually form an acoustic cavity and if this acoustic cavity is not accounted for in determining the modal density, there will be an underestimation of prediction is seen. Fig. 5 shows a

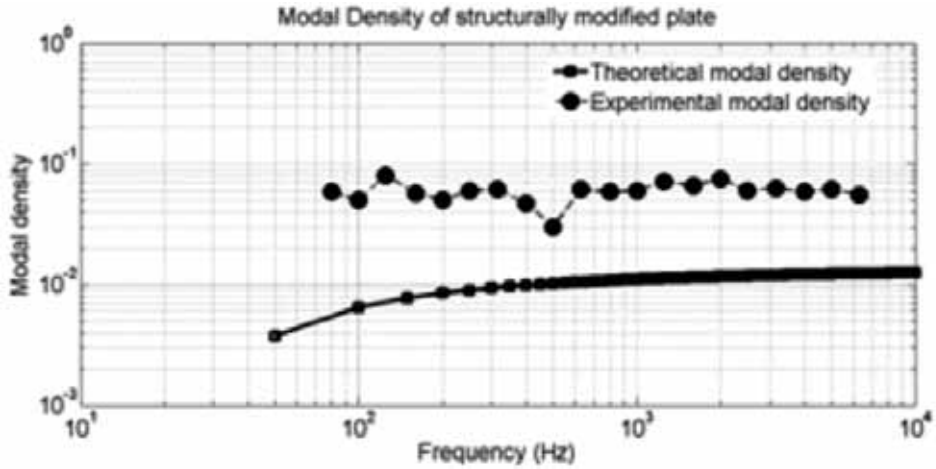

Fig. 5 Predicted and experimental modal densi-ties of plate-6

comparison between the predicted and experimental modal densities of plate 6, without accounting for the acoustic cavity formed by the stiffeners.

Due to the inclusion of acoustic cavities in the SEA model for plate 6 and plate 9, predictions are much improved for the case of plate 9 rather than plate 6 even at lower frequencies. This is because of major difference in cavity volumes of these plates. They are shown in Fig. 6.

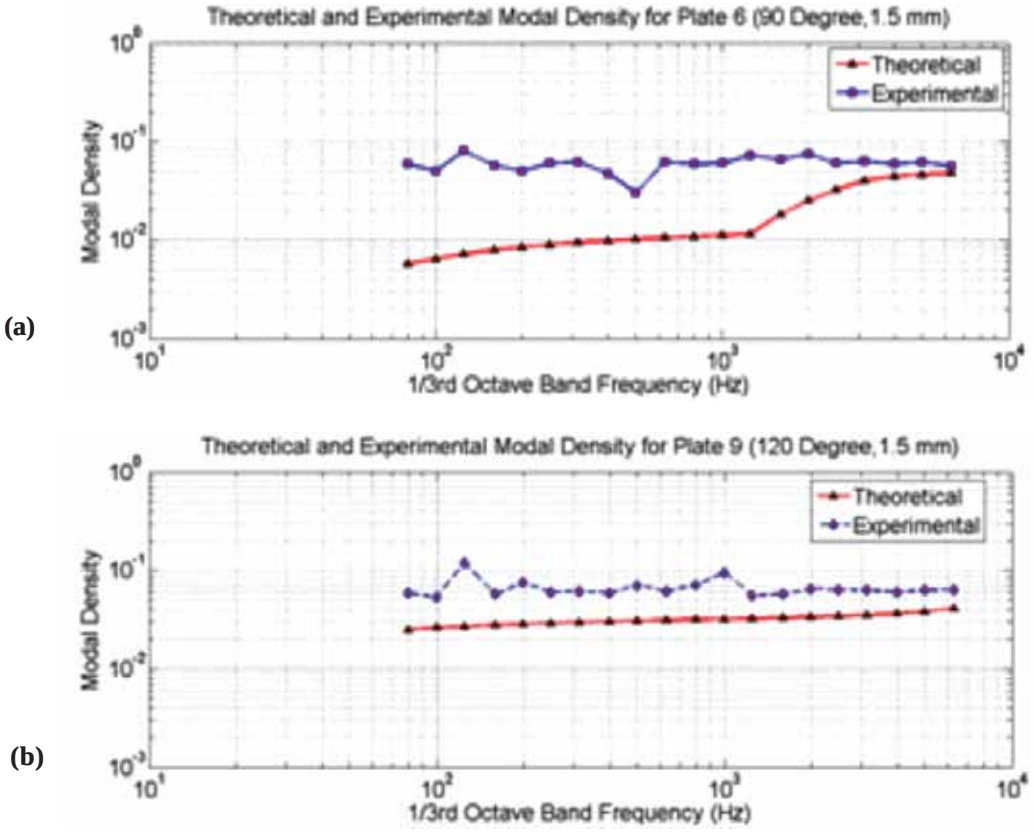

Fig. 6. Predicted and experimental modal densities; (a) Plate 6 and (b) Plate 9.

7. SOUND PRESSURE LEVELS

By giving the same impulsive excitation to all the plates, sound pressure levels were measured. The experiments were repeated for the plates by filling up cavities with foam so the sound generated by the acoustic cavity doesn't interfere with the sound generated due to vibration of the plates. It is observed that for all the plates, insertion of foam absorbs acoustic modes contributing in sound radiation. Fig. 7 for plate 10 shows decrease in sound levels due to the presence of foam inside the cavities for all the plates, specifically at high frequencies. From Fig. 7 it can be seen that acoustic modes are contributing at higher frequencies for all the plates. Not much advantage of absorbing acoustic modes is found in plate 4 (Fig. 9) as it is little affected by the cavity as compared to plate 2 (Fig. 8). This is due to the presence of local modes of the stiffeners getting coupled with the surrounding air, when the thickness is less, i.e. stiffeners of plate 2 become locally flexible sound sources compared to those of plate 4.

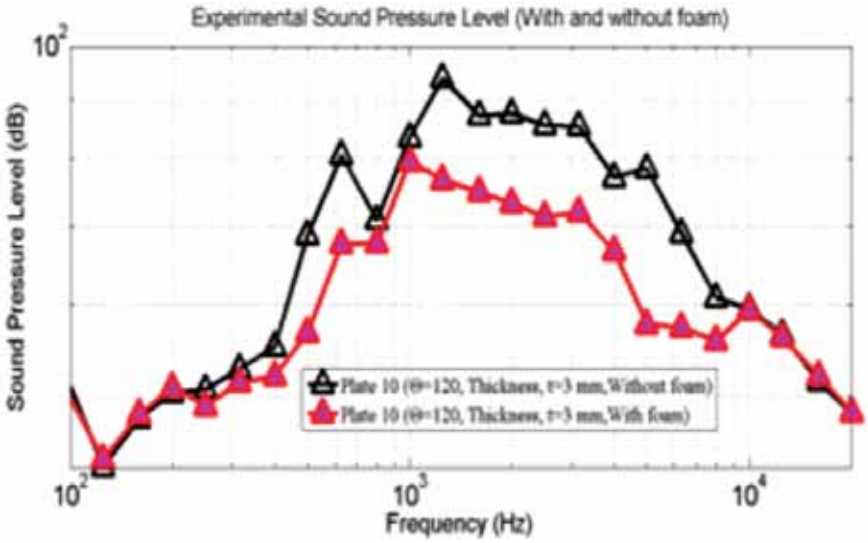

Fig. 7. Sound pressure levels due to impulse excitation of plate 10, with and without foam

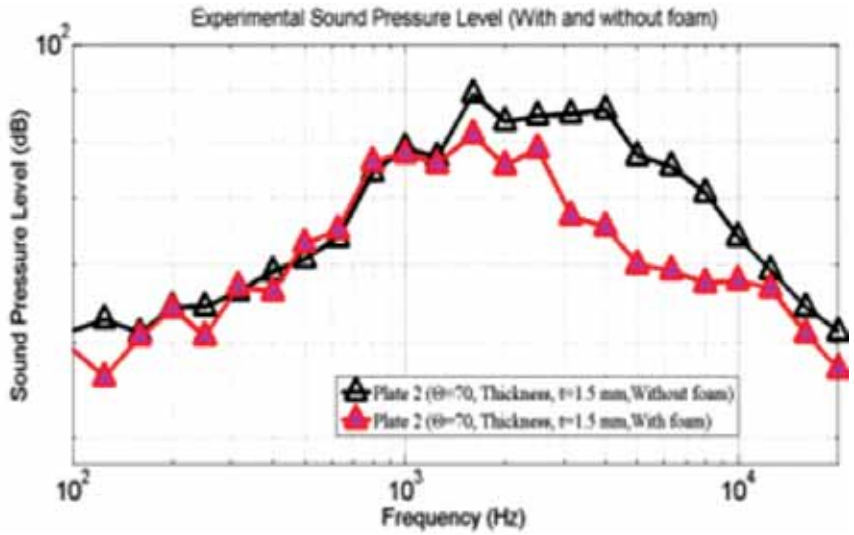

Fig. 8. Sound pressure levels due to impulse excitation of plate 2, with and without foam

For plates 8, 9 and 10 (whose sound pressure levels could not be shown here) where the dimensions of cavities are comparatively larger than the rest of the plates, a wide frequency band of 400 Hz to 8 kHz is affected by the acoustic modes. For plate 9, the sound level reduces appreciably.

8. CONCLUSIONS

Flat plates were modified for the purpose of studying the effect of stiffening the plate on sound radiation. The effects of modifications on sound radiated by flat plates are predicted and verified by conducting experiments.

Modal densities are very important parameters of SEA and are therefore predicted and verified with experimentation. It has been shown that plates with the largest modal density radiate much less sound.

Since sound radiation occurs in a wide range of frequencies, it is important to determine the effect of stiffeners at frequencies below 300 Hz. In addition, stiffeners will also affect transmission loss. These results will be presented at the conference. Low frequency studies using BEM and determination of transmission loss of the stiffened plates will be taken up next.

9. REFERENCES

[1] G. MAIDANIK, 1962. Response of ribbed panels to reverberant acoustic fields, *Journal of Acoustical Society of America*, **34**, 809-826.

[2] F.G. LEPPINGTON, 1982. Broadbent F.R.S., Heron K.H.,, The acoustic radiation efficiency of rectangular panels, Proceedings of the Royal Society London, **A382**, 245-271.

[3] C.E. WALLACE, 1972. Radiation resistance of a rectangular panel, *Journal of Acoustical Society of America,***51**, 946-952.

[4] M. BONILHA and F.J. FAHY, 1999. An approximation to the frequency-average radiation efficiency of flat plates, *Acoustical Society of America*, 138th meeting, Ohio.

[5] T. ONSAY, A. AKANDA and G. GREGORY, 1998. Vibroacoustic behavior of bead stiffened flat panels: FEA, SEA and experimental analysis, *Society of Automotive Engineers.*

[6] G. XIE, D.J. THOMPSON and C.J.C. JONES, 2004. Mode count and modal density of structural systems: relationships with boundary conditions, *Journal of sound and vibration*, **274**, 621-651.

[7] G. XIE, D.J. THOMPSON and C.J.C. JONES, 2006. A modelling approach for the Vibroacoustic behaviour of aluminium extrusions used in railway vehicles, *Journal of sound and vibration*, **29**3, 921-932.

[8] R.H. LYON and R.G. Dejong, 1995. *Theory and Application of Statistical Energy Analysis*, Boston: Butterworth-Heinemann, second edition.

[9] L. CREMER, M. HECKL and E.E. UNGAR, 1987. *Structure-Borne Sound*. Berlin: Springer-Verlag.

Journal of Acoustical Society of India : Vol. 42, No. 4, 2015 (pp. 217-222)

Performance Evaluation of Ultra-low Frequency Underwater Acoustic Projectors

B. Dubus[1], P. Mosbah[1]*, J.-R. Hartmann[2] and J. Garcin[2]
[1] IEMN UMR 8520 CNRS, département ISEN,
41 boulevard Vauban 59046 Lille Cedex, France
[2]DGA Techniques Navales /SDT/SCN/LSM/DSM, avenue de la tour royale,
BP 40915 83050 Toulon cedex, France
**e-mail: pascal.mosbah@isen.fr*

[Received: 29.04.2014; Revised: 25.08.2014; Accepted: 25.04.2015]

ABSTRACT

Ultra Low Frequency (ULF) underwater waves can travel great distance and are generally used in sonar or oceanography. To generate these waves, underwater transducers, utilized in the 10-400 Hz frequency range, have radiating surfaces whose dimensions are small with respect to the acoustic wavelength. To radiate a high acoustic power with a monopolar ULF transducer, a large volume velocity is required to counterbalance the low radiation resistance. Large volume displacement is generally difficult to obtain using common transduction mechanisms and under the constraint of getting a compact device. Three transduction technologies are available to realize compact high power ULF transducers: hydroacoustic, electromagnetic and active material-based. In the latter case, piezoelectric ceramics and magnetostrictive rare-earth alloys are often associated to flexural vibration such as found in flextensional transducers. Compared to these materials, piezoelectric single crystals which exhibit lower stiffnesses and produce higher strains together with higher energy densities, are potential active materials for future ULF underwater transducers. When dealing with high power, projectors are often evaluated using two figures of merit relative to their total volume or total mass. However, scaling down transducers from few kHz to ultra-low frequency range leads to projectors exhibiting gigantic size and huge power that cannot be reasonably considered by designers. Thus, to identify and evaluate the effective frequency range of a projector technology, it is necessary to express the acoustic radiated power at resonance frequency for families of projectors using homothetic transformations. In this study, acoustic radiated power is obtained by homothetic transformation and represented versus frequency in a log-log scale. Sets of parallel lines corresponding to the optimized solution for given total mass and projector technology are drawn. These graphs produce a global evaluation of existing ULF sources technologies in terms of acoustic power, resonance frequency, and total mass. They can provide a quick evaluation of potential improvement brought by new projector technologies and new active materials on ULF source performance according to these three criteria. In this work, ULF transducers are analyzed in terms of their working frequencies, acoustic powers and total masses. Thirty-two ULF underwater projectors build over the last 25 years are considered. For single crystal transducers, prototypes working at higher frequencies as well as transducers modelled with finite element method are taken into account. Using these data and classical scaling laws, abacuses displaying acoustic power-frequency curves for given masses are constructed for each technology. They show that single crystals transducers at the cost of high price may provide more compact solutions than current ULF projectors with identical radiated power and frequency.

1. INTRODUCTION

Ultra-Low Frequency (ULF) underwater projectors, used for sonar or oceanography in the 10-400 Hz frequency range, have usually radiating surfaces the dimensions of which are small with respect to the acoustic wavelength [1, 2]. To radiate a high acoustic power with a monopolar ULF transducer, a large volume velocity is required to counterbalance the low radiation resistance. Three transduction technologies are currently used to realize compact high power ULF transducers: hydroacoustic, electromagnetic and active material-based. In the latter case, piezoelectric ceramics and magnetostrictive rare-earth alloys are often associated to flexural vibration such as found in flextensional transducers. Compared to these materials, piezoelectric single crystals which exhibit lower stiffnesses and produce higher strains together with higher energy densities [3] are potential active materials for future ULF underwater projectors. The objective of this work is twofold:

1. To produce a global evaluation of each existing ULF source technology in term of source level and frequency;
2. To identify the improvement which could be brought by single crystal ULF sources.

A simple theoretical analysis of ULF sources is provided in section I to describe source level versus frequency. In section II, collected data concerning existing ULF sources are used to produce power versus frequency charts for each technology. Finally, available data on single crystal materials and transducers are extrapolated to evaluate the expected performance of single crystal ULF underwater sources.

2. GENERAL STYLE PARAMETERS

High power projectors are often evaluated using two figures of merit [4] relative to the total volume

$$FOM_V = P_0 \,/\left(V_0 f_r Q_m\right) \tag{1}$$

or to the total mass

$$FOM_M = P_0 \,/\left(M_0 f_r Q_m\right) \tag{2}$$

where V_0, M_0, f_r, P_0 and Q_m are respectively projector total volume, total mass, resonance frequency, radiated acoustic power at resonance frequency and quality factor. These figures are unchanged when the projector is scaled by a factor a leading to a total volume or mass scaled in α^3, an acoustic power scaled in α^2 (assuming that the driving field is kept constant), a resonance frequency scaled in α^{-1}, and a unchanged quality factor [1]. As stated by Woollett in [1], scaling down transducers from few kHz to ultra-low frequency leads to projectors exhibiting gigantic size and huge power which are never considered by designers. Thus, to identify the effective frequency range of a projector technology, it is necessary to express the acoustic radiated power at resonance for a family of projectors generated by a homothetic transformation. Let us consider a projector with the following characteristics: total volume V_0 and mass M_0, resonance frequency f_r, quality factor Q_m and peak quasi-static strain S. Assuming that the projector is a monopole radiator at ultra-low frequency, the acoustic radiated power is written as [1, 2, 4]:

$$P_0 = \left(\pi \rho_0 / c_0\right) Q_0^2 \; f_r^2 \tag{3}$$

where r_0 and c_0 are the density of water and the sound speed in water respectively.

$$Q_0 = A\, v_n = A\, 2\pi f_r \; u_n \tag{4}$$

is the source volume velocity with A, v_n and u_n being radiating surface area, normal velocity and normal displacement respectively. u_n can be related to peak quasi-static strain by introducing a nondimensional coefficient denoted β which depends upon projector geometry :

$$u_n = \beta\, S \left(V_0 / A\right) Q_m \tag{5}$$

By combining equations (3) to (5), an expression for acoustic radiated power is obtained :

$$P_0 = \left(4\pi^2\beta^2\rho_0 / c_0\right) S^2\ V_0^2\ Q_m^2\ f_r^4 \tag{6}$$

V_0 can be replaced by M_0/ρ_{av} in equation (6), where ρ_{av} is the average projector density is order to obtain an equation depending upon total mass rather than total volume. All terms appearing in the right-hand side term of equation (6), V_0 and f_r excepted, are unchanged when an homothetic transformation is applied. Thus, acoustic radiated power obtained by homothetic transformation will be represented versus frequency in a log-log scale by a set of parallel lines of slope equal to 4, each line corresponding to given total mass. The exact position of this set of lines is determined by the parameters β, S and Q_m which are not modified by the homothetic transformation.

3. EVALUATION OF CURRENT ULTRA-LOW FREQUENCY SOURCE TECHNOLOGIES

Twenty-three ULF underwater projectors build during the last 25 years are considered [5]. They rely upon different transduction mechanisms: hydroacoustic conversion (5 projectors), variable reluctance (6) or piezoelectricity (12). For each projector, experimental values of M_0, f_r, P_0 and Q_m are firstly used to extrapolate the resonance frequencies and acoustic powers that would be obtained for total masses of 100, 200, 500 and 1000 kg after homothetic transformation. Then, for each given transduction mechanism, all extrapolated data are reported on the same acoustic power versus resonance frequency chart. Finally, power-frequency lines connecting the "best" extrapolated projectors at constant mass are drawn and compared to theoretical solution given by equation (6).

The obtained charts are given in Figures 1 to 3. Hydroacoustic (Fig. 1) and piezoelectric projectors (Fig. 3) display (dashed) lines at constant mass for "best" projectors with respective slopes equal to 4.04 and 4.61, close to the theoretical value of 4 given by equation (6). For variable reluctance projectors (Fig. 2), the extrapolated slope is equal to 2.33. This discrepancy could be due to the limited number of projectors which exhibit a broad variation of quality factors (from 10 to 23). "Best" solutions at constant mass for each transduction mechanism can be reported in a global chart to give a view of the power-frequency lines in the whole ranges of powers and (ultra-low) frequencies (Fig. 4). With this chart, preferred transduction mechanism and required projector mass can be rapidly evaluated for given resonance frequency and acoustic power.

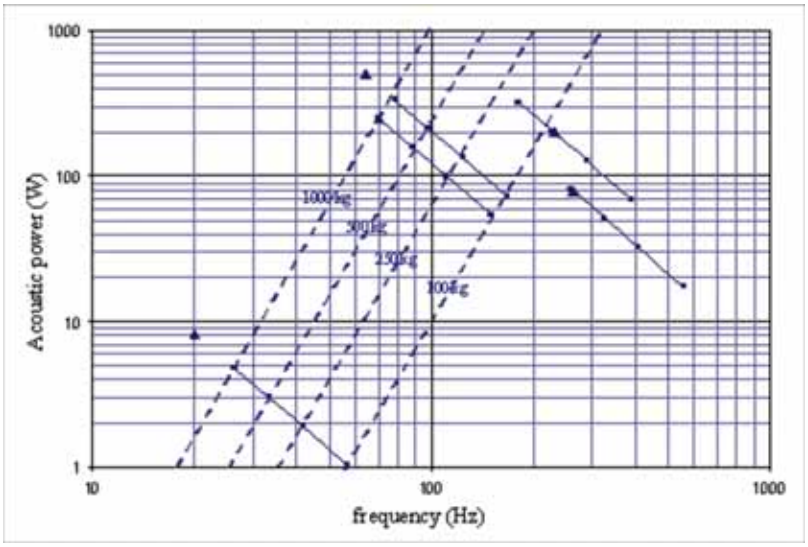

Fig. 1. Power-frequency curves of ULF hydroacoustic projectors. Triangles correspond to experimental values of fabricated projectors. Full lines connect data extrapolated from the same fabricated projector (masses of 100, 200, 500 and 1000 kg). Dashed lines connect "best" extrapolated projectors with identical masses.

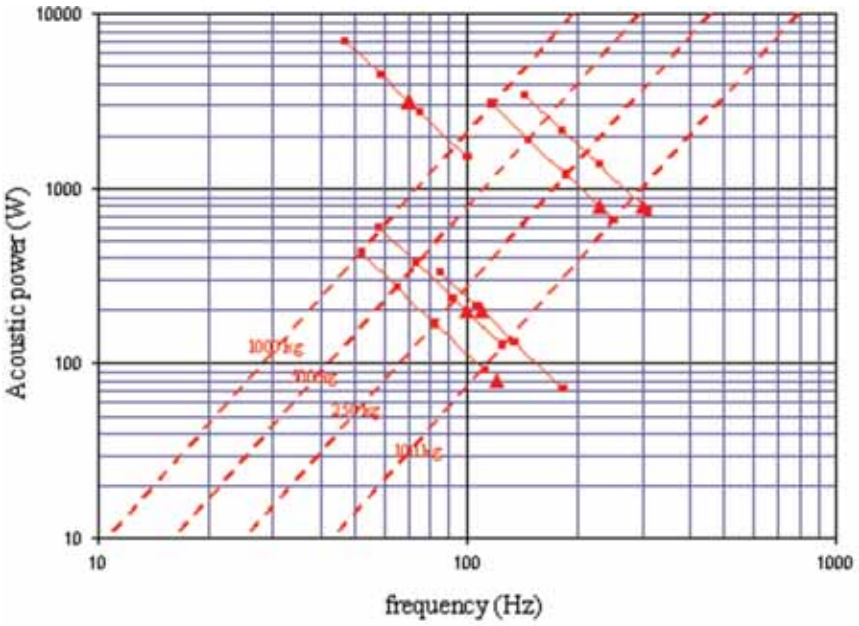

Fig. 2. Power-frequency curves of ULF variable reluctance projectors. Triangles correspond to experimental value of fabricated projectors. Full lines connect data extrapolated from the same fabricated projector (masses of 100, 200, 500 and 1000 kg). Dashed lines connect "best" extrapolated projectors with identical masses (projector with highest acoustic power is not considered because it displays very high quality factor).

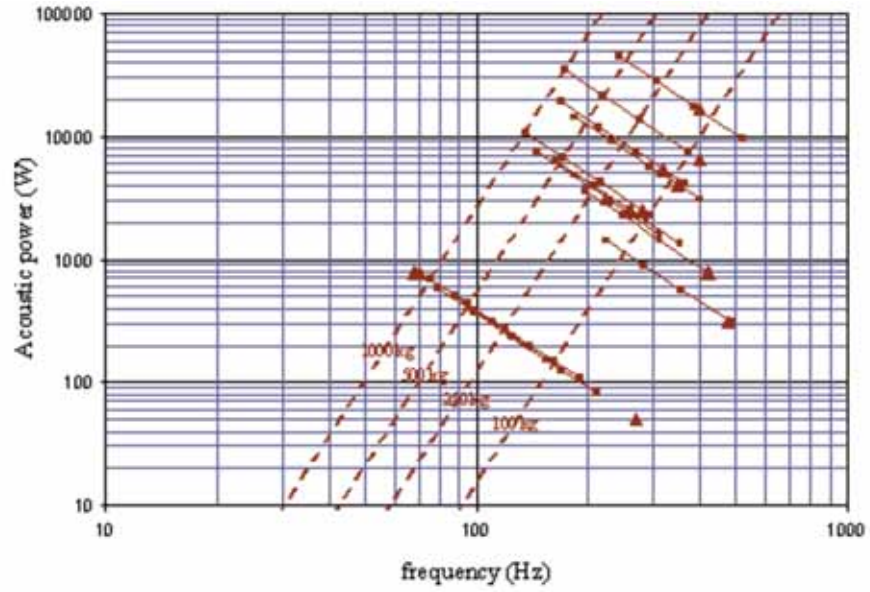

Fig. 3. Power-frequency curves of ULF piezoelectric projectors. Triangles correspond to experimental value of fabricated projectors. Full lines connect data extrapolated from the same fabricated projector (masses of 100, 200, 500 and 1000 kg). Dashed lines connect "best" extrapolated projectors with identical masses.

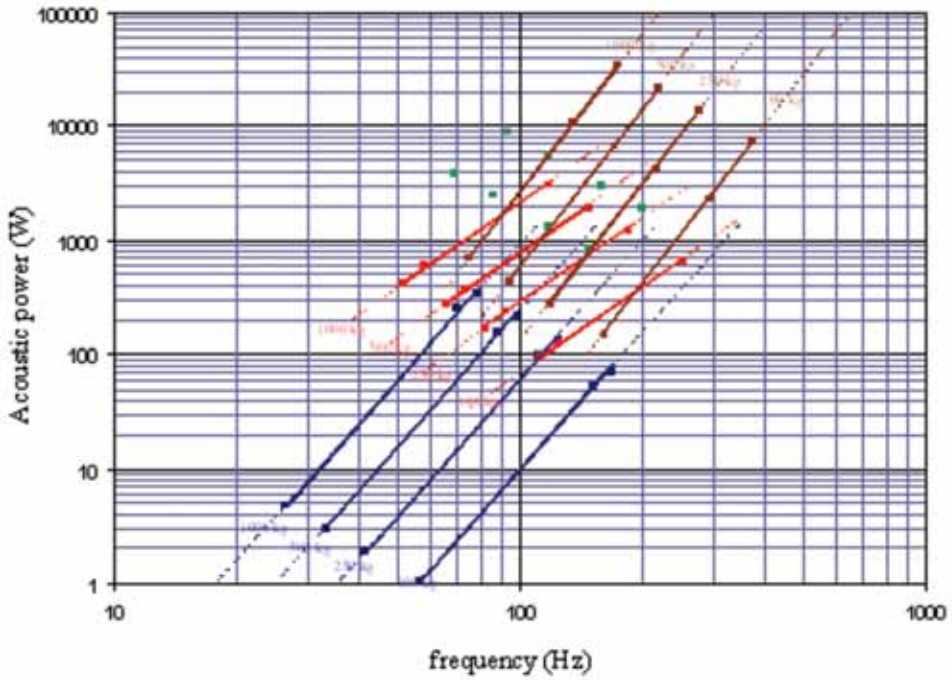

Fig. 4. Power-frequency curves displaying the optimal characteristics of hydroacoustic (blue curves), variable reluctance (red curves) and piezoelectric projectors (brown curves) for masses ranging from 100 to 1000 kgs. Extrapolated characteristics of PMN-PT projectors are denoted by green squares (flexural disc displays lower frequencies and powers than the array of cymbal transducers).

4. EVALUATION OF SINGLE-CRYSTAL ULF SOURCES

With PMN-PT single crystal materials, quasi-static peak strain can be increased by a factor of 12 and Young's modulus reduced by a factor of 3,7 with respect to Navy III type PZT ceramic [3]. No realization of single crystal projector is reported yet in the ultra-low frequency range. Two single-crystal transducers working at higher frequencies are therefore considered: an array of cymbal transducers [6] and a flexural disc [7]. The procedure described previously is applied to extrapolate by homothetic transformation, acoustic power and frequency of single crystal transducers with mass ranging between 100 and 1000 kgs. These data are reported in Fig. 4. Acoustic power is increased a factor of 4,5 compared to PZT projectors for identical resonance frequencies and mass. The design of these transducers is clearly not optimized for ultra-low frequencies considering that quasi-static mechanical energy stored in the active material is increased by a factor 38 between PZT and PMN-PT single-crystal [3]. Higher power should be obtained with single crystal flextensional transducers.

5. ACKNOWLEDGMENTS

This work was supported by DGA TN / SDT / SCN / LSM / NP.

6. REFERENCES

[1] R.S. WOOLLETT, 1980. Basic problems caused by depth and size constraints in low-frequency underwater transducers, *J. Acoust. Soc. Am*. **68**, 1031-1037.

[2] J.-N. DECARPIGNY, B. HAMONIC and O.B. WILSON, 1991. The design of low frequency underwater acoustic projectors: present status and future trends, *IEEE J. Oceanic Eng.* **16**, 107-122.

[3] J. LINDBERG, 2002. Material challenges for transducer designers in the 21st century, *Proc. SPIE smart structure and materials 2012: active materials: behaviour and mechanics*, **4699**, 485-498

[4] C.H. SHERMAN and J.L. BUTLER, 2007. Transducers as projectors in *Transducer and arrays for underwater sound*, **3**, 76-151 .

[5] B. DUBUS and P. MOSBAH, 2012. Study of ultra-low frequency active sonar – part 1: high power ultra-low frequency acoustic sources (in french), *DGA TN/SDT/SCN/LSM/NP* report 2010-107552.

[6] J.F. TRESSLER, T.R. HOWARTH and D. HUANG, 2006. A comparison of the underwater acoustic performance of single crystal versus piezoelectric ceramic-based "cymbal" projectors, *J. Acoust. Soc. Am.* **119**, 879-889.

[7] R.A.G. FLEMING, A. HERBIN and C.J. PURCELL, 2012. PMN-PT vs PZT4 flexural disk study, *ONR workshop on Acoustic Transduction Materials and Devices*, **4**.

Journal of Acoustical Society of India : Vol. 42, No. 4, 2015 (pp. 223-228)

Potential Use of Sonochemistry in Endocrine Disruptive Compounds Elimination: Case of Bisphenol A

Christian Pétrier[1]*, Ricardo Torres-Palma[2] and César Pulgarin[3]
[1]Laboratoire Rhéologie et Procédés, Université de Grenoble,
France.Abdulaziz University, Jeddah, Saudi Arabia.
[2]Universidad de Antioquia, Medellin, Columbia.
[3]Ecole Polytechnique Fédérale de Lausanne, Suisse.
**e-mail: christian.petrier@ujf-grenoble.fr*

[Received: 17.04.2014; Revised: 18.09.2014; Accepted: 21.04.2015]

ABSTRACT

Several micropollutants of water, suspected to interfere with hormone action, present endocrine disrupting effect (EDE) in aquatic organisms and micro-organisms

Bisphenol A (BPA), an organic compound largely used in the plastic industry as a monomer for production of epoxy resins and polycarbonate, is a xenobiotic that can be released in the environment from bottles, packaging, landfill leachates, paper, and plastics plants. This compound disturbs the behavior of aquatic life by EDE at low level concentrations. To some extent, BPA can be eliminated through usual physical, chemical, or biological treatments. Nevertheless, because of its estrogenic action, and the fact that chlorination disinfection processes can lead to products with higher EDE and/or toxicity, BPA should be completely removed from wastewater and water sources.

Physicochemical methods, based on the production and use of hydroxyl radical called advanced oxidation processes (AOPs) (*e.g.*, H_2O_2 + UV, UV + O_3, H_2O_2 + O_3, TiO_2

photocalalysis, Fenton's reagent, photo-Fenton), have been successfully tested for elimination of organic pollutants of waters.

Since 1962 it has been recognized that the propagation of an ultrasonic wave (20 kHz-1 MHz) can be used to eliminate organic pollutants from water.

Centered on kinetics data and chemical pathways of BPA elimination, the presentation provides description and analysis of the principles of sonochemistry that are involved in the process and connect ultrasound action with AOPs.

Application of the technology requires optimization of the process and cost estimation.

In this purpose, the parameters that affect the sonochemical kinetics and yields of BPA elimination in natural water include pH, frequency, nature of dissolved gases, presence of inorganic salts and organic matter are discussed and evaluated.

Ultrasound alone does not conduct to complete BPA mineralization. The method generates often secondary products that are not significantly eliminates and can exhibit some hazardous character.

Taking advantage of hydrogen peroxide production that goes with ultrasonic cavitation and organic matter oxidation in oxygenated water, complete mineralization can be achieved by combination of ultrasound action and AOPs.

Investigation on the hybrid technologies: -Ultrasound/UV radiation; -Ultrasound/Fe(II); Ultrasound/Fe(II)/UV radiation; -Ultrasound/photocatalyst/UV radiation: -Ultrasound/

photocatalyst / solar light, evidence the great advantage of these combinations that conduct to fast mineralization and reduce the water remediation cost.

1. INTRODUCTION

Human activity disperses in the environment a large amount of organic compounds that alter aquatic life and water resource. One of these compounds, Bisphenol A (BPA) used in industry for the production of epoxy resins and polycarbonate exhibits endocrine disrupting properties. BPA released in the environment from bottles, landfill leachates, plastic plant… induces for example gonadal ontogeny of fishes, even at low dose exposure. BPA is one of the most important xenobiotic substances that present adverse effects on human health and wildlife [1-2].

Because of the oestrogenic action occurring at very low concentrations, BPA has to be completely removed from waste water and drinking water. This elimination cannot be achieved using usual physical, chemical and biological treatments.

In the recent years, there is an increase interest in the used of technics named Advanced Oxidative Processes (AOPs) for an overall removal of micro pollutants from water [3]. AOPs are based on the production and use of hydroxyl radical: °OH. This very reactive entity reacts with organic compounds with high rate constant (10^6 to 10^9 mol L^{-1} s^{-1}) conducting to the complete mineralization of the undesirable and hazardous structures [4].

Propagation of an ultrasonic wave in water can induce the formation of °OH. Hydroxyl radical generation does not result from a direct interaction of the wave with matter. They are produced during the phenomenon of acoustic cavitation that is caused, in water, by periodic variation of the pressure wave. Upon pressure change, the cavitation bubble that contained vaporized water and dissolved gas, pulsates and can collapse in a very short period of time (less than 10^{-5}s). In such condition, compression occurs mostly in an adiabatic manner conducting to a residual “hot spot” characterized by high temperature and high pressure: 3000°K, 300 atm. As consequence of these extreme conditions, molecule of water and oxygen dissociates, releasing °OH in the bulk (reactions 1-3) [5-6].

-1 H-O-H $\rightarrow$ H + °OH

-2 O=O $\rightarrow$ 2O

-3 O + H-O-H $\rightarrow$ 2°OH

The use of ultrasound for treatment of water has gained great interest in recent year. No organic compounds have been found resistant to ultrasound action [7-8]. This document focuses on main parameters that affect the sonochemical kinetics and yields of BPA elimination in deionized and natural waters. Emphasis is given to practical aspects and to presentation of the hybrid processes that combine ultrasound action with other AOPs.

2. EXPERIMENTAL PART

Experiments were conducted in a 500 mL cylindrical water-jacketed glass reactor containing BPA dissolved in water. Ultrasonic wave were emitted from the bottom of the reactor through a piezo-electric disc with a diameter of 4 cm fixed on a Pyrex plate. Ultrasonic energy dissipated in the reactor was estimated using the calorimetric method.

- Quantitative analysis of BPA was done by HPLC using a Waters 590 instrument with a Supelcosil LC-18 column (250 × 4.6 cm, 5 mM) and a tunable UV detector set at 190 nm.
- The organic compound mineralization: Total Organic Carbon (TOC) removal was followed in a LABTOC analyzer using a solution of potassium phthalate as the calibration standard.
- Hydrogen peroxide concentration was determined iodometrically.

3. RESULTS AND DISCUSSION

3.1 Characteristic of BPA sonochemical degradation

Treatment of an aerated BPA solution by an ultrasonic wave conducts to the reduction of the initial concentration. The BPA concentration decreases exponentially with time following an apparent first-order kinetic (Figure 1). Degradation products that are detected in the first instant of the treatment are hydroxylated products that evidences clearly the °OH involvement (Reaction 4). It has to be observed that the ultrasonic application results also in a concurrent formation of hydrogen peroxide. This hydrogen peroxide is produced at a lower rate than for an aerated solution that does not contain BPA because presence of BPA at the interface of the bubble competes with H_2O_2 formation (Reaction 5) [9].

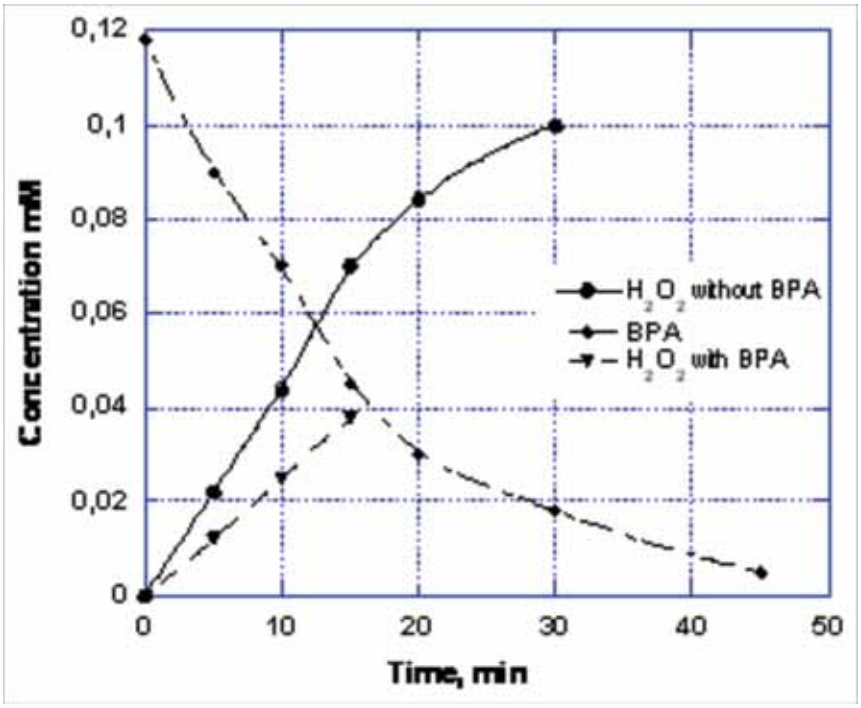

Fig. 1. BPA degradation and hydrogen peroxide formation for aerated water. BPA concentration: 118 mM. Ultrasonic frequency: 300 kHz. Ultrasonic power: 80 W. Volume: 300 mL. Temperature: 20°C. (Adapted from ref. 9)

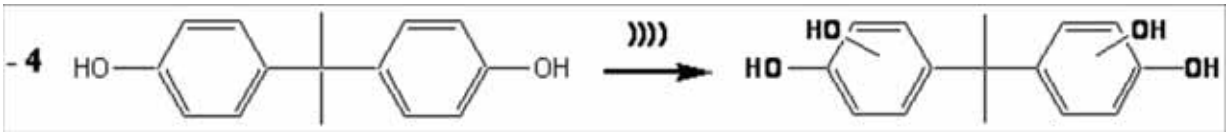

-5 °OH + °OH → H-O-O-H

3.2 Parameters affecting the sonochemical yields

The yield of processes involving the use of ultrasound depends of several parameters: -amplitude of the wave, -temperature, -vapour pressure and viscosity of the liquid that is treated, -temperature, -presence of saturating gases, frequency of the wave…

In the case of water treatment it has been clearly evidenced from several works that frequency and dissolved gases are key parameters for the process

3.2.1 Effect of the frequency

In sonochemistry of water, frequency was found as a critical parameter. The use of frequency under 60 kHz appears of very limited efficiency for °OH and hydrogen peroxide production, better yields being obtained in the range 200 – 800 kHz. [10].

In the case of BPA water solution the investigation conducted at four frequencies: 300, 500, 600, 800 kHz displays the best yield for the lowest frequency. Frequency can affect cavitation in different ways: - modifying the number and the size of the bubbles, - changing the duration and the final step temperature of the collapse. Best result observed at 300 kHz could be attributed to better release of °OH at this frequency [11].

3.2.2 Effect of saturating gases

It is well established that cavitation threshold and number of cavitation bubbles depend of amount of dissolved gasses in the liquid. On other hand, polytropic ratio of the gas (Cp / Cv) that affects temperature of the collapse has great importance in °OH generation. It is quite unrealistic to envisage saturation of the water by other gas than air or oxygen.

In this way oxygen reveals great superiority when it is compared to atmospheric air for the following reasons :

- Presence of nitrogen in air induces release of nitrate and nitrite ions, harmful chemical compounds for drinking water and water resource [9].
- Rate of °OH production, most of the time, is found higher for oxygen saturated water than when air is used [12].
- In the bulk, oxygen reacts at high rate with organic radicals, enhancing hydrogen peroxide generation.

3.3 Hybrid processes for BPA degradation

From a general point of view, ultrasound conducts to rather fast elimination of organic pollutants but mineralization of organic matter, the complete elimination of the pollutants and the by-products cannot be obtained (transformation of organic into carbon dioxide).

Mineralization can be obtained in different ways, combining ultrasound action with use of other AOPs.

3.3.1 Combination of ultrasound and UV or solar source

In part 3.1, it has been underlined that hydrogen peroxide production occurs during the course of sonochemical BPA elimination. This hydrogen peroxide would be the source of additional °OH upon UV light irradiation with an expected increase of BPA degradation rate.
UV irradiation of H_2O_2 solution with a light source at wavelength under 254 nm conducts directly to °OH generation (reaction 6) [13].

-6 $H_2O_2 + h\nu(254\ nm) \rightarrow 2\ °OH$

This supplementary °OH formation occurs in the bulk and does not increase rate of BPA elimination at the interface of the bubble, but it reacts with by-products, hence it amplifies mineralization of organic matter.

Intensification of the mineralization can be obtained with addition of Fe(II) or Fe(III).

In a dark process, the Fenton's reaction, Fe(II) decomposes H_2O_2 in °OH and ^{-}OH with Fe(III) formation (reaction 7).

-7 $Fe^{2+} + H\text{-}O\text{-}O\text{-}H \rightarrow Fe^{3+} + °OH + {}^{-}OH$

Fenton's process can be improved by artificial or solar irradiation in a photo-assisted Fenton reaction, or "photo-Fenton" . This enhancement results from H_2O_2 photodecomposition and the photolysis of Fe(III) hydroxide [$Fe(OH)^{2+}$] that produces additional °OH and regenerates Fe(II) (reactions 7-9) [12].

-8 $Fe^{3+} + {}^{-}OH \rightarrow Fe(OH)^{2+}$

-9 $Fe(OH)^{2+} + h\nu \rightarrow Fe^{2+} + {}^{\circ}OH$

This additional Fe(II) restoration in the Fenton reaction ensures an additional source of °OH and a fast consummation of H_2O_2 resulting from the ultrasonic action [14].

Comparison of electrical energy cost in the case of Bisphenol A mineralization over ultrasound and the three hybrid processes: ultrasound / UV, ultrasound / Fenton, and ultrasound / photo(UV)-Fenton. The results of this cost comparison support the great advantage of the process combining ultrasound / photo-Fenton for BPA treatment (Table 1).

Table 1: Electric energy cost estimation for bisphenol A mineralization in different hybrid AOPs (BPA concentration 118 mmol L^{-1}; volume treated 300 mL)

Process	Power,W	Time, min	TOC,% removed	Energy costKWh m^{-3}
UV (254 nm)	25	600	Less than 60%	
Ultrasound (300 kHz)	80	600	Less than 60%	
Ultrasound / UV	105	300	66	6010
Ultrasound / Fe(II)	80	600	64	3735
Ultrasound / Fe(II) / UV	105	120	79	1033

3.3.2 Ultrasound and photocatalysis combination

TiO_2 photocatalysis is an AOP that currently receives a great deal of attention as a means for water remediation . In the process, irradiation with light (l < 400 nm) transfers an electron from the TiO_2 valence band to the conduction band with the generation of an electron-hole pair (reaction 10).

Adsorbed water molecules and surface bound hydroxide species may be oxidized to form the °OH radical (reaction 11)

-10 $TiO_2 + h\nu\ (\lambda < 400\ nm) \rightarrow TiO_2\ (h^+ + e^-)$

-11 $TiO_2(h^+) + H_2O\ /\ HO^- \rightarrow {}^{\circ}OH + H^+ + TiO_2$

Addition of TiO_2 powder to a sonochemical reactor (300 kHz) illuminated with simulated solar light has demonstrated that BPA removal from a polluted water can be achieved with greater efficiency than that can be obtained with the separated AOP [15].

Improvement in photocatalyst activity can result from mechanical coming from ultrasound action. Cavitation should enhance the photocatalytic system performance through high-speed displacement and the collision of particles that increase deaggregation and mass transfer at the catalyst surface. In addition, collisions also lead to the structural modification of the surface, creating oxygen defects that would render the surface more active [16].

4. CONCLUSION

The use of ultrasonic cavitation for EDC elimination is a simple technique requiring only electrical energy. However, good practice requires knowledge in the basic principles and parameters governing the goal required. Attention must be taken to the frequency of the wave that is important for the disposal of hydroxyl radicals in water.

If the application of ultrasound alone for BPA mineralization water can be considered expensive, the combined process have to be chosen for economic viability in regard to other AOPs under development.

5. REFERENCES

[1] D. A. CRAIN, M. ERIKSEN, T. IGUCHI, S. JOBLLING, H. LAUFER, G.-H. LEBLANC and L.-J. GUILLETTE, 2007. An ecological assessment of bisphenol-A: evidence for from comparative biology. *Reprod. Toxicol.* **14**, 225-239.

[2] C. A. STTAPLES, P. B. DRN, G. M. KLECKA, S. T. O'BLOCK and L. R. HARRIS, 1998. A review of the environmental fate, effect, and exposure of bisphenol-A, *Chemosphere*, **36**, 2149-2173.

[3] S. PARSONS and A. BYRNE, 2004. In advanced oxidation processes for water and wastewater treatment, Parsons S. Ed., IWA Publishing, London, 329-346.

[4] J. J. PIGNATELLO, E. OLIVEROS and A. MACKAY, 2006. Advanced oxidation processes for organic contaminant destruction based on the Fenton reaction and related chemistry, *Crit. Rev. environ. Sci. Technol*. **36**, 1-84.

[5] T. J. MASON and C. PÉTRIER. 2004. Ultrasound Processes. In : S. Parson(Ed), Advanced oxidation processes for water and waste water treatment. IWA publishing, London, 185-208.

[6] A. HENGLEIN, 1987. Sonochemistry: historical developments and modern aspects, *Ultrasonics*, **25**(1) 6-16.

[7] P. GOGATE and A. B. PANDIT, 2004. A review of imperative technologies for wastewater treatment. II hybrid method, *Adv. Environ. Res*. **8**(3-4), 553-597.

[8] P. COLARUSSO and N. SERPONE, 1996. Effect of ultrasounds on homogeneous chemical reactions and in environmental detoxification, *Res. Chem. Intermed*. **22**(1) 61-89.

[9] R. A. TORRES, C. PÉTRIER, E. COMBET, M. CARRIER and C. PULGARIN, 2008. Ultrasonic cavitation applied to the treatment of bisphenol A. Effect of sonochemical parameters and analysis of BPA by-products, *Ultrasonics Sonochemistry*, **15**, 605-611.

[10] C. PÉTRIER and A. FRANCONY, 1997. Incidence of wave-frequency on the reaction rates during ultrasonic wastewater treatment, *Wat. Sci. Tech.* **35**, 175-180.

[11] C. PÉTRIER, M.-F. LAMY, A. FRANCONY, A. BENHACENE, B. DAVID, V. RENAUDIN and N. GONDREXON, 1994. Sonochemical degradation of phenol in dilute aqueous solutions: comparison of the reaction rates at 20 and 487 kHz, *J. Phys. Chem.*, **98**, 1514-1520.

[12] R. A. TORRES, C. PÉTRIER, E. COMBET, F. MOULET and C. PULGARIN, 2007. Bisphenol A mineralization by integrated Ultrasound-UV-Iron(II) treatment, *Environ. Sci. Technol*. **41**, 297-302.

[13] O. LEGRINI, E. OLIVEROS and A. M. BRAUN, 1993. Photochemical processes for water treatment, *Chem. Rev*., **93**, 671-698.

[14] R. A. TORRES, G. SARANTAKOS, E. COMBET, C. PÉTRIER and C. PULGARIN. 2008. Sequential helio-photo-Fenton and sonication processes for the treatment of bisphenol A. *J. Photochem*. Pho*tobiol*. **199**, 193-203.

[15] R. A. TORRES, J. NIETO, E. COMBET, C. PÉTRIER and C. PULGARIN, 2010. An innovative ultrasound, Fe^{2+} and TiO_2 photoassisted process for bisphenol A mineralization. *Wat. Res*. **44**, 2245-2252.

[16] P. OSORIO-VARGAS, C. PULGARIN, A. SIENKIEWICZ, L. R. PIZZIO, M. N. BLANCO, R. TORRES-PALMA, C. PÉTRIER and J. A. RENGIFO-HERRERA, 2012. Low-frequency ultrasound induces oxygen vacancies formation and visible light absorption in TiO_2 P-25 nanoparticles, *Ultrason. Sonochem.*, **19**, 38-3386.

Journal of Acoustical Society of India : Vol. 42, No. 4, 2015 (pp. 229-237)

Gaps in the Acoustic Theory of Speech Production

T.V. Ananthapadmanabha
Voice and Speech Systems, Malleshwaram, Bangalore 560 003, India
tva_vss@yahoo.com or tva.blr@gmail.com

[Received: 18.04.2014; Revised: 18.09.2014; Accepted: 25.01.2015]

ABSTRACT

Speech technology has demonstrated impressive applications such as low bit-rate speech coding, text-to-speech-synthesis, automatic speech recognition and speaker recognition *etc*. Such technological applications rely on speech analysis which in turn is based on a model for speech production. A success in these applications gives rise to an impression that we have a scientifically sound model for speech production. In this paper we review the articulatory-acoustics and the source-filter models of speech production and show that there exist gaps in our present knowledge. We propose a holistic approach of speech signal analysis for future research.

1. INTRODUCTION

Speech production may be modeled at various levels, ranging from the mental to the cognitive to the neuro-physiological to the physiological to the physical. At the physical or peripheral level, a model of speech production may be articulatory or acoustic based. The articulatory-acoustic theory of speech production (AATSP) predicts the transfer function of a passive vocal tract given the articulatory positions. The source mechanism is modeled separately. The acoustic theory of speech of production (ATSP) proposes a source-filter model where a speech signal is modeled as the output of a formant filter excited by an appropriate source signal; For voiced sounds, the source signal happens to be the derivative of glottal pulses, referred to as voice source. In a linear prediction (LP) model, which is a gross engineering approximation to the source-filter model, a speech signal is modeled as the output of an all-pole filter excited either by a quasi-periodic sequence of impulses for voiced sounds and white noise for unvoiced sounds.

Considering the great success in speech technology areas such as speech coding, text-to-speech synthesis (TTS), automatic speech recognition and speaker recognition it may appear that we have a complete and highly successful theory of speech production. But, these technological advances do not imply that we have a full understanding of speech production or perception. Speech coding is successful since it exploits perceptual abilities of a human listener. A TTS system based on a parametric model, formant or LP based, is not natural sounding. Concatenative synthesis is natural sounding but it is difficult to change the speaker's voice and the intonation is often not natural as spliced segments may belong to different syntactic positions. The accuracy of an automatic speech or speaker recognition system drops significantly when there is a change of microphone and / or a change of channel bandwidth. Some believe that these bottle necks may be overcome by intense data collection and statistical modeling. However, the author believes that it is time to get back to the basics. Some criticism on the existing approaches of modeling as well as a probable new approach to study speech signal is presented in this paper.

2. GAPS IN THE EXISTING MODELS

2.1. Overview

The movement of articulators determines the complex 3-D shape of the vocal tract (VT) which has a distinct frequency response. But, vocal tract is passive. Acoustic energy has to be supplied to the vocal tract in order to produce speech sounds. The identification of the two components in speech production, *viz.*, the vocal tract filter and source is known since 1950s, Dunn, 1950, Stevens *et al.*, 1953. Source-Filter theory adopts a reductionistic approach which is commonly used in many scientific disciplines and suffers from the criticism that it does not meet the adage that *"the whole is greater than the sum of its parts"* [Lerner, 1963]. Source-filter theory tacitly assumes that the source and filter parts can be specified and studied independently of each other. In fact, most research relating to speech analysis is based on this supposition of independence of source and filter parts. However, a close look at the mechanism of speech production clearly shows a strong inter-dependence of these two aspects as will be discussed in Sec.II.3.

There are two popular models for speech production (See Fig. 1) [Flanagan, 1965, 1972; Fant, 1960]:

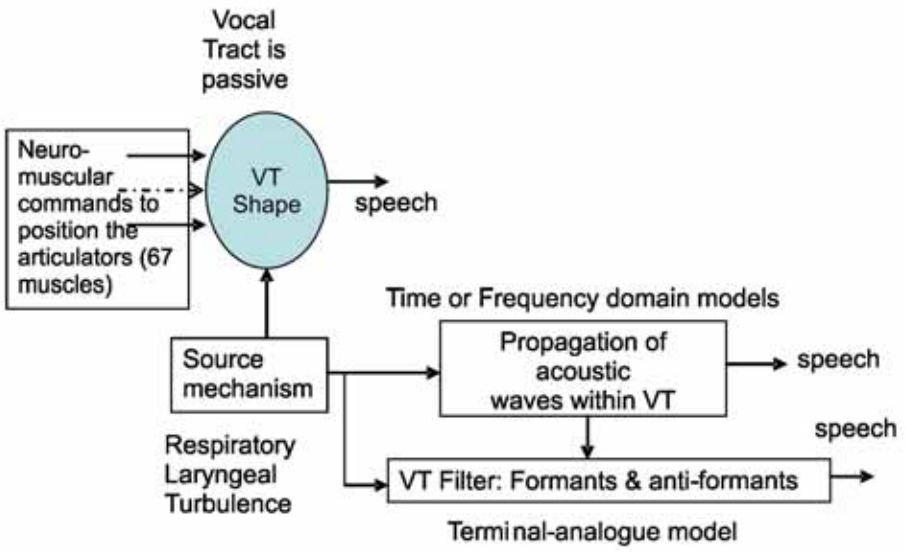

Fig. 1. Modeling Speech Production

(a) **Articulatory-acoustics model:** Within the articulatory-acoustics theory, there are two approaches: (i) the frequency domain approach and (ii) the time domain approach. In both the approaches, the voice source has to be independently specified. But, the source for the unvoiced and stop sounds can be derived from the articulatory process itself, if properly handled.

(b) **Terminal-analogue or formant based model** involves modeling the frequency response or the transfer function of vocal tract filter by means of formants and anti-formants. The source signal is specified independently.

2. 2. Articulatory-acoustics

VT has a complex 3-D shape. But, assuming one-dimensional wave propagation, the VT shape is modeled as a sequence of cylindrical sections of approximately 0.5 cm in length, Fig. 2. The section lengths need not be equal. Each cylindrical section is represented by its equivalent electrical network, Fig. 3. Some of the elements in this electrical network are frequency dependent. This is called lumped parameter network or the transmission line analogue model.

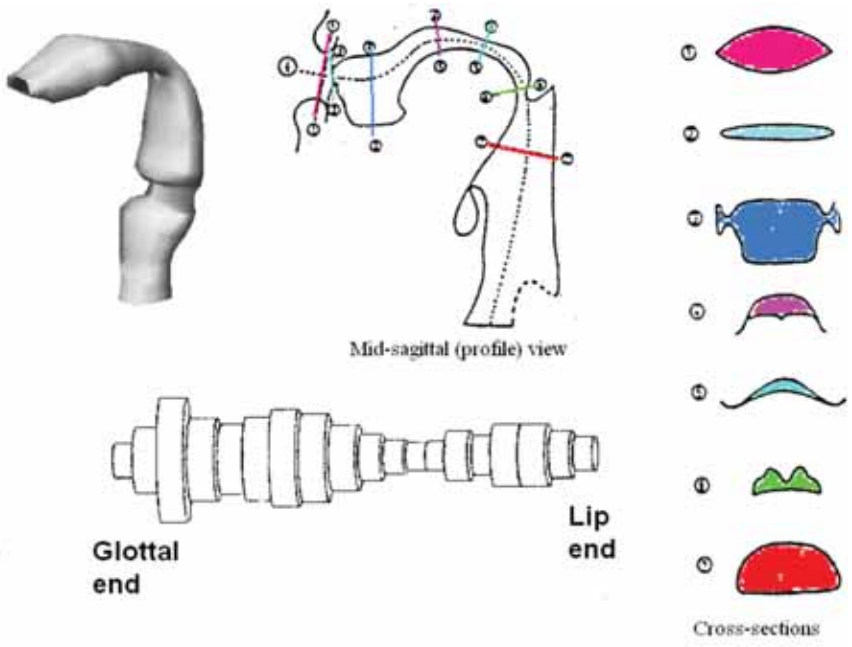

Fig. 2. From a 3-D VT shape to VT area function

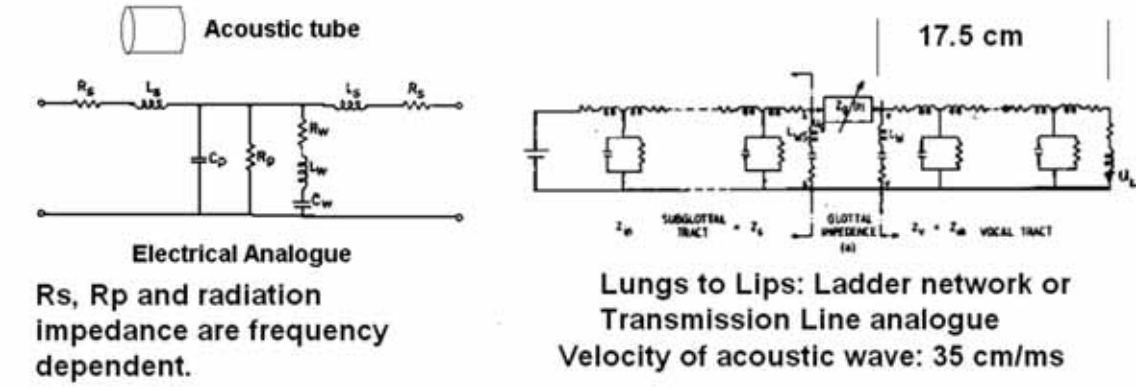

Fig. 3. Electrical analogue equivalent of a single cylindrical section

This electrical analogue has been known sine a long time Dunn, 1950, Stevens et al., 1953. Also, the inverse filtering technique for estimating the voice source was proposed by Miller in 1959. The early theories used two or four tube models of the vocal tract for computing the frequency response. Fant, 1960 validated the articulatory-acoustic theory by a simultaneous recording of cine-radiographic x-ray pictures and also the speech sounds. Using the x-ray pictures he deduced the vocal tract shape with a spatial resolution of about 0.5 cm and thus modeled VT as a large number of cylindrical sections instead of the earlier studies of 2 or 4 tube models. He compared the predicted frequency response based on the articulatory-acoustic theory with the measured short-time spectrum of simultaneously recorded speech sounds. He thus validated the articulatory-acoustic theory for all the speech sounds. However, he made certain assumptions: (a) He assumed hard walled vocal tract. The yielding wall vocal tract model was introduced much later, Sondhi, 1974. (b) He assumed the glottal pulse shape to be constant for voiced speech sounds. But, see Ananthapadmanabha, 1984. (c) He ignored source-filter interaction [Ananthapadmanabha and Fant, 1982]. Not withstanding these assumptions, his contribution has made a very big impact on the field.

There are two approaches to compute the transfer function of a given VT shape, ignoring glottal source and vocal tract coupling effects: (i) the frequency domain approach and (ii) the time domain approach. An ambitious integrated model [Sondhi and Schroeter, 1987], combining the effects of source and filter, has also been attempted where at every instant of time the computations are switched from the time to the frequency domain. The limitations of time and frequency domain approaches are built-into such an integrated model.

There are certain basic limitations in the existing articulatory-acoustic theory. Both time and frequency domain approaches assume 'conservation of mass' which implies that there is no mean air-flow which in turn implies that one must be able to speak for any desired duration with a single breath. However, this is not true. By placing one's palm in front of the lips for sounds such as 'oo' and stops, the presence of the mean flow can be experienced.

Comments on the frequency domain approach : In the case of an electrical network, since the velocity of EM wave propagation is extremely high compared to the physical dimensions of an electrical circuit, the effect of time delay in the propagation of electrical signal within the network may be neglected. But, one has to look into the effect of a finite velocity of acoustic wave propagation (35 cm per mill-second) in the equivalent analogue network. It takes about 0.5 ms for the acoustic waves to propagate from the glottis to the lips, a quantity which is not negligible and is comparable to the duration of a stop burst or the return phase of a glottal cycle. For example, in the production of a labial stop, the acoustic waves have to propagate to the glottis and back to the lips which takes about 1 milli-second. Hence at the instant of labial release, the entire vocal tract does not determine the frequency response of the filter. In fact, within 1 msec, the lips would have separated further and jaws would have opened. Thus there is a continual variation of the VT shape. The interplay between the changing VT shape and acoustic wave propagation has not been studied.

FD approach assumes stationarity, which may be acceptable for an isolated steady sound, i.e., when articulators are not moving. But, in speech production, the articulators are continually moving and during the production of stops there is a rapid change in the articulatory positions. The only advantage of the frequency domain approach is that frequency dependent analogue elements can be accurately represented and the formant frequencies and their bandwidths as well as anti-formants and their bandwidths can be estimated.

Comments on the time domain approach : There are two methods within the time domain approach; lumped parameter method and lattice filter method. Time domain methods can not represent the frequency dependent electrical elements accurately. A lumped parameter method [Ishizaka and Flanagan, 1972] assumes an appropriate input and computes the output signal response using differential equations for the 'L' and 'C' elements. This is a standard linear circuit theory approach. In the digital domain, the replacement of derivatives by difference equations and integrals by trapezoidal rule implies the use of so called bi-linear transformation. The bi-linear transformation warps the spectrum such that the infinite frequency of the analog domain coincides with the folding frequency of the digital domain. The electrical elements can be made time-varying. Both the terms such as Ldi/dt (CdV/dt) as well as idL/dt (VdC/dt) must be included. The latter term is not included in the existing time domain lumped parameter approach. Any change in the electrical analogue parameters introduces transients which also have to be dealt with.

The second method in the time domain approach makes use of reflection coefficients. See for example, Liljencrants, 1985. This approach, called the lattice filter approach, ignores internal losses and assumes all losses to be only at the source end. Some attempts have been made to approximately model the internal losses within the paradigm of a lattice filter approach. The frequency dependent acoustic loss elements cannot be represented accurately. This approach can explicitly handle the acoustic delay between two sections. But, it demands that all sections be of equal length and that the vocal tract length (VTL) be a constant and be an integer multiple of the section length. The delay in propagation of the acoustic wave from one section to the adjacent section is determined by the sampling interval and the velocity of acoustic waves. If the section length is made small to improve the spatial resolution, then the sampling frequency has to be increased there by increasing the number of computations. It is well known that the vocal tract

length continually changes and is different for different sounds. Example: For vowel /a/, VTL=17 cm, for vowel /i/, VTL=16 cm and for vowel /u/, VTL=19.5 cm. If we assume a fixed VT length of 17 cm then the formants of vowel /i/ are scaled up by a factor 16/17 (6%) and the formant frequencies of vowel /u/ are scaled down by a factor 17/19.5 (15%) resulting in incorrect predictions.

Summary of the gaps in articulatory-acoustics :

All models assume 'conservation of mass' and hence an absence of mean air flow. VT frequency response at f=0 is assumed to be unity.

Most models ignore the source-filter interaction effect.

Gaps in FD Approach :

1. Effect of finite velocity (35 cm/ms) is ignored.
2. Assumes stationary articulatroy positions

Gaps in TD Approach: Lumped parameter model :

1. Frequency dependent terms are not accurately represented.
2. Effect of time-varying parameters not taken into account.
3. Using differencing in place of derivative introduces spectral warping due to bi-linear transformation.

Gaps in TD Approach: Lattice or reflection coefficient model :

1. Frequency dependent terms are not accurately represented.
2. Assumes the vocal tract length to be a constant for all speech sounds. This introduces errors in the estimation of formant frequencies.

2.3. Comments on Source-Filter (Terminal analogue) Model

The common assumption in a source-filter model is that the two components are independent of each other. In this context we present some aspects of the strong mutual dependency of source and filter parts.

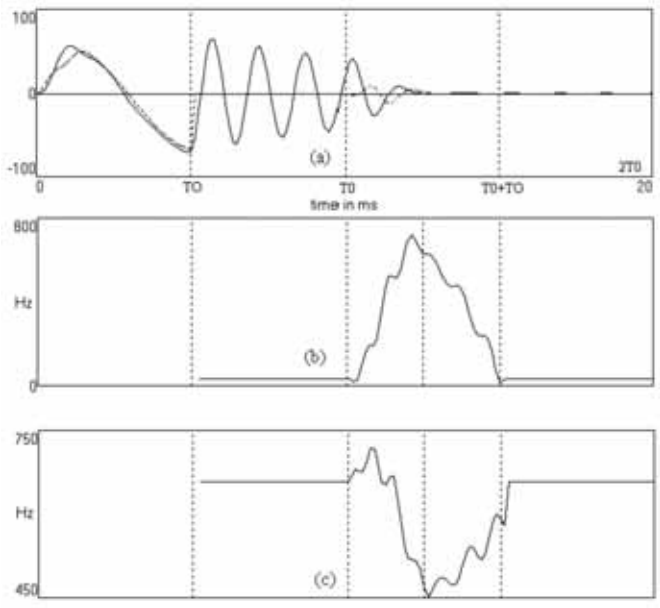

Fig. 4. (a) Response of first formant showing the effect of glottal opening. (b) Estimated instantaneous bandwidth. (c) Estimated instantaneous resonant frequency.

For example, in the production of vowels, it is well known that the bandwidths and hence the levels of the first two formants are determined by the area of glottal opening and open quotient [Flanagan, 1965, 1972]. Within a pitch period, due to the source-filter interaction the formant frequency and bandwidth continually change and hence a resonator or a formant filter model is not accurate [Ananthapadmanabha and Fant, 1982, Ananthapadmanabha, 2012]. See Fig. 4. In the case of a breathy voice, due to sub-glottal coupling, tracheal pole-zero pairs may be expected even for a vowel sound. During a CV or VC transition, the glottal abduction affects the formant data and especially the formant bandwidths [Stevens, 1998]. See Fig.5. It is well known that the intrinsic pitch is higher for of high vowels (/i/, /u/) compared to mid and low vowels. Perception experiments show that for the same formant data, a change of pitch changes the vowel quality.

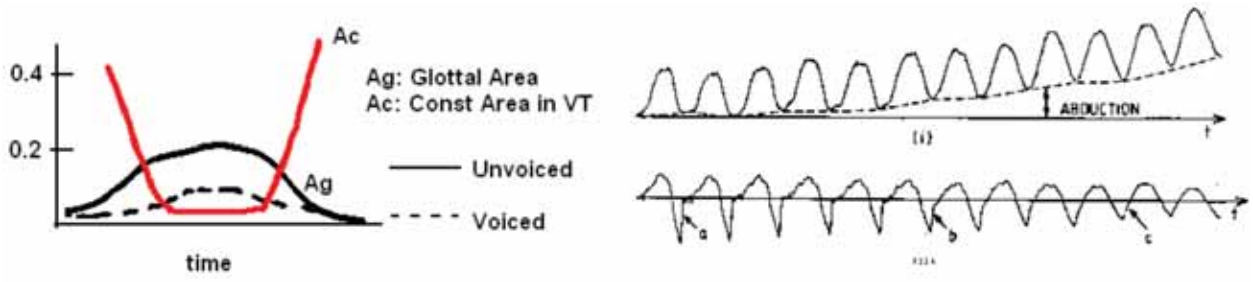

Fig. 5. Mutual dependence of vocal tract constriction and glottal abduction resulting in varying formant bandwidths, formant levels and spectral slope during a CV and VC transition.

The mutual dependence of source and filter is even more explicit in the case of production of fricatives and stops. It is the specific articulatory configuration and the dynamics of the articulators that at once determines both the source as well as the filter characteristics. In the case of fricatives, the source is of bandpass type centered at a very high frequency and with a broad bandwidth and has asymmetric characteristics with respect to the peak in the spectrum, Stevens, 1998. See Fig. 6. But, linear prediction theory and most text books and research papers incorrectly describe the source for unvoiced sounds as white noise. White noise is an approximation to the actual unvoiced source and the frequency response of a fricative speech segment combines the vocal tract filter response and noise source spectral characteristics. The two components cannot be easily separated. In the case of production of a stop there are rapidly varying temporal and spectral features [Stevens, 1998]. Fig. 7.

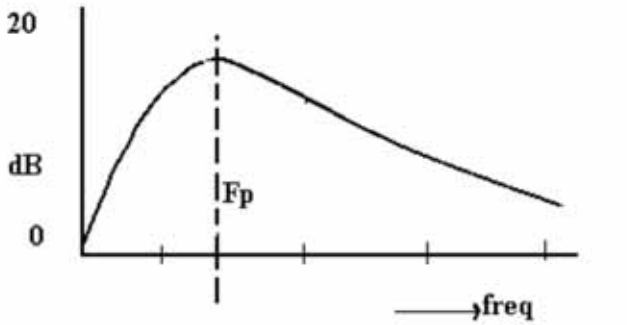

Fig. 6. A typical source spectrum of a fricative is a broad bandpass filer and not white noise.

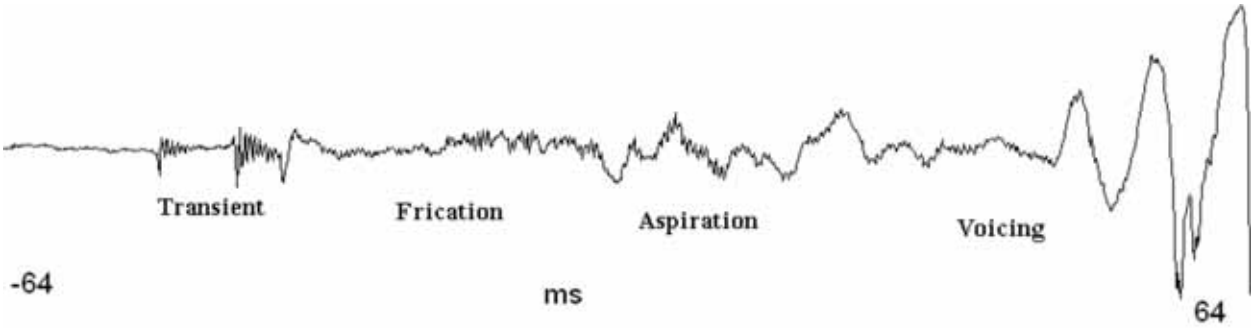

Fig. 7. Rapidly changing temporal and spectral events associated with a stop.

This mutual dependence between the source and VT filter parts can be demonstrated through a simple experiment of listening only to the source component [Ananthapadmanabha, 1982]. Digitized speech signal of an utterance is analyzed. The formant data are determined frame-wise and corrected for any formant tracking errors. The speech signal is then inverse filtered with appropriate interpolation of the frame-wise formant data to obtain a source signal. Further, a parametric model is fitted to the source signal. The spectrogram of such a signal is shown in Fig. 8. It may be noticed that there are no traces of formant tracks.

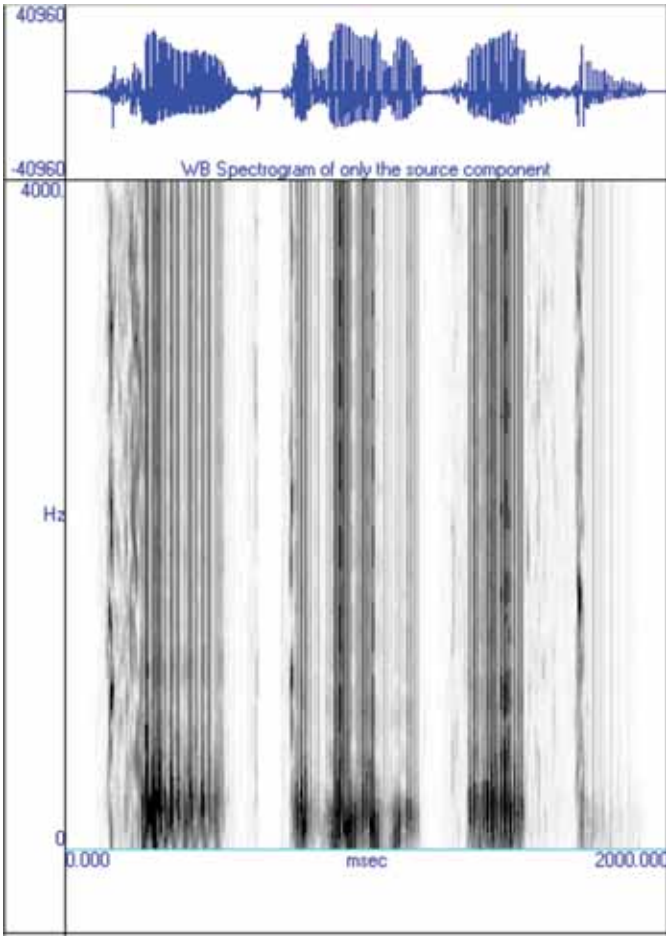

Fig. 8. Spectrogram of only the source component of the utterance 'speech communication'.

When one listens to the so called 'source component only' one can hear a 'phonetic message', especially when one has an a priori knowledge about the utterance. An audio demonstration will be presented. The issue here is 'how come the phonetic message' is heard when there are no formant tracks? It shows that the dynamics of source signal components is able to stimulate the appropriate cortical areas and give rise to a phonetic or linguistic impression.

A corollary to the above experiment is relating to the speaker's identity. The term perceived 'voice' is often confused with the physical 'voice source'. After separating the speech signal into source and filter components, if the voice source (glottal) parameters are kept constant for all the voiced sounds and the speech signal is re-synthesized, the speaker's identity is still perceived. An audio demonstration is presented. This clearly demonstrates that 'voice' and 'voice source' are distinctly different phenomena. Voice quality also carries phonetic message along with it. That is, a speaker's identity is preserved in the formant tracks [Laver, 1980]

3. HOLISTIC APPROACH VIA SPEECH ANALYSIS

The author believes that the problem of articulatory-acoustics requires a new approach which is yet to be formulated. In its absence we can only begin with the speech signal and try to study the mutual dependence of the so called source and filter parts. For example, Peterson and Barney, 1952 have not only published the formant data but also the formant levels (indirectly the bandwidths) and F0. We have to study the co-variation of all the acoustic parameters. In other words we have to study the mutual dependence of the various parameters. Also, the subtle differences between the digital and analog representations have to be clearly understood. The digital representation of an analog transfer function often ignores the higher-pole correction factor and approximates the analog phase response. A complete and satisfactory solution to speech analysis is also yet to emerge.

4. CONCLUSION

We have presented some gaps in the existing approaches for computing the vocal tract filter response based on articulatory-acoustics theory. We have demonstrated that there exists a strong mutual dependence between the source and filter components contrary to the belief that these two components are mutually independent. We have argued that speech analysis must consider all the relevant parameters together and study their mutual dependency. Such an experimental study has to be conducted on a large scale, an area which is wide open.

5. REFERENCES

[1] T.V. ANANTHAPADMANABHA, and G. FANT, 1982. *Calculation of true glottal flow and its components*, STL-QPSR 1, pp.1-30. Also Speech Communication, **1**, 167-184.

[2] T.V. ANANTHAPADMANABHA, 1982. *Intelligibility carried by the source function*, STL-QPSR-4, 49-64.

[3] T.V. ANANTHAPADMANABHA, 1984. *Acoustic analysis of voice source dynamics*, STL-QPSR 2-3, 1-24.

[4] T.V. ANANTHAPADMANABHA, 2012. *Aerodynamic and acoustic theory of voice production*, in *Forensic Speaker Recognition*, Eds. Amy Neustein and Hemant Patil, Springer, NY, 2012. Ch.12.

[5] H.K. DUNN, 1950. *The calculation of vowel resonances and an electrical vocal tract*, JASA, 22, 740-753.

[6] G. FANT, 1960. *Acoustic theory of speech production*, Mouton Hague.

[7] J. L. FLANAGAN, 1965, 1972. *Speech Analysis, Synthesis and Perception*, Springer Verlag, NY First Edn. 1965, Sec. Edn. 1972. Also see Third Edn. Flanagan et al, 2008.

[8] AK. ISHIZ and J.L. FLANAGAN, 1972. *Synthesis of voiced sounds from the two mass model of the vocal cords*, BSTJ, **51**, 1233-1267.

[9] J. LAVER, 1908. *Phonetic Description of Voice Quality*, Cambridge University Press, UK, 1980.

[10] LERNER DANIEL, Editor, 1963. *Parts and Wholes* Hayden Colloquium on Scientific Method and Concept, The Free Press of Gelncoe, London. See also: (a) Edward Pucell, *Parts and Wholes in Physics.* (b) Ernest Nagel, *Wholes, Sums and Organic Unities*.

[11] J. LILJENCRANTS, 1985. *Speech synthesis with a reflection-type line analog*, D.Sc. Thesis, RIT, Stockholm.

[12] R.L. MILLER, 1959. *N**ature of vocal cord wave,*** JASA 3**1**, 667-677.

[13] G.E. PETERSON and H.L. BARNEY, 1952. *Control methods in a study of vowels,* JASA **24**, 175-184.

[14] M.M. SONDHI, 1974. *Model for wave propagation in a lossy vocal tract*, JASA. **55**(5), 1070-1075.

[15] M.M. SONDHI and J. SCHROETER, 1987. *A hybrid time-frequency domain articulatory speech synthesizer*, IEEE Trans. Ac. Speech and Sig Proc., **35**(7), 955-967.

[16] K.N. STEVENS, S. KAOWSKI and G. FANT, 1953. An electrical analog of the vocal tract, JASA., **25**(4), 734-742.

[17] K.N. STEVENS, 1998. *Acoustic Phonetics*, MIT Press, Cambridge.

INFORMATION FOR AUTHORS

ARTICLES

The Journal of Acoustical Society of India (JASI) is a refereed publication published quarterly by the Acoustical Society of India (ASI). JASI includes refereed articles, technical notes, letters-to-the-editor, book review and announcements of general interest to readers.

Articles may be theoretical or experimental in nature. But those which combine theoretical and experimental approaches to solve acoustics problems are particularly welcome. Technical notes, letters-to-the-editor and announcements may also be submitted. Articles must not have been published previously in other engineering or scientific journals. Articles in the following are particularly encouraged: applied acoustics, acoustical materials, active noise & vibration control, bioacoustics, communication acoustics including speech, computational acoustics, electro-acoustics and audio engineering, environmental acoustics, musical acoustics, non-linear acoustics, noise, physical acoustics, physiological and psychological acoustics, quieter technologies, room and building acoustics, structural acoustics and vibration, ultrasonics, underwater acoustics.

Authors whose articles are accepted for publication must transfer copyright of their articles to the ASI. This transfer involves publication only and does not in any way alter the author's traditional right regarding his/her articles.

PREPARATION OF MANUSCRIPTS

All manuscripts are refereed by at least two referees and are reviewed by the Publication Committee (all editors) before acceptance. Manuscripts of articles and technical notes should be submitted for review electronically to the Chief Editor by e-mail or by express mail on a disc. JASI maintains a high standard in the reviewing process and only accept papers of high quality. On acceptance, revised articles of all authors should be submitted to the Chief Editor by e-mail or by express mail.

Text of the manuscript should be double-spaced on A4 size paper, subdivided by main headings-typed in upper and lower case flush centre, with one line of space above and below and sub-headings within a section-typed in upper and lower case understood, flush left, followed by a period. Sub-sub headings should be italic. Articles should be written so that readers in different fields of acoustics can understand them easily. Manuscripts are only published if not normally exceeding twenty double-spaced text pages. If figures and illustrations are included then normally they should be restricted to no more than twelve-fifteen.

The first page of manuscripts should include on separate lines, the title of article, the names, of authors, affiliations and mailing addresses of authors in upper and lowers case. Do not include the author's title, position or degrees. Give an adequate post office address including pin or other postal code and the name of the city. An abstract of not more than 200 words should be included with each article. References should be numbered consecutively throughout the article with the number appearing as a superscript at the end of the sentence unless such placement causes ambiguity. The references should be grouped together, double spaced at the end of the article on a separate page. Footnotes are discouraged. Abbreviations and special terms must be defined if used.

EQUATIONS

Mathematical expressions should be typewritten as completely as possible. Equation should be numbered consecutively throughout the body of the article at the right hand margin in parentheses. Use letters and numbers for any equations in an appendix: Appendix A: (A1, (A2), etc. Equation numbers in the running text should be enclosed in parentheses, i.e., Eq. (1), Eqs. (1a) and (2a). Figures should be referred to as Fig. 1, Fig. 2, etc. Reference to table is in full: Table 1, Table 2, etc. Metric units should be used: the preferred from of metric unit is the System International (SI).

REFERENCES

The order and style of information differs slightly between periodical and book references and between published and unpublished references, depending on the available publication entries. A few examples are shown below.

Periodicals:

[1] S.R. Pride and M.W. Haartsen, 1996. Electroseismic wave properties, *J. Acoust. Soc. Am.*, **100** (3), 1301-1315.

[2] S.-H. Kim and I. Lee, 1996. Aeroelastic analysis of a flexible airfoil with free play non-linearity, *J. Sound Vib.*, **193** (4), 823-846.

Books:

[1] E.S. Skudzryk, 1968. *Simple and Comlex Vibratory Systems*, the Pennsylvania State University Press, London.

[2] E.H. Dowell, 1975. *Aeroelasticity of plates and shells*, Nordhoff, Leyden.

Others:

[1] J.N. Yang and A. Akbarpour, 1987. Technical Report NCEER-87-0007, Instantaneous Optimal Control Law For Tall Buildings Under Seismic Excitations.

SUMISSIONS

All materials from authors should be submitted in electronic form to the JASI Chief Editor: B. Chakraborty, CSIR - National Institute of Oceanography, Dona Paula, Goa-403 004, Tel: +91.832.2450.318, Fax: +91.832.2450.602,(e-mail: bishwajit@nio.org) For the item to be published in a given issue of a journal, the manuscript must reach the Chief Editor at least twelve week before the publication date.

SUMISSION OF ACCEPTED MANUSCRIPT

On acceptance, revised articles should be submitted in electronic form to the JASI Chief Editor (bishwajit@nio.org)